River Rapids

Conference Proceedings of the Society for Experimental Mechanics Series

Dynamics of Civil Structures, Volume 2

P. Scott Harvey
Fernando Moreu

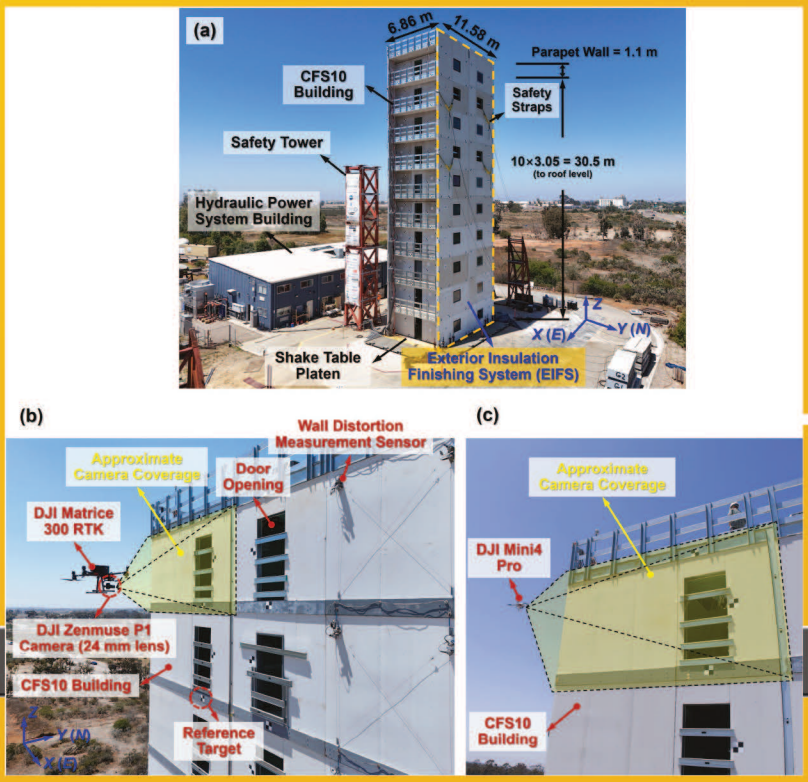

Proceedings of the 44th IMAC, A Conference and Exposition on Structural Dynamics 2026

River Publishers

Conference Proceedings of the Society for Experimental Mechanics Series

Series Editor

Kristin B. Zimmerman
Society for Experimental Mechanics, Inc.,
Bethel, USA

The Conference Proceedings of the Society for Experimental Mechanics Series presents early findings and case studies from a wide range of fundamental and applied work across the broad range of fields that comprise Experimental Mechanics. Series volumes follow the principle tracks or focus topics featured in each of the Society's two annual conferences: IMAC, A Conference and Exposition on Structural Dynamics, and the Society's Annual Conference & Exposition and will address critical areas of interest to researchers and design engineers working in all areas of Structural Dynamics, Solid Mechanics and Materials Research.

P. Scott Harvey · Fernando Moreu
Editors

Dynamics of Civil Structures, 2026, Vol. 2

Proceedings of the 44th IMAC, A Conference and Exposition on Structural Dynamics 2026



River Publishers

Published, sold and distributed by:

River Publishers
Broagervej 10
9260 Gistrup
Denmark

www.riverpublishers.com

ISBN 97887-438-1441-2 (Hardback)

ISBN 97887-438-1413-9 (eBook)

https://doi.org/10.13052/rp-9788743814139

Conference Proceedings of the Society for Experimental Mechanics

An imprint of River Publishers

© The Society for Experimental Mechanics, Inc. 2026

This work is subject to copyright. All rights are solely and exclusively licensed by the Publisher, whether the whole or part of the material is concerned, specifically the rights of translation, reprinting, reuse of illustrations, recitation, broadcasting, or reproduction in any other physical way, and transmission or information storage and retrieval, electronic adaptation, computer software, or by similar or dissimilar methodology now known or hereafter developed.

The use of general descriptive names, registered names, trademarks, service marks, etc. in this publication does not imply, even in the absence of a specific statement, that such names are exempt from the relevant protective laws and regulations and therefore free for general use. The publisher, the authors, and the editors are safe to assume that the advice and information in this book are believed to be true and accurate at the date of publication. Neither the publisher nor the authors or the editors give a warranty, expressed or implied, with respect to the material contained herein or for any errors or omissions that may have been made. The publisher remains neutral with regard to jurisdictional claims in published maps and institutional affiliations.

Preface

Dynamics of Civil Structures represents one of ten volumes of technical papers presented at the 44th IMAC, A Conference and Exposition on Structural Dynamics, organized by the Society for Experimental Mechanics, and held January 19-22, 2026. The full proceedings also include volumes on Nonlinear Structures & Systems; Model Validation and Uncertainty Quantification; Dynamic Substructuring & Transfer Path Analysis; Special Topics & Experimental Techniques in Structural Dynamics; Computer Vision & SLDV for Structural Dynamics; Dynamic Environments & Durability Testing; Topics in Modal Analysis & Parameter Identification in Structural Dynamics; Data Science in Engineering; and Structural Health Monitoring, Metamaterials, Metastructures & Additive Manufacturing and Dynamics of Biomedical and Bioinspired Systems.

Each collection presents early findings from analytical, experimental and computational investigations on an important area within Structural Dynamics. Dynamics of Civil Structures is one of these areas which cover topics of interest of several disciplines in engineering and science.

The Dynamics of Civil Structures Technical Division serves as a primary focal point within the SEM umbrella for technical activities devoted to civil structures analysis, testing, monitoring, and assessment. This volume covers a variety of topics including structural vibrations, damage identification, human-structure interaction, vibration control, computer vision, model updating, modal analysis of in-service structures, innovative measurement techniques and mobile sensing, and bridge dynamics among many other topics.

Papers in this volume cover testing and analysis of different kinds of civil engineering structures, including buildings, bridges, wind turbine towers, marine structures, historical constructions, and light poles.

The organizers would like to thank the authors, presenters, session organizers, and session chairs for their participation in this track.

Editors:

P. Scott Harvey – University of Oklahoma, OK, USA;
Fernando Moreu – University of New Mexico, NM, USA

Contents

1 **Seismic Damage Assessment of a Full-Scale 10-Story Building Using UAV Vision-Based Sensing** 1
Ruipu Ji, Hilda Lozano Bravo, Eric Lo, Tanner J. Norton, John W. Driscoll, Jiachen Zhang, Falko Kuester, and Tara C. Hutchinson

2 **Examination of the Dynamic Performance of Textile Reinforced Concrete with Post-consumer Waste Denim Fibers** 9
Rachel Hollingsworth and Yohanna MejiaCruz

3 **Structural Integrity Assessments of a Train Bridge Using SHM Data** 17
Bjørn T. Svendsen, Niels Dollerup, and Eimantas Poskus

4 **Human-Induced Building Vibrations: A Perspective on Their Role for Long-Term Health Monitoring** 31
Jinsi Guo and Yiwen Dong

5 **Experimental Evaluation of an Elastomeric Tuned Mass Damper Device for Vibration Suppression on a Laboratory Floor** 35
Sahabeddin Rifai, Russell A. Larsen, Robert Baxter, Joshua M. Mouras, Ronald Klemencic, and Onur Avci

6 **A Comparative Study of Developing Seismic Fragility Models using Random Sampling Simulations and Machine Learning** 47
Mohamed Tareq Soliman, Ufuk Yazgan, and Onur Avci

7 **Performance Evaluation of an Eddy Current Tuned Mass Damper on a Full-Scale Laboratory Floor** 55
Sahabeddin Rifai, Russell A. Larsen, Robert Baxter, Joshua M. Mouras, Ronald Klemencic, and Onur Avci

8 **Effect of Stationary Occupants on Damping and Vibration Response of a Modular All-Steel Laboratory Floor** 65
Sahabeddin Rifai, Ahmad Rababah, Feras Abla, Mohamed Tareq Soliman, and Onur Avci

9 **Vibration Serviceability of a Modular All-Steel Floor Under Simulated Façade and Service Loads** 75
Sahabeddin Rifai, Ahmad Rababah, Feras Abla, Mohamed Tareq Soliman, and Onur Avci

10 **Influence of Electrical Components and Supports on the Modal Characteristics of Timber Distribution Poles** 83
Timothy Kernicky and Matthew Whelan

11 **Preliminary Design of Liquid-Based Damping Systems for Building Motion Control in Wind** 93
Lee, Chien-Shen, McNamara, Kevin, Mills, Matthew J., and Robinson, Jamieson K.

12 **Modal Identification and MCMC-Based Bayesian Model Updating for Optimization of Material Parameters in Bridges** 99
Sangwon Park and Minwoo Chang

13 **Impact of Support Settlement on the Seismic Fragility of a Substandard RC Frame with Plan Irregularity: Static Response and Fragility Assessment** 107
Feras Abla, Shahin Huseynli, Ufuk Yazgan, and Onur Avci

14 Dynamic Properties by OMA and Modal Updating of a Mayan Temple 117
T. Nunez and C. E. Ventura

15 The Great Train Disaster of 2025: Isolating Sensitive Equipment from Rail-Induced Vibration 127
Michael J. Wesolowsky, Ph.D., P.Eng., Muhammad Rahman, M.A.Sc., P.Eng.,
Rabih Alkhatib, Ph.D., P.Eng., Brad Pridham, Ph.D., P.Eng.

16 Design and Construction of a Low-Cost Portable Seismic Shaking Table 137
Eliú Pineda and A. Ortiz

17 Performance Evaluation of a Damped Vibration Absorber for Traffic Signal and Sign Structures 143
Richard Christenson and Carl Macchietto

18 A Pilot Study on Pedestrian Comfort Under Vertical Vibrations 147
Rajesh Govindan, Bintian Lin, Genevieve K. R. Williams, and Stana Živanović

Chapter 1
Seismic Damage Assessment of a Full-Scale 10-Story Building Using UAV Vision-Based Sensing

Ruipu Ji, Hilda Lozano Bravo, Eric Lo, Tanner J. Norton, John W. Driscoll, Jiachen Zhang, Falko Kuester, and Tara C. Hutchinson

Abstract Seismic damage assessment is critical for safety evaluation and functional recovery of structures after earthquakes. Unmanned aerial vehicle (UAV) vision-based sensing has become an emerging technology supplementing and advancing conventional data collection practices for post-disaster evaluation due to its accessibility and efficiency. This study presents a UAV vision-based sensing application for damage assessment of a full-scale 10-story cold-formed steel (CFS) framed building during a series of shake table tests conducted at the 6 degree-of-freedom Large High-Performance Outdoor Shake Table (LHPOST6) at UC San Diego. The proposed damage assessment methodology integrates high-resolution aerial imagery collected before and after seismic tests and multiple image processing and computer vision algorithms to enable the assessment of structural and nonstructural damage with small scales. The location and scale of the damage is determined based on the thresholded absolute difference within the intensity normalized co-registered image pairs. A selected damage detection result using the proposed method applied on the north façade of the building is presented and compared to photogrammetry and manual inspection results. These findings highlight the potential of UAV vision-based sensing for post-earthquake reconnaissance, enabling assessment of even minor, small-scale damage realized during seismic excitations.

Keywords Unmanned Aerial Vehicle · Vision-Based Sensing · Image Processing · Shake Table Tests · Damage Assessment

Introduction

Unmanned aerial vehicle (UAV) vision-based sensing has emerged as a cost-effective approach supplementing and advancing conventional data collection practices for safety evaluation and functional recovery of infrastructure after earthquakes [1, 2]. Notable benefits of using UAV-based tools include its non-invasive and remote capture potential, aspects that are particularly useful for infrastructure with large scales. Besides tracking the structural displacement from the UAV-based imagery under seismic excitations [3–5], capturing the post-earthquake state of the structures for rapid and accurate assessment of structural and nonstructural damage is also critical. Researchers have been investigating the application of UAV vision-based sensing for seismic damage assessment for years with a focus on the major structural damage with a relatively large scale with respect to the size of the image frame [6, 7]. However, modern civil structures are more likely to have minor damage to the nonstructural components than to suffer extensive damage to the major structural members with the use of high-strength structural materials and improved structural design approaches [8]. Detection and assessment of such minor damage remain essential since they indicate early signs of structural deterioration and affect the overall safety and functionality of the structure.

This study investigates UAV vision-based sensing for damage assessment of a full-scale 10-story cold-formed steel (CFS) framed building during a series of shake table tests conducted at the 6 degree-of-freedom Large High-Performance

Ruipu Ji · Jiachen Zhang · Falko Kuester · Tara C. Hutchinson
Department of Structural Engineering, University of California San Diego
e-mail: r5ji@ucsd.edu; jiz149@ucsd.edu; fkuester@ucsd.edu; tara@ucsd.edu

Hilda Lozano Bravo · Eric Lo · Tanner J. Norton · John W. Driscoll
Qualcomm Institute, University of California San Diego
e-mail: hlozanobravo@ucsd.edu; eklo@ucsd.edu; tanorton@ucsd.edu; jwdrisco@ucsd.edu

© The Author(s), under exclusive license to River Publishers 2026

Kristin B. Zimmerman, PhD (eds.), *Dynamics of Civil Structures, 2026, Vol. 2*, Conference Proceedings of the Society for Experimental Mechanics Series, https://doi.org/10.13052/rp-9788743814139

Outdoor Shake Table (LHPOST6) at UC San Diego. The schedule and implementation plan for two UAV vision-based inspection approaches during the seismic test program are presented including photogrammetry and image-based inspection. A damage assessment methodology for the image-based inspection is proposed, which integrates high-resolution aerial imagery collected before and after the seismic test and multiple image processing and computer vision algorithms to enable the assessment of structural and nonstructural damage observable at small scales. The location and scale of the damage is extracted by the thresholded absolute difference within the intensity normalized co-registered image pairs with baseline (pre-test) and damage (post-test) images. The proposed methodology is illustrated using a selected damage from the exterior insulation finishing system (EIFS) on the north façade of the building. The damage detected by the image-processing based methodology shows reasonable agreement with photogrammetry results and manual inspection results.

UAV Vision-Based Seismic Damage Assessment Plan for CFS10 Seismic Test Program

A full-scale 10-story cold-formed steel (CFS) framed building, coined CFS10, was constructed and tested under a series of shake table tests [9] at the 6-DOF Large High-Performance Outdoor Shake Table (LHPOST6) [10] at UC San Diego. The CFS10 building has a total height of 30.5 m (to the roof level) and a floor plan measuring 6.86 m × 11.58 m as shown in Fig. 1(a). In addition to the load bearing CFS studs and CFS-sheathed shear walls, the building was detailed with various nonstructural components including an exterior face with a stucco-based exterior insulation and finishing system (EIFS) on the north side of the building. Stucco-based EIFS is a common exterior finish system for CFS buildings, though it has lower strength compared to CFS structural components and nonstructural drywall systems. Therefore, it is more likely to be damaged during extreme events such as earthquakes. A pair of images of a cracked region from the EIFS on the north side of the building is selected as an example to illustrate the proposed damage detection methodology.

A series of shake table tests with 18 multi-directional earthquake motions scaled to various hazard levels were performed on the CFS10 building as presented in Table 1 [9, 11]. The UAV vision-based seismic damage assessment flights were conducted following significant milestones during the test program, applying two different sensing approaches, namely photogrammetry inspection and image-based inspection as shown in Fig. 1(b) and 1(c). For the photogrammetry inspection, which aimed at creating a digital twin for the building specimen, a quadrotor UAV with real-time kinematic (RTK) support (DJI Matrice 300 RTK) equipped with a 45-megapixel resolution image sensor (DJI Zenmuse P1 camera) and 24 mm lens, was deployed in a vertical lawnmower flight pattern for each side of the building followed by a horizontal lawnmower pattern for the roof [12, 13]. Details of the photogrammetry model development are provided in Lozano Bravo et al. [13]. The image-based inspection, which aimed for direct comparison between images captured after each test phase, utilized a small quadrotor UAV (DJI Mini4 Pro) with its default onboard camera, and the flight was conducted in the vertical lawnmower pattern around the building. The UAV hovered in front of each structural or nonstructural component of interest at a distance varying between 1 and 5 m from the building façade to cover the entire exterior of the building including exterior drywalls, windows, exterior door openings, and exterior insulation finishing system (EIFS). Table 2 presents the specifications of the UAV platforms and the camera models used for inspection flights, while Table 3 presents the raw image collection from

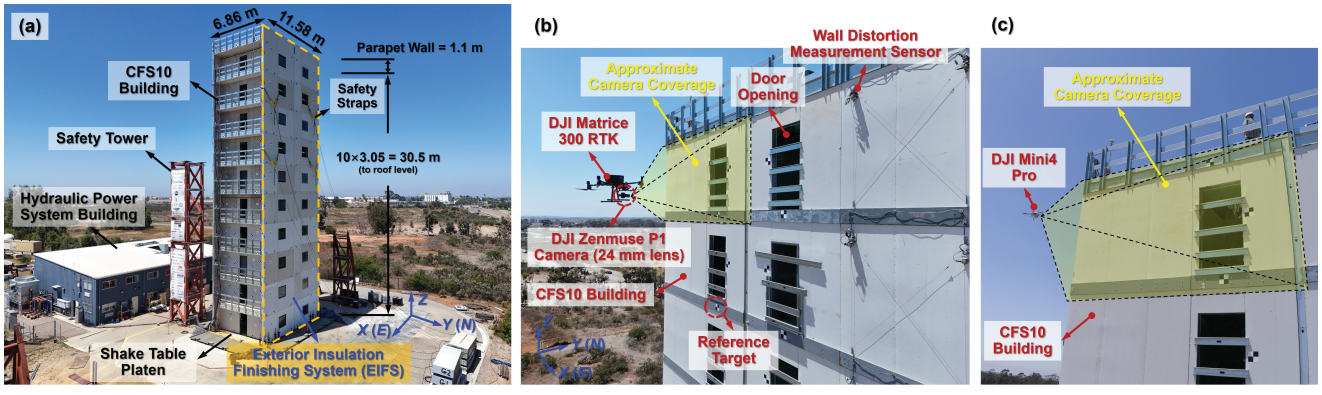

Fig. 1 Overview of the CFS10 building specimen and image collection for the UAV vision-based post-earthquake structural damage assessment: (a) Northeast aerial view of the CFS10 building, (b) Photogrammetry inspection flight, (3) Image-based inspection flight.

Table 1 Seismic test protocol imposed on the CFS10 building and schedule for UAV vision-based structural inspection [9, 11].

Hazard Level	MID[1]	Earthquake Event				Input DOF	Components		$D_{5\text{-}95}$[2] [sec]	Achieved Peak Input Acceleration [g]		
		Name, Location	Year	M_w	Recording Station		X	Y		X	Y	Z
Photogrammetry Inspection #1												
Image-Based Inspection #1												
SLE[3]	1[4]	Loma Prieta, California	1989	6.9	Gilroy Array #3	XYZ	90°	0°	11.4	0.126	0.122	0.082
Image-Based Inspection #2												
SLE	2	Loma Prieta, California	1989	6.9	Gilroy Array #3	XYZ	90°	0°	11.4	0.118	0.114	0.096
	3					X	90°		11.4	0.133	0.041	0.025
	4					Y		0°	6.4	0.042	0.109	0.024
	5	Northridge, California	1994	6.7	LA City Terrace	XYZ	90°	180°	11.9	0.125	0.121	0.081
	6					XYZ	180°	90°	11.9	0.184	0.094	0.084
	7					X	180°		11.9	0.168	0.027	0.023
	8					Y		90°	11.6	0.026	0.093	0.021
	9	Cape Mendocino, California	1992	7.0	Rio Dell Overpass	XYZ	270°	360°	15.3	0.084	0.109	0.099
	10					XYZ	360°	270°	15.3	0.078	0.122	0.151
	11[5]	Kahramanmaras, Türkiye	2023	7.8	4611	XYZ	E	N	43.4	0.095	0.075	0.050
	12					XYZ	E	N	43.4	0.117	0.110	0.064
	13	Elbistan, Türkiye	2023	7.5	4611	XYZ	E	N	35.1	0.100	0.061	0.052
	14	Maule, Chile	2010	8.8	Curico Hospital	XY	EW	NS	45.2	0.097	0.091	0.033
Photogrammetry Inspection #2												
Image-Based Inspection #3												
SLE	15	Kahramanmaras, Türkiye	2023	7.8	4611	XYZ	E	N	43.4	0.119	0.089	0.063
DE[3]	16	Loma Prieta, California	1989	6.9	Gilroy Array #3	XY	90°	0°	11.4	0.454	0.388	0.014
Photogrammetry Inspection #3												
Image-Based Inspection #4												
MCE_R[3]	17	Loma Prieta, California	1989	6.9	Gilroy Array #3	XY	90°	0°	11.4	0.723	0.619	0.016
Photogrammetry Inspection #4												
Image-Based Inspection #5												
MCE_R	18	Cape Mendocino, California	1992	7.0	Rio Dell Overpass	XY	360°	270°	15.3	0.782	0.336	0.025
Photogrammetry Inspection #5												
Image-Based Inspection #6												

[1] MID = motion identification.
[2] $D_{5\text{-}95}$: Significant duration of strong shaking computed as the time interval between 5% and 95% Arias Intensity per original record (max component).
[3] SLE = service level earthquake, DE = design earthquake, and MCE_R = risk-targeted maximum considered earthquake.
[4] MID1 was conducted with the stairs in a locked configuration.
[5] MID11 was targeted to 75% SLE.

Table 2 Specifications of the UAV platforms and camera models for CFS10 post-earthquake structural inspection [14].

UAV Model	Inspection Type	Unfolded Size [$L \times W \times H$-mm]	Battery Life [min]	Camera Model	Image Resolution
DJI Matrice 300 RTK	Photogrammetry	810×670×430	55	DJI Zenmuse P1 camera (24 mm lens)	8192×5460
DJI Mini4 Pro	Image-based	298×373×101	39	Default onboard camera	8064×6048

Table 3 Statistics of the raw image collection for CFS10 post-earthquake structural inspection.

Inspection Event	Image-Based Inspection		Photogrammetry Inspection	
	Inspection #	Raw Image Count	Inspection #	Raw Image Count
Pre-test	#1	199	#1	1920
End of locked stairs configuration	#2	177	-	-
End of SLE test phase	#3	156	#2	1931
End of DE test phase	#4	276	#3	2442
End of the 1st MCER test	#5	235	#4	2809
End of the 2nd MCER test	#6	246	#5	2493

photogrammetry inspection flights and image-based inspection flights statistics, as obtained during the CFS10 seismic test program.

Damage Detection Based on Intensity Normalized Co-Registered Image Pairs

This section presents the seismic damage detection methodology proposed for use with the imagery collected from the image-based inspection flights, see Fig. 2. The general idea is to extract the thresholded absolute difference between the intensity normalized co-registered image pairs with baseline (pre-test) and damage (post-test) images. For the scope of this paper, a selected crack damage at the upper-right corner of the Level 8 west window from the EIFS on the north façade of the building is presented for illustration purposes. The baseline image without damage was captured during image-based inspection #1 before MID1 and the damage image was captured during image-based inspection #6 at the end of the seismic test program.

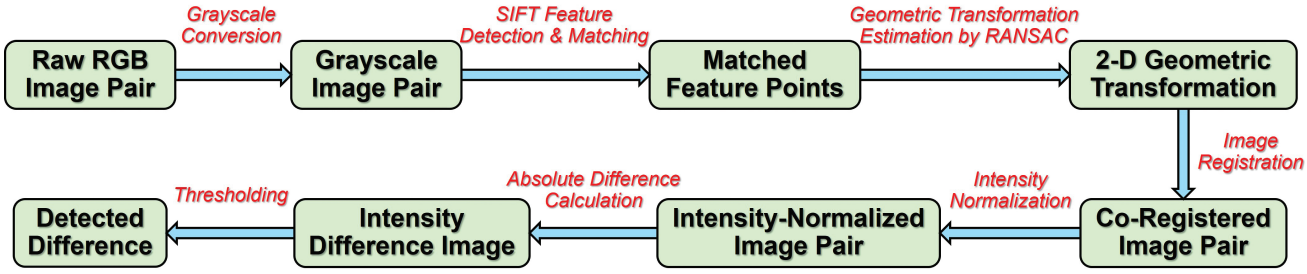

Fig. 2 Flowchart of the proposed damage detection methodology.

The following procedures are applied in the proposed method: (1) The raw RGB images are converted into grayscale for reduced computational cost as shown in Fig. 3. (2) Scale-invariant feature transform (SIFT) is applied to both grayscale images for feature detection and matching. (3) Given the matched SIFT feature points, the random sample consensus (RANSAC) algorithm is applied to remove the outliers and make a robust estimation for the 2-D geometric transformation from the baseline image to the damage image as presented in Fig. 4. (4) A pair of co-registered images (Fig. 5) is obtained by applying the 2-D geometric transformation to the damage image. (5) The damage image is normalized by multiplying a scale factor to ensure the non-zero part in the co-registered damage image has the same average intensity as the baseline image, where the intensity difference caused by the various lighting conditions is largely reduced. (6) The final detected difference is calculated as the thresholded absolute difference between the baseline image and intensity-normalized co-registered damage image as the binary image in Fig. 6(a), where the white pixels are considered as difference between baseline image and damage image.

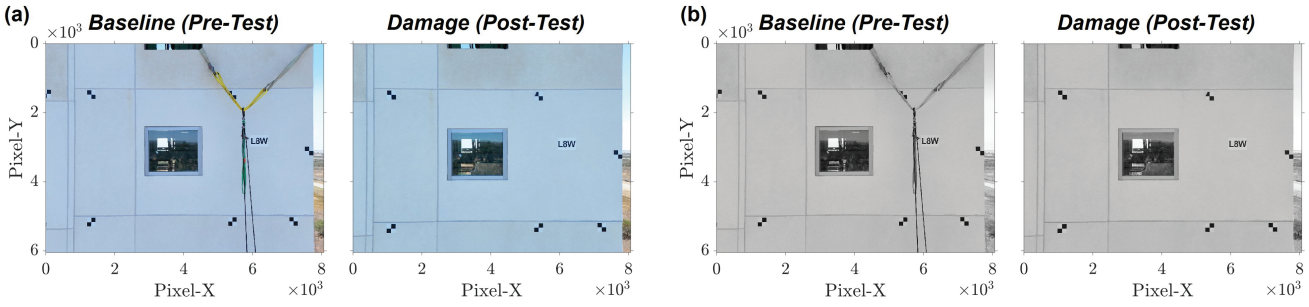

Fig. 3 (a) Raw RGB images captured by UAV, and (b) Converted grayscale images.

It is noted that the binary image result represents all detected differences between the baseline (pre-test) and damage (post-test) image. Therefore, it may include other non-damage differences in the test scene. For the presented example, the non-damage differences include the removal of the safety straps around the building and the difference caused by the various reflection from the window glazing. The final candidate damage could be extracted by excluding the known non-damage differences in the detection result. In addition, the scale of the damage could be estimated from the pixel resolution of the

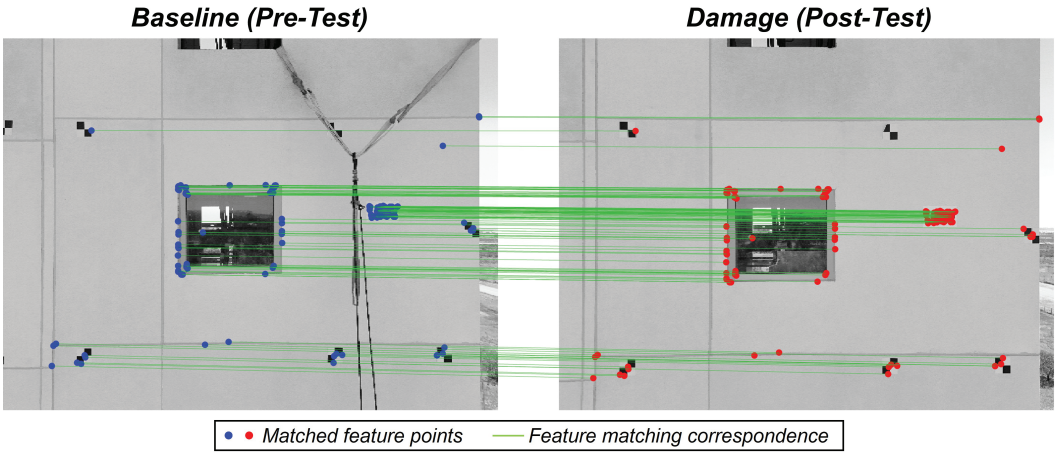

Fig. 4 Inliers of matched features from geometric transformation estimation by RANSAC algorithm.

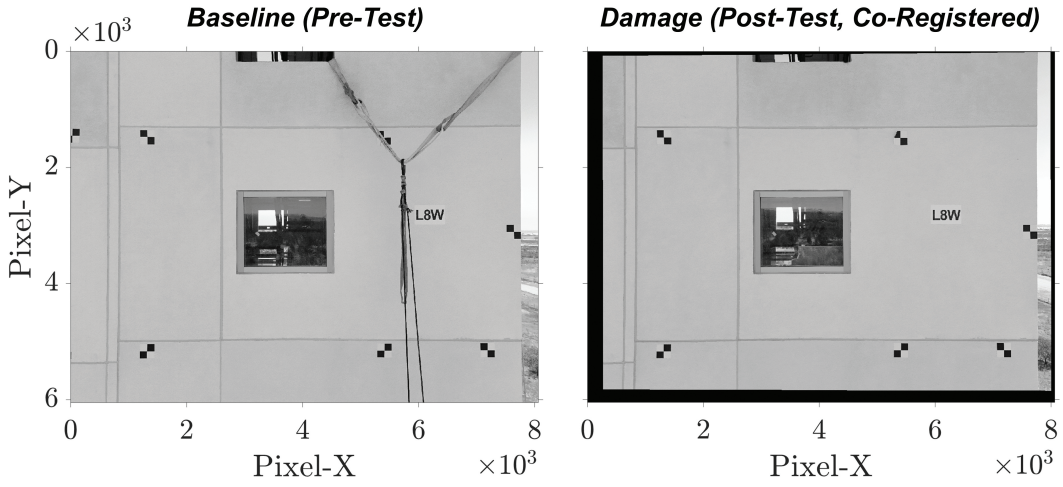

Fig. 5 Co-registered grayscale image pair after geometric transformation.

image extracted from features with known dimensions in the image frame. In the presented case, the pixel resolution of the image frame is 0.85 mm/pixel extracted using the black-and-white checkerboard reference target on the building façade as shown in Fig. 6(b). The total scale of the detected damage is extracted as 104 pixels which correspond to 8.84 cm in length.

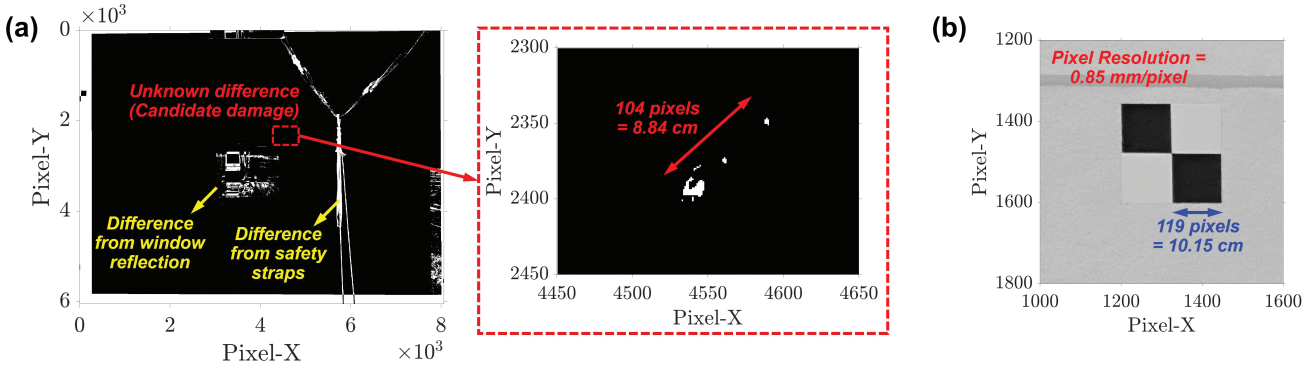

Fig. 6 (a) Detected difference with zoom-in view for candidate damage, and (b) Pixel resolution calculation using features with known dimensions from the pre-test grayscale image.

Discussion and Conclusions

For the selected crack damage located at the upper-right corner of the Level 8 west window from the EIFS on the north façade of the building, the damage is successfully located and extracted with an identified length of 8.84 cm. Fig. 7 presents the same damage observed from a point cloud model based on photogrammetry and a close-up view obtained with manual inspection using a traditional digital single-lens reflex (DSLR) camera. The length of the crack was measured as around 15 cm from the point cloud model and around 8.75 inches (22.23 cm) from the manual inspection. Although it is noted that the scale of the damage extracted from the image-based inspection and photogrammetry inspection are smaller than the actual dimension measured during manual inspection as shown in Fig. 7(b), the proposed damage detection methodology for image-based inspection could provide rapid localization and coarse scale estimation using the UAV-captured images with minimized manual operations.

The presented results offer preliminary results for a comprehensive damage assessment of the CFS10 building, and aid in evaluating the feasibility of a proposed UAV vision-based damage assessment methodology. The method involves extraction of the location and scale of the damage by calculating the thresholded absolute difference within the intensity normalized co-registered image pair with baseline (pre-test) and damage (post-test) images. These findings highlight the potential of UAV vision-based sensing for post-earthquake reconnaissance, enabling assessment of even minor or small-scale damage under seismic excitations.

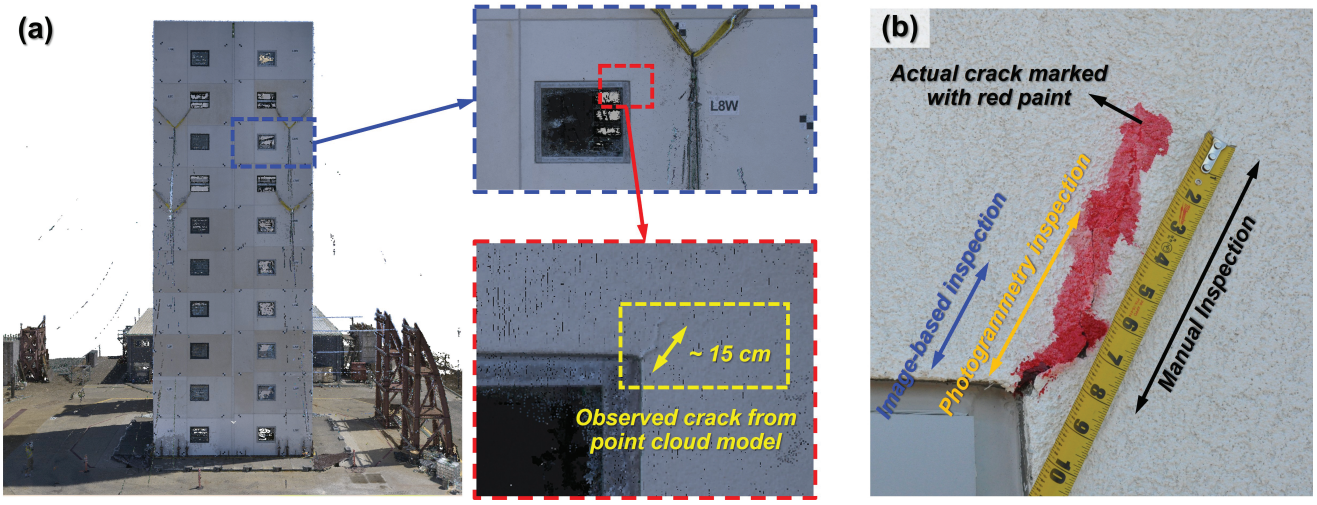

Fig. 7 Crack at the upper-right corner of the L8 west window observed from (a) point cloud model based on photogrammetry, and (b) close-view manual inspection.

Acknowledgments This research is funded by the California Office of Emergency Services (CalOES) and the California Seismic Safety Commission (CSSC) with Agreement #A211006635. The CFS-NHERI 10-story building capstone test program is supported by the National Science Foundation (NSF) with CMMI 1663569 and 1663348 (project entitled: Collaborative Research: Seismic Resiliency of Repetitively Framed Mid-Rise Cold-Formed Steel Buildings), and numerous federal/state and industry partners (listed at: cfs10.ucsd.edu/sponsors-partners). The efforts of all undergraduate and graduate students, visiting scholars (listed at: cfs10.ucsd.edu/people), and the technical support from the LHPOST6 staff (listed at: nheri.ucsd.edu/about/personnel) are greatly appreciated. Findings, opinions, and conclusions are those of the authors and do not necessarily reflect those of the sponsoring organizations.

References

1. Terzic, V., Villanueva, P.K., Saldana, D., and Yoo, D.Y. (2021). Framework for modelling post-earthquake functional recovery of buildings. *Engineering Structures*, 246: 113074. DOI: https://doi.org/10.1016/j.engstruct.2021.113074.
2. Hariri-Ardebili, M.A., and Speicher, M.S. (2025). Reconnaissance-informed post-earthquake functional recovery: Observations and challenges. *Earthquake Spectra*, 41 (1): 88-125. DOI: https://doi.org/10.1177/87552930241290488.
3. Ji, R., Sorosh, S., Lo, E., Norton, T.J., Driscoll, J.W., Kuester, F., Barbosa, A.R., Simpson, B.G., and Hutchinson, T.C. (2025). Application framework and optimal features for UAV-based earthquake-induced structural displacement monitoring. *Algorithms*, 18 (2): 66. DOI: https://doi.org/10.3390/a18020066.

4. Cao, P., Ji, R., Ma, Z., Sorosh, S., Lo, E., Norton, T., Driscoll, J., Wang, X., Hutchinson, T., Pei, S., and Kuester, F. (2024). UAV-based video analysis and semantic segmentation for SHM of earthquake-excited structures. *Proceedings of the 18th World Conference of Earthquake Engineering*, Milan, Italy. 2024.
5. Ji, R., Zhang, J., Lo, E., Norton, T.J., Driscoll, J.W., Kuester, F., Schafer, B.W., Hutchinson T.C. (2026). Multi-view UAV-based imagery for seismic displacement tracking of a full-scale 10-story cold-formed steel building. *Proceedings of the 13th National Conference on Earthquake Engineering*, Portland, OR.
6. Liu, Z., Xue, J., Wang, N., Bai, W., and Mo, Y. (2023). Intelligent damage assessment for post-earthquake buildings using computer vision and augmented reality. *Sustainability*, 15: 5591. DOI: https://doi.org/10.3390/su15065591.
7. Cheng, M.-Y., Sholeh, M.N., and Kwek, A. (2024). Computer vision-based post-earthquake inspections for building safety assessment. *Journal of Building Engineering*, 94: 109909. DOI: https://doi.org/10.1016/j.jobe.2024.109909.
8. Bianchi, S., Ciurlanti, J., and Pampanin, S. (2021). Comparison of traditional vs low-damage structural and non-structural building systems through a cost/performance-based evaluation. *Earthquake Spectra*, 37 (1): 366-385. DOI: https://doi.org/10.1177/8755293020952445.
9. Hutchinson, T.C., Eladly, M., Ji, R., Rivera, D., Rukundo, F.C., Singh, A., Sorosh, S., Zhang, J., Zhang, X., Padgett, L., Jones, H., Karns, J., and Schafer B.W. (2026). Advancing use of cold-formed steel framing systems for mid-rise residential construction in seismic zones via full-scale shake table testing. *Proceedings of the 8th Residential Building Design & Construction Conference*, State College, PA.
10. McCartney, J.S., Van Den Einde, L., Morrison, M., Palermo, A., Lotfizadeh, K., Lai, C.-T., and Conte, J.P. (2025). Multi-degree of freedom shake table testing of large-scale structural and geotechnical systems with NHERI-UCSD LHPOST6. *Frontiers in Built Environment*, 11: 1573390. DOI: https://doi.org/10.3389/fbuil.2025.1573390.
11. Zhang, J., Sorosh, S., Ji, R., Lotfizadeh, K.H., Schafer, B.W., Hutchinson, T.C. (2026). Full-scale 10-story cold-formed steel building shake table test: Protocol development and shake table performance. *Proceedings of the 13th National Conference on Earthquake Engineering*, Portland, OR.
12. Driscoll, J., Lo, E., Norton, T., Ji, R., Hutchinson, T., Driscoll, N., Kuester, F. (2026). Unmanned aerial vehicle (UAV) flight strategies for post-earthquake inspections. *Proceedings of the 13th National Conference on Earthquake Engineering*, Portland, OR.
13. Lozano Bravo, H., Ji, R., Lo, E., Norton, T., Driscoll, J., Zhang, J., Zazueta Hernandez, I., Romo Andrade, A., Hutchinson, T.C., Kuester, F. (2026). Post-earthquake damage assessment using a UAV-acquired photogrammetry model. *Proceedings of the 13th National Conference on Earthquake Engineering*, Portland, OR.
14. DJI - Official Website. Available from: https://www.dji.com/ (accessed on 27 September 2025).

Chapter 2
Examination of the Dynamic Performance of Textile Reinforced Concrete with Post-consumer Waste Denim Fibers

Rachel Hollingsworth and Yohanna MejiaCruz

Abstract The disposal of clothing and textiles represents a rapidly growing environmental burden, with post-consumer denim comprising a large share of the waste stream that is rarely recycled into high-value products. At the same time, cementitious composites, one of the most widely used construction materials, are limited by their brittle nature and low energy dissipation capacity under dynamic loads. This study explores a potential link between these two challenges by evaluating post-consumer denim fibers as reinforcement in textile-reinforced concrete (TRC). For this purpose, denim fibers were incorporated at 0.5% and 1.0% by weight of cement and compared with control specimens through compression, three-point bending, and free vibration tests at various load stages. The results indicate that the addition of denim fibers enhances damping capacity and stiffness retention after cracking, and also increases the modulus of rupture, with the most consistent improvements observed at a 1.0% addition. A slight reduction in compressive strength was also observed compared with the control mix, which could reflect trade-offs in fiber–matrix interaction. However, given the limited number of specimens and the variability in the results, further testing is needed to establish the robustness of these trends. The findings suggest that denim fibers have the potential to improve the dynamic performance of cementitious composites while simultaneously offering a scalable reuse pathway for post-consumer textile waste.

Keywords Dynamic performance · Textile reinforced concrete · Free vibration · Damping ratio · Denim fibers

Introduction

Clothing and textile disposal poses a growing environmental challenge [1]. More than 90 million tons of textiles are discarded annually worldwide, including 16 million tons in the US, which significantly contributes to landfill volumes, greenhouse gas emissions, and water pollution [2, 3]. Producing denim is a resource-intensive process, as a single pair of jeans requires a considerable amount of water and generates substantial carbon emissions. Despite the scale of this problem, studies report that less than 1% of post-consumer textiles are recycled into new textiles, where most are down-cycled into low-value products, such as insulation or industrial materials. Given the limited recycling options currently available, identifying alternative sectors that can utilize textile waste on a large scale is essential. The construction industry, with its constant and high-volume demand for cementitious materials, presents a promising pathway for reusing post-consumer textiles, such as denim, combining environmental benefits with potential improvements in structural performance. Cementitious composites, such as concrete and mortar, are indispensable to modern infrastructure because of their strength, durability, and relatively low cost [4]. These advantages explain their widespread use and make them one of the most consumed construction materials worldwide. Recent advances, including the incorporation of alternative aggregates, have further expanded their applications [5]. Nevertheless, despite these benefits, the brittle nature and low inherent damping of concrete and mortar contribute to vibration-induced serviceability concerns, since limited energy dissipation capacity leads to higher vibration amplitudes under dynamic loads [6]. Common sources of such excitations include wind, machinery, human and vehicle traffic, and seismic loading. Addressing these shortcomings requires reinforcement strategies that not only retain the advantages of cementitious

Rachel Hollingsworth · Yohanna MejiaCruz
Department of Civil Engineering, Montana Technological University
1300 W Park St, Butte, MT 59701
e-mail: rhollingsworth@mtech.edu; lmejiacruz@mtech.edu

© The Author(s), under exclusive license to River Publishers 2026

Kristin B. Zimmerman, PhD (eds.), *Dynamics of Civil Structures, 2026, Vol. 2*, Conference Proceedings
of the Society for Experimental Mechanics Series, https://doi.org/10.13052/rp-9788743814139

composites, but also enhance their performance under dynamic effects. In this capacity, textile fibers have shown potential in improving stiffness, crack resistance, and energy dissipation [7, 8, 9, 10], thereby offering an alternative pathway to more resilient and sustainable cementitious materials.

Textile Reinforced Concrete (TRC) is a relatively new approach that has demonstrated potential in improving properties such as toughness and crack control in cementitious composites, although research in this area remains relatively limited [11, 12]. Most existing studies have emphasized strength, toughness, and crack control under static or quasi-static loading, while damping and vibration response are comparatively unexplored. In the few cases where dynamic behavior has been examined, the focus has been mainly on high-performance fiber textiles made from carbon, glass, or aramid materials [13, 14, 8, 15, 16, 17]. In contrast, post-consumer textiles such as denim remain largely unexplored in cementitious composites. This could be partly due to concerns about the long-term durability of cellulose-based fibers in the alkaline cement matrix, where degradation processes can weaken untreated natural fibers [18]. However, denim offers potential advantages in terms of availability, low cost, and sustainability that warrant investigation, particularly with respect to its influence on dynamic performance.

Some research on denim fibers has primarily focused on applications outside structural concrete. For example, denim has been investigated as an eco-friendly binder in acoustic panels [19] and as a modifier in bitumen, where it improved rutting resistance and reduced penetration, ductility, and temperature susceptibility [20]. While these findings highlight the potential of denim as an enhanced concrete addition, they leave open important questions about how alternative, low-cost fibers influence stiffness, energy dissipation, and mechanical behavior in cementitious composites. Addressing this gap, the present work investigates how post-consumer denim can be utilized to enhance the mechanical and dynamic properties of cementitious materials. In this study, shredded denim fibers from post-consumer jeans were incorporated into concrete mixes at 0.5% and 1.0% by weight of cement, alongside a control mix without fibers. The methodology involved a comprehensive evaluation of the impact of fiber additions on both cylinders and short-beam specimens. Simply supported beams were subjected to free vibration testing at different stages of load application to evaluate stiffness retention and dynamic response. This manuscript presents the detailed results and comparisons across mixes, highlighting the role of denim in modifying both static and dynamic properties of cementitious composites.

Experimental Methods

This section outlines the experimental program developed to evaluate the incorporation of post-consumer denim fibers into cementitious composites. The methodology details the materials used, the preparation of cylindrical and beam specimens, and the testing protocols adopted to assess both mechanical and dynamic behavior. By combining different specimen geometries, the program captures fundamental material properties while also addressing dynamic performance under more applied loading conditions. The testing framework was selected to investigate not only strength and stiffness retention but also the dynamic response of fiber-reinforced composites, thereby providing insights into the potential of denim fibers as a sustainable reinforcement material.

Materials

Denim Fibers

Post-consumer denim textile fibers were used to reinforce the TRC specimens. The denim was collected, washed, and dried before being manually shredded into fibers measuring approximately 50 × 0.5 mm, as illustrated in Figure 1. The fiber length corresponds to roughly one-third of the beam depth (152 mm), a ratio recommended to control preferential orientation effects during the casting process and to promote effective crack bridging [21]. The fiber width, on the other hand, was determined by the natural yarn structure of the denim, resulting in an aspect ratio of approximately 100:1, which falls within the range commonly reported for natural and recycled fibers used in cementitious composites [22, 23, 24]. To minimize bias from the fabric source or condition, fibers were shredded from multiple post-consumer garments and combined before being incorporated into the concrete mixtures.

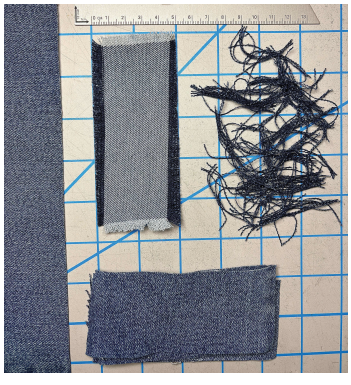

Fig. 1 Post-consumer Denim Fibers

Specimen Preparation

For this study, beam specimens measuring 152 × 152 × 610 mm (6 × 6 × 24 in.) and cylindrical specimens measuring 102 mm (4 in.) in diameter and 203 mm (8 in.) in height were cast and tested to evaluate their mechanical and dynamic properties. Three fiber contents were investigated: 0% (control), 0.5%, and 1.0% by weight of cement. These percentages were selected based on previous studies of natural and recycled fibers in cementitious composites that indicate low-volume additions showed toughness and energy dissipation enhancement while avoiding significant reductions in workability or strength [25]. The number of specimens prepared for each mix and test type is summarized in Table 1. Three replicates were produced for each fiber content to provide a minimum of data for statistical comparison.

Table 1 Test Specimen Matrix.

Specimen	0%	0.5%	1.0%
Cylinders	3	3	3
Beams	3	3	3

Concrete Mix and Casting

Quikrete Portland Cement Type I was used for all mixes conforming to ASTM C150 specifications for Type I Portland cement and contains no additives. Coarse aggregates with a maximum size of 19 mm (¾ in.) and river sand with a fineness modulus of 2.70 were used for the mix. The water-to-cement ratio was fixed at 0.68 for all batches.



Fig. 2 Cylinder & Beam Specimens

Mixing was performed in a Marshalltown 300DD steel drum mixer. The coarse aggregate, sand, and cement were first dry-mixed, after which water was gradually added to control uniform hydration. Once the water was incorporated (approximately after three minutes of mixing), the shredded denim fibers were added in small increments. However, because the fibers tended to clump, care was taken to separate them manually during addition. Despite this, some fiber agglomeration was unavoidable; its potential influence on the results is discussed later in this paper.

After all the fibers were added, the concrete was mixed for an additional two minutes to enhance fiber dispersion. The workability of the concrete was checked using the slump test. The fresh concrete was cast into beam and cylinder molds, as shown in Figure 2, and then placed in a curing room maintained at 95% relative humidity for 14 days. To limit evaporation and control adequate hydration, water was periodically applied to the beam specimens during curing.

Testing

Samples were tested at 14 days. Compressive strength tests on the concrete cylinders were performed using a Forney F-250-FL manual compression testing machine, as shown in Figure 3. The procedure followed ASTM C39 specifications. A constant load was applied at a frame de-rated to 30,000 lbf [130 kN] over a cross-sectional area of $81.07 cm^2$, and the maximum load at failure was recorded to obtain the compressive strength of each specimen.

Flexural strength of the beam specimens was determined using a Humboldt Model H-3030 concrete beam tester (see Figure 4). The first control beam (0% fibers) was subjected to a gradually applied load to observe crack initiation along the tensile face before free vibration testing. However, no visible cracking occurred, and the specimen failed abruptly. A second control beam was then loaded incrementally and tested in free vibration to establish an appropriate load range that could induce controlled cracking without premature failure. Based on these trials, along with the maximum failure loads recorded, the testing protocol was refined to include loading stages of 3000 lbf and 4000 lbf. All subsequent specimens were tested in free vibration at three intervals: prior to loading, after 3000 lbf, and after 4000 lbf. The maximum applied load at failure was recorded for each specimen to obtain the modulus of rupture for all elements.



Fig. 3 Compression Test Machine

]

The free vibration tests were carried out to identify the first mode of vibration of the short beam specimens, including the fundamental frequency and damping ratio. A PCB accelerometer with a sensitivity of (±5%) 10.0 V/g (1.02 V/(m/s²)) was mounted at midspan on the top surface of each beam to record the response. Excitation was applied by a light tap at midspan on the underside of the beam, aligned with the accelerometer location using the rubber end of a hammer. The signals were acquired using a National Instruments M-9234 input module, with custom Python v.3.13 scripts and the `nidaqmx` library used for data collection at a sampling frequency of 2048 Hz. After reviewing the sensor specifications, it was noted that the operational frequency range of the accelerometer was below the fundamental frequency of the beam specimens. Therefore, the authors advise that the reported results should be interpreted with caution, as the measurements may underestimate the true dynamic response. The free vibration testing setup is illustrated in Figure 5.

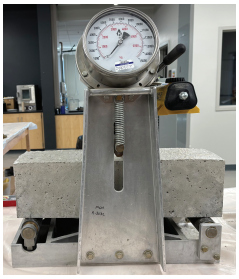

Fig. 4 Three Point Bending Test

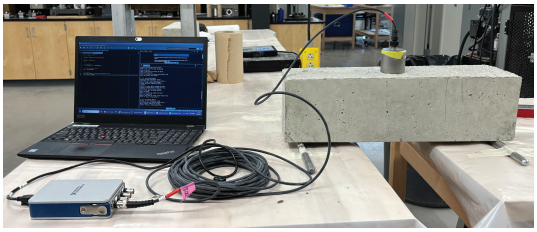

Fig. 5 Free Vibration Testing Setup

Results and Analysis

The experimental program generated results on both the dynamic response (damping and flexural stiffness) and the static mechanical properties (modulus of rupture and compressive strength) of the TRC specimens. The following sections present these findings.

Dynamic Properties: Damping and Flexural Stiffness

Damping Ratio

The damping ratios of the beam specimens were extracted from the free vibration responses using the logarithmic decrement method. Multiple acceleration–time signals were recorded for each specimen to control consistency, and the mean and standard deviation of the damping ratios were computed for each fiber content. The results are summarized in Figure 6, which compares damping behavior across three load stages: (a) unloaded (elastic range), (b) 3000 lbf (pre-cracking), and (c) 4000 lbf (cracking).

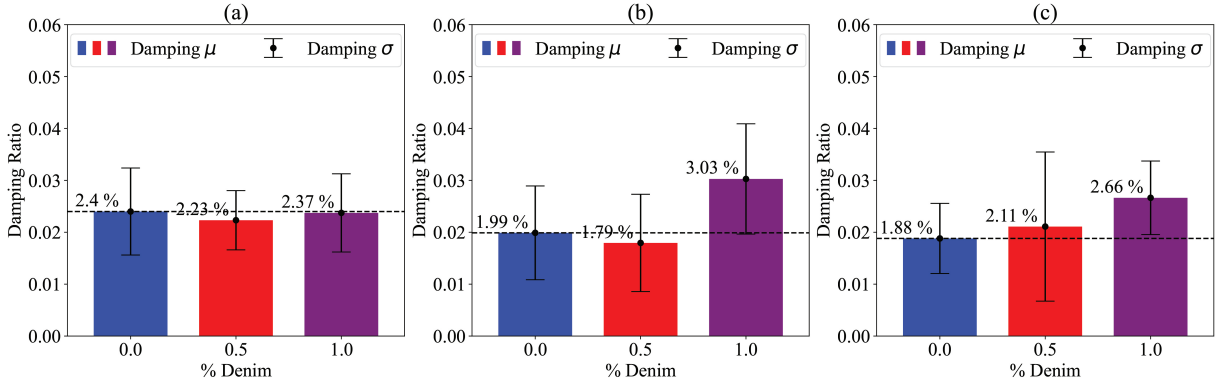

Fig. 6 Damping Extracted From Free Vibration Tests At 3 Load Stages a) Unloaded, b) 3000 lbf Load, c) 4000 lbf Load

In the unloaded condition, no significant differences were observed between the control, 0.5%, and 1.0% mixes, with average damping ratios ranging from 2.2% to 2.4%. This suggests that denim fibers did not significantly influence energy dissipation at small strain levels, likely because microcracking had not yet initiated and the fiber–matrix interaction was not activated.

At 3000 lbf, corresponding to early post-cracking behavior, the mixes diverged. The 0.5% specimens exhibited a reduction in damping ratio to approximately 1.8%, indicating that the fiber may have been insufficient to counteract the loss of energy dissipation caused by crack initiation. In contrast, the 1.0% specimens exhibited an increase in damping capacity to approximately 3.3%, indicating that a higher fiber content could have promoted effective crack bridging, resulting in enhanced energy absorption once cracks began to form.

At 4000 lbf, representing further crack development, both fiber-reinforced mixes performed better than the control, with average damping ratios of 2.1% for the 0.5% specimens and 2.7% for the 1.0% specimens. These results indicate that denim fibers mitigated the reduction in damping typically associated with crack propagation. A plausible explanation is that the fibers delay the transition from distributed microcracking to localized macrocracking, thereby sustaining energy dissipation capacity at higher load levels.

Flexural Stiffness (EI) & Stiffness Retention Ratio (REI)

The dynamic flexural stiffness of the beam specimens was extracted from the fundamental natural frequencies obtained during the free vibration tests, using Equation Equation 1. In this context, ω_n represents the angular natural frequency, L is the free span length of the beam, EI denotes the dynamic stiffness, and M stands for the mass per unit length of the beam. EI dynamic values were calculated both before cracking (within the elastic range) and after cracking at the defined load stages, namely 3000 lbf and 4000 lbf.

$$\omega_n = \left(\frac{n\pi}{L}\right)^2 \sqrt{\frac{EI}{M}} \tag{1}$$

$$REI = \frac{EI_{post}}{EI_{pre}} \tag{2}$$

To evaluate post-cracking performance, the stiffness retention ratio (REI) was defined as the ratio of post-cracking stiffness to pre-cracking stiffness of the control sample, as shown in Equation 2. The calculated REI values at 3000 lbf and 4000 lbf are presented in Figure 7.

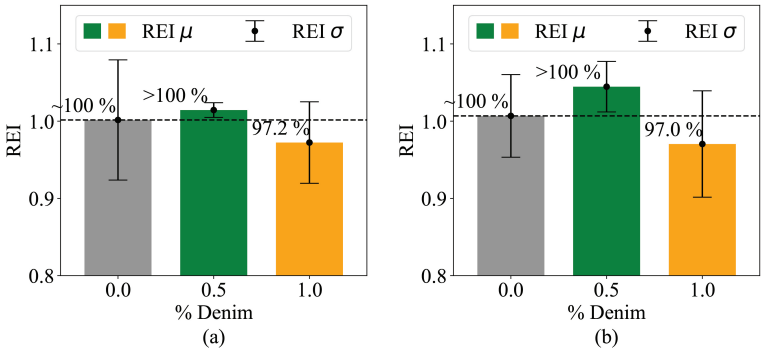

Fig. 7 REI for (a) 3000 lbf and (b) 4000 lbf

At 3000 lbf (Figure 7a), the 0.5% fiber specimens showed a modest increase in REI of approximately 1.4% relative to the control, with a standard deviation of 3.3%. Although the 0.5% specimens appeared to retain stiffness above 100%, this outcome is not physically meaningful, as stiffness should not increase once beams are subjected to higher loads and begin to crack. These values are therefore inconclusive and are attributed to the low resolution of the displacement sensors relative to the small changes being recorded, which introduced variability and inflated values in this group.

In contrast, the 1.0% fiber specimens exhibited a reduction of about 2.8%, with a higher deviation of 5.3%. The last suggests that although the average stiffness retention remained close to 97%, the large scatter between sample points shows inconsistent performance. Considering this variation, the data indicates the addition of denim at this dosage effectively maintained stiffness at this stage of loading, preventing the loss typically associated with early cracking.

Table 2 Comparison of REI and Damping at Loading Conditions

% Denim	REI μ (%)		Damping μ (%)	
	3000	4000	3000	4000
0	100.15	100.68	1.99	1.88
0.5	101.44	104.46	1.79	2.11
1	97.23	97.04	3.03	2.66

At 4000 lbf (Figure 7b), the trends persisted. The 0.5% specimens exhibited an average gain of 4.5% in REI with a relatively low deviation from the mean (3.3%), which reinforces that moderate fiber content may contribute to stable stiffness retention under progressive cracking. On the other hand, the 1.0% specimens again showed a reduction of nearly 3.0%, this time with an even larger deviation of 6.9%. On average, these specimens retained approximately 97% of their stiffness. A comparison of the REI results with the damping results at each condition is presented in Table 2.

Modulus of rupture

The modulus of rupture (MOR) values obtained from the three-point bending tests are summarized in Table 3. The control specimens (0% fiber content) exhibited an average MOR of 4.29 MPa, while the 0.5% and 1.0% fiber-reinforced specimens reached 4.59 and 4.63 MPa, respectively, which is an increase of 6.99% and 7.93%. These results demonstrate that the inclusion of denim fibers increased the ultimate flexural capacity of the TRC beams relative to the control. As shown in Table 3, the improvement was most pronounced at 1.0% fiber content, which achieved the highest MOR among all groups. This trend indicates that denim fibers enhance the crack-bridging capacity of TRC and delay the onset of brittle failure. While the increases were moderate compared to stiffness and damping improvements, the MOR results confirm that denim fibers contribute to the overall flexural strength of TRC elements.

Table 3 Modulus of Rupture.

Specimen	0%	0.5%	1.0%
fr (MPa)	4.29	4.59	4.63

Compressive strength

The results of the compression tests on the concrete cylinders are summarized in Figure 8. The 0.5% and 1.0% fiber-reinforced specimens exhibited average compressive strengths of 18.86 and 21.84 MPa, corresponding to decreases of 22.6% and 10.4% compared with the control specimens. It is worth noting that there was a considerable standard deviation present in the data for the 0.5% cylinder samples, this was likely due to visible voids in the base of one of the cylinder samples that had not been sufficiently compacted, resulting in a much lower compressive strength measured for that sample.

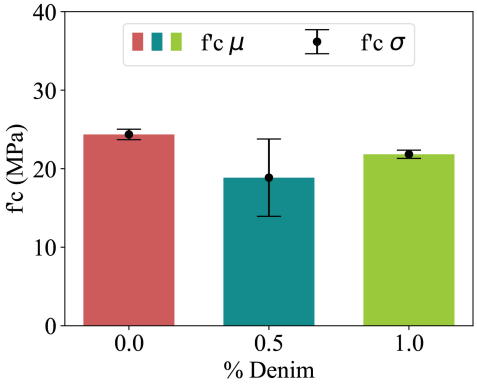

Fig. 8 f'c control 0%, 0.5% and 1.0% samples

This trend aligns with other studies that showed findings where fibers slightly reduced compressive capacity due to increased porosity or weak fiber–matrix bonding [23, 26, 27]. Larger decreases in compressive strength were generally seen at higher percentages of fiber content. However, one study did see an increase in compressive strength at a higher fiber content of 1.5% [28]. Further investigation into the effects of higher fiber contents is necessary to determine the optimum percentage of fiber to improve the mechanical properties of TRC.

It was necessary to test the specimens after 14 days of curing rather than the standard 28 days. According to previous studies, this shorter cure time likely contributed to the lower compressive strengths that were measured in the lab[28, 23]. The relationship between compressive strength and fiber content in this study is illustrated in Figure 8.

Conclusion

This study investigated the dynamic performance of textile-reinforced concrete (TRC) incorporating post-consumer denim fibers as a sustainable reinforcement material. The results demonstrated that denim fibers improved the damping capacity and post-cracking stiffness retention of TRC beams, with the 1.0% fiber content samples showing the greatest enhancement in damping and around 97% stiffness retention post-cracking. The stiffness retention ratio and modulus of rupture confirmed that fiber reinforcement contributed to greater ductility and delayed brittle failure. Although compressive strength decreased slightly with fiber addition, the tradeoff was offset by gains in flexural behavior and energy dissipation capacity.

In the interpretation of the data, it should be remembered that there was a considerable amount of variability, especially in the results from the 0.5% fiber content specimens. Results showed a stiffness retention ratio (REI) of over 100%, which does not have any physical meaning as stiffness in concrete should decrease post-cracking. It was determined that low sensor resolution in the range of the fundamental frequencies of these elements is likely the reason for this variability. Further investigation with a larger number of specimens and proper sensor frequency band is necessary to obtain more conclusive results.

Overall, the findings highlight the potential of denim fibers to improve the dynamic performance of TRC while also providing a viable recycling pathway for a significant textile waste stream. By integrating waste-derived fibers into cementitious composites, this work advances both structural performance and sustainability objectives, offering an alternative to more costly technical textiles. By addressing both performance gaps in TRC research and the challenge of textile waste

management, this study demonstrates that post-consumer denim can serve as a practical and sustainable fiber reinforcement for concrete applications.

Future Work

While the present study demonstrates the potential of denim fiber reinforcement in TRC, further research is needed to expand the scope and strengthen the reliability of the findings. Future investigations should focus on extending the testing program to longer structural elements to excite multiple modes of vibration, with measurements taken from multiple sensors rather than a single accelerometer. Additional studies are also needed to evaluate a wider range of fiber contents to identify the optimal percentage for maximizing improvements in damping and stiffness. Further work should examine the influence of denim fibers on the stress–strain behavior of TRC, as well as incorporate a larger number of specimens to improve the statistical reliability of the results. In addition, Scanning Electron Microscopy (SEM) analysis would be a valuable contribution, providing a detailed assessment of fiber dispersion, orientation, and bonding mechanisms, and better correlating microstructural observations with observed mechanical and dynamic properties.

References

1. Chrobot, P., Faist, M., Gustavus, L., Martin, A., Stamm, A., Zollinger, M., and Zah, R. "Measuring fashion: Environmental impact of the global apparel and footwear industries study". *Full report and methodological considerations* (2018)ifnextchar.gobble.
2. Fashion, M. "Environmental impact of the global apparel and footwear industries study". *Full report and methodological considerations. Quantis* (2018)ifnextchar.gobble.
3. USEPA. "Textiles: Material-specific data". *USEPA* (2018)ifnextchar.gobble.
4. Li, Z., Zhou, X., Ma, H., and Hou, D. *Advanced concrete technology*. John Wiley & Sons (2022)ifnextchar.gobble.
5. Zamora-Castro, S.A., Salgado-Estrada, R., Sandoval-Herazo, L.C., Melendez-Armenta, R.A., Manzano-Huerta, E., Yelmi-Carrillo, E., and Herrera-May, A.L. "Sustainable development of concrete through aggregates and innovative materials: A review". *Applied sciences*, 11(2):629 (2021)ifnextchar.gobble.
6. Bala, A. and Gupta, S. "Thermal resistivity, sound absorption and vibration damping of concrete composite doped with waste tire rubber: A review". *Construction and Building Materials*, 299:123939 (2021)ifnextchar.gobble.
7. Li, C., Zhong, J., and Sun, Y. "Novel approach to enhance the damping performance of cement-based materials through polymer/carbon nanotube composite coating and gradation of aggregates". *Construction and Building Materials*, 471 (2025)ifnextchar.gobble.
8. Sofuoğlu, M.A., Çakır, F.H., and Çelikten, S. "Influence of steel fiber addition on the vibrational characteristic of high strength cementitious composites". *Arabian Journal for Science and Engineering*, 46:4677–4685 (2021)ifnextchar.gobble.
9. Guo, J., Cai, J., Chen, Q., Liu, X., Wang, Y., and Zuo, Z. "Dynamic behaviour and energy dissipation of reinforced recycled aggregate concrete beams under impact". *Construction and Building Materials*, 214:143–157 (2019)ifnextchar.gobble.
10. Gopinath, S., Prakash, A., and Ahmed, A.K. "Flexural impact response and energy absorption characteristics of textile reinforced mortar". *Construction and Building Materials*, 262 (2020)ifnextchar.gobble.
11. Wu, C., Pan, Y., and Yan, L. "Mechanical properties and durability of textile reinforced concrete (trc)—a review". *Polymers*, 15(18):3826 (2023)ifnextchar.gobble.
12. Scheurer, M. and Gries, T. "Comparative evaluation of textiles for use in textile reinforced concrete". *Materials Today: Proceedings* (2023)ifnextchar.gobble.
13. Grzymski, F., Musiał, M., and Trapko, T. "Mechanical properties of fibre reinforced concrete with recycled fibres". *Construction and Building Materials*, 198:323–331 (2019)ifnextchar.gobble.
14. Li, R., Deng, M., Guo, L., Wei, D., Zhang, Y., and Li, T. "Tensile behavior of high-strength highly ductile fiber-reinforced concrete with embedded carbon textile grids". *Construction and Building Materials*, 414 (2024)ifnextchar.gobble.
15. Teixeira, F.P., de Souza, F.R., Garcia, S.L.G., and de Andrade Silva, F. "Strengthening and repair of rc beams using natural sisal fabric-reinforced cementitious matrix composite". *Construction and Building Materials*, 447 (2024)ifnextchar.gobble.
16. Yao, Y., Sun, Y., Zhai, M., Chen, C., Lu, C., and Wang, J. "Tensile behavior of textile reinforced ultra-high performance concrete". *Construction and Building Materials*, 411 (2024)ifnextchar.gobble.
17. Zhu, D., Liu, H., Rahman, M.Z., Tang, H., and Guo, S. "Fatigue behavior of textile reinforced concrete with different textile types and short steel fiber contents". *Construction and Building Materials*, 443 (2024)ifnextchar.gobble.
18. Addis, L.B., Sendekie, Z.B., and Satheesh, N. "Degradation kinetics and durability enhancement strategies of cellulosic fiber-reinforced geopolymers and cement composites". *Advances in Materials Science and Engineering*, 2022(1):1981755 (2022)ifnextchar.gobble.
19. Juciene, M., Dobilaitė, V., Albrektas, D., and Bliūdžius, R. "Investigation and evaluation of the performance of interior finishing panels made from denim textile waste". *Textile Research Journal*, 92(23-24):4666–4677 (2022)ifnextchar.gobble.
20. Al-Sabaeei, A., Napiah, M., Sutanto, M., and Alaloul, W. "Effects of waste denim fibre (wdf) on the physical and rheological properties of bitumen". In *IOP conference series: materials science and engineering*, volume 527, page 012047. IOP Publishing (2019)ifnextchar.gobble.
21. Georgiou, A.V. and Pantazopoulou, S.J. "Effect of fiber length and surface characteristics on the mechanical properties of cementitious composites". *Construction and Building Materials*, 125:1216–1228 (2016)ifnextchar.gobble.

22. Onuaguluchi, O. and Banthia, N. “Plant-based natural fibre reinforced cement composites: A review”. *Cement and Concrete Composites*, 68:96–108 (2016)ifnextchar.gobble.
23. Tran, N.P., Gunasekara, C., Law, D.W., Houshyar, S., and Setunge, S. “Utilization of recycled fabric-waste fibers in cementitious composite”. *Journal of Materials in Civil Engineering*, 35 (2023)ifnextchar.gobble.
24. SEZGİN, H. “The effect of various textile wastes on the mechanical properties of composite materials”. *Tekstil ve Konfeksiyon*, 33:95–103 (2023)ifnextchar.gobble.
25. Kufner, F., Rucker-Gramm, P., Horstmann, M., Haemmelmann-Breul, E., Breul, F., Hahn, E., Hettwer, S., and Pachow, U. “Short-fiber-reinforced concrete meeting the demands of wrapping textile-reinforced concrete”. *Journal of Building Engineering*, 98:111189 (2024)ifnextchar.gobble.
26. Tang, Z., Li, Z., Hua, J., Lu, S., and Chi, L. “Enhancing the damping properties of cement mortar by pretreating coconut fibers for weakened interfaces”. *Journal of Cleaner Production*, 379 (2022)ifnextchar.gobble.
27. MejiaCruz, Y., Caicedo, J.M., and Matta, F. “Probabilistic comparative assessment of structural cement composite compressive strength–porosity models”. *Journal of Structural Engineering*, 150(11):04024165 (2024)ifnextchar.gobble.
28. Kalkan, Ş.O., Öcal, H.İ., and Gündüz, L. “Effect of denim waste fibres on technical properties of cementitious lightweight composite mortars”. *Journal of Innovations in Civil Engineering and Technology*, 5(2):71–90 (2023)ifnextchar.gobble.

Chapter 3
Structural Integrity Assessments of a Train Bridge Using SHM Data

Bjørn T. Svendsen, Niels Dollerup, and Eimantas Poskus

Abstract This paper presents the structural integrity assessment of a train bridge using data obtained from a comprehensive SHM system. The bridge, which consists of three similar bridge spans supported by two foundations, was repaired and re-installed in 2024 for normal operation after a collapse during a severe flooding. Overviews of the bridge damage condition and the SHM system are presented. Results from the structural integrity assessment are evaluated, with a particular focus on static inclination and the structural dynamic behaviour over time and for different temperatures, based on data obtained from one year of measurements. The effects of environmental conditions, i.e., the temperature, on the modal parameters of the bridge are mapped and the actual structural behaviour is validated by comparing the performance of all three bridge spans and assessing the performance over time to ensure increased bridge safety.

Keywords Structural health monitoring · Damage detection · Bridge · Operational and environmental variability · Temperature · Collapse · Modal tracking · Gaussian mixture modelling.

Introduction

Although bridges are essential parts of the infrastructure, an increasing trend of bridge collapses worldwide has been observed in recent years. Bridge collapses are, in many cases, caused by sudden changes in the operational and environmental loads affecting the structural behaviour. A fundamental challenge in structural health monitoring (SHM) is the process of separating changes caused by operational and environmental conditions from changes caused by damage. It is well known that variability in operational and environmental conditions affects the structural response and can mask changes caused by damage. An important part of the work towards solving this challenge is to understand the effects of environmental conditions on modal properties, such as natural frequencies, mode shapes and damping. Therefore, deploying long-term SHM systems on bridges are important to map such effects as well as performing structural integrity assessments. Automatic operational modal analysis (OMA) and modal tracking are examples of important tools that are used for such mapping [1], [2]. It is well known that SHM systems can result in enhanced decision support and structural diagnosis of the structure [3]–[6]. Consequently, the use of SHM systems for structural integrity evaluation of bridges has become increasingly important.

For bridges, variability in operational conditions is mainly caused by traffic, while variability in environmental conditions is mainly caused by humidity, wind and temperature effects. The most influential source of variability in the modal properties is due to temperature effects. In general, significant variations of the natural frequencies can be expected on a yearly (seasonal) basis for bridges [7]–[14], particularly for bridges located in cold climates such as Nordic and Scandinavian climates. A step-like variation in the natural frequencies of certain concrete and composite steel-concrete highway and railway bridges can be obtained during a yearly season, particularly around or below the freezing point. In the context of SHM, Gaussian mixture models (GMMs) have been used to characterize the effects of environmental variability, such as

Bjørn T. Svendsen
Department of Structural Engineering, Norwegian University of Science and Technology
e-mail: bjorn.t.svendsen@ntnu.no

Bjørn T. Svendsen · Niels Dollerup · Eimantas Poskus
Department of Marine Structures, Ramboll Energy
e-mail: bjorn.t.svendsen@ntnu.no; nsd@ramboll.com; eipo@ramboll.com

© The Author(s), under exclusive license to River Publishers 2026

Kristin B. Zimmerman, PhD (eds.), *Dynamics of Civil Structures, 2026, Vol. 2*, Conference Proceedings
of the Society for Experimental Mechanics Series, https://doi.org/10.13052/rp-9788743814139

temperature effects, on features such as natural frequencies [15]–[17]. There are, however, few such studies reported in the literature on full-scale bridges in operation. Understanding the temperature effects on the structural behaviour and bridge performance is crucial for performing reliable structural integrity evaluations.

This paper presents the structural integrity assessment of an operational train bridge using data obtained from a comprehensive SHM system. Results from the structural integrity assessment are evaluated, with a particular focus on static inclination and the structural dynamic behaviour over time and for different temperatures, based on data obtained from one year of measurements. The effects of environmental conditions, i.e., the temperature, on the modal parameters of the bridge are mapped and the actual structural behaviour is validated by comparing the bridge performance and assessing the performance over time to ensure increased bridge safety. The outline of this paper is as follows. Sections 2 and 3 provide overviews of the bridge damage condition and SHM system, respectively. Section 4 presents the static structural assessment. Section 5 presents the dynamic structural assessment, which includes modal tracking and the implementation of a GMM on the modal tracking data. Finally, section 6 summarizes and concludes the work.

Damage overview

The bridge considered in this study is a steel riveted truss train bridge consisting of three similar spans. The bridge was originally built in 1957 and is located in Norway. The structural system of each bridge span consists of two bridge walls, a bridge deck, and upper and lower lateral bracings. The total length of the bridge is approximately 180 m, where each bridge span is 57.5 m long and has a total width of 5 m and a height of 7.5 m. Figure 1 shows a schematic overview of the structural system of one bridge span. Figure 2 provides a damage overview and the state of the condition of the bridge spans after the collapse and prior to repair. During the collapse, bridge span 1 remained in its original position and thus experienced negligible structural damage. Bridge spans 2 and 3, however, collapsed into the river and experienced major structural damage. The damage was mostly local damage at the bridge ends. The typical damage types observed were tear (cracking), member separation, dents and overloading in terms of loss of rivets. The overall bridge damage situation was taken into consideration in the proposed alternatives and final design of the SHM system.

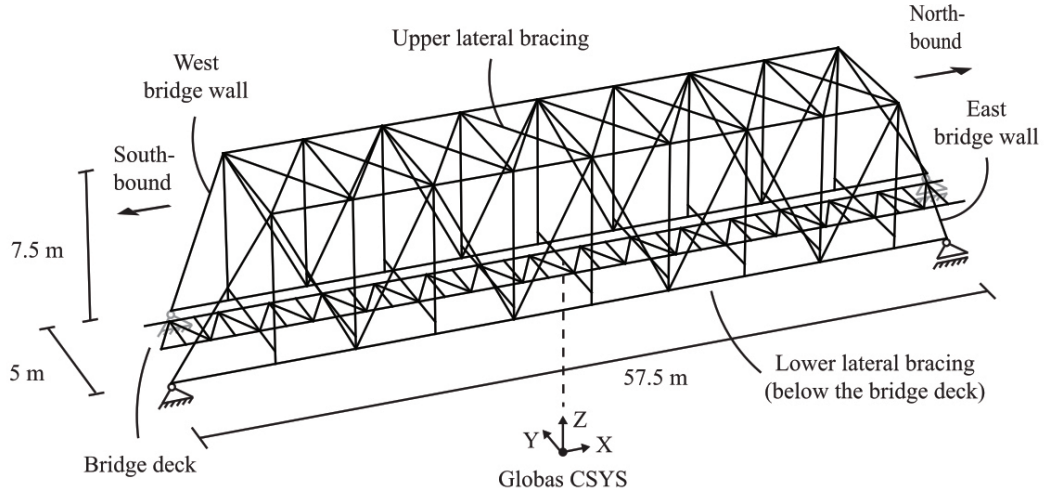

Fig. 1 Overview of the bridge span structural system

Structural health monitoring system

The SHM system of the bridge, shown in Figure 3, is a cabled system consisting of accelerometers, inclinometers, a weather station and a cabinet. The cabinet contains all relevant data acquisition units, an industrial computer, power supplies and a

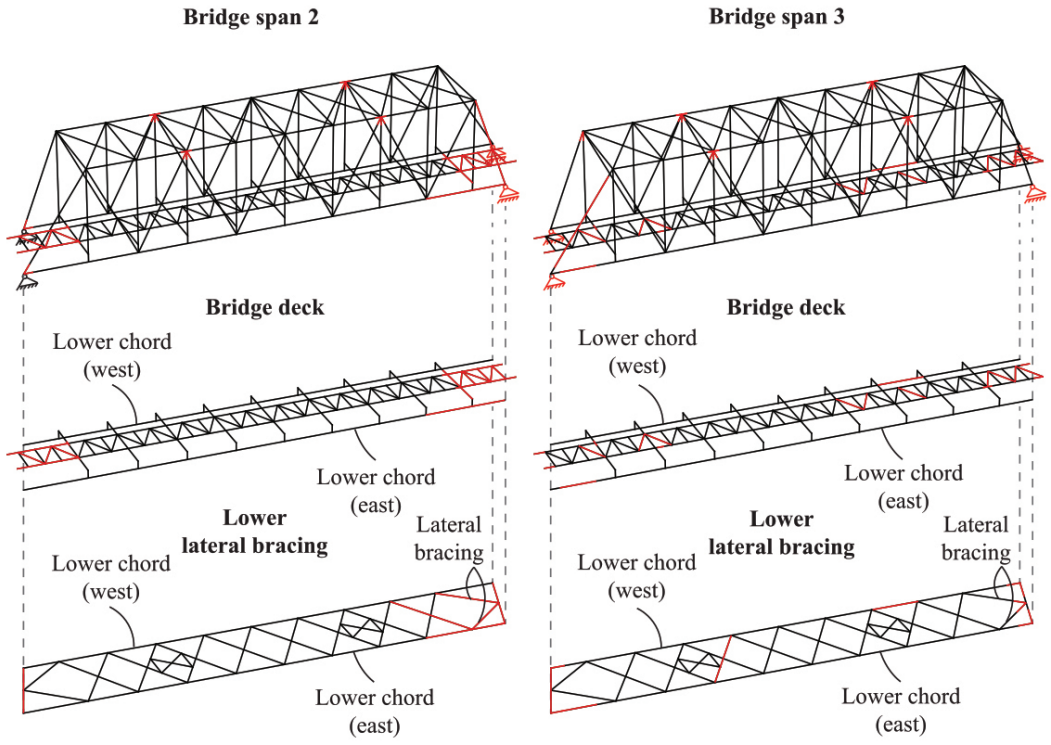

Fig. 2 Damage overview and bridge condition after the bridge collapse. Damaged areas of beam members and joints are highlighted in red

router for wireless data transfer. Altogether, the SHM system comprises 30 sensors in addition to the weather station and is designed as one system to provide fully synchronized data. Table 1 summarizes the sensors that are included in the SHM system and installed on each of the bridge spans. Apart from the weather station, the sensors consist of 1) accelerometers that measure acceleration and 2) biaxial static inclinometers (tiltmeters) that measure pitch and roll angles. All sensors, apart from the weather station, are micro-electro-mechanical system (MEMS) sensors. Data are collected and streamed continuously with a sampling rate of 100 Hz for the accelerometers and 1 Hz for the inclinometers and weather station.

The SHM system is designed to capture the global response of the bridge using accelerometers and inclinometers and the environmental load using the weather station. The SHM system was originally designed as a temporary system allowing short-term measurements for a period of approximately one full year. However, the original design of the system allows both an expansion of the system using additional sensors and an extension of the operating period, if needed. Data from the SHM system are streamed continuously to a Grafana dashboard using a Historian database service over the MQTT protocol.

Based on data obtained from the SHM system, two types of structural integrity assessments are performed. The first assessment considers the bridge static structural behaviour. The objective of this assessment is to compare and evaluate the static behaviour of all three bridge spans by considering inclination. The second assessment considers the bridge dynamic structural behaviour. The objective of this assessment is to compare and evaluate the behaviour of all three bridge spans by considering modal tracking. Common for both structural integrity assessments are the evaluation of the structural integrity over time and for different temperatures.

Table 1 Overview of the sensors included in the SHM system

Sensor type	Bridge span 1	Bridge span 2	Bridge span 3	Total
Accelerometer	8	8	8	24
Accelerometer and inclinometer	2	2	2	6
Weather station	-	-	1	1

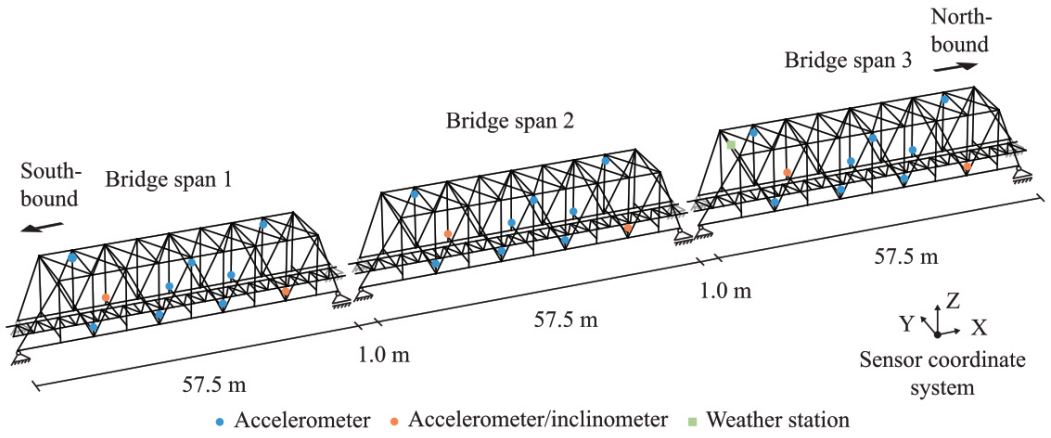

Fig. 3 The bridge SHM system

Static structural assessment

The static behaviour of all three bridge spans is compared and evaluated by considering inclination. The assessment is performed by comparing and evaluating the static inclination over time, including considerations of temperature variations. Figure 4 shows an overview of the inclinometers and inclination angles, i.e., roll and pitch, that are evaluated. A clockwise tilt provides positive inclination values.

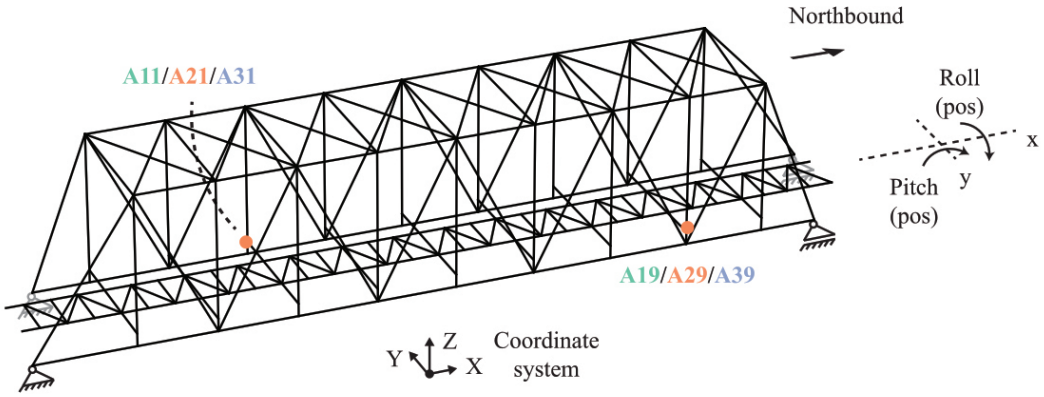

Fig. 4 Inclinometers and the corresponding angles evaluated

One dataset per day is chosen as a basis for performing analyses. Each dataset provided from the SHM system between 12.00-13.00 local time is chosen. If the dataset at the chosen time of a specific day is incomplete, data from the nearest complete hour has been chosen. Each dataset contains a time series of 60 min. The average value of the inclination for each channel of each sensor is computed for the time series in addition to the average value of the temperature. The daily average static inclination of the bridge spans throughout one year are summarized in Figure 5 and Figure 6 for roll and pitch motions, respectively.

From the results presented in Figure 5 and Figure 6, two important observations are made. First, the variation in the roll motion for all sensors is low in the period October 2024 to March 2025. The low variation appears to be related to the low temperature in this period, which is around and below the freezing point. As such, these results indicate a more stable static inclination behaviour during low temperatures than high temperatures. This variation is more distinct for the sensors located on the upstream side of the bridge, i.e., sensors A11, A21 and A31, than the sensors located on the downstream side of the bridge, i.e., sensors A19, A29 and A39. The variation is assumed to be related to different exposure of sun affecting the structural behaviour. Second, the curves generally follow each other well and the inclination values for roll and pitch

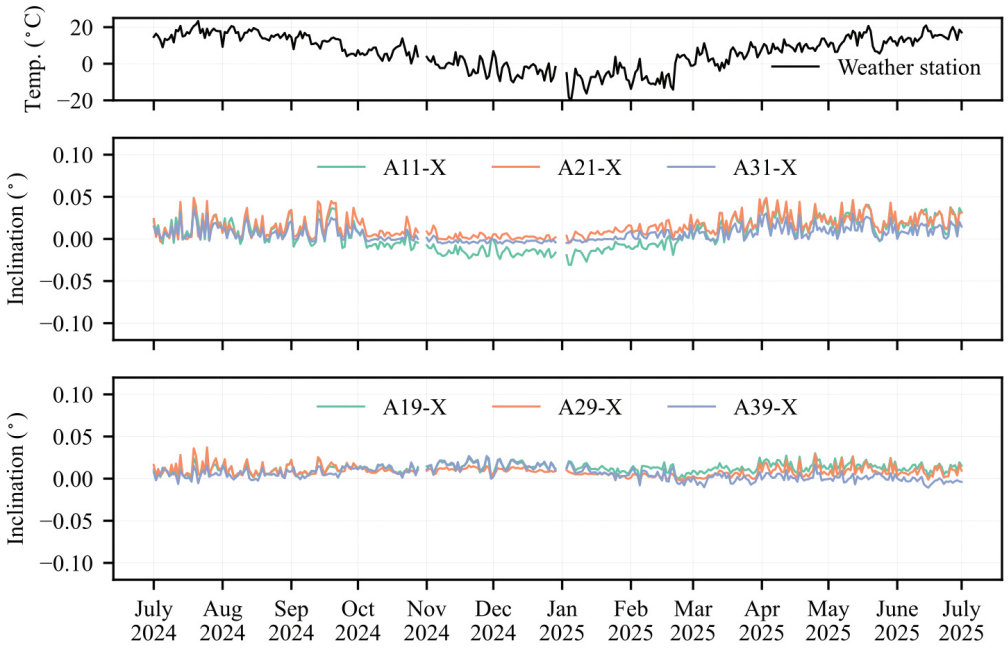

Fig. 5 The daily average static inclination about the bridge (sensor) x-axis (roll motion) of all three bridge spans, including the temperature, throughout one year

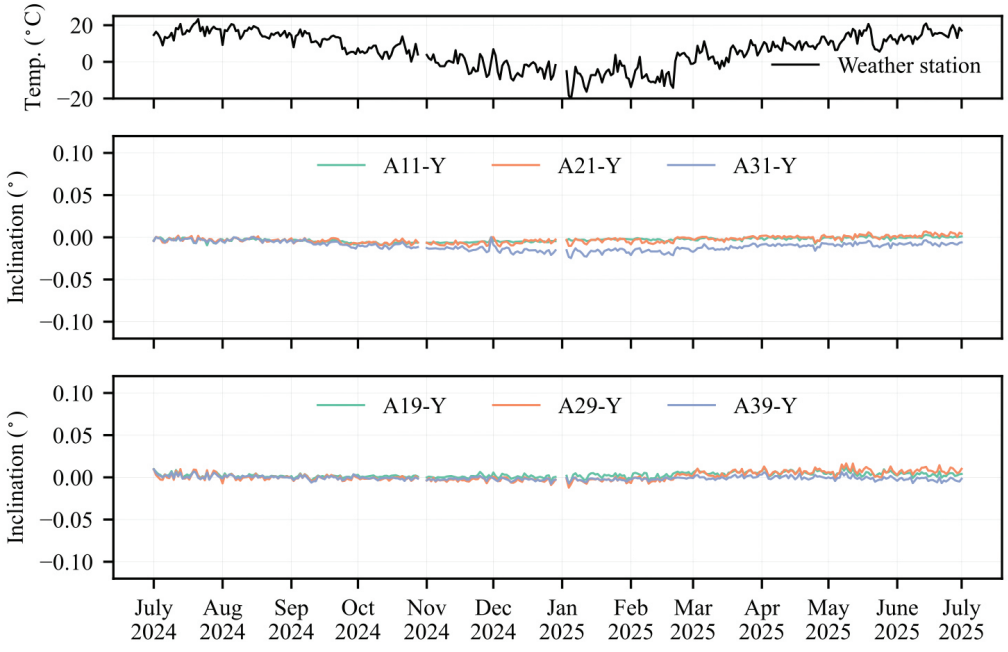

Fig. 6 The daily average static inclination about the bridge (sensor) y-axis (pitch motion) of all three bridge spans, including the temperature, throughout one year

motions are stable, low and with low variations. As such, the bridge spans compare well considering static inclinations over time.

No changes in the structural integrity of the bridge occurred during the period. Consequently, the variations in the static inclination of the bridge spans are mainly caused by environmental variability, such as the temperature. From the results

presented, it is concluded that the effect of temperature on the static inclination is low. Some variation is observed; however, this variation is the level of variation to be expected for such bridges in typical Nordic and Scandinavian climates.

Dynamic structural assessment

Modal tracking

The dynamic behaviour of all three bridge spans is compared and evaluated by considering modal tracking. The assessment is performed by comparing and evaluating the modal properties over time, including considerations of temperature variations. The modal tracking is implemented as an automatic procedure to detect modes from multiple datasets. The modal tracking procedure, shown in Figure 7, consists of two parts. In the first part, a reference analysis is performed to establish the modes to be tracked. The reference analysis is based on data representing the yearly average temperature at the bridge location (4.0°C). In the second part, modes are automatically extracted from each dataset in a defined time period and identified.

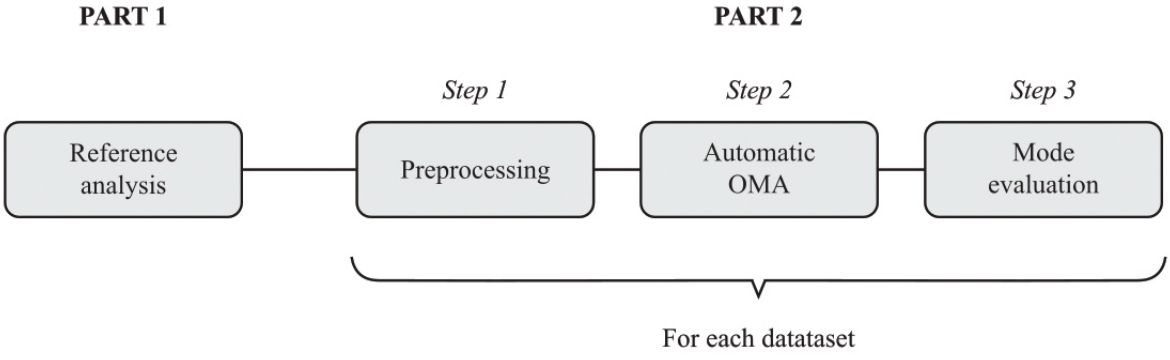

Fig. 7 The modal tracking procedure

Modes in a particular dataset are identified using a mode match index (MMI) based on the modes established in the reference dataset. The MMI is defined as [18], [19]:

$$MMI = (1-\gamma)\, MAC_{r,i} - \gamma \frac{|f_r - f_i|}{f_r} \tag{1}$$

where γ is a value between 0 and 1 that provides the weighting to be considered between the modal assurance criterion (MAC) numbers and natural frequencies, f. The subscripts r and i are denoted for the reference mode and dataset mode being evaluated, respectively. The cov-SSI method is used as an automatic OMA method with a range of order between 20-120 and a minimum of 15 poles as a general requirement, with some deviations, to determine stable modes. Examples of other applications of the considered OMA method is given in [20].

Modal tracking of the first 11 modes of each bridge span throughout one year is performed. The tracked modes are considered the most relevant modes that excites the bridge globally. One dataset per day is chosen as a basis for the modal tracking, where each dataset between 12.00-13.00 local time is used. If the chosen time of a specific day is incomplete, data from the nearest complete hour has been chosen. A 20 min time series is chosen from each dataset with no restrictions regarding traffic in terms of regular train passings. Consequently, time series with and without traffic are used as a basis for analysis in the modal tracking.

The modal tracking results for bridge spans 1, 2 and 3 based on one year of monitoring are summarized in Figure 8. The statistical distributions of the modal tracking results for each bridge span are shown in Figure 9. Table 2 summarizes the basic statistics from the modal tracking, such as the mean frequency value and standard deviation, whereas Table 3 summarizes statistics such as the detection rate and correlation with temperature. The statistics in Table 2 and Table 3 are provided for all modes of each bridge span.

From the results presented in Figure 8, Figure 9, Table 2 and Table 3, four important observations valid for all the bridge spans are made. First, when considering the modes separately, there is a low variation of the modes with varying temperature, i.e., the tracked modes appear stable. Second, some outliers of natural frequencies in terms of low minimum and high maximum values of each mode of each bridge span are observed. Third, there is a higher uncertainty, i.e., a large

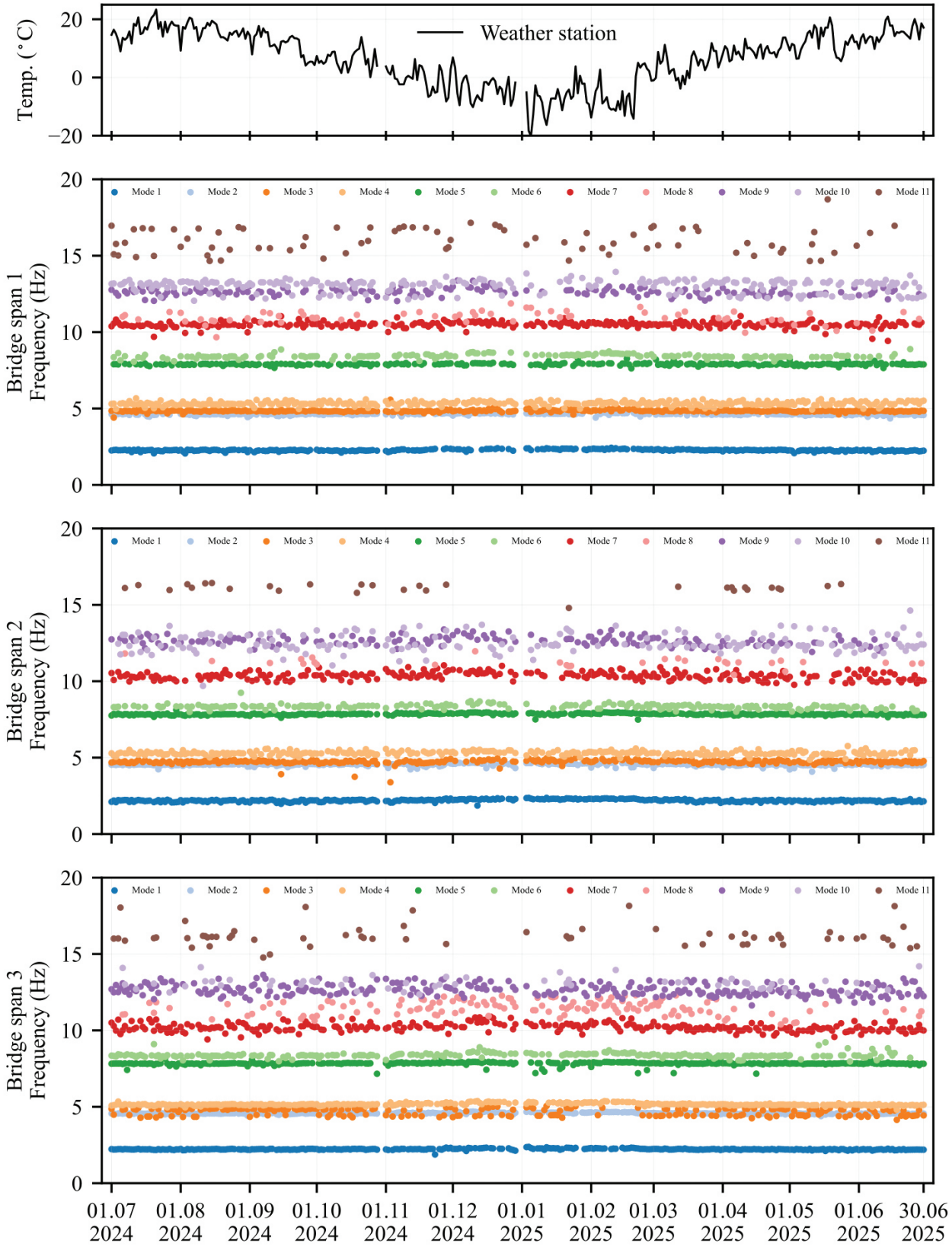

Fig. 8 One year of modal tracking results for bridge spans 1, 2 and 3

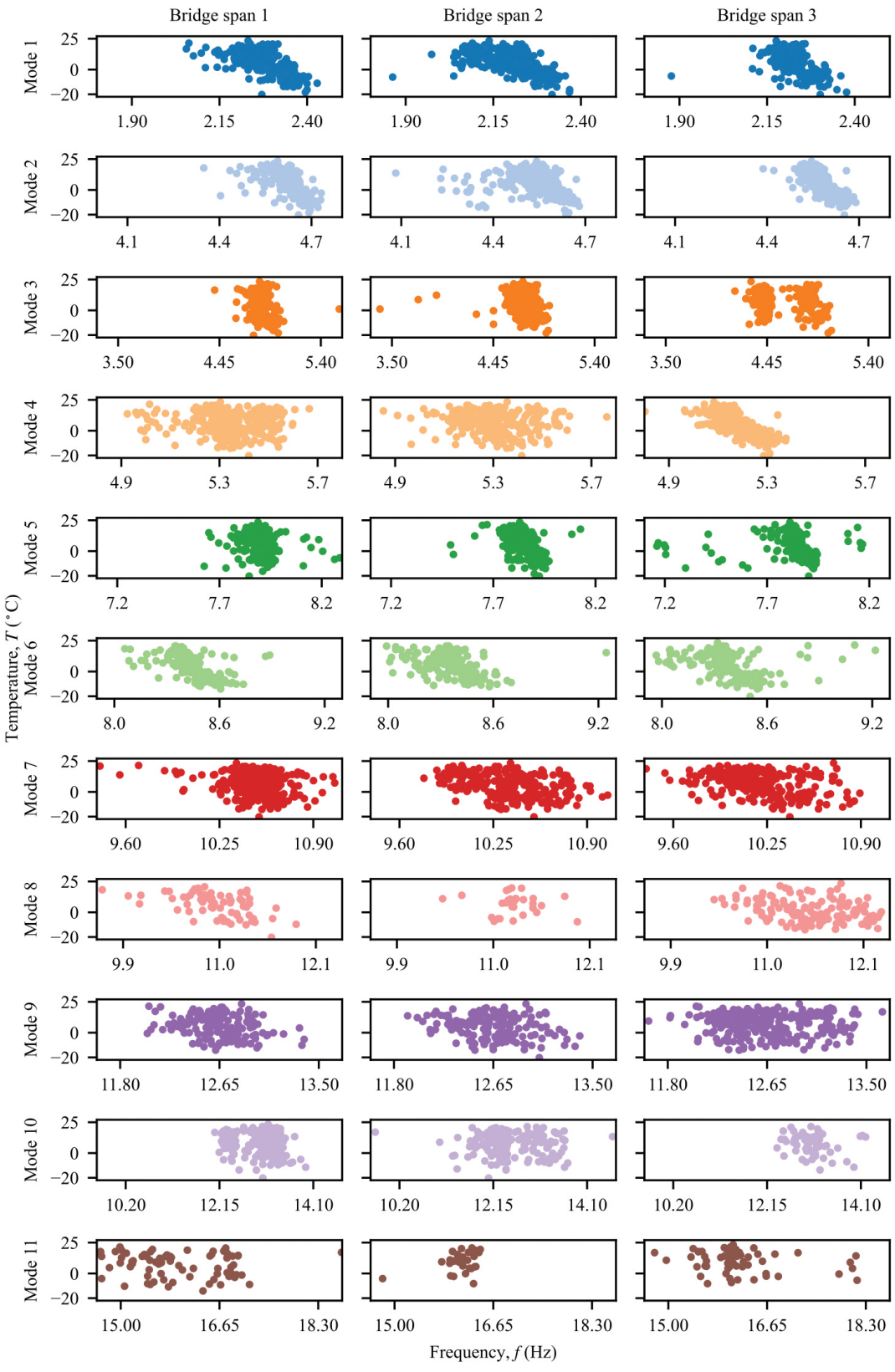

Fig. 9 Statistical distributions of the modal tracking results.

Table 2 Mean frequency values and standard deviation for all modes of bridge spans (BS) 1, 2 and 3

	Mean (Hz)			Standard deviation (Hz)		
Mode	BS1	BS2	BS3	BS1	BS2	BS3
1	2.273	2.199	2.224	0.058	0.076	0.044
2	4.621	4.542	4.576	0.053	0.080	0.040
3	4.842	4.729	4.672	0.074	0.137	0.228
4	5.334	5.302	5.163	0.129	0.125	0.077
5	7.899	7.848	7.827	0.074	0.063	0.116
6	8.442	8.351	8.380	0.127	0.142	0.157
7	10.497	10.361	10.206	0.192	0.244	0.255
8	10.964	11.239	11.507	0.399	0.285	0.449
9	12.643	12.656	12.660	0.240	0.287	0.367
10	13.021	12.502	13.093	0.391	0.598	0.394
11	15.992	16.107	16.180	0.800	0.292	0.676

Table 3 Detection rate and correlation with temperature for all modes of bridge spans (BS) 1, 2 and 3

	Detection rate* (%)			Correlation coefficient		
Mode	BS1	BS2	BS3	BS1	BS2	BS3
1	86.3	95.6	91.8	-0.55	-0.61	-0.48
2	75.3	90.1	91.8	-0.54	-0.24	-0.71
3	94.0	82.7	62.7	-0.21	-0.14	0.04
4	85.2	74.0	83.0	-0.09	-0.19	-0.71
5	72.3	93.4	90.7	-0.16	-0.46	-0.07
6	47.7	54.0	63.8	-0.55	-0.38	-0.29
7	79.2	71.8	76.7	-0.24	-0.37	-0.35
8	18.4	8.2	38.6	-0.49	-0.11	-0.32
9	45.2	43.3	75.6	-0.26	-0.25	-0.05
10	66.6	49.6	16.4	-0.10	-0.01	-0.18
11	21.6	8.2	17.5	-0.16	0.36	-0.23

* The detection rate is based on the total number of days throughout the defined period (365 days), including maintenance and downtime of the SHM system (7 days).

scatter, in the tracking of higher modes (modes 7-11) compared to lower modes (modes 1-6). This uncertainty can also be clearly seen from the standard deviations presented in Table 2. Furthermore, from Table 3, it is also observed that the mode detection rate is lower for the higher modes compared to the lower modes. It should be noted, however, that the mode detection rate depends, to a certain degree, on the quality of the identified modes in the reference analysis. Fourth, and lastly, a similar behaviour of the bridge spans is observed, indicating that all three bridge spans generally compare well.

The correlation coefficients between the tracked modes and the temperature are presented in Table 3. From the results presented in Table 3, it is observed that the correlation coefficients are consistently negative, with two exceptions. These results indicate that the natural frequencies increase when the temperature decreases. Increasing natural frequencies imply a stiffer structural behaviour. Consequently, the bridge spans become stiffer for lower temperatures.

The temperature effects and their subsequent influence on the bridge structural behaviour are important for structural integrity evaluations. Table 4 summarizes the details of the frequency values, whereas Table 5 summarizes the variations of the mean frequencies of all modes for each bridge span. By considering the total difference as presented in Table 5, i.e., the difference between the maximum and minimum values over the mean of the natural frequencies, variations of approximately 8-25%, 8-40% and 7-23% for bridge spans 1, 2 and 3, respectively, of the natural frequencies can be expected on a yearly (seasonal) basis.

It is important to highlight that these variations are not solely caused by temperature effects, since some of the outliers of the natural frequencies in terms of low minimum and high maximum values of each mode of each bridge span are found from datasets containing traffic, i.e., passing trains. An improved modal tracking can be obtained by filtering, i.e., replacing time series that contain traffic with time series that contain no traffic. Such a filtering may significantly improve the results in terms of lower variations of the natural frequencies considering only temperature effects. As such, the actual variability

Table 4 Details of frequency values for all modes of bridge spans 1, 2 and 3

	Bridge span 1			Bridge span 2			Bridge span 3		
Mode	Min (Hz)	Max (Hz)	Mean (Hz)	Min (Hz)	Max (Hz)	Mean (Hz)	Min (Hz)	Max (Hz)	Mean (Hz)
1	2.056	2.429	2.273	1.863	2.368	2.199	1.877	2.377	2.224
2	4.349	4.732	4.621	4.082	4.680	4.542	4.387	4.689	4.576
3	4.405	5.573	4.842	3.388	4.975	4.729	4.149	5.052	4.672
4	4.925	5.666	5.334	4.852	5.763	5.302	4.802	5.377	5.163
5	7.625	8.288	7.899	7.491	8.126	7.848	7.161	8.167	7.827
6	8.060	8.887	8.442	7.991	9.245	8.351	7.967	9.218	8.380
7	9.422	11.049	10.497	9.769	11.043	10.361	9.412	10.893	10.206
8	9.662	11.875	10.964	10.422	11.960	11.239	10.395	12.304	11.507
9	12.032	13.375	12.643	11.917	13.390	12.656	11.636	13.637	12.660
10	12.053	13.942	13.021	9.696	14.629	12.502	12.357	14.198	13.093
11	14.650	18.688	15.992	14.800	16.433	16.107	14.770	18.154	16.180

Table 5 Variations of the mean frequencies for all modes of bridge spans 1, 2 and 3

	Bridge span 1			Bridge span 2			Bridge span 3		
Mode	Min (%)	Max (%)	Total (%)	Min (%)	Max (%)	Total (%)	Min (%)	Max (%)	Total (%)
1	-9.6	6.9	16.4	-15.3	7.7	23.0	-15.6	6.9	22.5
2	-5.9	2.4	8.3	-10.1	3.1	13.2	-4.1	2.5	6.6
3	-9.0	15.1	24.1	-28.4	5.2	33.6	-11.2	8.1	19.3
4	-7.7	6.2	13.9	-8.5	8.7	17.2	-7.0	4.1	11.1
5	-3.5	4.9	8.4	-4.5	3.6	8.1	-8.5	4.3	12.8
6	-4.5	5.3	9.8	-4.3	10.7	15.0	-4.9	10.0	14.9
7	-10.2	5.3	15.5	-5.7	6.6	12.3	-7.8	6.7	14.5
8	-11.9	8.3	20.2	-7.3	6.4	13.7	-9.7	6.9	16.6
9	-4.8	5.8	10.6	-5.8	5.8	11.6	-8.1	7.7	15.8
10	-7.4	7.1	14.5	-22.4	17.0	39.5	-5.6	8.4	14.1
11	-8.4	16.9	25.3	-8.1	2.0	10.1	-8.7	12.2	20.9

caused by only temperature effects are somewhat lower than reported here. Nevertheless, the results indicate the expected yearly (seasonal) variability caused by operational and environmental variability for modal properties of such bridges.

Modal tracking allows, to a certain extent, to monitor the development, including potentially unwanted changes, in the modal properties within a defined time period. Here, modal tracking has provided an overview of the modal properties of each bridge span over time. From the results obtained, it is concluded that the bridge spans compare well to each other over time when considering the dynamic structural behaviour and performance. No changes in the structural integrity of the bridge occurred during the period. Consequently, the observations made are mainly caused by operational and environmental variability.

Gaussian mixture modelling

Understanding the temperature effects on the structural behaviour and bridge performance is crucial for structural integrity evaluations. A two-component GMM is implemented on the modal tracking data [21]. The GMM is implemented with the constraints of using only two mixture components with all components sharing the same general covariance matrix. In general, a GMM is a probabilistic model that works under the assumption that all data points in a data set are generated from a mixture of a finite number of Gaussian (normal) distributions, where each Gaussian distribution has a set of unknown parameters. As such, the assumption is based on the data points representing a finite number of subpopulations, or components (clusters), which are Gaussian. The expectation-maximization (EM) algorithm is commonly used for estimating the parameters of the mixture of Gaussian models. The statistical distributions obtained by the GMM of the modal tracking data are shown in Figure 10. The dashed horizontal line indicates the freezing point (0°C).

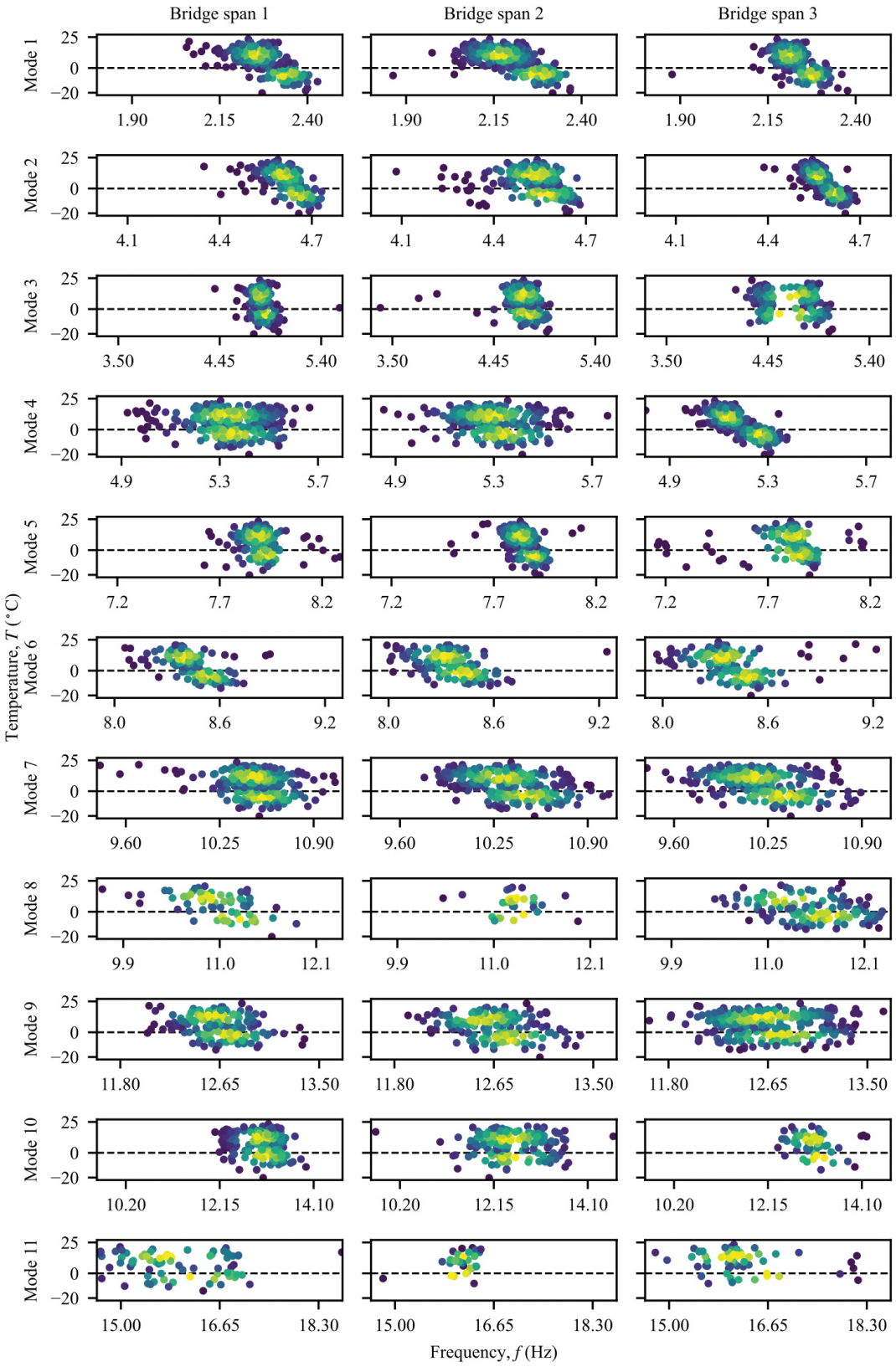

Fig. 10 Statistical distributions by GMM of the modal tracking results

From the results presented in Figure 10, it is clearly observed that the GMM separates the statistical distributions of the modal tracking data based on temperatures above and below the freezing point. This separation is consistent across all modes for all three bridge spans. The separation is less distinct for certain modes, such as modes 8 and 11, where the statistical representation is low. It is noteworthy, however, that despite the low detection rate for certain modes, the GMM still separates the data into two distributions based on the temperature, i.e., above and below the freezing point, under the predetermined constraints.

In the context of damage detection and SHM, the results obtained are important because they clearly show that the bridge has a distinct behaviour around the freezing point. The results clearly confirm a step-like variation in the natural frequencies of the bridge for many of the modes. Such a behaviour is explained by a contribution to the global stiffness of the structure, most likely from the timber sleepers in the bridge deck.

Summary and conclusion

This paper presented the structural integrity assessment of a train bridge using data obtained from a comprehensive SHM system. The structural integrity assessment focused on static inclination and the structural dynamic behavior over time for different temperatures, based on data obtained from one year of measurements. The effect of environmental conditions, i.e., the temperature, on the modal parameters of the bridge were investigated based on modal tracking and the implementation of a GMM on the modal tracking data. Lastly, the actual structural behavior was validated by comparing the performance of all three bridge spans and assessing the performance over time.

From the static structural assessment, it was shown that the effect of temperature is low. From the dynamic structural assessment, several important findings were established from the modal tracking. First, the correlation between temperature and natural frequencies showed that the bridge spans become consistently stiffer for lower temperatures. Second, significant variations in the natural frequencies can be expected on a yearly (seasonal) basis, typically in the range of 7-40%, of modes that excite the bridge globally. It should be noted, however, that this variation is caused by both operational and environmental variability and not only environmental variability, such as temperature effects. Third, through the implementation of the GMM on the modal tracking data, it was demonstrated that the bridge has a different behavior above the freezing point compared to below the freezing point. A step-like variation in the natural frequencies of the bridge was confirmed, most likely explained by a contribution to the global stiffness of the structure from the timber sleepers in the bridge deck for temperatures below the freezing point. Since the bridge has such a distinct behavior with respect to temperature, any damage detection and structural integrity evaluations, in the context of SHM, should be considered using separate data from above and below the freezing point.

In conclusion, the effects of operational and environmental variability, particularly the temperature effects and their subsequent influence on the structural behavior of the bridge, are important for structural integrity evaluations. Furthermore, it is concluded that the results presented represent the level of variation to be expected for similar steel truss bridges in typical Nordic and Scandinavian climates.

It is important to highlight that, since no known changes in the structural integrity of the bridge occurred during the period, the results obtained are attributed to variability in the operational and environmental conditions. Furthermore, the datasets used as a basis for the structural integrity assessments of static inclination and the structural dynamic behavior had no restrictions regarding operational variability, such as traffic in terms of train passings. Consequently, although the main source of variability in the results presented is mostly believed to be caused by the effect of environmental conditions, i.e., the temperature, some variability may also be attributed to operational conditions, i.e., train passings, particularly for the modal tracking results. The potential variability caused by operational conditions is believed, however, to be low compared to the variability caused by the environmental conditions, such as the temperature effects.

The main limitations of this study include (1) the low, or limited, statistical representation of the data, and (2) the consideration of both operational and environmental variability in the assessment. For the latter, operational variability should be excluded to establish only the environmental variability in terms of the temperature effect, since the temperature effect is the most influential source of variability in modal properties. Further work includes addressing the limitations and evaluating the basic statistics of the GMM for each component of each mode for all bridge spans.

Acknowledgments The project was funded by Bane NOR. The authors gratefully acknowledge the cooperation with the project team and the structural department in Bane NOR.

References

1. G. A. del Pozo, B. T. Svendsen, Ø. W. Petersen, and O. Øiseth, "Long-Term Monitoring of the Hell Bridge Test Arena: The Effects of Environmental Variability and Damage on the Natural Frequencies," 2025, pp. 432–441, doi: 10.1007/978-3-031-96114-4_45.
2. A. C. Dederichs, G. A. del Pozo, B. T. Svendsen, and O. Øiseth, "A new damage detector for bridges based on natural frequencies with missing data," Struct. Heal. Monit., 2024, doi: 10.1177/14759217241259621.
3. B. T. Svendsen, "Numerical and experimental studies for damage detection and structural health monitoring of steel bridges," Norwegian University of Science and Technology, 2021.
4. B. T. Svendsen, G. T. Frøseth, O. Øiseth, and A. Rønnquist, "A data-based structural health monitoring approach for damage detection in steel bridges using experimental data," J. Civ. Struct. Heal. Monit., no. 0123456789, 2021, doi: 10.1007/s13349-021-00530-8.
5. B. T. Svendsen, O. Øiseth, G. T. Frøseth, and A. Rønnquist, "A hybrid structural health monitoring approach for damage detection in steel bridges under simulated environmental conditions using numerical and experimental data," Struct. Heal. Monit., vol. 0, no. 0, pp. 1–22, 2022, doi: 10.1177/14759217221098998.
6. B. T. Svendsen, G. T. Frøseth, O. Øiseth, and A. Rønnquist, "A data set from an extensive experimental benchmark study of the Hell Bridge Test Arena subject to imposed damage," vol. 151, no. 12, pp. 1–15, 2024, doi: 10.1061/JSENDH.STENG-14818.
7. E. J. Cross, K. Y. Koo, J. M. W. Brownjohn, and K. Worden, "Long-term monitoring and data analysis of the Tamar Bridge," Mech. Syst. Signal Process., vol. 35, no. 1–2, pp. 16–34, 2013, doi: 10.1016/j.ymssp.2012.08.026.
8. S. Soyoz and M. Q. Feng, "Long-term monitoring and identification of bridge structural parameters," Comput. Civ. Infrastruct. Eng., vol. 24, no. 2, pp. 82–92, 2009, doi: 10.1111/j.1467-8667.2008.00572.x.
9. J. M. Ko and Y. Q. Ni, "Technology developments in structural health monitoring of large-scale bridges," Eng. Struct., vol. 27, no. 12, pp. 1715–1725, 2005, doi: 10.1016/j.engstruct.2005.02.021.
10. I. Gonzales, M. Ülker-Kaustell, and R. Karoumi, "Seasonal effects on the stiffness properties of a ballasted railway bridge," Eng. Struct., vol. 57, pp. 63–72, 2013, doi: 10.1016/j.engstruct.2013.09.010.
11. V. Zabel, M. Brehm, and S. Nikulla, "The influence of temperature varying material parameters on the dynamic behavior of short span railway bridges," in Proceedings of ISMA 2010 - International Conference on Noise and Vibration Engineering, including USD 2010, 2010, pp. 1519–1529.
12. J. T. Kim, J. H. Park, and B. J. Lee, "Vibration-based damage monitoring in model plate-girder bridges under uncertain temperature conditions," Eng. Struct., vol. 29, no. 7, pp. 1354–1365, 2007, doi: 10.1016/j.engstruct.2006.07.024.
13. B. Peeters, J. Maeck, and G. De Roeck, "Vibration-based damage detection in civil engineering: excitation sources and temperature effects," Smart Mater. Struct., vol. 10, no. 3, pp. 518–527, Jun. 2001, doi: 10.1088/0964-1726/10/3/314.
14. B. Peeters and G. De Roeck, "One-year monitoring of the Z24-Bridge: environmental effects versus damage events," Earthq. Eng. Struct. Dyn., vol. 30, no. 2, pp. 149–171, Feb. 2001, doi: 10.1002/1096-9845(200102)30:2<149::AID-EQE1>3.0.CO;2-Z.
15. E. Figueiredo and E. Cross, "Linear approaches to modeling nonlinearities in long-term monitoring of bridges," J. Civ. Struct. Heal. Monit., vol. 3, no. 3, pp. 187–194, 2013, doi: 10.1007/s13349-013-0038-3.
16. A. Santos, E. Figueiredo, M. Silva, R. Santos, C. Sales, and J. C. W. A. Costa, "Genetic-based EM algorithm to improve the robustness of Gaussian mixture models for damage detection in bridges," Struct. Control Heal. Monit., vol. 24, no. 3, pp. 1–9, 2017, doi: 10.1002/stc.1886.
17. F. Lucà, S. Manzoni, F. Cerutti, and A. Cigada, "A Damage Detection Approach for Axially Loaded Beam-like Structures Based on Gaussian Mixture Model," Sensors, vol. 22, no. 21, 2022, doi: 10.3390/s22218336.
18. E. Simoen, G. De Roeck, and G. Lombaert, "Dealing with uncertainty in model updating for damage assessment: A review," Mech. Syst. Signal Process., vol. 56, pp. 123–149, 2015, doi: 10.1016/j.ymssp.2014.11.001.
19. B. T. Svendsen, Ø. W. Petersen, G. T. Frøseth, and A. Rønnquist, "Improved finite element model updating of a full-scale steel bridge using sensitivity analysis," Struct. Infrastruct. Eng., vol. 0, no. 0, pp. 1–17, 2021, doi: 10.1080/15732479.2021.1944227.
20. P. Holmstrøm, D. Lang, T. Friis, M. N. Svendsen, and M. D. Havelykke, "Service life strategies on hanger cables of the Great Belt Bridge," in Bridge Maintenance, Safety, Management, Digitalization and Sustainability, no. June, London: CRC Press, 2024, pp. 3169–3177.
21. F. Pedregosa et al., "Scikit-learn: Machine Learning in Python," J. Mach. Learn. Res., vol. 12, pp. 2825–2830, 2011.

Chapter 4
Human-Induced Building Vibrations: A Perspective on Their Role for Long-Term Health Monitoring

Jinsi Guo and Yiwen Dong

Abstract What if our buildings could play an active role in understanding our health? As cities grow and populations age, finding ways to monitor health within everyday living spaces becomes increasingly important for delivering personalized and preventative care. Since the average American spends more than 80% of their time indoors, making our buildings "health-aware" is essential. Today's health monitoring methods often rely on clinic visits, cameras, or wearable devices. While useful, these solutions can raise privacy concerns, feel intrusive, or disrupt daily routines, making them less practical for continuous use at home. This paper explores an alternative: using the natural vibrations people create as they move through buildings as a lens into their health. These vibrations can reveal physical and even mental health status, offering a low-cost, non-intrusive, and privacy-friendly way to support long-term monitoring in everyday environments. Most prior studies have been limited to short-term lab or field experiments, leaving open the question of how such systems perform over months or years in real-world homes. To address this, we introduce a framework that brings together the three key players in this process: humans, buildings, and AI systems. Through real-world examples, like gait analysis, monitoring heart and breathing patterns, assessing personal hygiene, and tracking sleep stages, we show how vibrations can become a meaningful health signal. Finally, we highlight the unique challenges of long-term monitoring and propose directions for future research. By integrating civil engineering, human biomechanics, and physics-informed AI, this perspective lays the groundwork for smarter buildings that can quietly and continuously support healthier lives.

Keywords Structural vibration · Health monitoring · Gait analysis · AI for health · Cyber-physics system

Introduction

With the growing urbanization and global aging population, health monitoring in daily living spaces has become a critical need [1]. Conditions such as diabetes, cardiovascular disease, and neurodegenerative disorders such as Alzheimer's and Parkinson's are often most manageable when detected early, yet traditional healthcare mainly relies on episodic clinic visits and often fails to identify precursors of these diseases [2]. Daily living environments, where individuals spend over 80% of their time [3], present an untapped opportunity for long-term, personalized health monitoring. By transforming homes, workplaces, and other everyday spaces into health-aware environments, we can reduce the pressure on healthcare systems and empower individuals to monitor and improve their well-being in their daily living spaces.

Existing health monitoring approaches in daily living spaces have practical issues with operations and privacy [4]. For example, wearables often require daily maintenance, such as charging and wearing, which can disrupt user's daily activities and discourage long-term usage. Camera-based systems, despite their accuracy, often raise privacy concerns and are impractical for spaces like bedrooms and bathrooms. Pressure/force-based systems require direct human-sensor contact, limiting their area of coverage. Radio frequency-based systems are sensitive to the change of layout in physical objects in the space

Jinsi Guo
Ph.D. Student, University of Illinois Urbana-Champaign, 104 S Mathews Ave, Urbana, IL 61801
e-mail: jinsig2@illinois.edu

Yiwen Dong
Ph.D., Assistant Professor, University of Illinois Urbana-Champaign, 104 S Mathews Ave, Urbana, IL 61801
e-mail: yiwen@illinois.edu

© The Author(s), under exclusive license to River Publishers 2026

Kristin B. Zimmerman, PhD (eds.), *Dynamics of Civil Structures, 2026, Vol. 2*, Conference Proceedings
of the Society for Experimental Mechanics Series, https://doi.org/10.13052/rp-9788743814139

and thus pose challenges for long-term monitoring. These limitations highlight the need for alternative approaches to achieve seamless, non-intrusive, and privacy-friendly health monitoring in daily living environments.

This perspective paper focuses on **Human-Induced Building Vibrations** and their potential for long-term health monitoring in daily living. Figure 1 illustrates how human-induced structural vibrations can be used for health monitoring. When people move through a building, their footsteps and activities excite the structures to produce vibrations. These vibrations, captured by sensors, can be analyzed from both time and frequency domains to extract gait-related features. Modeling and inference methods then map these features to health traits, enabling applications ranging from individual injury detection to community-level monitoring. Prior studies have leveraged vibrations generated from everyday activities like walking or resting to extract meaningful health insights. For example, studies have shown that footstep-induced vibrations can reveal gait abnormalities [5], which are critical indicators of fall risk and neuromuscular diseases. Similarly, vibration sensors embedded in furniture can monitor subtle physiological signals, such as heartbeats and respiration rates, with accuracy comparable to medical-grade equipment [6].

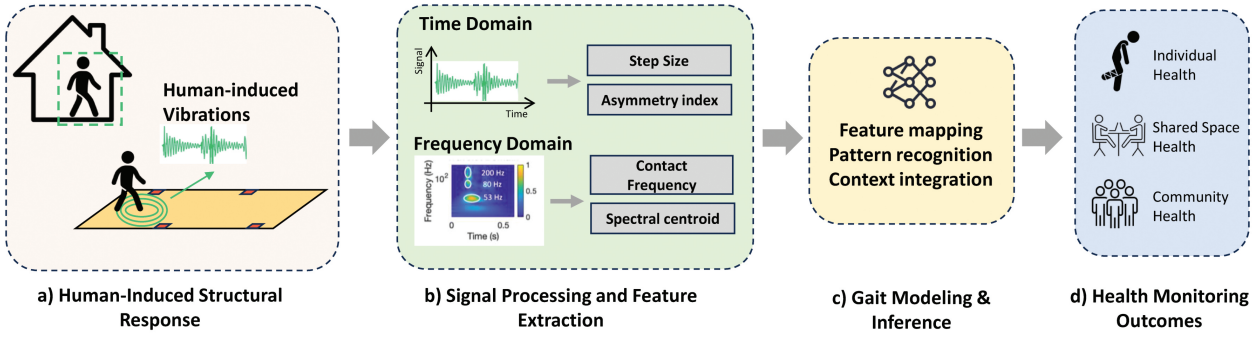

Fig. 1 Conceptual framework: a) Human-induced structural vibrations are captured by sensors. b) Transformed into features. c) modeled through inference. d) Mapped to health outcomes across individual, shared-space, and community levels

However, prior research has largely focused on assessing the feasibility of this approach through controlled laboratory settings and/or short-term field experiments on an hourly basis. Such studies often neglect the complex and unique challenges of deploying these systems in real-world, long-term monitoring scenarios. This paper introduces a conceptual framework that integrates human behavior, building structures, and AI-driven analytics, aiming to establish a foundation for long-term, non-intrusive health monitoring.

Review of Human-Induced Building Vibrations for Health Monitoring

Structural vibrations offer a unique window into human health, enabling monitoring that spans from the individual to entire communities. Since it operates non-intrusively through everyday structures, vibration sensing enables continuous and privacy-preserving health monitoring. Figure 2 illustrates this layered applications landscape, individuals, shared-space and community health. For individual health, vibrations reveal important health traits such as vital signs, sleep and daily activities, allowing continuous health monitoring for a single person [5], [6]. With the addition of identification and localization, it becomes possible to know who generated a vibration and where it occurred, enabling multi-person monitoring and the tracking of interactions [7], [8]. Finally, the scope expands to community health, where collective vibrations reflect crowd behavior, public safety, and even animal welfare [9], [10]. The following section reviews the recent progress in human-induced vibrations for health monitoring across these levels, providing an understanding of how vibrations sensing advances from personal monitoring in the home to population-scale.

A Conceptual Framework

To unify these advances, we propose a Human–Structure–Health framework that links behavior, structural response, and AI-driven inference. Everyday actions such as walking or sitting excite the structure, generating vibrations that encode health-relevant signals. AI models can infer metrics such as gait asymmetry, cadence, or respiration rate from these vibrations,

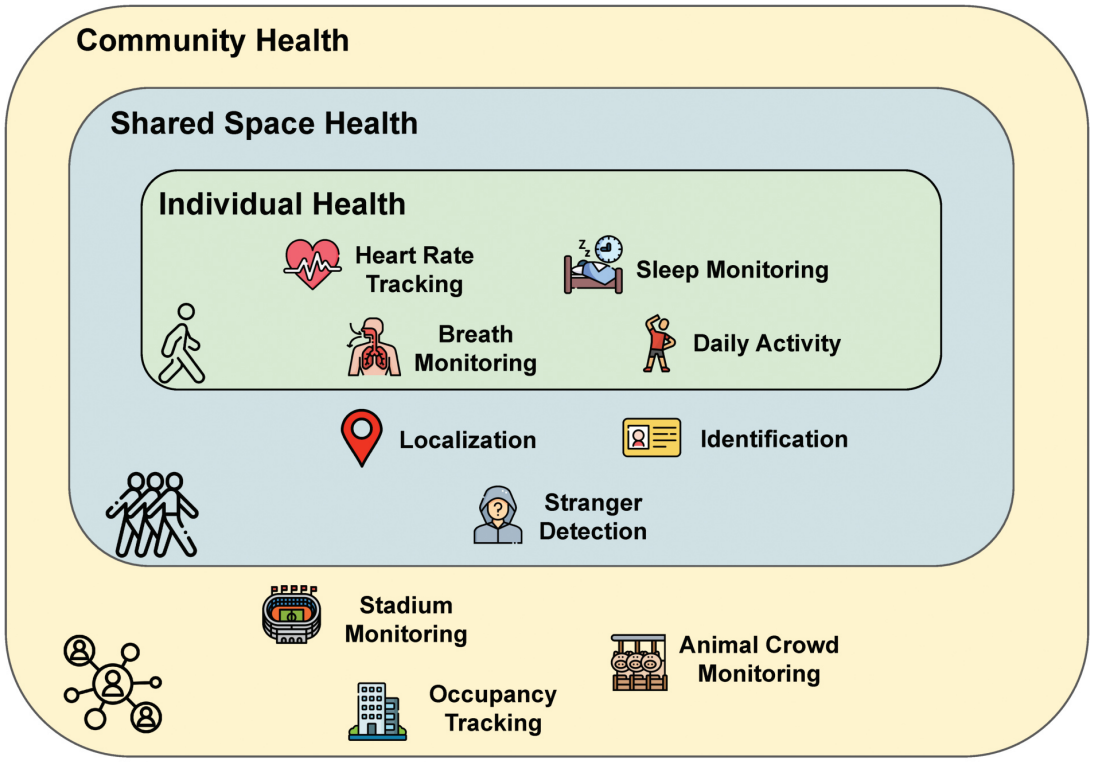

Fig. 2 Application landscape of vibration-based sensing for health: from individual-level monitoring to shared-space functions and community-scale applications

which in turn inform feedback and interventions for individuals. This framework positions buildings as active participants in health monitoring, creating a closed loop where human health both shapes and is reflected in the built environment.

Future Perspectives

Looking ahead, future research must address the unique challenges of long-term and real-world monitoring. This includes developing drift-aware methods that can adapt to daily contextual changes, attribution pipelines that preserve personalization in multi-occupant settings, and integration strategies that fuse in-home vibration data with wearable or outdoor signals. Achieving this will allow vibration sensing to move beyond feasibility demonstrations toward systems that support continuous, clinically meaningful evaluation in everyday environments.

References

1. S. Ohta, H. Nakamoto, Y. Shinagawa, and T. Tanikawa, "A health monitoring system for elderly people living alone," J. Telemed. Telecare, vol. 8, no. 3, pp. 151–156, 2002, doi: 10.1177/1357633X0200800305.
2. P. J. Nestor, P. Scheltens, and J. R. Hodges, "Advances in the early detection of Alzheimer's disease," Nat. Med., vol. 10, no. 7, pp. S34–S41, July 2004, doi: 10.1038/nrn1433.
3. A. Farrow, H. Taylor, and J. Golding, "Time Spent in the Home by Different Family Members," Environ. Technol., vol. 18, no. 6, pp. 605–613, June 1997, doi: 10.1080/09593331808616578.
4. N. Y. Philip, J. J. P. C. Rodrigues, H. Wang, S. J. Fong, and J. Chen, "Internet of Things for In-Home Health Monitoring Systems: Current Advances, Challenges and Future Directions," IEEE J. Sel. Areas Commun., vol. 39, no. 2, pp. 300–310, Feb. 2021, doi: 10.1109/JSAC.2020.3042421.
5. Y. Dong and H. Y. Noh, "Ubiquitous Gait Analysis through Footstep-Induced Floor Vibrations," Sensors, vol. 24, no. 8, Art. no. 8, Jan. 2024, doi: 10.3390/s24082496.

6. J. R. Codling et al., “FloHR: Ubiquitous Heart Rate Measurement using Indirect Floor Vibration Sensing,” in Proceedings of the 11th ACM International Conference on Systems for Energy-Efficient Buildings, Cities, and Transportation, Hangzhou China: ACM, Oct. 2024, pp. 44–54. doi: 10.1145/3671127.3698170.
7. S. Pan et al., “FootprintID: Indoor Pedestrian Identification through Ambient Structural Vibration Sensing,” Proc. ACM Interact. Mob. Wearable Ubiquitous Technol., vol. 1, no. 3, pp. 1–31, Sept. 2017, doi: 10.1145/3130954.
8. M. Mirshekari, S. Pan, J. Fagert, E. M. Schooler, P. Zhang, and H. Y. Noh, “Occupant localization using footstep-induced structural vibration,” Mech. Syst. Signal Process., vol. 112, pp. 77–97, Nov. 2018, doi: 10.1016/j.ymssp.2018.04.026.
9. Y. Dong et al., “GameVibes: Vibration-based Crowd Monitoring for Sports Games through Audience-Game-Facility Association Modeling,” in Proceedings of the 10th ACM International Conference on Systems for Energy-Efficient Buildings, Cities, and Transportation, in BuildSys ’23. New York, NY, USA: Association for Computing Machinery, Nov. 2023, pp. 177–188. doi: 10.1145/3600100.3623750.
10. Y. Dong et al., “PigSense: Structural Vibration-based Activity and Health Monitoring System for Pigs,” ACM Trans Sen Netw, vol. 20, no. 1, p. 1:1-1:43, Oct. 2023, doi: 10.1145/3604806.

Chapter 5
Experimental Evaluation of an Elastomeric Tuned Mass Damper Device for Vibration Suppression on a Laboratory Floor

Sahabeddin Rifai, Russell A. Larsen, Robert Baxter, Joshua M. Mouras, Ronald Klemencic, and Onur Avci

Abstract This paper presents the experimental evaluation of a novel tuned mass damper (TMD) featuring an elastomeric sphere damping element on a full-bay 30 ft × 40 ft laboratory floor specimen. The TMD was designed by Magnusson Klemencic Associates (MKA) and tested at West Virginia University (WVU). The performance of the TMD was evaluated using frequency response functions (FRFs) from shaker excitations, free-vibration decay tests, and metronome-guided human walking tests. Analysis of the FRFs demonstrated successful tuning, with the TMD suppressing the peak resonant response by 87%. Furthermore, resonance and free decay tests showed the TMD increased structural damping over a range of 10% to 39%, with performance dependent on vibration amplitude. Under serviceability-level walking excitations, the TMD reduced the 90th percentile Equivalent Sinusoidal Peak Acceleration (ESPA) by 7%. These results provide a successful experimental proof-of-concept, validating the TMD's effectiveness and establishing its potential as a practical solution for mitigating vibration serviceability issues in modern floor systems.

Keywords Tuned mass damper · Elastomeric damper · Vibration control · Floor vibrations · Steel floor systems

Introduction

The design of modern building floors increasingly favors open-plan layouts, longer spans, and lightweight materials. While this approach creates aesthetically pleasing and functional spaces, it often results in floor systems with low mass and stiffness, making them more susceptible to perceptible vibrations from human activities like walking or rhythmic exercises. A key factor governing this vibrational performance is the floor's inherent damping, its natural ability to dissipate energy. Modern construction methods, however, have led to systems with significantly lower damping values than their more traditional, heavier counterparts.

Resonant response in floors can occur when a harmonic of a rhythmic human activity (e.g., the pace of walking, the beat of an aerobics class, or synchronized crowd movement) excites a natural frequency of the floor, leading to serviceability issues that affect occupant comfort [1, 2]. Mitigating these vibrations often requires supplementary damping, typically introduced through dedicated devices. These devices are broadly categorized as active or passive. Active systems require an external power source to apply adaptive control forces to the structure. In contrast, passive systems generate control forces through their own motion in response to the structure's vibration, requiring no external power [3].

Among passive solutions, the tuned mass damper (TMD) is a particularly efficient and targeted device. A TMD consists of a mass, spring, and damper element tuned to a specific natural frequency of the structure. When that frequency is excited, the TMD resonates out of phase with the floor. This counter-motion allows the TMD to absorb energy from the floor and dissipate it, effectively suppressing the resonant response at its target mode [3, 4].

Sahabeddin Rifai · Onur Avci
Department of Civil and Environmental Engineering, West Virginia University, Morgantown, WV 26506
e-mail: sr00090@mix.wvu.edu; onur.avci@mail.wvu.edu

Russell A. Larsen · Robert Baxter · Joshua M. Mouras · Ronald Klemencic
Magnusson Klemencic Associates, Seattle, WA 98101
e-mail: rlarsen@mka.com; rbaxter@mka.com; jmouras@mka.com; rklemencic@mka.com

© The Author(s), under exclusive license to River Publishers 2026

Kristin B. Zimmerman, PhD (eds.), *Dynamics of Civil Structures, 2026, Vol. 2*, Conference Proceedings of the Society for Experimental Mechanics Series, https://doi.org/10.13052/rp-9788743814139

This paper presents the experimental evaluation of a novel tuned mass damper (TMD), designed by Magnusson Klemencic Associates (MKA), on a full-scale 30 ft × 40 ft laboratory floor at West Virginia University (WVU). The TMD, installed near the floor's center, comprises a steel plate mass supported by steel spring strips welded to the floor's beam webs. Its unique damping element consists of elastomeric spheres housed within a 3D-printed casing, which connects the mass to a steel channel section below. A key advantage of this design is its low-profile form factor, enabling installation within the structural depth of a typical floor system and thereby preserving architectural ceiling heights.

The objective of this study is to provide an experimental proof-of-concept for a novel TMD featuring a damper element with elastomeric spheres and to evaluate its performance in mitigating floor vibrations. The scope of this investigation involves quantifying the floor's response, both with and without the TMD, by generating frequency response functions (FRFs) from shaker excitation. Additionally, changes in system damping are determined using resonance and free-decay tests, and the TMD's effectiveness is ultimately assessed for serviceability under human-walking tests.

Elastomeric Sphere Tuned Mass Damper

The design of the MKA tuned mass damper (TMD) assembly and its damper element are illustrated in Fig. 1. Installation of the TMD begins by welding the support angles to the beam webs (Fig. 1-a) at a convenient height that leaves enough space for mass tuning plates. Second, the bottom steel channel section is aligned and connected to the bottom beam flanges by welding. Third, the bottom TMD mass plate spring strips are bolt-connected on two sides to the support angles. Finally, the damper element (Fig. 1-b) is aligned and installed between the mass plate at the top and the channel section at the bottom.

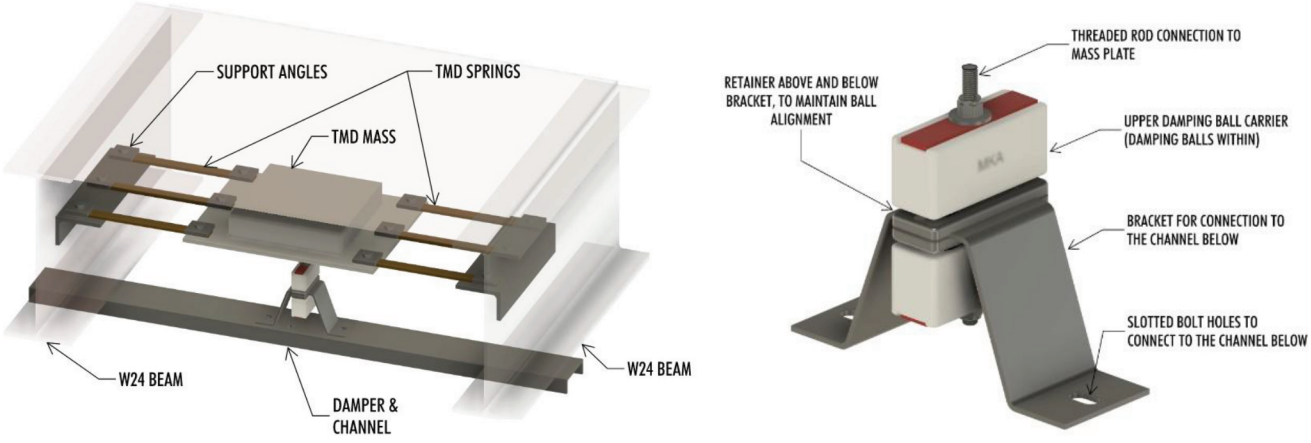

(a) (b)

Fig. 1 Schematic of the MKA TMD design. (a) View of the installed TMD with names of components. (b) A view of the MKA elastomeric sphere damper element

The TMD was installed and tested on a 30 ft × 40 ft all-steel laboratory floor structure (FastFloor) as shown in Fig. 2. The TMD was installed at the center of module 3 of the floor specimen. The plan layout of this specimen and the TMD location are shown in Fig. 3. FastFloor is a novel floor system for commercial building construction that utilizes prefabricated modules made from steel beams and plates. The modules are connected to girders on-site using field bolted connections. The tested full-bay floor specimen comprises 6 modules; 3 of which are prefabricated, and the remaining are formed by simply connecting infill plates to the prefabricated 3 modules. The steel beams are W24×68 and all the plates are $\frac{1}{2}$ in. thick. The two girders supporting the beams are W30×108. A raised access floor (RAF) was also installed on top of the steel plate.

The TMD is shown after installation in Fig. 4. During the tuning and testing process, two accelerometers were attached: one to the mass plate and one to the channel section running between the W24 bottom flanges. An additional nine accelerometers were placed on top of the floor along the centerline of Module 3 (Fig. 3). Excitations for the experimental modal analysis were provided by an electrodynamic mass shaker. The baseline FastFloor specimen without TMD includes horizontal angle blocking members connecting the beams' bottom flanges at L/3 and 2L/3 on Modules 1, 3, 5, and 6. All tests were conducted with the raised access floor (RAF) installed.

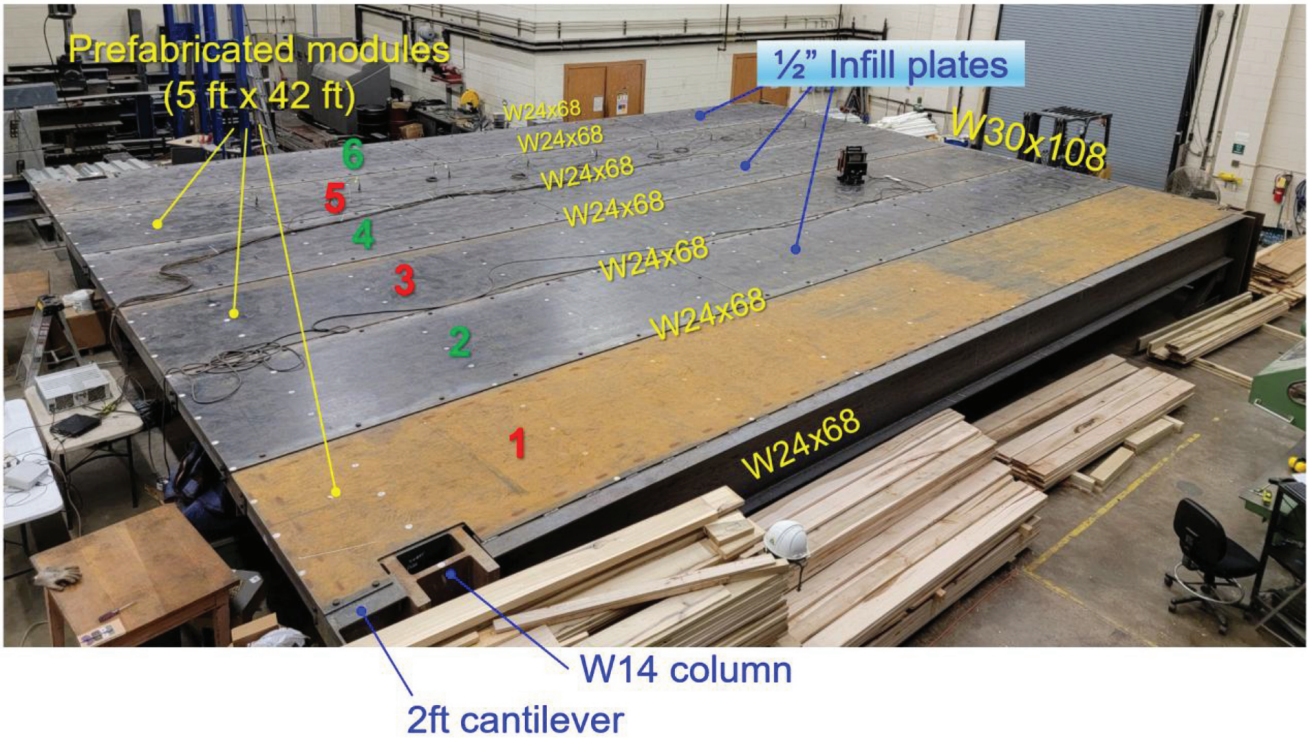

Fig. 2 View of the 30 ft × 40 ft All-Steel Floor Specimen with Components Annotated

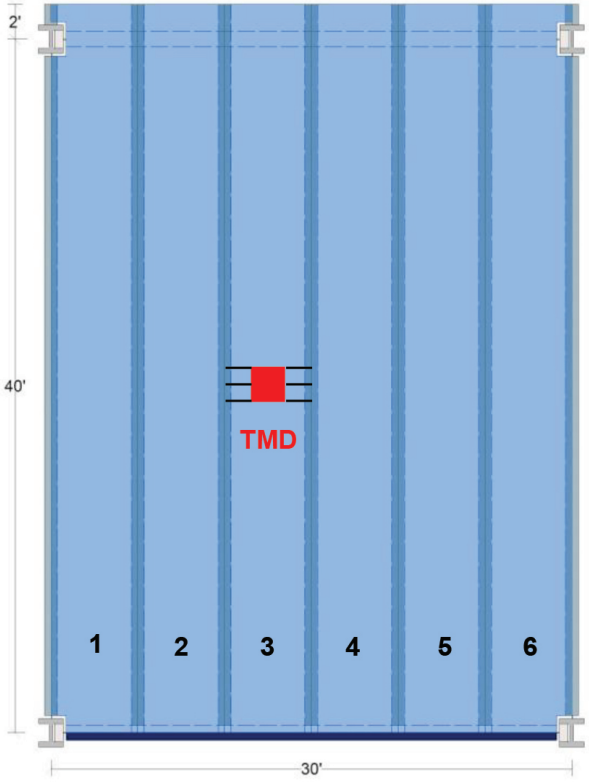

Fig. 3 Plan Layout of the FastFloor Specimen with the TMD Installed at the Center of Module 3



(a) (b)

Fig. 4 The TMD assembly after installation on Module 3: (a) view of the assembly with four spring strips; (b) the damper element, showing the elastomeric spheres separated by gaps

Tuning the Damper System

The first step was to tune the mass damper system such that its natural frequency closely matched the floor's fundamental frequency. This fundamental mode is targeted because it has the highest mass participation and is therefore the most significant contributor to the overall dynamic response. The shape of this mode, shown in Fig. 5, is characterized by the floor beams and plates bending together in a single curvature. Before the TMD was installed, the floor's baseline frequency was measured at 7.46 Hz. The tuning process was accomplished by adjusting the steel mass plates and modifying the internal gaps within the elastomeric damper element. Specifically, two different gap sizes inside the damper element were investigated to observe their effect on the system's performance.

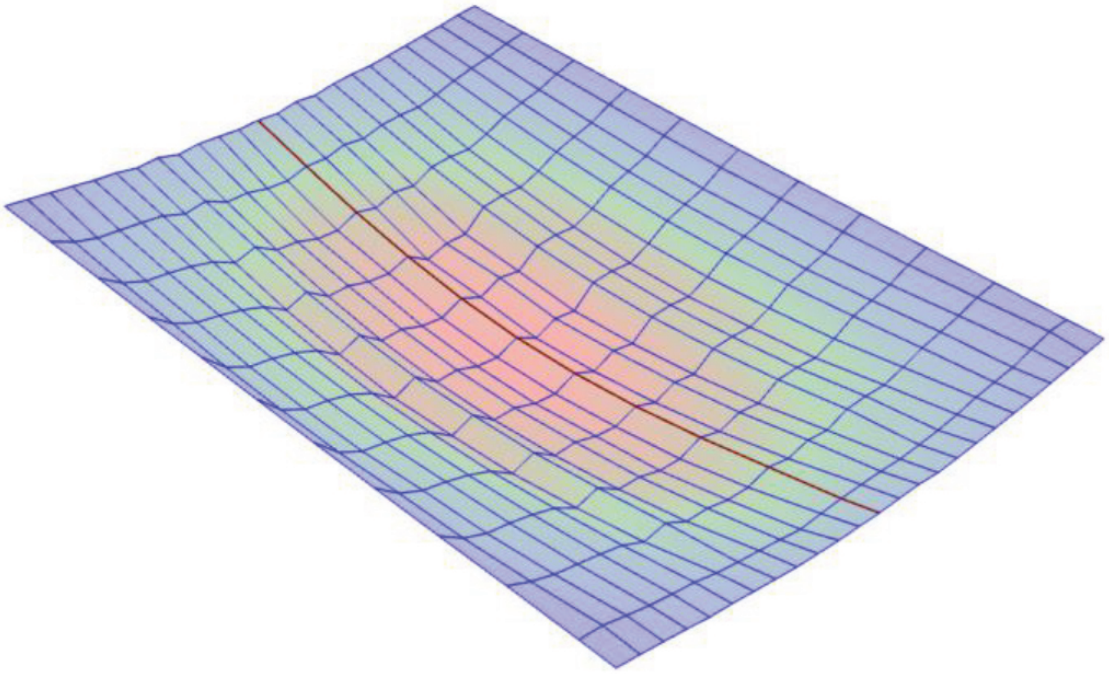

Fig. 5 Experimental Shape of the Fundamental (First) Vibration Mode of The Full-Bay Specimen

Initial Design Calculations and Experimental Optimization

Initial tuning calculations were provided by the TMD designers to guide the tuning process. Based on these calculations, a configuration of four spring strips and five standard mass tuning plates was selected to target a TMD frequency of approximately 7.4 Hz. It was anticipated that the fundamental frequency of the floor specimen would decrease slightly after the TMD was installed due to its self-weight.

To determine the optimal number of mass plates experimentally, five distinct mass configurations (0, 2, 4, 5, and 6 plates) were investigated while holding each of the two internal damper gaps at 3/16 in. The effect of each configuration was evaluated by analyzing the frequency response functions (FRFs) obtained from low-amplitude shaker excitations. The resulting FRFs, including the baseline configuration without a TMD, are presented on a logarithmic scale in Fig. 6. One observation was that the FRFs for the TMD configurations appeared rougher than the smooth baseline FRF, suggesting that the TMD introduced some nonlinear behavior into the system. The primary goal of this investigation was to identify the number of plates that produced the lowest FRF peak amplitude near the 7.4 Hz target frequency.

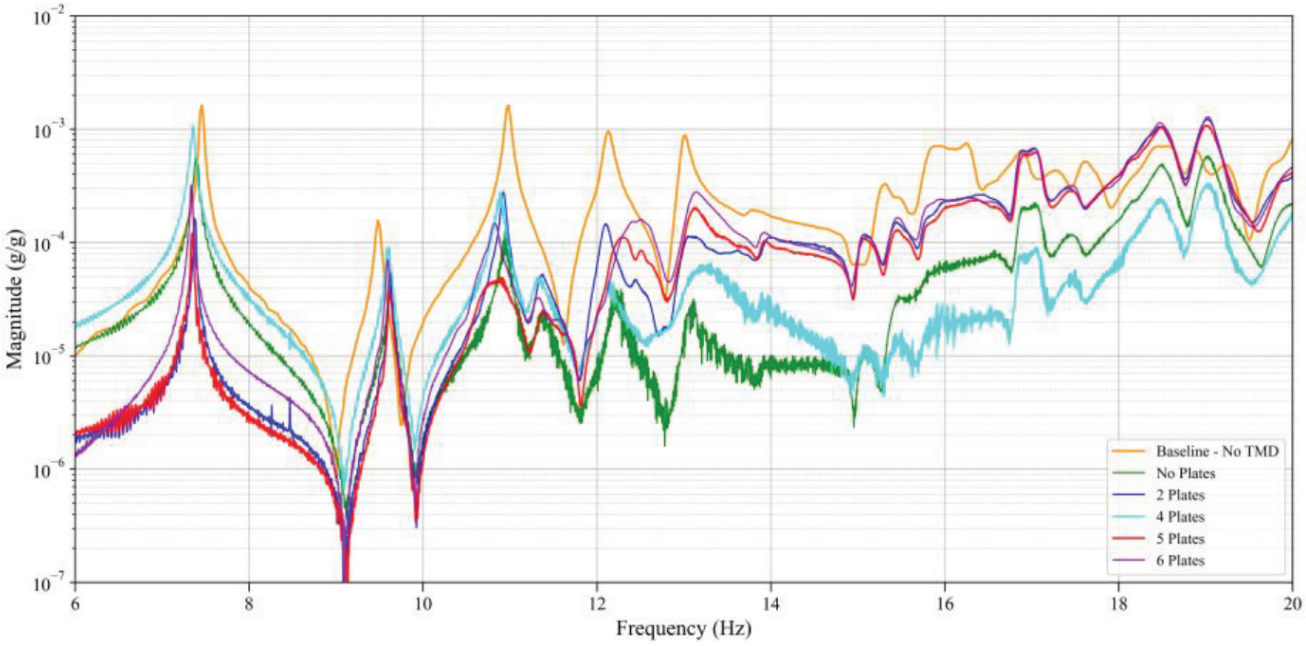

Fig. 6 Frequency response functions (FRFs) measured at the center of module 3 for different TMD mass configurations, generated using shaker excitation (logarithmic scale). The gaps in the damper are 3/16 in. each

A closer look at the 7.2–7.6 Hz frequency range, shown in Fig. 7, confirms that the five-plate configuration yielded the greatest reduction in FRF magnitude. This setup successfully reduced the peak dynamic response by approximately 87% compared to the baseline floor, a result that aligned well with the initial tuning calculations. However, an interesting phenomenon was observed: the peak FRF magnitudes for the other mass configurations did not decrease in a simple, linear trend. For instance, the configurations with four and six plates did not necessarily yield the second and third-lowest peak magnitudes. This can be attributed to the known challenges of testing large, flexible floor structures. As noted by [5], floors can exhibit nonlinear behavior, and dynamic interaction between the shaker and the structure can cause force drop-offs at resonance. These effects can lead to slight variations in measured FRF peaks, which highlights why this empirical tuning approach was valuable for identifying the configuration that most effectively reduced the peak response.

Further tuning of the TMD was conducted by adjusting the internal gap spacing within the damper element (the location of the gaps is shown in Fig. 4). Two gap sizes, 1/8 in. and 3/16 in., were investigated. It is important to note that the damper balls were always in compression with these gap widths. The amount of elastic compression varied according to the gap width. The frequency response functions (FRFs) for each configuration are compared to the baseline in Fig. 8. Based on this comparison, the 3/16 in. gap was found to provide a greater reduction in the FRF magnitude at the fundamental frequency. Gaps larger than 3/16 in. were not considered because the internal components of the damper began to show signs of looseness. Therefore, the 3/16 in. gap was identified as the optimal setting for the damper element.

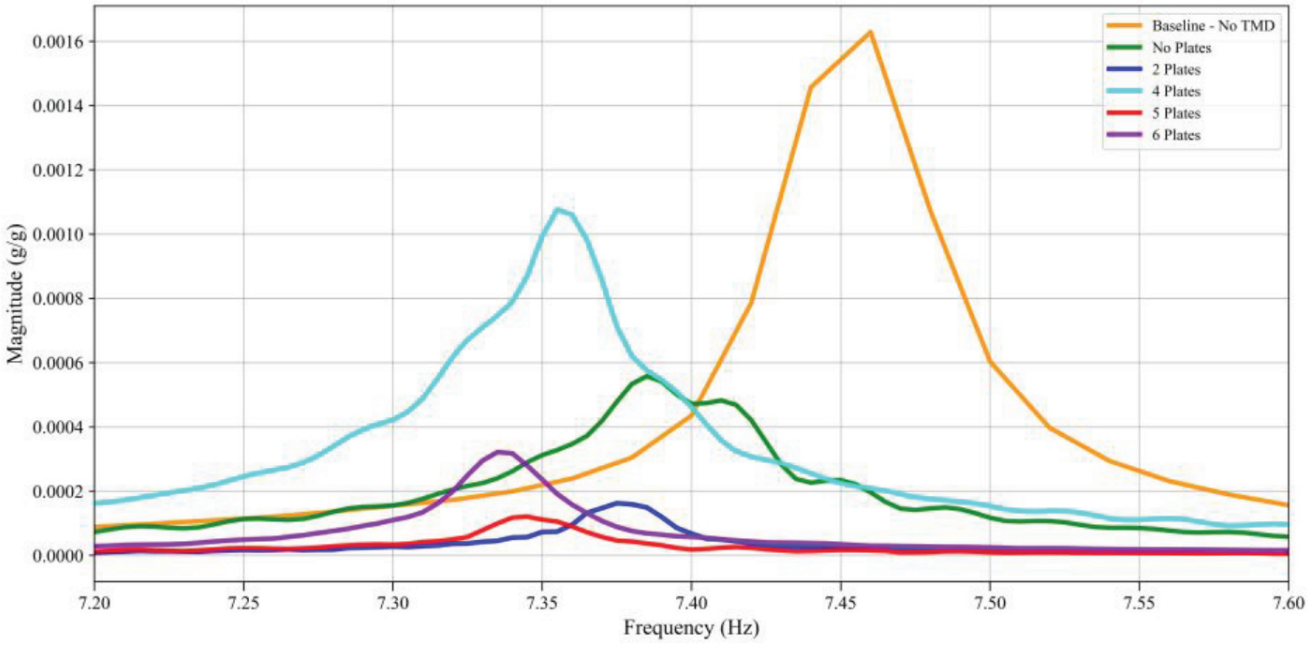

Fig. 7 Linear-scale plot of the FRFs near the fundamental mode, comparing the effect of different TMD mass configurations

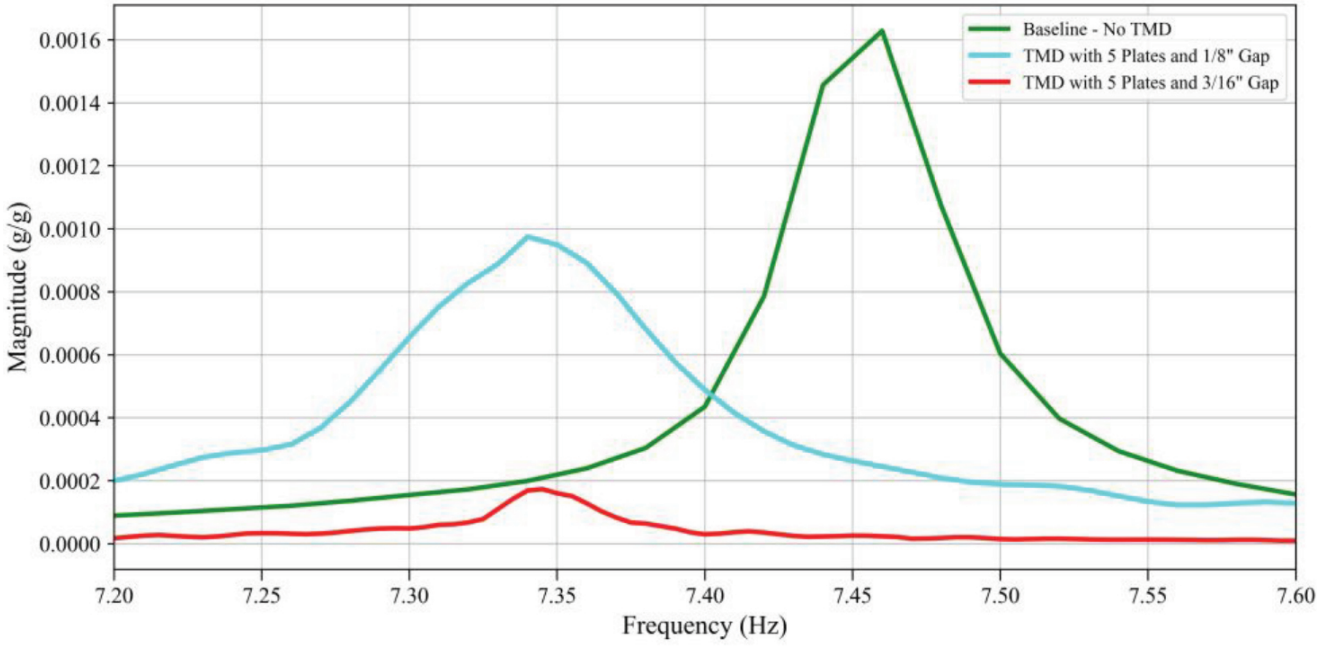

Fig. 8 Effect of the internal damper gap size on the FRFs for the TMD (linear scale)

Effect of the TMD on Structural Damping

The overall structural damping of the full-bay specimen was computed using the free vibration decay method. To do this, the floor was excited to resonance at its fundamental frequency with sine waves. The shaker was then abruptly stopped, and the resulting decay of the vibration was recorded. This test was repeated at various load amplitudes to assess any potential amplitude dependence. The structural damping ratio (β) was then calculated by curve-fitting the peaks of the decay curve to the exponential decay function shown in Equation 1. To improve the accuracy of this fit, the acceleration signal was first detrended and then filtered with a Butterworth filter to remove high-frequency noise.

$$a(t) = A \cdot e^{-\beta \omega_n t} \tag{1}$$

Baseline Damping

For the baseline case (without the TMD), the damping ratio (β) was observed to increase from 0.29% to 0.36% as the excitation level was raised from low to high (Fig. 9). This amplitude-dependent trend is further detailed in Fig. 10, which shows that the damping increased rapidly at acceleration amplitudes up to approximately 4% g, after which the rate of increase in damping lessened. It is likely that system nonlinearities contributed to this higher damping at greater excitation levels.

In addition to the changes in damping, a slight decrease in the system's natural frequency (f_n) was also observed at higher excitation amplitudes. This behavior is a known form of nonlinearity, defined in the literature as the "amplitude dependence of modal parameters" [5].

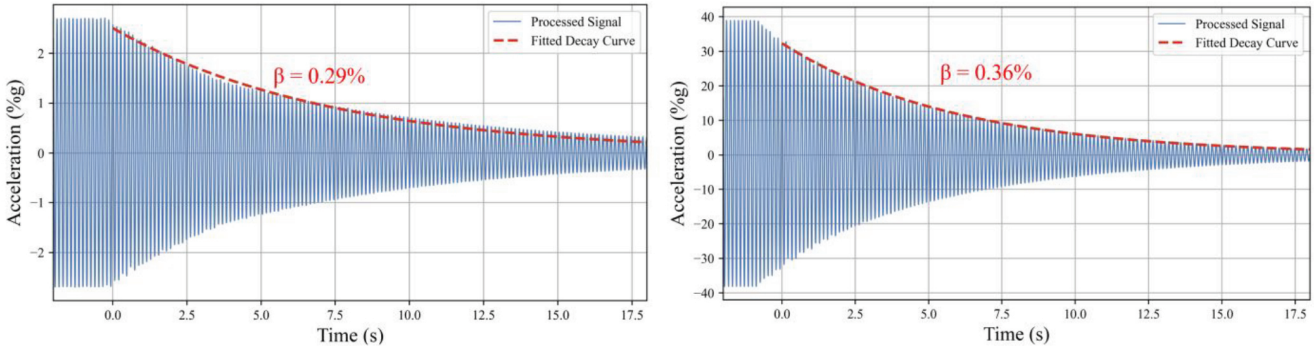

Fig. 9 Comparison of decay curves for the baseline specimen at (a) low and (b) high excitation amplitudes, with all signals measured at the center of module 3

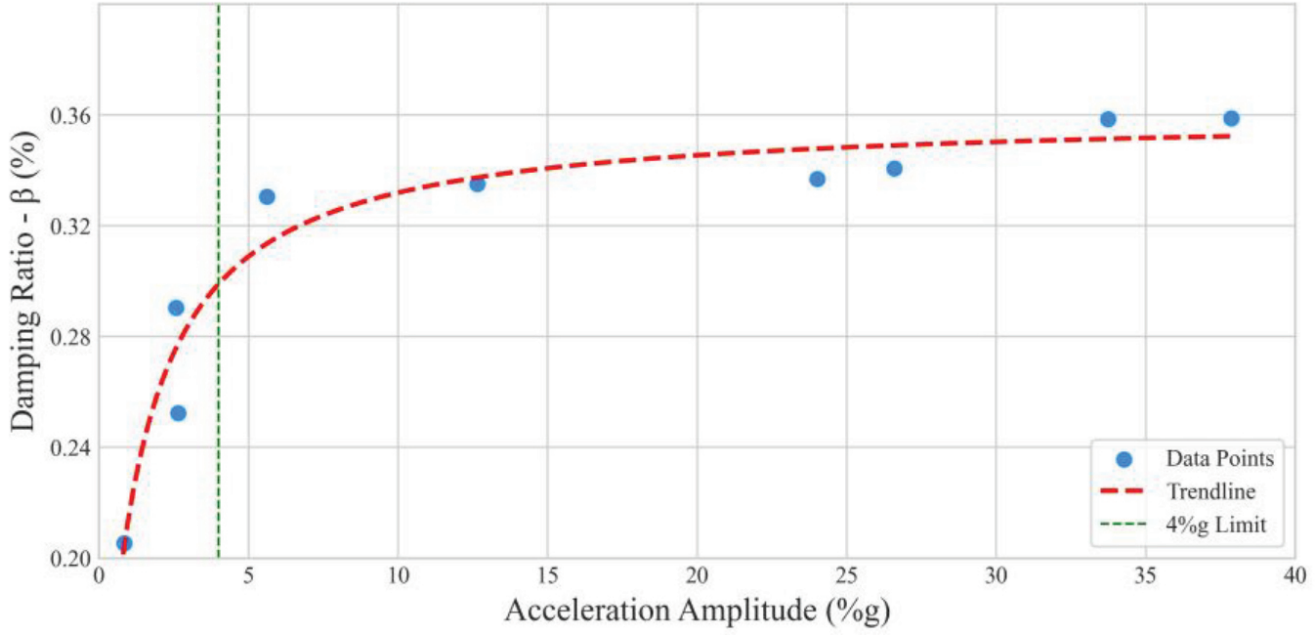

Fig. 10 Structural damping ratio as a function of excitation amplitude for the baseline case

Damping with TMD Installed

When compared to the baseline, a significant increase in the overall system damping was observed with the TMD installed. The damping ratio (β) was measured to be 0.32% at low excitation and 0.50% at high excitation (Fig. 11). These values represent an increase in damping over the baseline case of 10% and 39% for low and high amplitude excitations, respectively. Similar to the baseline case, an amplitude-dependent trend was observed, as shown in Fig. 12. The damping was found to increase rapidly with acceleration amplitudes up to approximately 4% g, after which the rate of increase slows.

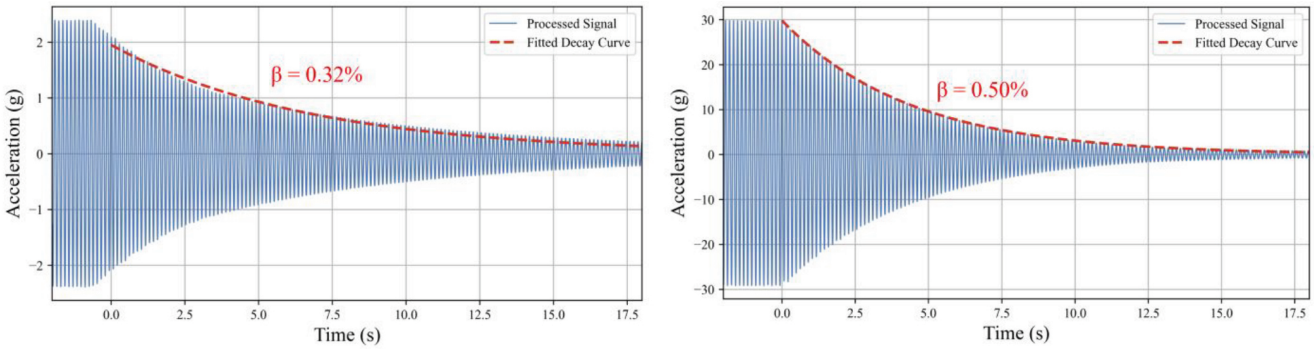

Fig. 11 Comparison of free-vibration decay curves for the TMD-equipped floor at (a) low and (b) high excitation amplitudes, with all signals measured at the center of module 3

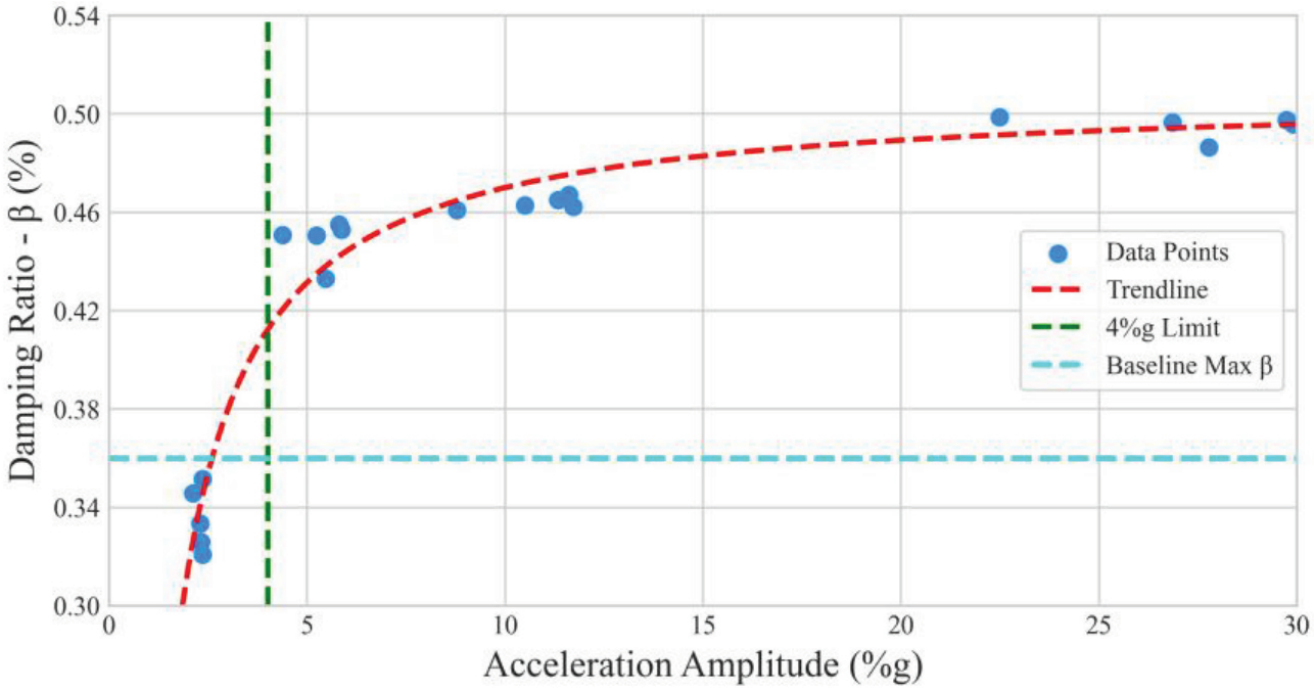

Fig. 12 Structural damping ratio as a function of excitation amplitude for the TMD-equipped floor

TMD Performance Under Resonance

The effectiveness of the TMD was evaluated by comparing its acceleration response to that of the floor's center (Module 3) during resonant sine excitation. A key indicator of effectiveness is the ratio of these two amplitudes; a higher ratio

signifies that the TMD is actively moving and dissipating energy. A higher acceleration response was consistently observed at the TMD mass compared to the floor, confirming that the device was working as intended. As shown in Fig. 13, the ratio of the TMD-to-floor acceleration amplitude was found to increase from 1.5 under low excitation to 2.0 under high excitation.

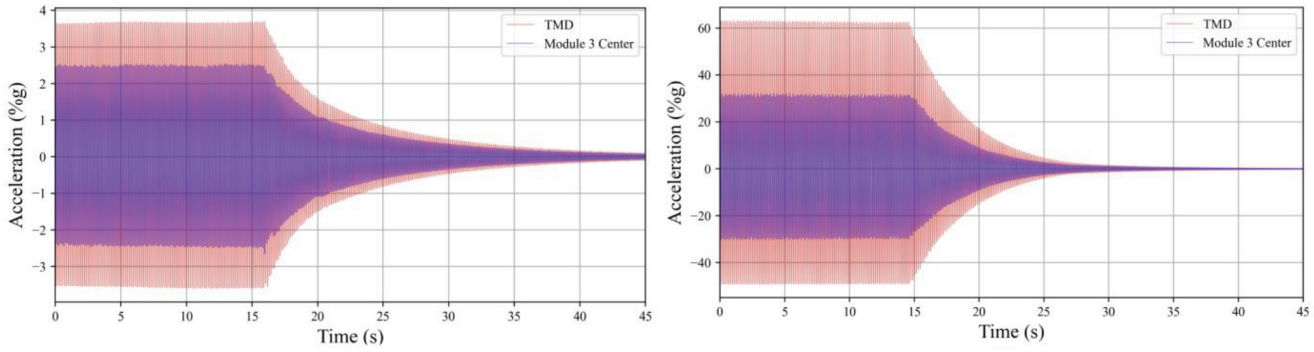

Fig. 13 Comparison of acceleration responses and decay curves at the TMD mass and the Module 3 center for (a) low-amplitude and (b) high-amplitude excitations

Effect of the TMD on the Floor's Response to Human Walking

We also conducted walking tests to investigate the effectiveness of the TMD design in reducing floor vibrations caused by human footfalls. To achieve resonant buildup in the floor with a normal walking pace, two individuals walked at the fourth subharmonic of the floor's fundamental frequency (f_n /4) on both baseline and TMD-equipped configurations.

Walking tests were conducted along the centerline of Module 4 at a metronome-guided pace (Fig. 14). The acceleration response was measured at the center of Module 3, and from these signals, the Equivalent Sinusoidal Peak Acceleration (ESPA) was calculated. This metric translates the complex vibration from footsteps into a standardized value that can be compared against human comfort limits.

Following the procedure in AISC Design Guide 11 and SCI P354, the ESPA was found by multiplying the maximum one-second root-mean-square (RMS) of the filtered acceleration signal by $\sqrt{2}$ [1, 6]. Since multiple trials were conducted for each configuration, the 90th percentile ESPA value was used as a robust statistical measure for the final comparison.

The ESPA results from the walking tests are summarized in Table 1. To ensure a direct comparison, the baseline data presented in the table were limited to the results from the two subjects who performed tests on both configurations. With the TMD installed, a 7% decrease in the 90th percentile ESPA and an 8% decrease in the maximum ESPA were observed, while the mean ESPA value remained largely unchanged. This modest level of improvement was anticipated for two main reasons. First, the previous resonance tests demonstrated that the TMD is most effective at higher vibration amplitudes, whereas normal walking is a relatively low-amplitude activity. Second, the harmonic of the walking pace that excites the floor is a higher, less impactful subharmonic of the fundamental frequency, which results in a lower input force compared to direct resonant excitation.

Table 1 Summary of ESPA results and statistics from the walking tests

			Equivalent Sinusoidal Peak Accelerations (ESPAs) [%g]				
Configuration	**# of Walking Tests**	**Step Frequency (steps/min)**	**Mean (μ)**	**Min**	**Max**	**STD (σ)**	**90th Percentile (μ+1.28σ)**
Baseline	14	112	1.53	1.17	1.92	0.26	1.86
TMD	6	110	1.51	1.30	1.76	0.17	1.73



Fig. 14 Setup for the metronome-guided walking tests along the centerline of module 4, with accelerometers deployed along the centerline of module 3

Conclusions

This paper presented the experimental evaluation of a novel tuned mass damper (TMD) featuring an elastomeric sphere damping element. The study's primary objective was to provide a proof-of-concept for this design and quantify its effectiveness in mitigating vibrations on a full-scale laboratory floor specimen. The main conclusions of the study are as follows:

1. The TMD was successfully tuned to the floor's fundamental frequency by empirically optimizing its mass and gaps inside its damper element. Analysis of frequency response functions (FRFs) showed that a five-plate mass configuration with 3/16 in. damper gaps provided the highest reduction in resonant response, decreasing the peak FRF magnitude by approximately 87% compared to the baseline floor.
2. Resonance and free decay tests demonstrated that the TMD increased the floor's effective damping. The damping ratio increased by approximately 10% at low vibration amplitudes and by nearly 39% at high amplitudes.
3. Under human walking tests, the TMD achieved a modest but notable reduction in the floor's response, decreasing the 90th percentile and maximum Equivalent Sinusoidal Peak Acceleration (ESPA) values by 7% and 8%, respectively. This result was consistent with the TMD's observed behavior, as its effectiveness is greatest at higher amplitudes than those typically generated by normal walking.

In summary, this study validates the performance of the novel MKA elastomeric sphere TMD. The experimental results confirm that the device effectively suppresses resonant vibrations and adds damping to the structural system, particularly at the higher vibration levels associated with serviceability issues.

Acknowledgments The authors would like to thank and acknowledge SteelFab steel fabricators of Charlotte, North Carolina for donation of the TMD fabrication.

References

1. T. M. Murray, D. E. Allen, E. E. Ungar, and D. B. Davis, "Design Guide 11: Vibrations of Steel-Framed Structural Systems Due to Human Activity (Second Ed.) | American Institute of Steel Construction."

2. M. Setareh and R. D. Hanson, "Tuned Mass Dampers to Control Floor Vibration from Humans," J. Struct. Eng., vol. 118, no. 3, pp. 741–762, Mar. 1992, doi: 10.1061/(ASCE)0733-9445(1992)118:3(741).
3. J. J. Connor, Introduction to Structural Motion Control. Prentice Hall Pearson Education, Incorporated, 2003.
4. A. K. Chopra, Dynamics of Structures: Theory and Applications to Earthquake Engineering. Prentice Hall, 2012.
5. O. Avci, "Amplitude-Dependent Damping in Vibration Serviceability: Case of a Laboratory Footbridge," J. Archit. Eng., vol. 22, Feb. 2016, doi: 10.1061/(ASCE)AE.1943-5568.0000211.
6. A. L. Smith, S. J. Hicks, and P. Devine, Design of Floors for Vibration: A New Approach (2009).
7. T. M. Murray, D. E. Allen, E. E. Ungar, and D. B. Davis, Design Guide 11: Vibrations of Steel-Framed Structural Systems Due to Human Activity (Second Ed.).

Chapter 6
A Comparative Study of Developing Seismic Fragility Models using Random Sampling Simulations and Machine Learning

Mohamed Tareq Soliman, Ufuk Yazgan, and Onur Avci

Abstract Seismic fragility analysis is an essential tool in evaluating structural reliability by quantifying the likelihood that a structure will exceed specific damage thresholds under varying ground motion intensities. Traditional approaches, such as Monte Carlo simulations, provide robust estimates by accounting for uncertainty in structural response; the approach's high computational demand, however, becomes particularly challenging for complex structures.

To address this issue, this study investigates developing fragility models of a structure exhibiting multiple failure modes using Monte Carlo simulations and machine learning driven techniques such as Response Surface Method (RSM) and Artificial Neural Networks (ANN). The structure's limit capacities are treated as random variables, and Incremental Dynamic Analysis (IDA) is used with scaled ground motions to capture record-to-record variability.

To ensure the invariability of the benchmark model, a sensitivity analysis was conducted to determine an appropriate size for the limit state set used in training, as well as to evaluate different sampling strategies. The results indicated that Latin Hypercube Sampling (LHS) demonstrated relatively lower variance in the fragility estimates compared to traditional random sampling methods, though it did not eliminate variance entirely and required a similar number of simulations to reduce this variability sufficiently. In addition, the variance of LHS-based estimates was observed to increase with the variance of the input random variables, reflecting the complexity of the relationship between the structural failure mechanisms.

Building on these findings, the study then evaluated RSM and ANN for developing fragility models. RSM offered a computationally efficient alternative by approximating fragility behavior through polynomial functions. However, it struggled to capture sharp transitions in mean fragility caused by sudden shifts of the dominant failure modes between the limit states, leading to inaccuracies, especially in highly nonlinear regions of the input domain. Conversely, ANN demonstrated superior performance, delivering more accurate and robust fragility models, even under high-variance conditions. Its ability to model complex nonlinear relationships without relying on predefined functional forms allowed it to outperform RSM in both predictive reliability and generalization.

Keywords Fragility · Monte carlo · Response surface · ANN.

Introduction

Seismic fragility models serve as a fundamental role in seismic risk assessment by quantifying the probabilistic relationship between ground motion intensity and structural damage states. These models express the conditional probability that a structure or component will exceed a designated damage state (e.g., collapse) given a specific ground motion intensity level measured through parameters like peak ground acceleration (PGA) or peak ground velocity (PGV). Fragility models are vital for several reasons, including: a) quickly assessing a structure's seismic performance [1]; b) informing government retrofitting and recovery plans [2]; c) developing mitigation strategies, such as for bridge design [2, 3]; d) creating vulner-

Mohamed Tareq Soliman · Onur Avci
Department of Civil and Environmental Engineering, West Virginia University, Morgantown, WV 26506
e-mail: mts00029@mix.wvu.edu; onur.avci@mail.wvu.edu

Ufuk Yazgan
Earthquake Engineering, Disaster Management Institute, Istanbul Technical University, Istanbul 34467, Türkiye
e-mail: yazgan@itu.edu.tr

© The Author(s), under exclusive license to River Publishers 2026

Kristin B. Zimmerman, PhD (eds.), *Dynamics of Civil Structures, 2026, Vol. 2*, Conference Proceedings
of the Society for Experimental Mechanics Series, https://doi.org/10.13052/rp-9788743814139

ability models for insurance and risk analysis [4, 5]; e) improving guidelines through life-cycle cost assessment, including for aging structures [6, 7]; and f) managing risk in seismic mega-cities [1].

Traditionally, the fragility function parameters are estimated from three main approaches: a) engineering judgment, b) numerical simulation methods through data generated from structural analyses of building archetypes, and c) empirical approaches based on observed damage data. While engineering judgment provide statistical estimations of probable damage based on expert assessments for different earthquake intensities [8], the analytical approach has gained significant prominence within the Performance-Based Earthquake Engineering (PBEE) framework, which enables the estimation of earthquake-induced damage and loss while considering various sources of uncertainty [9–11]. The empirical fragility models are traditionally derived from larger post-earthquake databases for various building classes. Existing empirical fragility functions often rely on municipal-level damage data, which aggregates information across large, geologically diverse areas. Despite this variability, each ground motion intensity level is typically estimated—via a Ground Motion Prediction Model GMPE or ShakeMap—at the municipality's centroid and used to represent the entire area [12].

Research on seismic fragility models has evolved through several key studies. One investigation examined how the number of incremental dynamic analyses impacts the reliability of models built using regression and maximum likelihood methods [13]. A separate study created a flexible framework for developing models for any damage state, provided post-earthquake damage data is available [14]. Later work evaluated existing European fragility models and proposed new design maps for the region [15]. More recently, intensity-based fragility models were developed for specific mid-rise Turkish residential buildings, using the Modified Mercalli Intensity scale to accommodate models derived from on-site damage observations [5].

Methodology

This study compares the advantages and limitations of employing machine learning algorithms to the traditional random sampling simulations in deriving fragility models for structures vulnerable to multiple failure modes. A key objective is the integration of two significant uncertainties that influence structural response during earthquakes: aleatoric and epismetic uncertainty. Aleatoric uncertainty stems from the inherent randomness in the strong motion characteristics. The epistemic uncertainty on the other hand arises from a lack of knowledge regarding material properties capacity of the structural elements and their load capacity.

The core architecture of our model is based on the work presented in [16, 17], which consists of a case study of an a 2D frame model with two columns and a beam. The structural configuration and load distribution are depicted in Figure 1. The reinforcement of the structural elements is configured as follows: the beam has a geometric percentage of 0.857%, with a top-to-bottom ratio of 2:1 at the ends (A-A) and 1:2 at midspan (B-B), while both columns have a reinforcement ratio of 1.2%, evenly distributed (C-C). The applied loads include 500 kN point loads on the columns and a 36 kN/m distributed load on the beam. the finite element analysis proceeds under the assumption that the concrete is unconfined, neglecting any confinement effects. OpenSeesPy was used in finite element analysis and dynamic analysis. This frame features three primary failure modes at the shorter column that represent the epistemic uncertainty: experiencing a shear force exceeding ultimate shear strength (Vu), and flexural failures due to concrete crushing at either top or bottom sections of the column. The shear strength is a random variable with a median of 170 kN and dispersion of 0.2, while the ultimate concrete crushing strain has a median of 0.006 and a dispersion of 0.35.

This structure is subjected to 12 ground motion records with a magnitude ranging between 6.0 and 7.6 with small epicentral distances up to 16 km, and soil profiles correspond to NEHRP C and D sites. The ground motions are listed in detail in the thesis work [17]. Incremental Dynamic Analysis (IDA) is performed such as that each earthquake is scaled to different levels, ranging from PGV = 5cm/s to PGV = 40 cm/s. The IDA process is performed for different limit state combinations meta-variables, and a fragility model is developed for each meta-variable by fitting the points to a log-normal cumulative density function. The cumulative distribution function of the equivalent log-normal fragility model (shown in Equation (1)) is characterized by the logarithmic mean (λ) and logarithmic standard deviation (ζ).

$$P(D > d \mid IM = x) = \Phi\left(\frac{\ln(x) - \lambda}{\zeta}\right) \tag{1}$$

To develop the benchmark model, random sampling simulations method is first employed, beginning with Monte Carlo simulations. This approach involves generating a large set of limit-state combinations and performing an Incremental Dynamic Analysis (IDA) for each. From the results, the probability of triggering each limit-state across various intensity measures is computed. Finally, a fragility model is fitted to the median probabilities using the maximum likelihood estimation method.

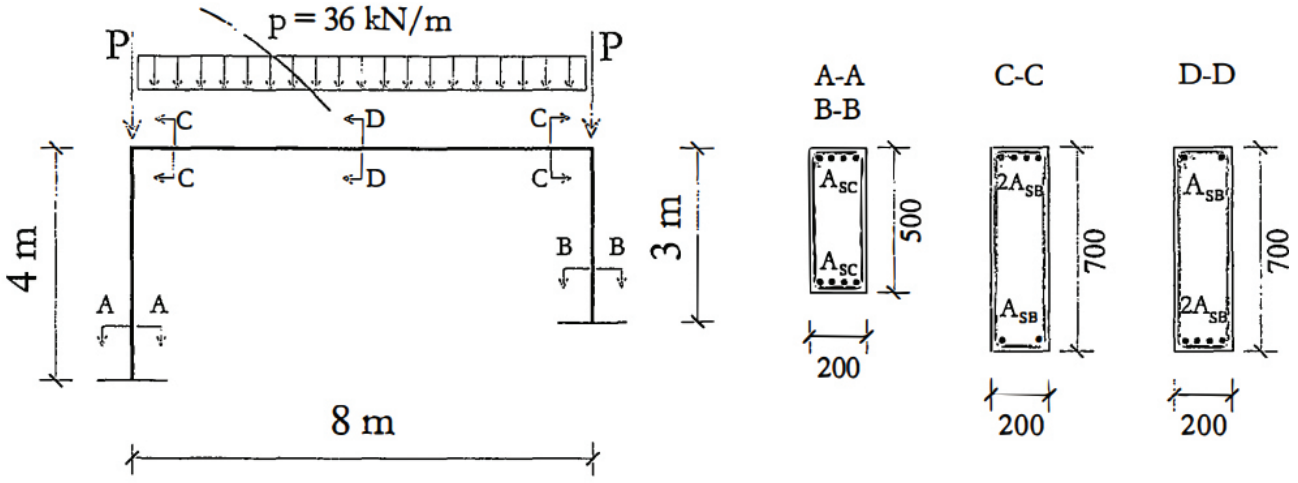

Fig. 1 Geometric and structural properties of the elements and sections

While the Monte Carlo method establishes a robust benchmark, its computational cost is prohibitive. To address this, our study focuses on reducing the computational effort relative to traditional MC sampling by employing more efficient techniques, such as Latin Hypercube Sampling (LHS). The LHS technique ensures uniform coverage of the input parameter space and a more accurate representation of distribution parameters with fewer samples compared to simple random sampling. In this approach, the distribution of each input variable is partitioned into N equal-sized intervals, and values are randomly paired across variables. LHS has been widely applied in many earthquakes and civil engineering fields; such as quantifying uncertainties in material properties that affect earthquake resistance of 9-story steel structure [18], deriving fragility models for masonry buildings [19], and capturing the influence of soil-foundation-structure interaction on system response [20].

The first machine learning tool used in this comparative study is the Response Surface Method (RSM) with Central Composite Design (CCD) as the sampling technique. CCD relies on experimental design points that are collected to cover the whole region of interest for the input limit states, while RSM fits these points into a polynomial bivariable surface. Then after fitting the surface, a mega set of randomly generated limit state combinations are generated into the RSM surface equation to determine their outcomes, and a log-normal cumulative density function is fitted using the median points of this mega set at each intensity measure level.

The second machine learning tool is Artificial Neural Networks (ANN) with grid sampling technique. The sample space is an evenly spaced region of dominating limit states divided into 7 combinations (total 49 training points) ranging from -2σ to 2σ each, which corresponds to the 3rd and 97th percentiles in the Z-score table. After developing fragility models for the 49 limit state combinations, a surface is fitted with the ANN model (MLP perceptron with back propagation) to fill the complete region. The ANN model consists of 5 neurons in 3 hidden layers each with L2 regularization parameter of 0.1%. And again, a mega set of randomly generated limit state combinations are generated into the neural networks model to develop fragility models, then fit an ultimate fragility model with the median points at each intensity measure level.

Discussion and Conclusions

In the process of developing benchmark model, a set of limit states was analyzed under 12 ground motion records to develop a fragility model that incorporates both structural and seismic uncertainties. These limit states were generated using two distinct random sampling techniques: the Monte Carlo simulations method and the Latin Hypercube Sampling method. A sensitivity analysis was performed to determine the optimal sample size for the limit state sets, ensuring the robustness of the benchmark fragility model. The results of this analysis (see Figure 2) indicate that at smaller sample sizes, the outcomes of different MC runs exhibited high variability. This variance decreased as the sample size increased. In contrast, LHS performed better with fewer samples, yielding a relatively lower variance in the estimated outcomes. However, for both methods, a non-negligible variance between different runs persisted even at larger sample sizes, requiring a comparable number of simulations to achieve stable results. This phenomenon is likely due to the complex relationships between the structural limit states.

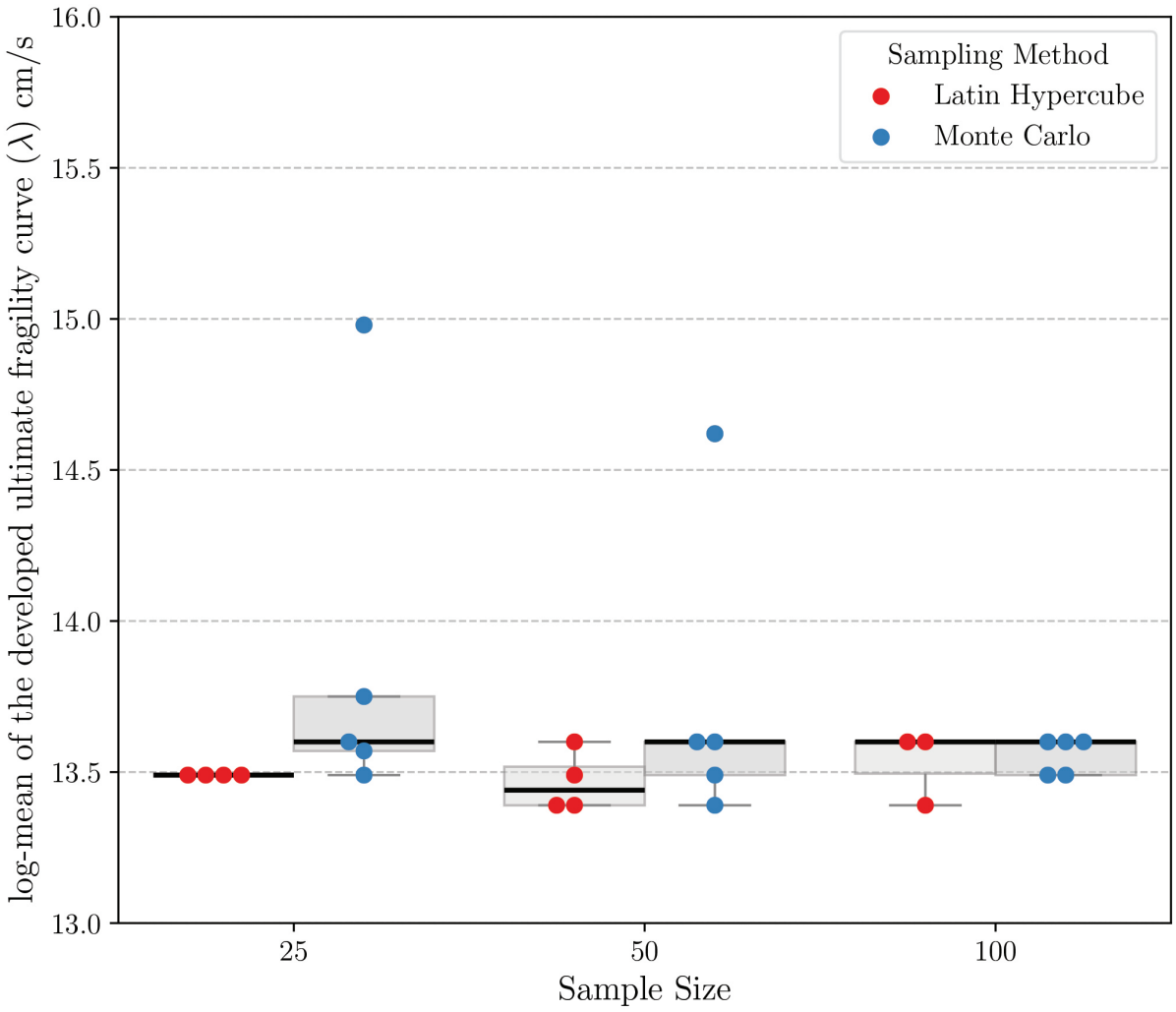

Fig. 2 Swarm plot of log-mean of the estimated ultimate fragility model for different sampling size and sampling techniques

Furthermore, as shown in Figure 3, the log-mean parameter from the MC simulations exhibits an increasing trend with the number of limit states. Conversely, Figure 4 demonstrates that for an equivalent sample size, both Monte Carlo and Latin Hypercube simulations produce nearly identical fragility models.

Looking into the two machine learning algorithms, RSM required little computational power to develop a predicting model for fragility function parameters. However, RSM failed to deal with the nonlinearity of the limit state function which has resulted in a sudden shift in the mean fragility, as shown in Figure 5. This has resulted in shifting the final fragility model developed by RSM to a lower mean value. On the other hand, ANN surface in Figure 6 is capable of detecting the plateau zone that the RSM failed to depict clearly. This plateau zone is the boundary line of shifting between the controlling limit states. In fact, ANN approach has demonstrated its effectiveness by delivering more accurate outcomes in predicting both fragility function parameters and final median fragility model compared to RSM approach (see Figure 7). Furthermore, the prediction errors (residuals) from RSM and ANN models are visualized for different levels of seismic intensity in Figure 8. The visualization uses violin plots, where the shape's width indicates how the errors are distributed at each intensity level. The results demonstrate that the ANN model consistently generates smaller errors than the RSM model at all intensity levels. This superior performance suggests that the ANN is more effective at modeling the complex, nonlinear behavior and inherent uncertainties of the structural system, leading to more precise fragility estimates. In contrast, the RSM model exhibits larger errors. This is attributed to the inherent smoothness of its fitted curves, which limits its capacity to accurately represent the system's nonlinear response.

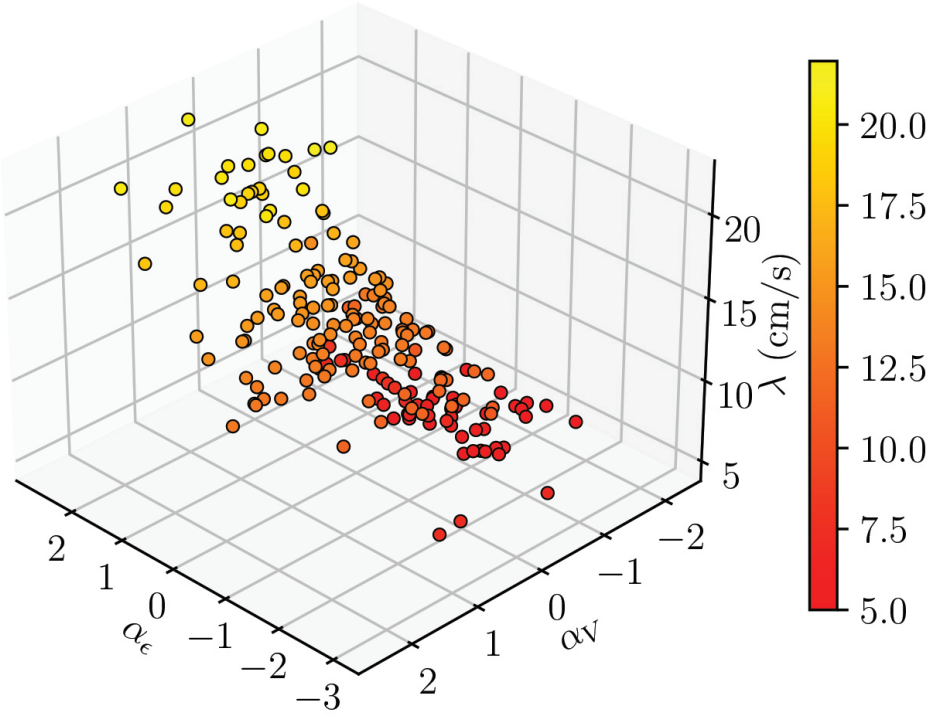

Fig. 3 Estimated median fragility (λ) of the Monte Carlo simulations using Maximum Likelihood Estimation and scaled to standard deviation

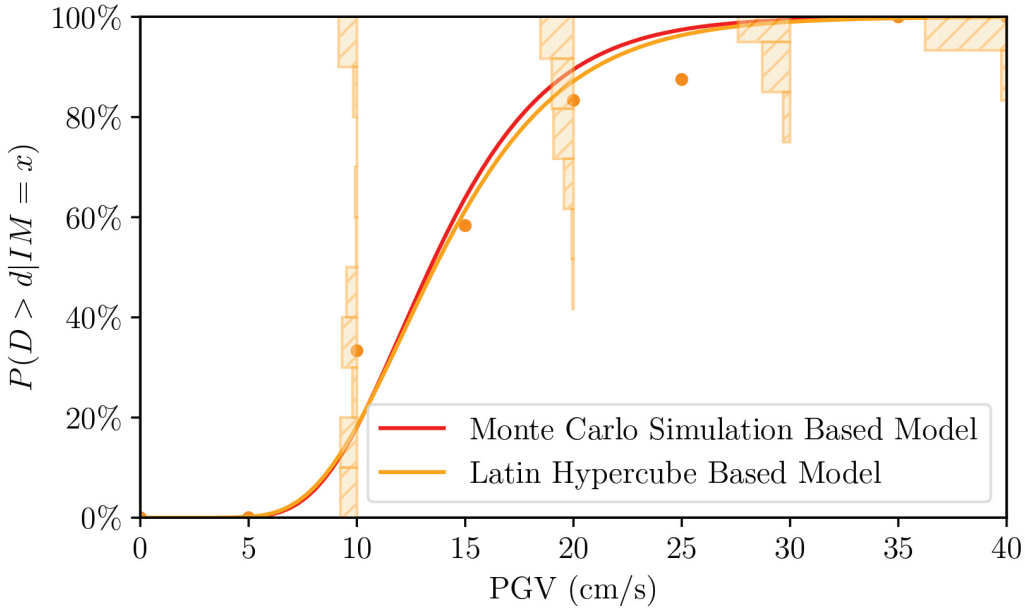

Fig. 4 Final fragility model estimated from Monte Carlo simulations and Latin Hypercube simulations

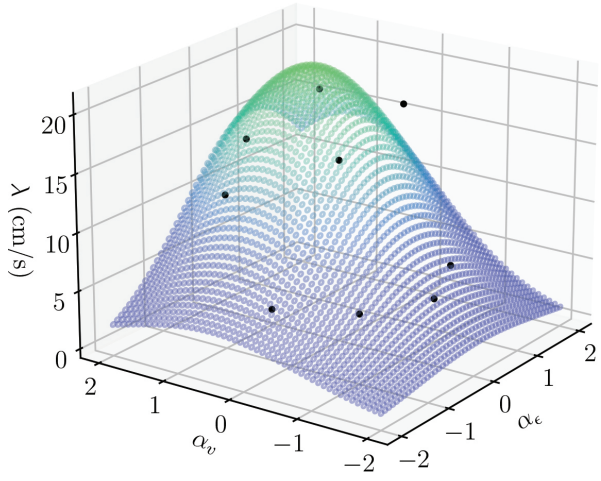

Fig. 5 Estimated median fragility (λ) of the Response Surface Method using Maximum Likelihood Estimation and scaled to standard deviation

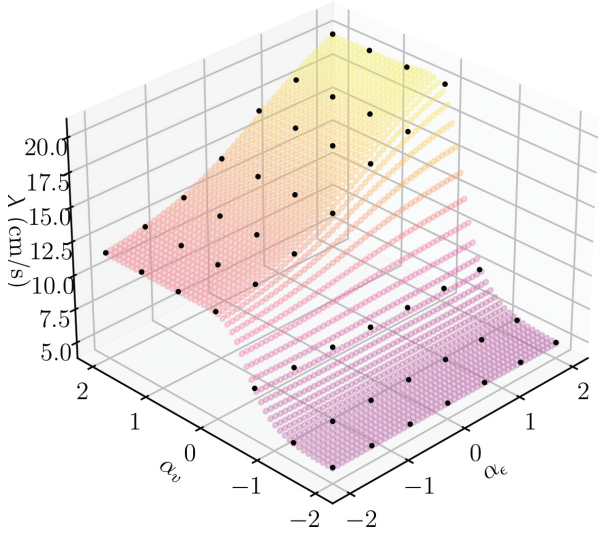

Fig. 6 Estimated median fragility (λ) of the ANNs using Maximum Likelihood Estimation and scaled to standard deviation

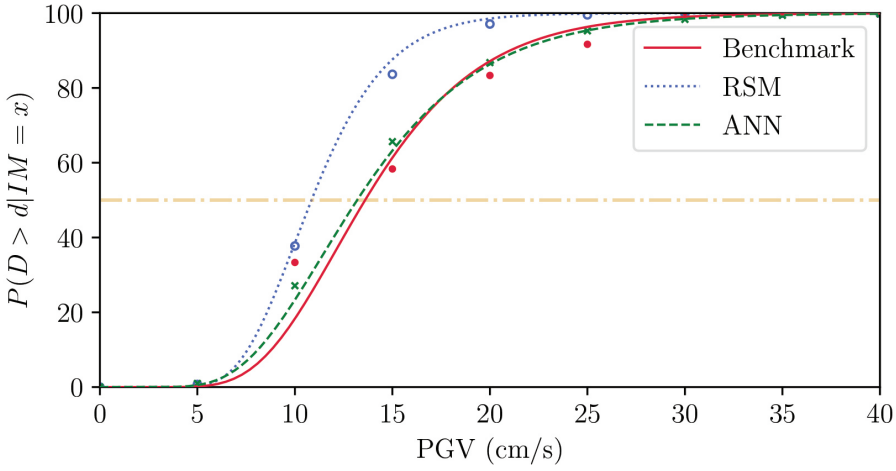

Fig. 7 Final fragility models of the benchmark Monte Carlo simulations, Response Surface Method, and ANNs

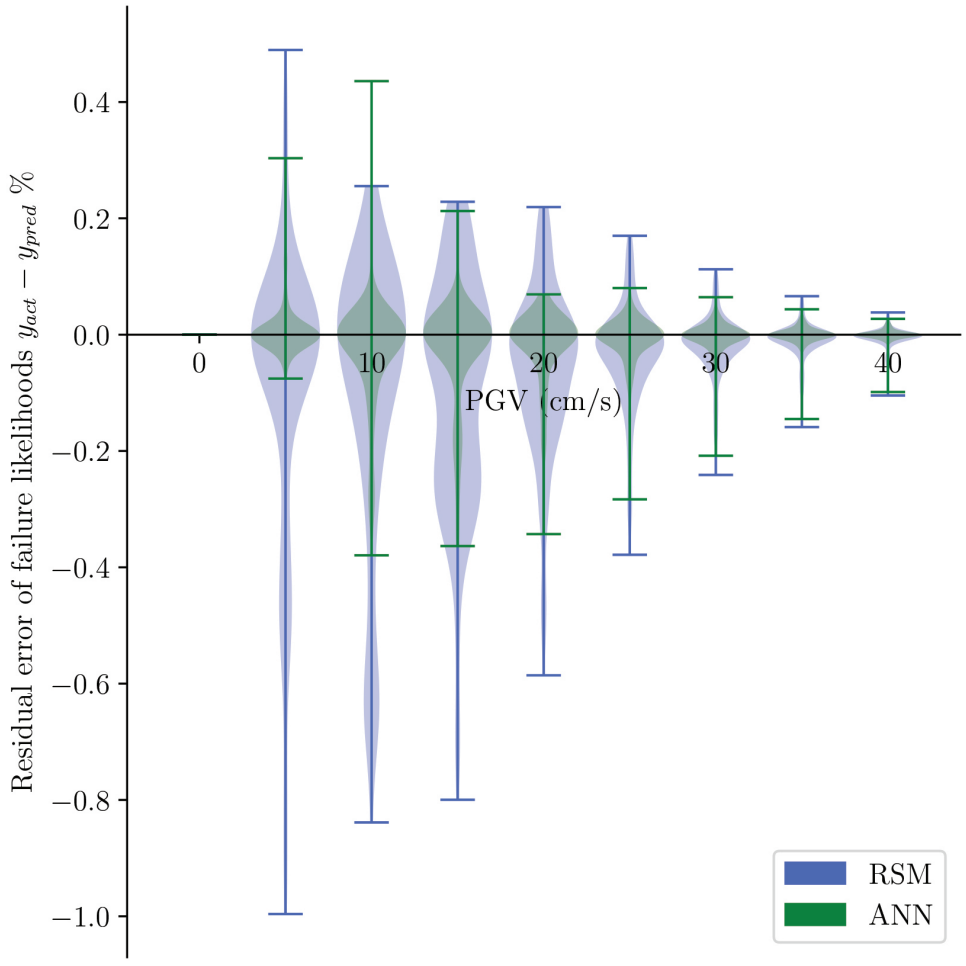

Fig. 8 Comparison between distribution of residuals for different seismic intensity measure of Response Surface Method, and ANNs to the benchmark model

Future work

To address the limitations of this study, future research should focus on:

1) Developing hybrid models that combine multiple algorithms with the Response Surface Method (RSM) to improve accuracy and reduce computational cost.
2) Testing these techniques on more complex, real-world structures with higher degrees of freedom to better assess their efficiency.
3) Enhancing the RSM approach by integrating adaptive algorithms to optimize Incremental Dynamic Analysis (IDA) that will pre-determine the necessary range of ground motion intensities, avoiding wasteful calculations at extreme levels.

Pursuing these questions will help overcome current limitations and advance the field.

References

1. L. Di Sarno, A. Elnashai, Seismic Fragility Relationships for Structures, in: 2021: pp. 189–222. https://doi.org/10.1007/978-3-030-68813-4_9.
2. A. Elnashai, L. Di Sarno, Fundamentals of Earthquake Engineering, From Source to Fragility, 2015.

3. M. Salkhordeh, E. Govahi, M. Mirtaheri, Seismic fragility evaluation of various mitigation strategies proposed for bridge piers, Structures 33 (2021). https://doi.org/10.1016/j.istruc.2021.05.041.
4. K. Pitilakis, H. Crowley, A.M. Kaynia, SYNER-G: Typology Definition and Fragility Functions for Physical Elements at Seismic Risk: Buildings, Lifelines, Transportation Networks and Critical Facilities, Geotechnical, Geological and Earthquake Engineering 27 (2014). https://doi.org/10.1007/978-94-007-7872-6.
5. S. Akkar, Earthquake Physical Risk/Loss Assessment Models and Applications: A Case Study on Content Loss Modeling Conditioned on Building Damage, in: Springer Tracts in Civil Engineering, 2021. https://doi.org/10.1007/978-3-030-68813-4_10.
6. G.M. Calvi, R. Pinho, G. Magenes, J.J. Bommer, L.F. Restrepo-Vélez, H. Crowley, Development of seismic vulnerability assessment methodologies over the past 30 years, ISET Journal of Earthquake Technology 43 (2006). https://doi.org/10.63898/busy2147.
7. J.G. Xu, Z.K. Cai, D.C. Feng, Life-cycle seismic performance assessment of aging RC bridges considering multi-failure modes of bridge columns, Eng Struct 244 (2021) 112818. https://doi.org/10.1016/J.ENGSTRUCT.2021.112818.
8. A. Hadlos, A. Opdyke, S.A. Hadigheh, Deriving expert-driven seismic and wind fragility functions for non-engineered residential typologies in Batanes, Philippines, Sci Rep 13 (2023). https://doi.org/10.1038/s41598-023-49398-2.
9. M. Shinozuka, M.Q. Feng, J. Lee, T. Naganuma, Statistical Analysis of Fragility Curves, J Eng Mech 126 (2000). https://doi.org/10.1061/(asce)0733-9399(2000)126:12(1224).
10. D. Lallemant, A. Kiremidjian, H. Burton, Statistical procedures for developing earthquake damage fragility curves, Earthq Eng Struct Dyn 44 (2015). https://doi.org/10.1002/eqe.2522.
11. J. Kohns, L. Stempniewski, A. Stark, Fragility Functions for Reinforced Concrete Structures Based on Multiscale Approach for Earthquake Damage Criteria, Buildings 12 (2022). https://doi.org/10.3390/buildings12081253.
12. I. Ioannou, R.E. Chandler, T. Rossetto, Empirical fragility curves: The effect of uncertainty in ground motion intensity, Soil Dynamics and Earthquake Engineering 129 (2020). https://doi.org/10.1016/j.soildyn.2019.105908.
13. P. Gehl, J. Douglas, D.M. Seyedi, Influence of the number of dynamic analyses on the accuracy of structural response estimates, Earthquake Spectra 31 (2015). https://doi.org/10.1193/102912EQS320M.
14. U. Yazgan, Empirical seismic fragility assessment with explicit modeling of spatial ground motion variability, Eng Struct 100 (2015). https://doi.org/10.1016/j.engstruct.2015.06.027.
15. V. Silva, H. Crowley, P. Bazzurro, Exploring risk-targeted hazard maps for Europe, Earthquake Spectra 32 (2016). https://doi.org/10.1193/112514EQS198M.
16. M.T.M. Soliman, U. Yazgan, Exploring the benefits and limitations of alternative machine learning techniques in seismic fragility assessment, in: DEU INTERNATIONAL SYMPOSIUM SERIES ON GRADUATE RESEARCHES-2022 GeoScience, 2023.
17. M.T. Soliman, Application of machine learning algorithms in seismic fragility analysis of structures, M.Sc. Thesis, Istanbul Technical University, 2023.
18. D. Vamvatsikos, Seismic Performance Uncertainty Estimation via IDA with Progressive Accelerogram-Wise Latin Hypercube Sampling, Journal of Structural Engineering 140 (2014). https://doi.org/10.1061/(asce)st.1943-541x.0001030.
19. S. and F.T.M. and R.P. and U.M. Del Carlo Federica and Caprili, Deriving Analytical Fragility Curves for Masonry Churches Based on Stochastic Nonlinear Analyses, in: P.B. and O.D.V. and B.J. and P.D. and S.R.A. and S.H.S. Matos José C. and Lourenço (Ed.), 20th International Probabilistic Workshop, Springer Nature Switzerland, Cham, 2024: pp. 115–124.
20. A. Karatzetzou, Uncertainty and Latin Hypercube Sampling in Geotechnical Earthquake Engineering, Geotechnics 4 (2024) 1007–1025. https://doi.org/10.3390/geotechnics4040051.

Chapter 7
Performance Evaluation of an Eddy Current Tuned Mass Damper on a Full-Scale Laboratory Floor

Sahabeddin Rifai, Russell A. Larsen, Robert Baxter, Joshua M. Mouras, Ronald Klemencic, and Onur Avci

Abstract This paper presents the experimental performance evaluation of a tuned mass damper (TMD) incorporating an eddy current damper on a full-scale 30 ft × 40 ft laboratory floor. The TMD was designed by Magnusson Klemencic Associates (MKA) and tested at West Virginia University (WVU). The system effectiveness was quantified through a set of dynamic tests, including shaker-induced frequency response functions (FRFs) to verify tuning, free-vibration decay tests to measure added damping, and human-walking tests to assess serviceability performance. The optimally tuned TMD suppressed the peak resonant response by 86% and increased the overall system damping by 34% to 53%, a value dependent on vibration amplitude introduced to the system as an input. Under serviceability-level human-walking tests, the TMD reduced the 90th percentile Equivalent Sinusoidal Peak Acceleration (ESPA) by 25%. The results validate the eddy current TMD is a promising passive control device, at the proof-of-concept stage. It offers a potential solution for mitigating excessive vibration levels in modern floor systems and other structures such as stadia. The future work on this damper will provide more information and shed more light on the potential of the proposed TMD device.

Keywords Tuned mass damper (TMD) · Eddy current damper · Floor vibrations · Vibration control

Introduction

Occupant comfort in modern buildings can be compromised by excessive floor vibrations. Architectural trends favoring open-plan layouts with long spans, combined with lightweight construction materials, create flexible floor systems with low inherent damping. These floors are easily excited into resonance by common human activities, such as walking or rhythmic group exercises. This creates significant serviceability challenges, where for many modern floor designs, the vibration serviceability limit state has become the governing design criterion rather than strength [1, 2].

Introducing supplemental damping is a remedial strategy for controlling excessive floor vibrations, often accomplished using specialized hardware like a Tuned Mass Damper (TMD). A TMD is an effective passive device for vibration control that adds damping and counteracts motion at a specific troublesome frequency without needing an external power source [3]. TMD's performance is influenced by its damping component, which is responsible for dissipating energy. Conventional dampers that rely on viscous fluids or friction can suffer from long-term performance issues like fluid leakage, temperature sensitivity, or mechanical wear [4].

To address these limitations, this paper investigates an eddy current damper as a method for vibration control. This technology operates on the principle of electromagnetic induction. When a conductive plate moves through a magnetic field, the changing magnetic flux induces circulating currents within the plate, known as eddy currents. According to Lenz's Law, these currents generate their own magnetic field that opposes the original change in flux, resulting in a Lorentz force that counteracts the motion. This phenomenon creates a stable, velocity-proportional damping force that effectively dissipates

Sahabeddin Rifai · Onur Avci
Department of Civil and Environmental Engineering, West Virginia University, Morgantown, WV 26506
e-mail: sr00090@mix.wvu.edu; onur.avci@mail.wvu.edu

Russell A. Larsen · Robert Baxter · Joshua M. Mouras · Ronald Klemencic
Magnusson Klemencic Associates, Seattle, WA 98101
e-mail: rlarsen@mka.com; rbaxter@mka.com; jmouras@mka.com; rklemencic@mka.com

© The Author(s), under exclusive license to River Publishers 2026

Kristin B. Zimmerman, PhD (eds.), *Dynamics of Civil Structures, 2026, Vol. 2*, Conference Proceedings of the Society for Experimental Mechanics Series, https://doi.org/10.13052/rp-9788743814139

the structure's kinetic energy as heat [5]. Because this force is generated without physical contact, eddy current dampers are not subject to the mechanical wear, fluid leakage, or temperature sensitivity that can degrade conventional dampers

This study presents the experimental evaluation of a Tuned Mass Damper (TMD) equipped with this eddy current damper element. The TMD, designed by Magnusson Klemencic Associates (MKA), was installed on a full-scale 30 ft × 40 ft all-steel laboratory floor at West Virginia University (WVU). The primary objective is to perform a proof-of-concept study, quantify the system's effectiveness and provide a direct performance comparison to other damping technologies previously evaluated on the same structural bay.

This paper is structured as follows: Section 2 details the design of the eddy current TMD and the full-scale laboratory specimen. Section 3 describes the analytical and experimental procedures used to tune the TMD mass. Section 4 presents the results from free-vibration decay tests, quantifying the TMD's effect on system damping. Finally, Sections 5 and 6 evaluate the TMD's performance under resonant shaker excitation and simulated human-walking tests, respectively.

Eddy Current Tuned Mass Damper

The MKA-designed eddy current tuned mass damper (TMD) is illustrated in Figure 1. As shown in the installed assembly (Fig. 1-a), the TMD's spring element consists of steel strips, and the system's stiffness can be adjusted by changing the number of these strips. The mass is composed of a base plate with additional tuning plates, allowing for precise mass adjustment. The eddy current damper element (Fig. 1-b) comprises a conductive copper plate and a 3D-printed holder containing an array of disc magnets.

The installation process begins by welding support angles to the beam webs and attaching a steel channel section to the bottom beam flanges. The steel spring strips are then bolted to the support angles. Finally, the eddy current damper element is installed between the mass plate and the bottom channel section. It is connected using a hinged linkage designed to permit the necessary rotational for the vertical movement of the copper plate as it moves through the magnetic field. The linkage additionally amplifies the velocity of the conductive copper plate and amplifies the resulting resistive force applied to the TMD mass plate.

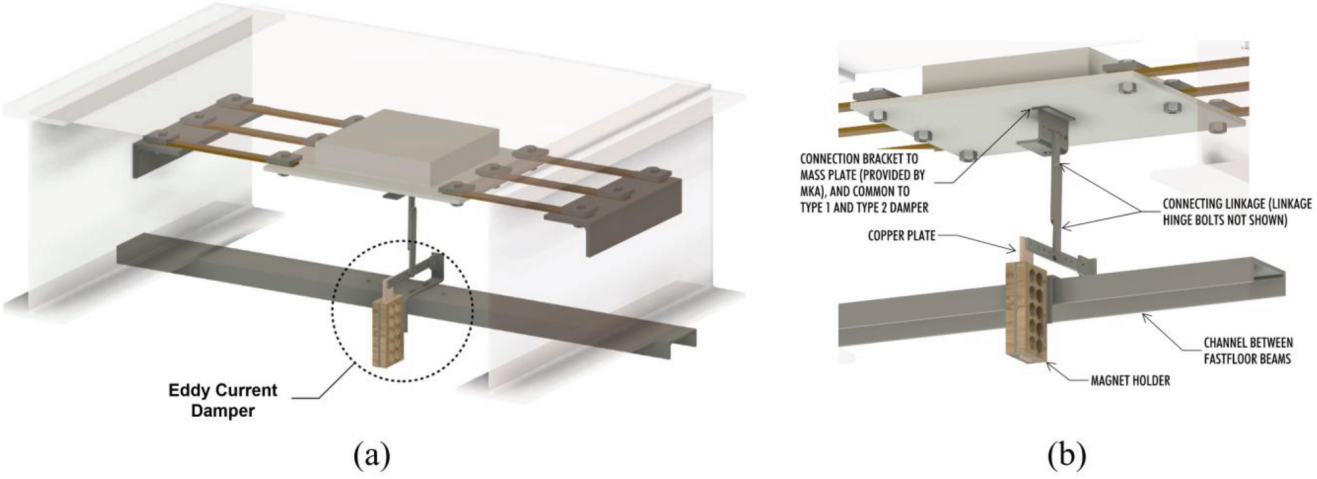

Fig. 1 Schematic of the eddy current TMD design by MKA. (a) View of the TMD assembly. (b) A view of the eddy current damper element with part names

The eddy current TMD was installed and tested on a 30 ft × 40 ft FastFloor laboratory specimen, a modular all-steel system designed to accelerate commercial building construction using prefabricated components. The full-bay specimen consisted of six modules supported by two W30×108 girders. Three of these modules were prefabricated units made from W24×68 steel beams and $\frac{1}{2}$ in. thick plates, while the remaining three were formed by connecting infill plates on-site. The modules were attached to the girders using bolted shear connections. Fig. 2-a shows the specimen in its bare condition. Fig. 2-b provides a plan layout, indicating the TMD location at the center of module 3. For all tests, a raised access floor (RAF) was installed over the steel plates (Fig. 3).

The installed eddy current TMD is shown in Fig. 4. The system's dynamic response was monitored using eleven accelerometers. Two sensors were mounted directly on the TMD assembly (one on the mass plate and one on the steel channel

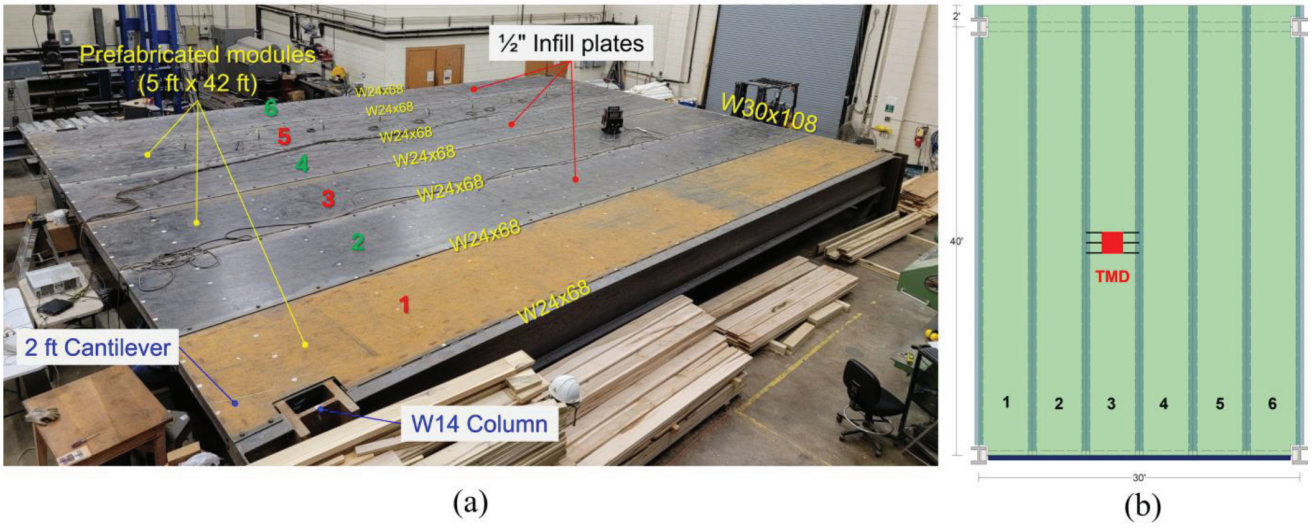

Fig. 2 30 ft × 40 ft All-Steel FastFloor specimen. (a) Laboratory specimen with components annotated. (b) Plan layout of the FastFloor specimen with module numbers and the TMD location shown

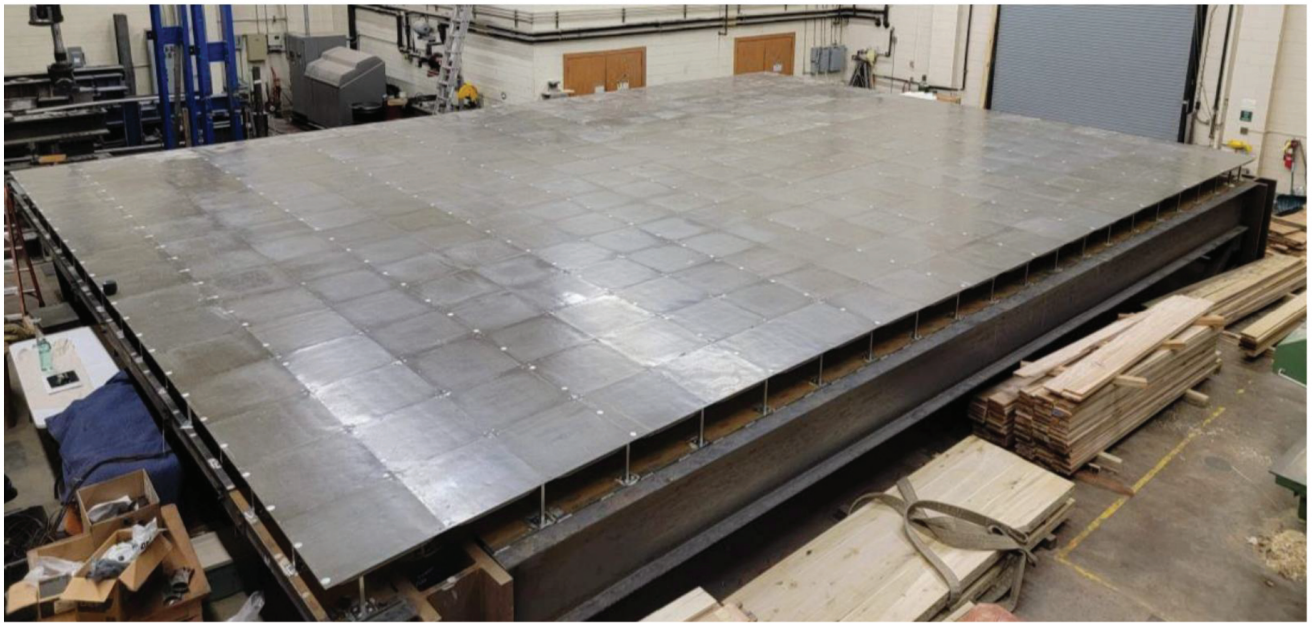

Fig. 3 The FastFloor test specimen with the raised access floor (RAF) installed

section at the bottom), and additional nine accelerometers along the centerline of the floor's third module. For modal analysis, excitation was provided by an electrodynamic shaker using a 3–30 Hz chirp frequency sweep. It is important to note that all tests, both with and without the TMD, were performed with the raised access floor (RAF) installed. The baseline configuration of the floor also included horizontal angle blocking members at L/3 and 2L/3 distances on modules 1, 3, 5, and 6.

Tuning the Damper System

The primary goal of the tuning process was to align the TMD's natural frequency with the floor's fundamental frequency, which was measured at 7.46 Hz. This mode was selected as the target because it exhibits the highest mass participation and

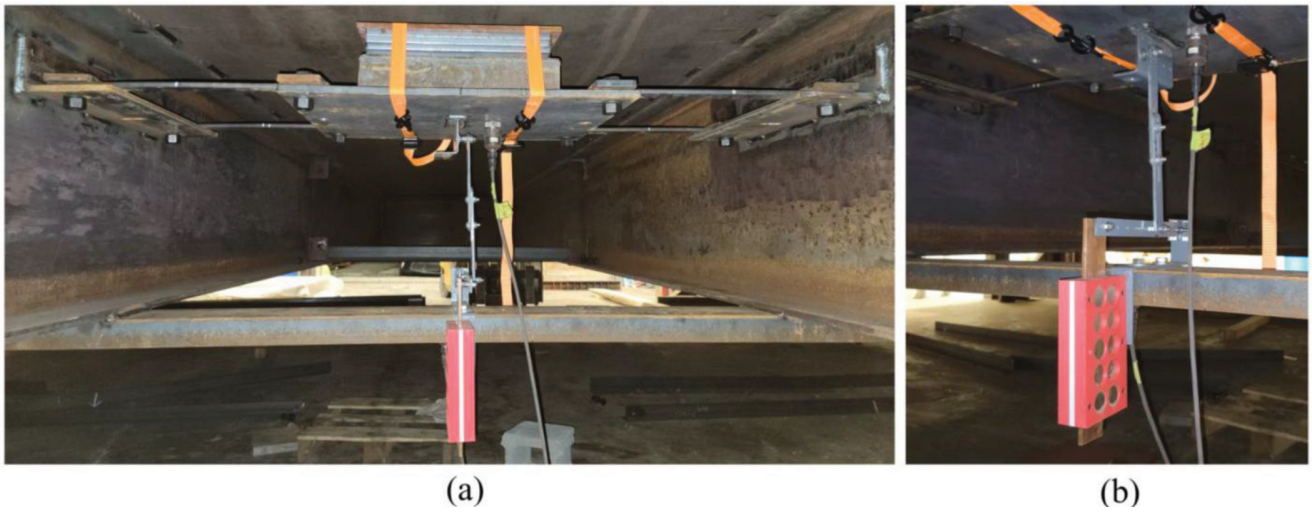

Fig. 4 The eddy current TMD assembly after installation on module 3: (a) view of the assembly with four spring strips and tuning mass plates; (b) the eddy current damper element with the copper plate and magnetss

therefore dominates the floor's dynamic response. As shown in Fig. 5, this mode shape is characterized by the entire floor bay bending in a single curvature. The optimization procedure involved systematically adjusting the TMD's mass by adding or removing steel tuning plates. Concurrently, the eddy current damper's configuration was verified under resonant excitation to ensure it provided an effective level of energy dissipation.

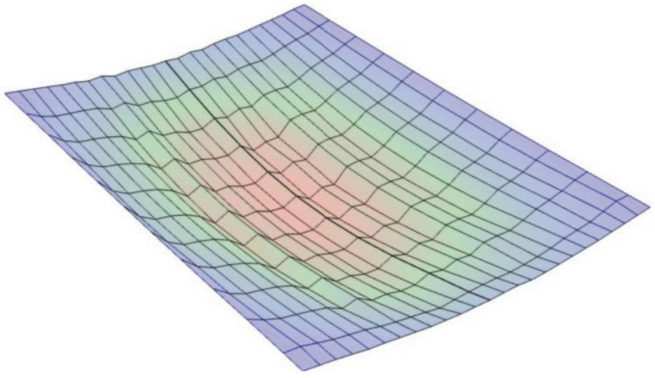

Fig. 5 Experimentally identified fundamental mode shape of the full-bay floor specimen

Mass Tuning: Analytical and Experimental

The initial tuning of the TMD was guided by analytical calculations from the designers at MKA, which suggested a configuration of four spring strips and five mass plates to target the floor's 7.4 Hz fundamental frequency. A key consideration in these calculations is the slight decrease in the floor's natural frequency that occurs after the TMD is installed due to its self-weight. The five-plate configuration resulted in a mass ratio of approximately 1.2%, which is the ratio of the TMD's total mass to the effective modal mass of the floor.

To experimentally verify the initial tuning calculations, modal tests were conducted using five distinct TMD mass configurations (0, 2, 4, 5, and 6 tuning plates). For each configuration, low-amplitude shaker excitations were used to generate a Frequency Response Function (FRF), and the results are compared in Fig. 6. It should be noted that these mass optimization tests were performed using another damper element. The primary goal of this experimental sweep was to identify the number of mass plates that resulted in the greatest suppression of the FRF peak near the 7.4 Hz target frequency.

FRFs from the mass tuning tests are presented on a logarithmic scale in Fig. 6, with a detailed view of the target frequency range shown in Fig. 7. The results confirmed that the five-plate mass configuration was optimal, reducing the peak FRF

magnitude by approximately 87% compared to the baseline floor, which aligned well with the initial analytical predictions. It was observed that the peak reductions for the other mass configurations did not follow a simple linear trend. This can be attributed to known challenges in testing large, flexible floor structures, where nonlinear behavior and complex shaker-structure interactions can cause slight variations in measured resonant peaks [6].

With the optimal five-plate mass configuration determined, the eddy current damper element was installed to complete the TMD assembly. A modal analysis was then performed, and the resulting FRF is compared to the baseline (no TMD) case in Fig. 7. The results are shown on both a logarithmic scale over a broad frequency range (Fig. 7-a) and a linear scale focused on the fundamental mode (Fig. 7-b). The comparison shows the TMD's effectiveness, reducing the peak resonant response by 86%. A slight reduction in the floor's fundamental frequency was also observed with the TMD installed.

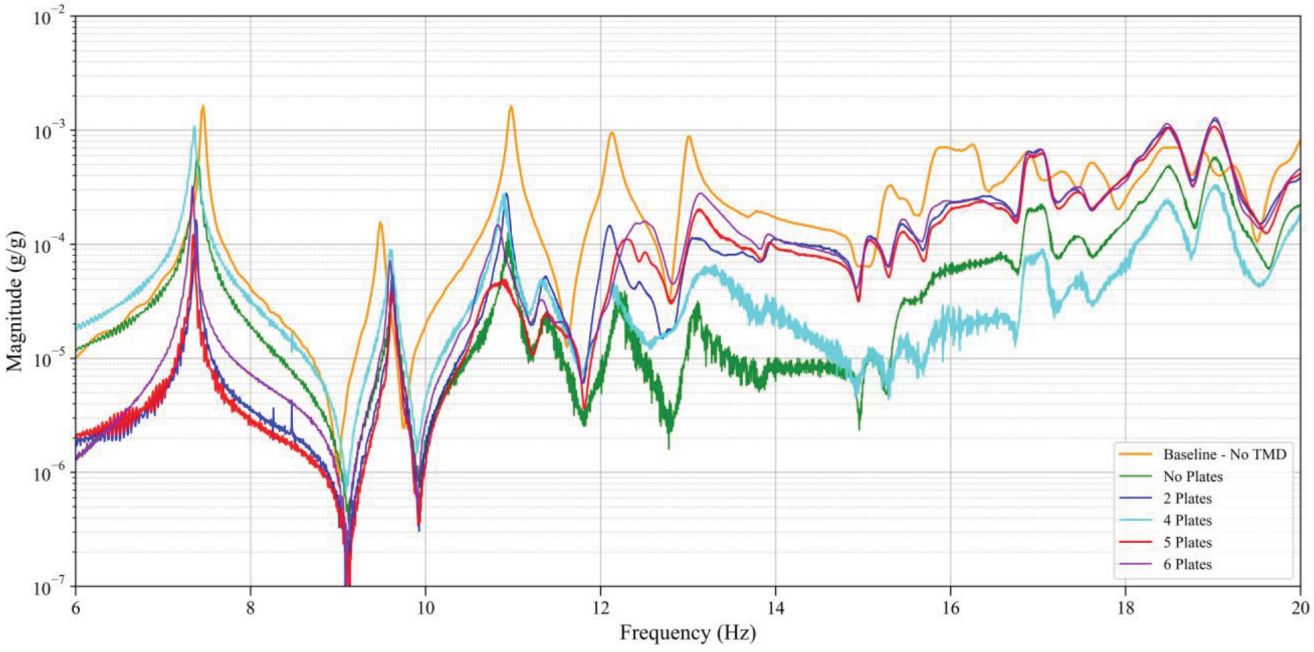

Fig. 6 Frequency response functions (FRFs) measured at the center of module 3 for different TMD mass configurations, generated using shaker excitation (logarithmic scale)

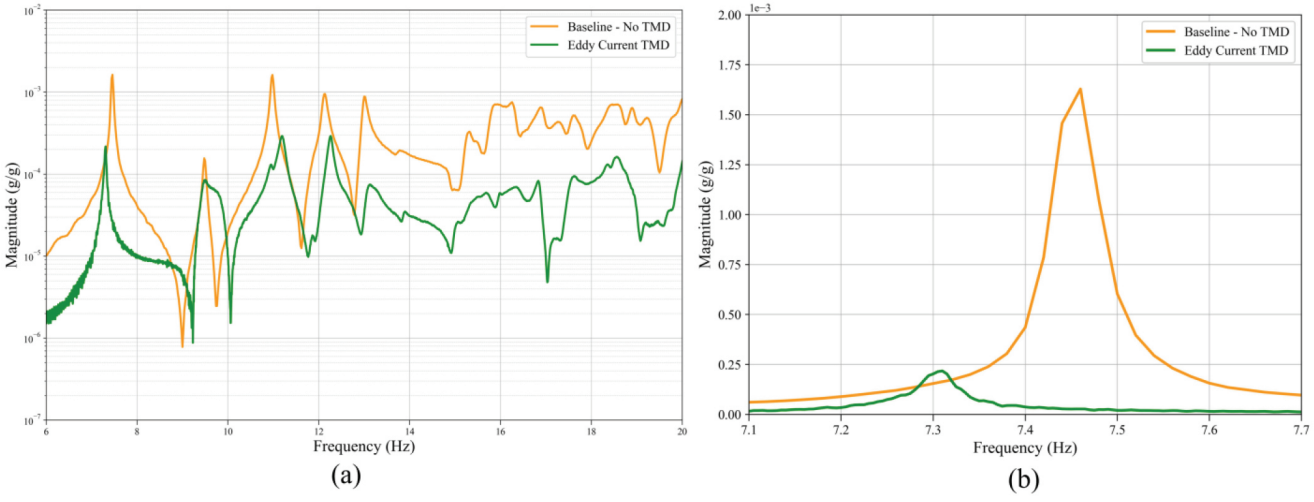

Fig. 7 FRFs measured at module 3 center for the baseline and TMD configurations: (a) Logarithmic-scale plot of the FRFs over the 6–20 Hz range; (b) Linear-scale plot of the FRFs near the fundamental mod

Effect of the TMD on Structural Damping

The structural damping of the floor system was quantified using the free-vibration decay method. This procedure involved exciting the floor to a steady-state resonance at its fundamental frequency, after which the shaker excitation was abruptly ceased. The resulting decay in acceleration was recorded, and the test was repeated across various excitation amplitudes to investigate the system's amplitude dependence. Prior to analysis, the raw acceleration signals were pre-processed by detrending and applying a Butterworth filter to eliminate high-frequency noise. The damping ratio (β) was then extracted by applying a curve fit of the signal's decaying peaks to an exponential function.

Damping Analysis

The damping of the baseline floor (without the TMD) was established first, with the decay curves shown in Fig. 8. The floor exhibited amplitude-dependent behavior, with the measured damping ratio (β) increasing from 0.29% at low-level excitations to 0.36% at high-level excitations.

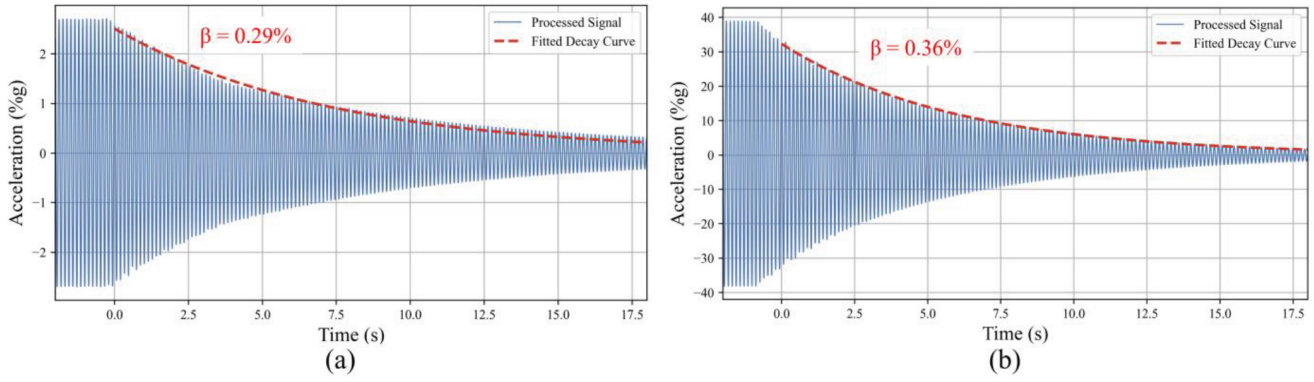

Fig. 8 Comparison of free-vibration decay curves for the baseline specimen at (a) low and (b) high excitation amplitude

The same tests were then performed with the eddy current TMD installed, and the results are shown in Fig. 9. The overall system damping was significantly higher and continued to show amplitude dependence. With the TMD, the damping ratio increased from 0.39% at low amplitudes to 0.55% at high amplitudes.

A direct comparison reveals the impact of the TMD. It increased the total system damping by 34% for low-amplitude vibrations and by 53% for high-amplitude vibrations. The TMD increases system damping by absorbing vibrational energy from the floor's resonant motion and using its eddy current damper to dissipate that energy as heat. The curve-fitted amplitude-damping curves are also shown and compared in Fig. 11.

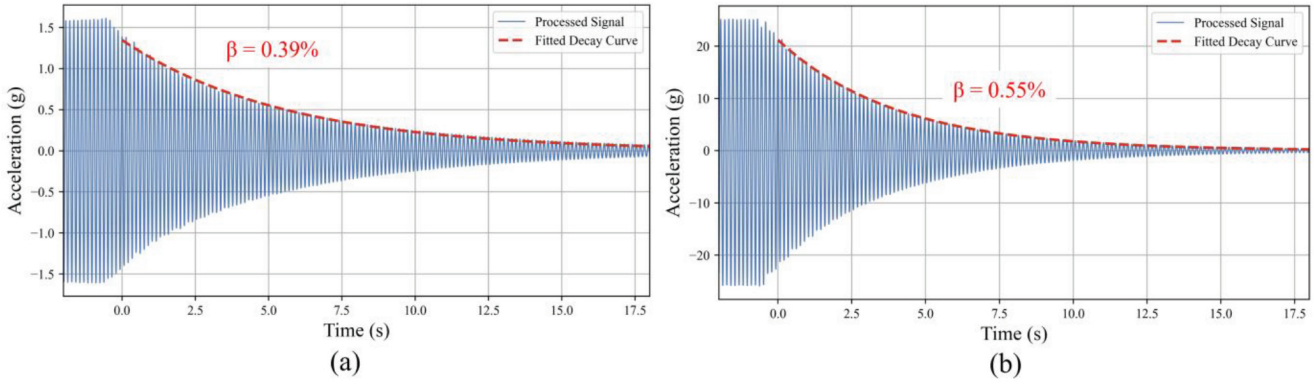

Fig. 9 Comparison of free-vibration decay curves for the TMD-equipped floor at (a) low and (b) high excitation amplitude

Amplitude-Dependent Damping

The amplitude dependence of the floor's damping was first quantified for the baseline case. As shown in **Fig. 10**, the damping ratio exhibits a clear nonlinear trend, increasing sharply for accelerations up to approximately 4% g, after which the rate of increase lessens. This phenomenon, known as the "amplitude dependence of modal parameters" [7], is attributed to inherent nonlinearities within the structural system.

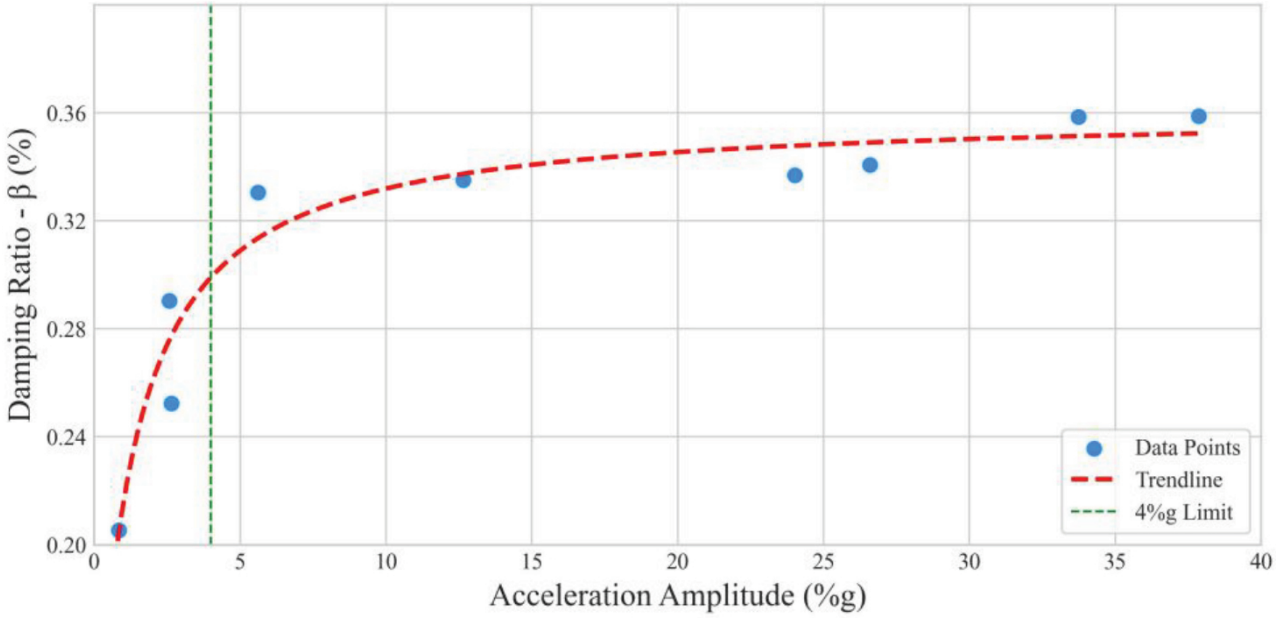

Fig. 10 Relationship between damping and acceleration amplitude for the baseline floor specimen

The same analysis was performed for the floor with the eddy current TMD installed, with the results plotted in Fig. 11. The TMD provided a significant increase in damping across all excitation levels while exhibiting a similar amplitude-

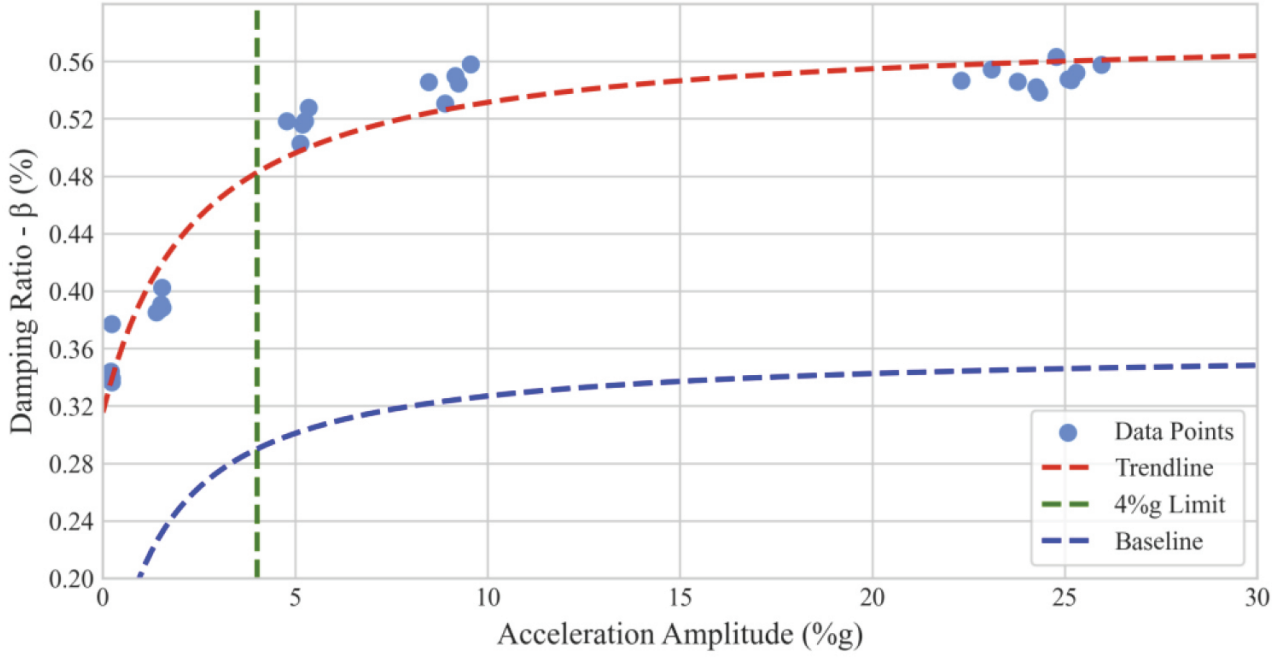

Fig. 11 Relationship between damping and acceleration amplitude for the TMD-equipped floors

dependent trend to the baseline case. The damping ratio again increased rapidly at lower amplitudes before the rate of increase began to slow.

TMD Performance Under Resonance

The TMD's effectiveness under resonant sine excitations was evaluated by comparing the acceleration of the TMD's mass to that of the floor at the center of module 3. A key performance metric is the response amplitude ratio between the TMD and the floor; a higher ratio indicates that the TMD is resonating as intended and actively dissipating energy. During resonant sine excitation, the TMD mass consistently exhibited a higher acceleration than the floor. As shown in Fig. 12, this amplitude ratio was measured to be 2.1 for both low- and high-level excitations, confirming the device was performing effectively.

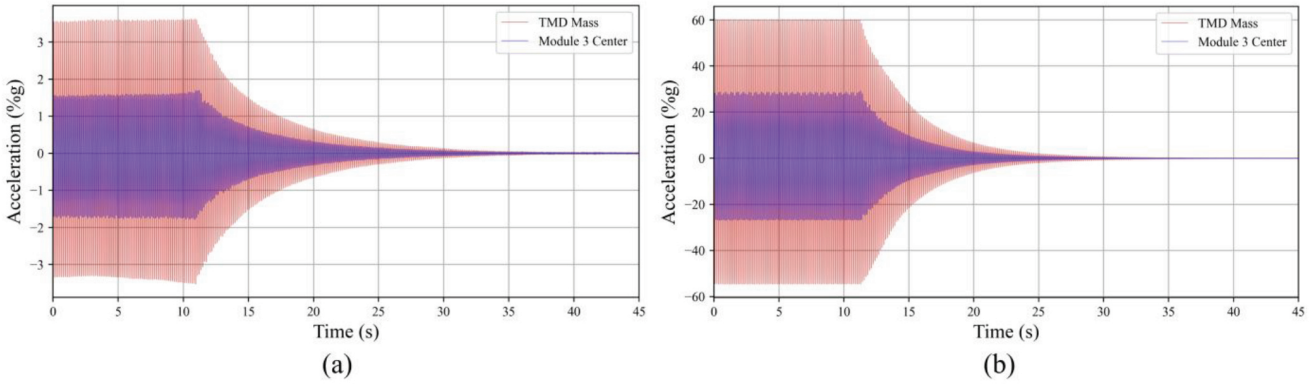

Fig. 12 Comparison of acceleration responses at the TMD mass and the module 3 center for (a) low-amplitude and (b) high-amplitude excitations

Effect of the TMD on the Floor's Response to Human Walking

To evaluate the TMD's effectiveness under realistic conditions, walking tests were conducted to simulate vibrations from human footfalls. To induce a resonant response, a walking pace corresponding to the fourth subharmonic of the floor's fundamental frequency (f_n /4) was maintained by two individuals. The tests were performed along the centerline of module 4, with a metronome used to ensure a consistent pace (Fig. 13). The resulting acceleration response was measured at the center of module 3.

From the acceleration signals, the Equivalent Sinusoidal Peak Acceleration (ESPA) was calculated. This metric is used to translate footfall vibrations for comparison against human comfort criteria. Following the procedures in AISC Design Guide 11 and SCI P354 [2, 7], the ESPA was determined by multiplying the maximum one-second root-mean-square (RMS) of the filtered signal by $\sqrt{2}$. The 90th percentile ESPA value was used for comparison to provide a robust statistical measure. The results, summarized in Table 1, show a significant improvement with the TMD installed: the 90th percentile ESPA decreased

Table 1 Statistical summary of ESPA results from human-walking tests

			Equivalent Sinusoidal Peak Accelerations (ESPAs) [%g]				
Configuration	**# of Walking Tests**	**Step Frequency (steps/min)**	**Mean (μ)**	**Min**	**Max**	**STD (σ)**	**90th Percentile (μ+1.28σ)**
Baseline	14	112	1.53	1.17	1.92	0.26	1.86
Eddy Current TMD	6	110	1.17	0.86	1.40	0.17	1.39



Fig. 13 Setup for the metronome-guided walking tests along the centerline of module 4, with accelerometers deployed along the centerline of module 3

by 25%, the maximum ESPA was reduced by 27%, and the mean ESPA decreased by 24%. This significant reduction demonstrates the TMD's effectiveness for the low-amplitude, subharmonic excitations typical of human walking.

Conclusion

This paper presented the experimental evaluation of a Tuned Mass Damper (TMD) that incorporates an eddy current damper. The objective of this study was to quantify the system performance in mitigating vibrations on a full-scale laboratory floor. The main conclusions of the study are as follows:

1. The TMD was successfully tuned to the floor's fundamental frequency by optimizing its mass configuration. Analysis of FRFs confirmed the TMD was working as intended, suppressing the peak resonant magnitude by 86% compared to the baseline floor.
2. Free-vibration decay tests demonstrated a significant increase in the floor's structural damping. The system damping ratio was increased by 34% at low vibration amplitudes and by 53% at high amplitudes, showing a good performance across a range of conditions.
3. Under human-walking tests, the TMD proved effective at improving the floor's response to walking-induced loads. It achieved a significant 25% reduction in the 90th percentile Equivalent Sinusoidal Peak Acceleration (ESPA), demonstrating a substantial improvement in the floor's response to footfall-induced vibrations.

In conclusion, this study demonstrated the successful performance of the eddy current TMD on an isolated laboratory floor. The experimental results from this proof-of-concept study confirm that this non-contact technology is a promising method for suppressing resonant vibrations. The future work on this damper will provide more information and shed more light on the potential of the proposed TMD device on modern floor systems and other structures such as stadia.

Acknowledgments The authors would like to thank and acknowledge SteelFab steel fabricators of Charlotte, North Carolina for donation of the TMD fabrication.

References

1. S. J. Hicks and A. L. Smith, “Design of floor structures against human-induced vibrations,” Steel Constr., vol. 4, no. 2, pp. 114–120, 2011, doi: 10.1002/stco.201110014.
2. T. M. Murray, D. E. Allen, E. E. Ungar, and D. B. Davis, “Design Guide 11: Vibrations of Steel-Framed Structural Systems Due to Human Activity (Second Ed.) | American Institute of Steel Construction.”
3. J. J. Connor, Introduction to Structural Motion Control. Prentice Hall Pearson Education, Incorporated, 2003.
4. “Passive Energy Dissipation Systems in Structural Engineering | Wiley.”
5. H. A. Sodano, “Development of Novel Eddy Current Dampers for the Suppression of Structural Vibrations,” Virginia Tech, 2005. Accessed: Sept. 27, 2025. [Online]. Available: http://hdl.handle.net/10919/27677
6. D. B. Davis, “Finite Element Modeling for Prediction of Low Frequency Floor Vibrations Due to Walking,” Virginia Tech, 2008. [Online]. Available: http://hdl.handle.net/10919/28634
7. A. L. Smith, S. J. Hicks, and P. Devine, Design of Floors for Vibration: A New Approach (2009).

Chapter 8
Effect of Stationary Occupants on Damping and Vibration Response of a Modular All-Steel Laboratory Floor

Sahabeddin Rifai, Ahmad Rababah, Feras Abla, Mohamed Tareq Soliman, and Onur Avci

Abstract This paper presents an experimental study on a full-scale, 30 ft × 42 ft modular all-steel floor system to quantify the relationship between supplemental damping and walking-induced vibrations. Increased damping levels were simulated by introducing stationary groups of two to thirteen human occupants. Structural damping ratios for each configuration were determined using free-vibration decay tests, while the floor's performance was evaluated through walking tests conducted at the critical fourth subharmonic of the floor's fundamental frequency. The response was quantified using the Equivalent Sinusoidal Peak Acceleration (ESPA) metric. The unoccupied floor possessed a very low baseline damping of 0.34%. The presence of occupants increased this value progressively to a maximum of 4.91%. This added damping had a significant effect on the floor's performance, reducing the 90th percentile ESPA from walking by up to 81% compared to the baseline. The results suggest that a damping ratio of approximately 2.30% is required for this floor to meet the 0.50%g acceleration limit recommended by common design guides. The findings provide a clear, quantitative link between system damping and vibration serviceability, offering valuable data for the design and remediation of similar low-damping floor structures.

Keywords Floor vibrations · Vibration serviceability · Structural damping · Human-induced damping · Human-structure interaction.

Introduction

Structural damping is a critical factor governing the vibration response of floor systems. Higher damping levels are generally beneficial for floor vibration serviceability; however, achieving adequate damping can be challenging, particularly in modern commercial buildings. Current design trends favoring long, uninterrupted spans with lighter materials and fewer non-structural components often result in flexible floor systems. These characteristics lead to inherently low damping, making floors susceptible to excessive vibrations from common human activities like walking. Consequently, vibration serviceability has become a governing design criterion for many modern floors, often proving more critical than strength requirements [1, 2].

A common strategy for mitigating excessive floor vibrations is supplemental damping. In a laboratory setting, a convenient method for simulating supplemental damping is to use stationary human occupants. It is well-established that the human body acts as a good damper; people occupying a floor can absorb vibrational energy, thereby reducing the floor's response [3].

In its bare laboratory condition, the full-bay test specimen for this study exhibits inherently low damping. As a result, preliminary tests of human walking induced peak accelerations higher than those recommended by design guidelines for human comfort. The primary objective of this research was, therefore, to determine the level of damping required for this specific floor to achieve an acceptable vibration response, particularly when subjected to walking at a critical step frequency ($f_n/4$).

To achieve this goal, this study investigates the damping provided by stationary humans standing on a 30 ft × 42 ft (9.1 m × 12.8 m) full-bay FastFloor laboratory specimen. Damping levels were varied by testing the floor with groups of two to thirteen standing people. Free-vibration decay tests were performed on each configuration by exciting the floor to resonance

Sahabeddin Rifai · Ahmad Rababah · Feras Abla · Mohamed Tareq Soliman · Onur Avci Department of Civil and Environmental Engineering, West Virginia University, Morgantown, WV 26506
e-mail: sr00090@mix.wvu.edu; ayr00002@mix.wvu.edu; fa00060@mix.wvu.edu; mts00029@mix.wvu.edu; onur.avci@mail.wvu.edu

© The Author(s), under exclusive license to River Publishers 2026

Kristin B. Zimmerman, PhD (eds.), *Dynamics of Civil Structures, 2026, Vol. 2*, Conference Proceedings of the Society for Experimental Mechanics Series, https://doi.org/10.13052/rp-9788743814139

and then recording the subsequent decay in vibration after excitation is stopped. Damping ratios for each case were then computed by applying a curve-fitting algorithm to the decay responses.

The tested floor system, called FastFloor, is a modular, all-steel system developed to accelerate steel construction [4]. Previous research on the FastFloor system includes the initial design and testing of single-module configurations [5, 6, 7], finite element model updating [8], and investigations into modal response and serviceability [5, 6, 7, 8, 9] with the overall research program outlined in [10].

Laboratory Floor Specimen

The floor specimen investigated in this study is a full-bay FastFloor system measuring 30 ft × 42 ft (9.1 m × 12.8 m) in plan. FastFloor is a modular, all-steel floor system developed to accelerate the steel construction of commercial buildings, consisting of prefabricated modules and infill plates that are rapidly assembled on-site with bolted connections.

As illustrated in Fig. 1, the bare floor is constructed from three prefabricated modules and nine infill plates. Its structural framing consists of two W30×108 girders and seven W24×68 beams supporting a $\frac{1}{2}$ in. (12.7 mm) thick steel plate deck. The girders and edge beams are attached to W14 columns using shear tab connections.

For this study, all tests were conducted with a raised access floor (RAF) installed over the steel deck (Fig. 2). This unoccupied configuration, supporting only its self-weight with no additional service loads, served as the baseline condition for all subsequent tests.

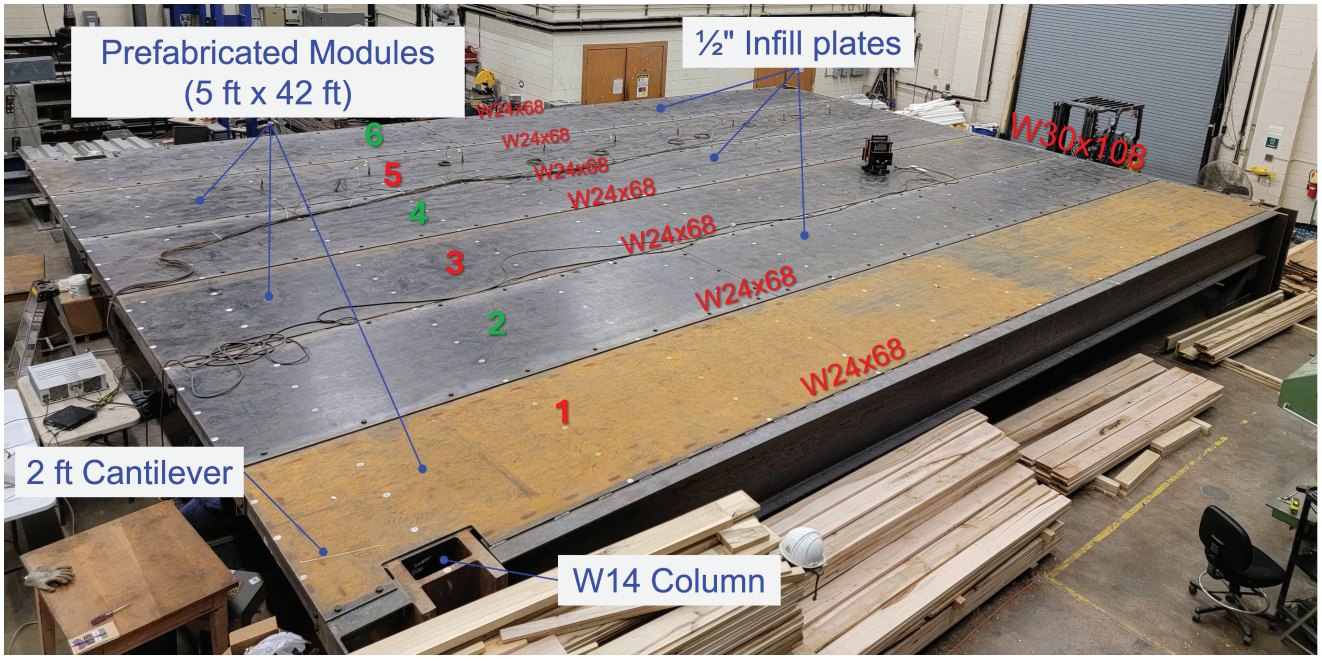

Fig. 1 The 30 ft × 42 ft all-steel FastFloor specimen in its bare condition with components annotated

Test Setups with Stationary Occupants

A series of tests were conducted with stationary human occupants to investigate the influence of supplemental damping on the floor's response. The baseline FastFloor specimen possesses inherently low damping due to its all-steel composition and isolated laboratory condition. To simulate the higher damping levels of an occupied floor, groups of people were asked to stand at specific locations close the specimen's centerline. Seven distinct configurations were tested, starting with the unoccupied baseline and incrementally adding people up to a maximum of thirteen. Table 1 details these configurations, which are ordered by an increasing number of occupants to correspond with a progressive increase in system damping.

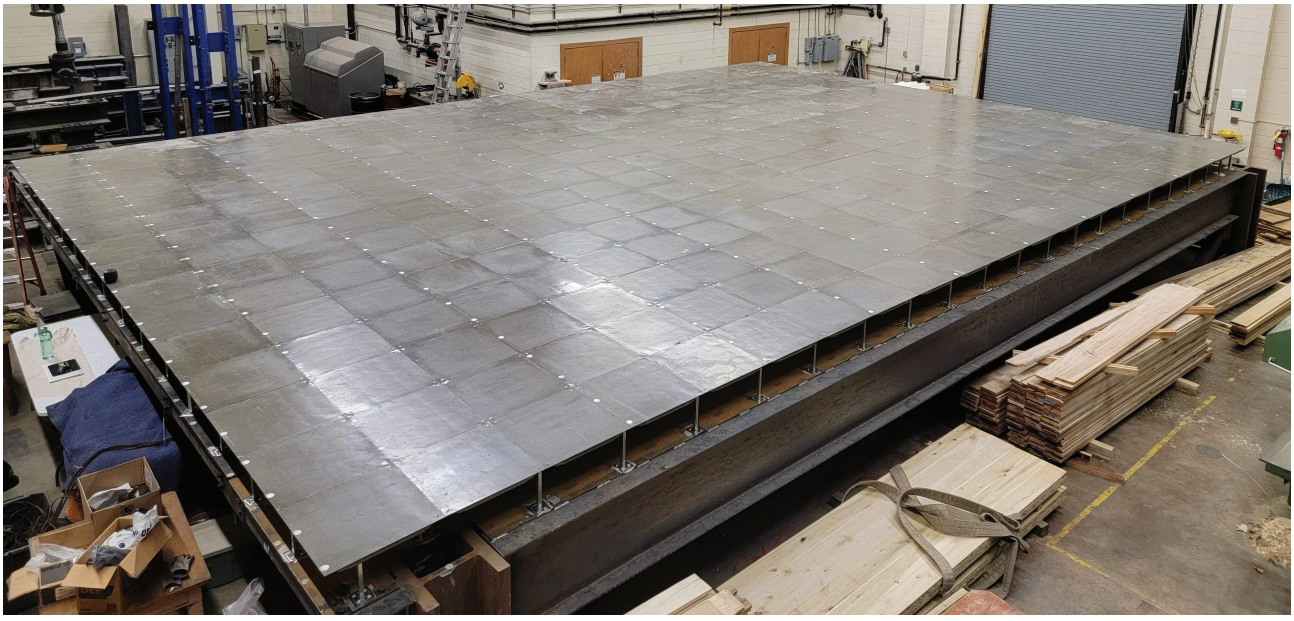

Fig. 2 The full-bay FastFloor specimen with the raised access floor (RAF) installed and no other load on the floor, representing the baseline test configuration

Table 1 Test configurations with notations and number of people standing

No.	Notation	Total Standers	Standers (Left of floor CL)	Standers (Right of floor CL)
0	Baseline	0	0	0
1	L1-R1	2	1	1
2	L2-R2	4	2	2
3	L3-R3	6	3	3
4	L4-R4	8	4	4
5	L11-R0	11	11	0
6	L7-R6	13	7	6

Four of the occupied test configurations are illustrated in Fig. 3. In these configurations, the "left" (L) and "right" (R) designations correspond to the specimen's layout, with module 1 defining the far-left side and module 6 defining the far-right. The figure shows several symmetric arrangements, such as the two-person (L1-R1) and six-person (L3-R3) cases, as well as an asymmetric configuration with eleven occupants on the left side (L11-R0).

Experimental Testing Results

Frequency Response Functions (FRFs)

Experimental modal analysis was performed using an electrodynamic shaker to obtain frequency response functions (FRFs) for all seven test configurations. The shaker was positioned at the quarter-point along the centerline of module 3, and responses were measured at several points, including the center of that same module.

The FRFs measured at the center of module 3 are shown on a logarithmic scale in Fig. 4. The baseline FRF (unoccupied floor) is characterized by clean, distinct peaks with the highest amplitudes. As human occupants are added, two primary effects are observed. First, the FRF magnitudes decrease progressively with an increasing number of people. Second, the FRF curves become noisy, particularly around the first mode. This noise is attributed to minor, involuntary movements of the occupants, creating complex floor-structured interaction, even though they were instructed to remain as still as possible.

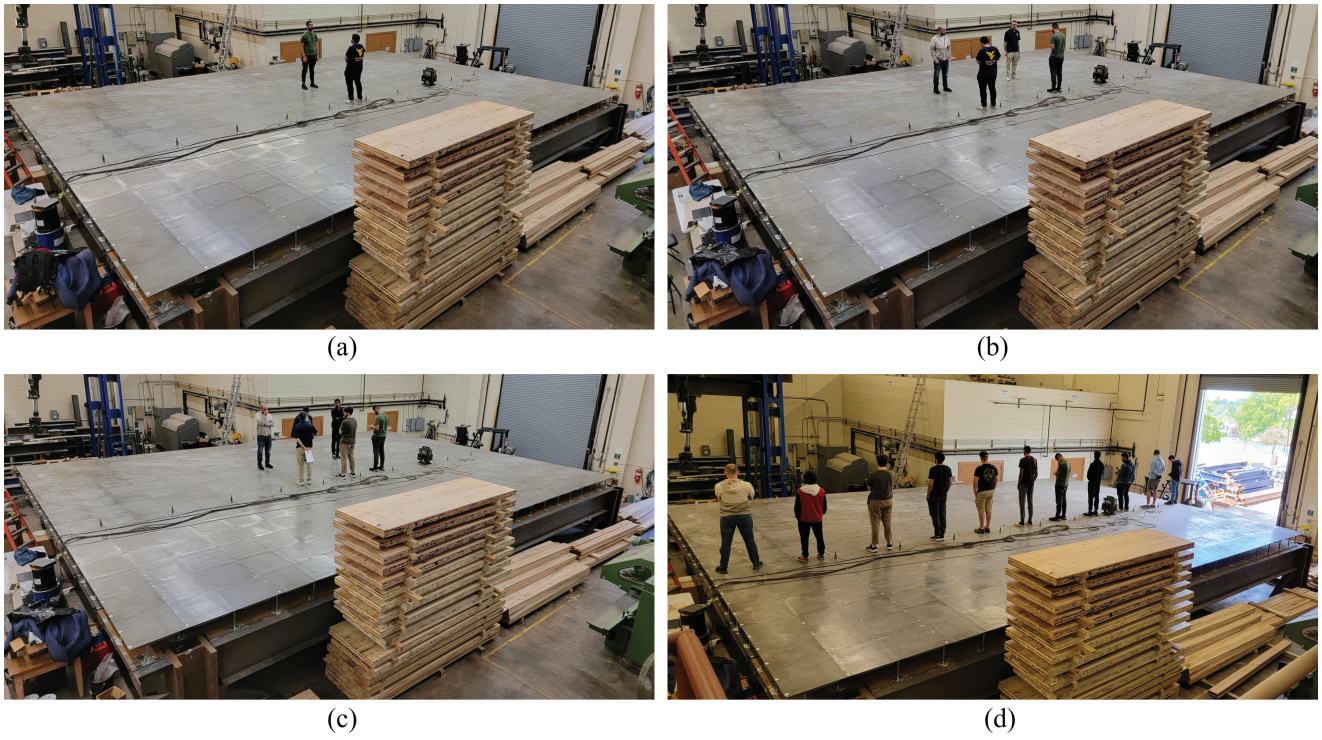

Fig. 3 Four configurations with people standing on the FastFloor specimen to simulate higher damping levels: (a) L1-R1, (b) L2-R2, (c) L3-R3, and (d) L11-R0

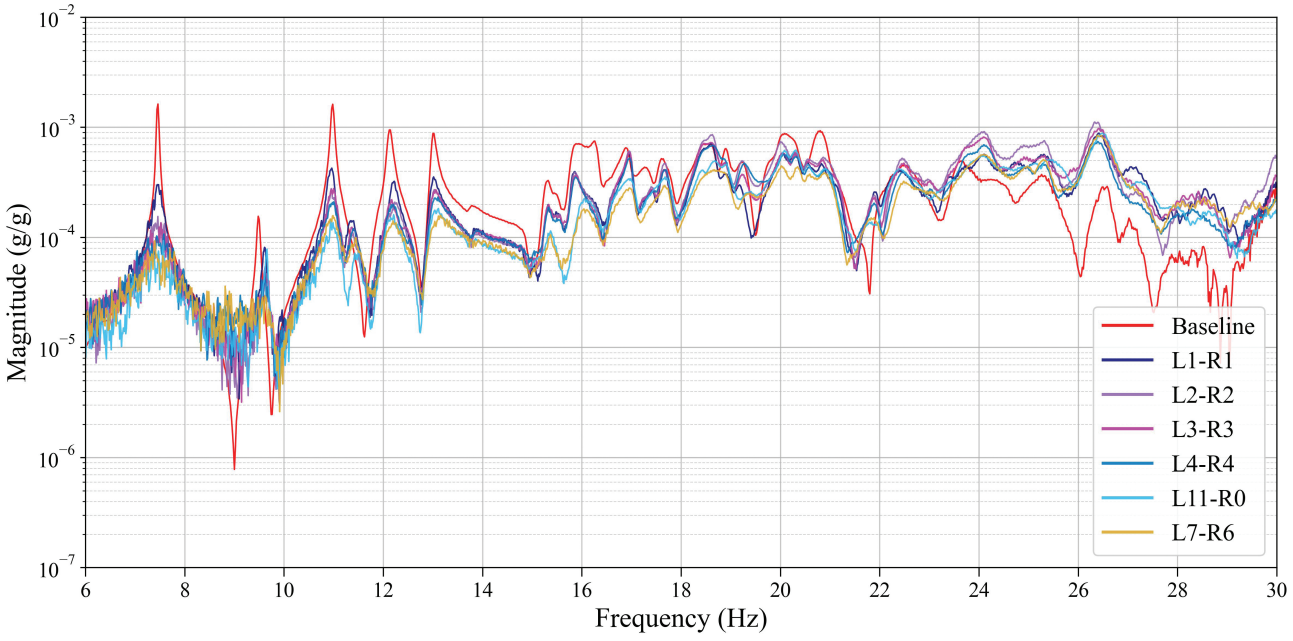

Fig. 4 Frequency response functions (FRFs) measured at the center of module 3 for all configurations, generated using shaker excitation (logarithmic scale)

Since the first (fundamental) mode has the highest mass participation in the vertical direction and typically dominates the floor's vibration response, it is examined more closely. Fig. 5 shows the FRFs on a linear scale, focused on a narrow frequency band around the fundamental mode. Despite the noise in the occupied test cases, the FRF magnitudes show a significant reduction, confirming the damping effect provided by the occupants. The reduction in the peak FRF magnitude at the first mode ranged from approximately 80% for the two-person (L1-R1) case to 95% for the eleven- and thirteen-person (L11-R0 and L7-R6) cases.

While the reduction in FRF amplitude provides a clear indication of increased damping, a more direct analysis of the damping ratios and floor performance under walking excitation is necessary. The following sections, therefore, present the calculated structural damping ratios and the measured floor response under human walking at a subharmonic of fundamental frequency (f_n/h).

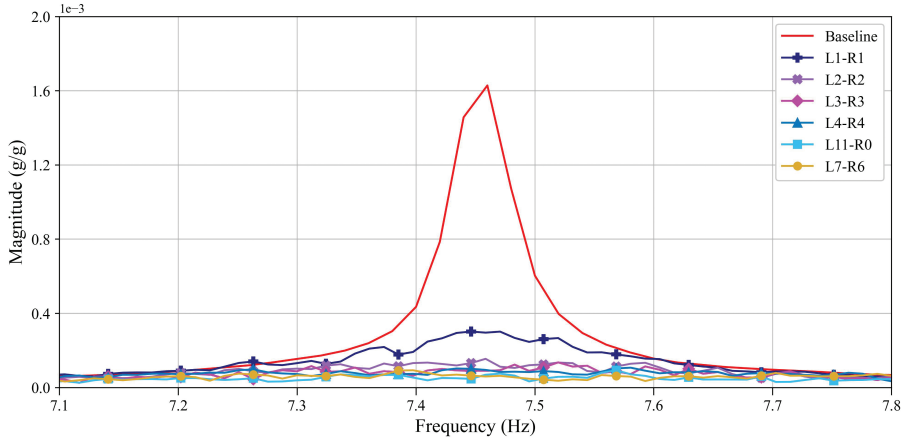

Fig. 5 Linear-scale FRFs measured at the center of module 3 for all configurations, showing the response near the fundamental mode

Effect on Structural Damping

This section presents the effect of the human occupants on the floor's overall structural damping ratio (β). For each configuration, the damping ratio was obtained from free-vibration decay tests. These tests involved exciting the floor to a steady-state resonance at its fundamental frequency, after which the excitation was suddenly stopped to record the decay. High-amplitude excitations were used, as the resulting decay curves are more clearly defined for curve-fitting. It is noted that excitation amplitude affects modal parameters; higher amplitudes tend to correspond to higher damping and slightly lower natural frequencies [11]. Prior to analysis, the recorded acceleration signals were pre-processed by detrending and applying a Butterworth filter to remove high-frequency noise. The damping ratio (β) was then extracted by fitting an exponential function to the decaying peaks of the filtered signal.

The baseline damping of the unoccupied floor was first established using the acceleration decay measured at the center of module 3 (Fig. 6). The structural damping ratio (β) was calculated to be 0.34%. This low value is characteristic of an unloaded, all-steel structure in a laboratory setting and serves as the reference for all subsequent occupied floor configurations.

The addition of human occupants immediately and significantly increased the floor's damping. For the first occupied case with two people (L1-R1), the damping ratio was found to be 1.12%, a 229% increase over the baseline, as illustrated by the decay curve in Fig. 7-a. When the number of occupants was doubled to four (L2-R2), the damping ratio more than doubled to 2.14%, representing a 529% increase from the baseline (Fig. 7-b).

As more occupants were added, the trend of increasing damping continued. The configuration with six people (L3-R3) yielded a damping ratio of 2.33% (a 585% increase), while the eight-person case (L4-R4) resulted in a damping ratio of 3.38% (an 894% increase). The corresponding decay curves in Fig. 8 show a visibly higher rate of decay compared to the previous configurations, indicating that vibrational energy was dissipating much more rapidly.

The most heavily occupied configurations produced the highest damping values recorded in the study. The asymmetric eleven-person case (L11-R0) resulted in a damping ratio of 3.01% (Fig. 9-a). The maximum damping was achieved with thirteen occupants (L7-R6), which raised the damping ratio to 4.91%. This represents a remarkable 1344% increase compared to the unoccupied floor (Fig. 9-b).

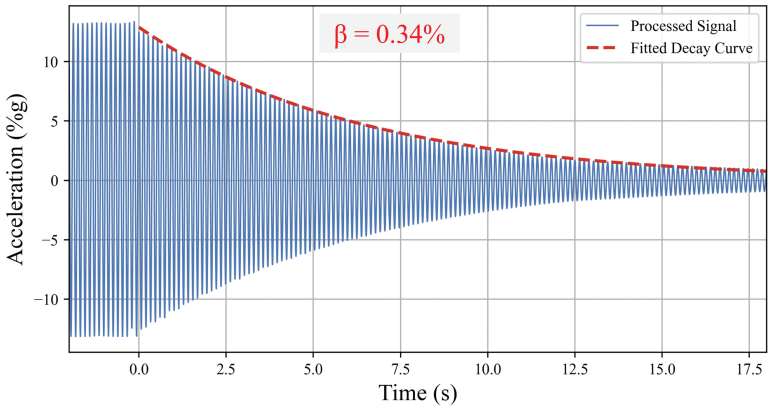

Fig. 6 Free-vibration decay curve for the baseline configuration

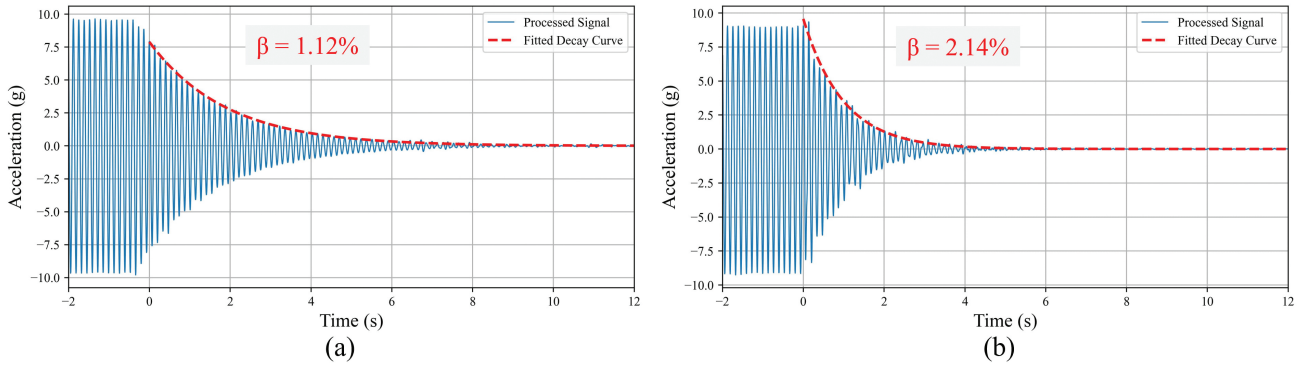

Fig. 7 Free-vibration decay curves for (a) L1-R1 and (b) L2-R2 configurations

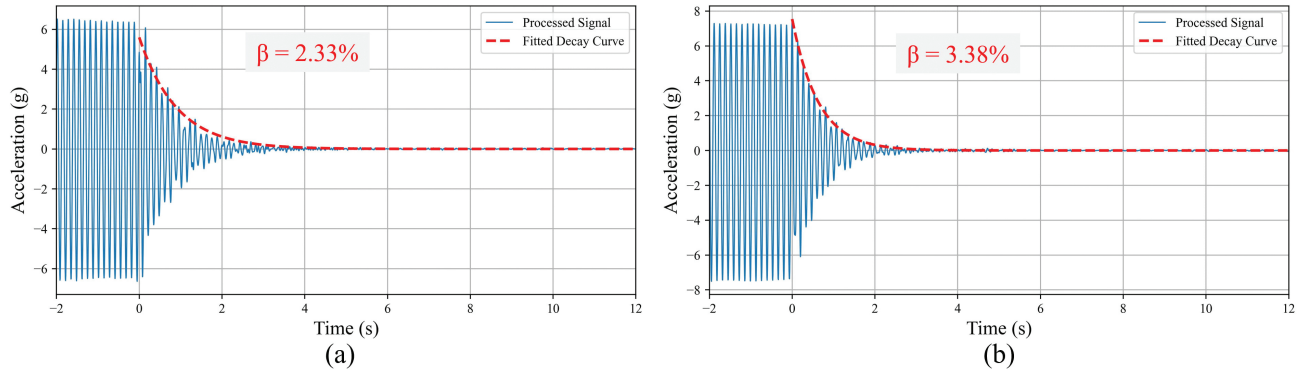

Fig. 8 Free-vibration decay curves for (a) L3-R3 and (b) L4-R4 configurations

Table 2 provides a comprehensive summary of the damping ratios and their corresponding percentage increases for all seven configurations, clearly documenting the relationship between the number of occupants and the measured structural damping.

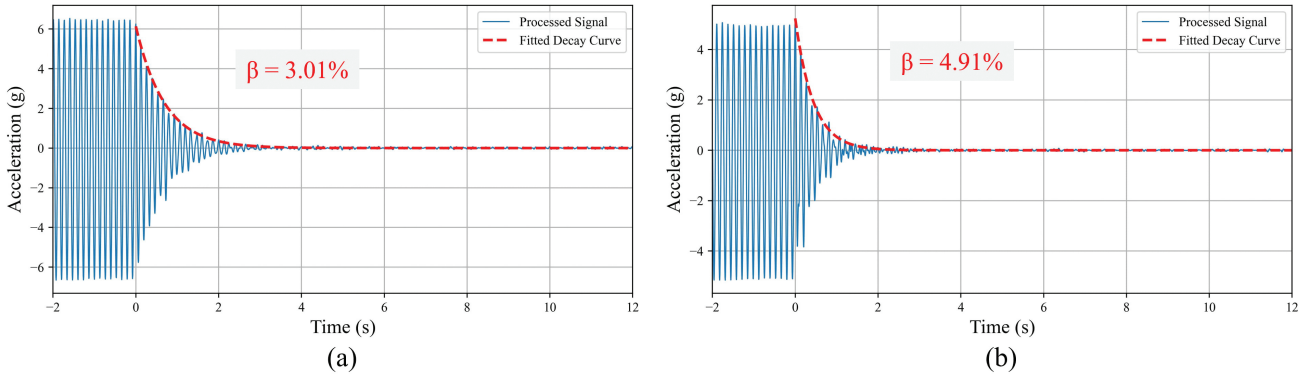

Fig. 9 Free-vibration decay curves for (a) L11-R0 and (b) L7-R6 configurations

Table 2 Summary of damping ratios and increase percentages relative to the baseline

Configuration	Damping Ratio (β)	Increase in β (%)
Baseline	0.34	-
L1-R1	1.12	229
L2-R2	2.14	529
L3-R3	2.33	585
L4-R4	3.38	894
L11-R0	3.01	785
L7-R6	4.91	1344

Response to Human Walking

To evaluate the floor's performance under realistic service conditions, a series of human walking tests was conducted for each damping configuration. These tests were designed to measure the floor's response to footfall vibrations. A few individuals walked along the centerline of module 4 at a controlled pace, maintained by a metronome. The step frequency was set to the fourth subharmonic of the floor's fundamental frequency ($f_n/4$), a pace known to be critical for inducing resonant response in floors of this type. The resulting acceleration was measured at the center of module 3.

The recorded acceleration signals were processed to assess the floor's performance against established human comfort criteria. This was done by calculating the Equivalent Sinusoidal Peak Acceleration (ESPA), following the procedures in AISC Design Guide 11 and SCI P354 [2, 3]. For each individual walking test, the ESPA was determined by finding the maximum one-second root-mean-square (RMS) value of the filtered acceleration signal and multiplying it by $\sqrt{2}$.

Since multiple walking tests were performed for each configuration, the 90th percentile ESPA was selected as the best representative value for comparison. This statistical approach provides a robust metric that accounts for the inherent variability in footfall forces and is less sensitive to outliers, which is especially important in low-damping cases where response data is often more scattered.

The results, summarized in Table 3, demonstrate that increasing the floor's damping progressively reduces its response to walking at the critical subharmonic frequency ($f_n/4$). The 90th percentile ESPA for the baseline configuration (0.34% damping) was 1.79 %g. The addition of just two people in the L1-R1 case (1.12% damping) reduced this response by 46% to 0.97 %g. The most significant reduction occurred in the L7-R6 configuration, where the high damping ratio of 4.91% led to a 90th percentile ESPA of 0.34 %g, an 81% reduction relative to the baseline. This strong correlation between increased damping and reduced vibration highlights the effectiveness of supplemental damping in controlling floor resonance caused by synchronous human movement. The experimental results indicate that for the floor specimen in its unloaded laboratory condition, a structural damping ratio of approximately 2.3% is required to meet the 0.50%g acceleration limit recommended by AISC Design Guide 11 (DG-11).

Table 3 Statistical summary of damping ratios and ESPA results from synchronous human-walking tests

			Equivalent Sinusoidal Peak Accelerations (ESPAs) [%g]				
Configuration	**# of Walking Tests**	**Damping Ratio β (%)**	**Mean (μ)**	**Min**	**Max**	**STD (σ)**	**90th Percentile (μ+1.28σ)**
Baseline	28	0.34	1.46	1.09	1.92	0.26	1.79
L1-R1	6	1.12	0.75	0.52	0.98	0.17	0.97
L2-R2	6	2.14	0.66	0.59	0.80	0.07	0.75
L3-R3	5	2.33	0.45	0.37	0.51	0.04	0.50
L4-R4	3	3.38	0.41	0.38	0.43	0.02	0.44
L11-R0	5	3.01	0.39	0.36	0.41	0.02	0.42
L7-R6	3	4.91	0.31	0.30	0.34	0.02	0.34

Conclusions

This study investigated the effect of supplemental damping, provided by stationary human occupants, on the vibration response of a full-bay modular steel floor system. Experimental tests were conducted on the unoccupied floor and six occupied configurations with two-to-thirteen standing individuals. The following conclusions are drawn from the results:

1. The unoccupied FastFloor specimen, in its laboratory condition, exhibited a very low inherent damping ratio of 0.34%. This low damping resulted in a high vibration response to simulated human walking, with a 90th percentile ESPA of 1.79%g.
2. The presence of stationary human occupants provided a significant and progressive increase in the total system damping. The damping ratio increased from 1.12% with just two people to a maximum of 4.91% with thirteen people, representing a more than 14-fold increase over the baseline.
3. This increase in damping led to a direct and substantial reduction in the floor response to walking at a critical subharmonic frequency. The 90th percentile ESPA was reduced by 46% with two occupants and by as much as 81% in the most heavily damped configuration.

The findings clearly demonstrate a strong correlation between the level of human-induced damping and the improvement in vibration serviceability for this low-damping floor system. The data provides a quantitative measure of how much damping is required to control resonant vibrations caused by human activity. Based on the results, it is estimated that a structural damping ratio of approximately 2.3% is required for this specific floor system to meet the 0.50%g acceleration limit recommended by AISC Design Guide 11 [2].

Acknowledgments This work was sponsored by the Charles Pankow Foundation, American Institute of Steel Construction (AISC), MKA Foundation, Nucor, Schuff Steel, Herrick Steel, Cives Steel, Zekelman Industries (Atlas Tube/Shuriken), and Metals Fabrication. In-kind support was provided by Cerami, Sherwin-Williams, Cooper Steel, Clark Construction, and Hensel Phelps. Any opinions, findings, and conclusions or recommendations expressed in this material are those of the authors and do not necessarily reflect the views of the sponsors and supporters.

References

1. S. J. Hicks and A. L. Smith, "Design of floor structures against human-induced vibrations," Steel Constr., vol. 4, no. 2, pp. 114–120, 2011, doi: 10.1002/stco.201110014.
2. T. M. Murray, D. E. Allen, E. E. Ungar, and D. B. Davis, "Design Guide 11: Vibrations of Steel-Framed Structural Systems Due to Human Activity (Second Ed.) | American Institute of Steel Construction."
3. L. Pedersen and L. P. Hansen, "Human damping and its capacity to control floor vibrations," in Smart Structures and Materials 2004: Damping and Isolation, SPIE, July 2004, pp. 141–152. doi: 10.1117/12.539931.
4. FastFloor – The Need for Speed – Session 1 [N24] 2024 | AISC. [Online Video]. Available: https://learning.aisc.org/local/catalog/view/product.php?productid=2508

5. O. Avci and M. A. M. Celin, “Vibration Serviceability Evaluation of a Modular Steel Plate Floor Assembly,” in Dynamics of Civil Structures, Volume 2, Springer.
6. O. Avci et al., “Vibration Testing of an All-Steel Modular Floor Assembly,” in Dynamics of Civil Structures, Vol. 2, M. Whelan, P. S. Harvey, and F. Moreu, Eds., Cham: Springer Nature Switzerland, 2025, pp. 17–23. doi: 10.1007/978-3-031-68889-8_3.
7. M. A. Mercado Celin, “Vibration Serviceability Assessment of a Steel Modular Floor System,” Virginia Tech, 2023.
8. S. Rifai et al., “Modal Testing and Finite Element Model Updating of a FastFloor Specimen: A Modular All-Steel Floor System,” in Dynamics of Civil Structures, Vol. 2, River Publishers, 2025. doi: 10.13052/rp-9788743801597A004.
9. S. Rifai, Abla, Feras, A. Rababah, R. C. M. Kumar, B. W. Schafer, and M. R. Eatherton, “Vibration Serviceability Evaluation of an All-Steel Floor System using the High-Frequency Floor Procedure,” in Dynamics of Civil Structures, Vol. 2, River Publishers, 2025. doi: 10.13052/rp-9788743801597A010.
10. B. Schafer, O. Avci, W. S. Easterling, M. R. Eatherton, and J. Hajjar, “FastFloor – Development of A Novel Modular Steel Floor System for Commercial Construction in The United States,” Dec. 02, 2024, Engineering Archive. doi: 10.31224/4183.
11. O. Avci, “Amplitude-Dependent Damping in Vibration Serviceability: Case of a Laboratory Footbridge,” J. Archit. Eng., vol. 22, Feb. 2016, doi: 10.1061/(ASCE)AE.1943-5568.0000211.
12. A. L. Smith, S. J. Hicks, and P. Devine, Design of Floors for Vibration: A New Approach (2009).

Chapter 9
Vibration Serviceability of a Modular All-Steel Floor Under Simulated Façade and Service Loads

Sahabeddin Rifai, Ahmad Rababah, Feras Abla, Mohamed Tareq Soliman, and Onur Avci

Abstract The dynamic properties and vibration serviceability of modern long-span steel floors are influenced by non-structural loads applied after construction, such as façades and service loads. This paper experimentally investigates these effects on a full-scale, 30 ft × 42 ft modular all-steel floor system. Three configurations were tested: an unloaded baseline, a 225 plf simulated façade line load, and a 12 psf simulated service area load. Modal properties were determined using shaker tests, while walking tests at a critical subharmonic frequency were performed to evaluate the vibration response, quantified by the Equivalent Sinusoidal Peak Acceleration (ESPA). The results showed that the distributed service load increased the structural damping by 40% (from 0.25% to 0.35%) and reduced the 90th percentile ESPA by 11%. In contrast, the façade load did not improve performance, with the 90th percentile ESPA slightly increasing compared to the baseline. The findings demonstrate that while all added mass reduces a floor's natural frequencies, only broadly distributed loads that also contribute to system damping may provide a tangible benefit to vibration serviceability.

Keywords Façade load · Service load · Floor vibrations · Modal analysis · Vibration serviceability

Introduction

Vibration serviceability in modern building floors has become a critical component of structural design to ensure occupant comfort [1]. Architectural trends that favor open-plan layouts with long spans and lightweight materials often produce highly flexible floor systems. A key consequence of these design choices is a reduction in inherent structural damping, which is the system's natural ability to dissipate vibrational energy. As a result, such floors can develop excessive vibrations when excited into resonant buildups by common human activities, like walking or rhythmic group exercises. This has elevated vibration serviceability from a secondary concern to primary design criterion for many structures, which is often more critical than strength requirements.

This study focuses on simulation of façade and service area loads on a full-bay FastFloor specimen. FastFloor is an innovative all-steel modular floor system composed of prefabricated components designed for faster steel-framed floor construction. Developed in response to the AISC "Need for Speed" initiative to accelerate steel construction [2]. FastFloor's lightweight and long-span characteristics make it an important case study for understanding its dynamic behavior and addressing potential serviceability issues. The development and research program of FastFloor was detailed in [3]. Prior research on FastFloor system includes initial vibration and modal testing on single modules [4, 5], finite element model updating , and serviceability assessments and predicted peak accelerations under synchronous walking [6, 7, 8]. The effect of lateral braces, called angle blocking, on modal parameters was also investigated in [9].

This study experimentally investigates the effects of simulated non-structural loads on the dynamic response of a full-scale, 30 ft × 42 ft FastFloor laboratory specimen. Two distinct load cases were evaluated against an unloaded baseline condition: a 225 plf (3.28 KN/m) line mass applied to the cantilever edge to represent a façade load, and a 12 psf (575 N/m^2) distributed area load representing a service load. The investigation focuses on quantifying changes in the floor's structural damping, and acceleration responses under human walking loads. To achieve this, experimental modal analysis

Sahabeddin Rifai · Ahmad Rababah · Feras Abla · Mohamed Tareq Soliman · Onur Avci
Department of Civil and Environmental Engineering, West Virginia University, Morgantown, WV 26506
e-mail: sr00090@mix.wvu.edu; ayr00002@mix.wvu.edu; fa00060@mix.wvu.edu; mts00029@mix.wvu.edu; onur.avci@mail.wvu.edu

© The Author(s), under exclusive license to River Publishers 2026

Kristin B. Zimmerman, PhD (eds.), *Dynamics of Civil Structures, 2026, Vol. 2*, Conference Proceedings
of the Society for Experimental Mechanics Series, https://doi.org/10.13052/rp-9788743814139

was conducted on all configurations, and free-vibration decay tests were performed to measure the damping of the baseline and service load conditions

This paper is organized as follows: Section 2 describes the full-bay FastFloor test specimen. Section 3 details the experimental setups used to simulate the façade and service loads. Section 4 presents the experimental results, including an analysis of the frequency response functions (FRFs), a quantification of the structural damping , and an evaluation of the floor's response to human walking. Finally, Section 5 summarizes the key findings and presents the conclusions of the study.

Tested FastFloor Specimen

The full-bay FastFloor specimen tested in this study measures 30 ft (9.1 m) wide and 42 ft (12.8 m) long. FastFloor is an innovative all-steel floor system developed to accelerate the construction of commercial buildings. It consists of prefabricated modules and infill plates that are rapidly assembled on-site with bolted connections.

A plan view of the FastFloor specimen, illustrating the location of the simulated façade load on the exterior cantilever edge, is shown in Fig. 1. The specimen is constructed from three prefabricated modules and nine infill plates. The structural framing consists of two W30×108 girders and seven W24×68 beams, all supporting a $\frac{1}{2}$ in. (12.7 mm) thick steel plate deck (Fig. 2-a). The girders and edge beams are attached to W14 columns using shear tab connections.

All tests reported in this study were conducted with a raised access floor (RAF) installed over the steel deck, as shown in Fig. 2-b. This configuration, without any additional applied loads, served as the baseline for all subsequent tests. During baseline testing, the specimen supported only self-weight.

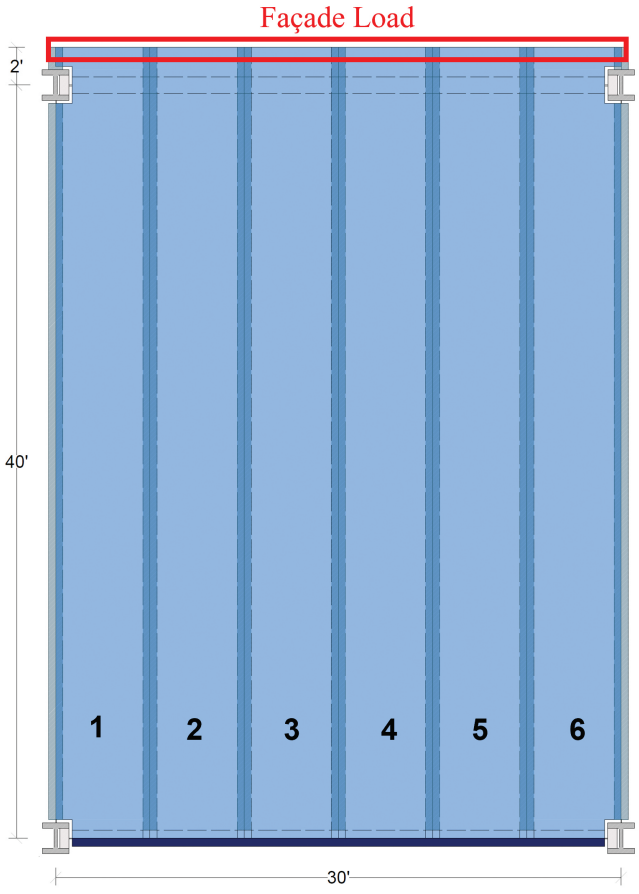

Fig. 1 Plan layout of the 30 ft × 42 ft all-steel FastFloor specimen, illustrating the location of the simulated façade load



(a) (b)

Fig. 2 The full-bay FastFloor specimen: (a) bare steel deck condition and (b) with the raised access floor (RAF) installed. The RAF configuration represents the unloaded baseline for all tests

Test Setups with Façade and Service Loads

To investigate the influence of added mass, three distinct configurations were tested, as detailed in Table 1. The reference case was the Baseline (BL) configuration, representing the as-built floor with no additional loads. The second configuration with façade load (FL), simulated the weight of a façade. As shown in Fig. 3, this was achieved by placing a line mass of panels and steel plates along an exterior edge, equivalent to a 225 plf linear load.

The third configuration with service load (SL) represented a typical superimposed dead load. A distributed mass equivalent to a 12 psf area load was applied by placing materials across the floor surface, as seen in Fig. 4. Due to the large floor area, this corresponded to a total applied mass of 15.12 kips (7.56 metric tons). Small areas were left clear to accommodate the mass shaker, accelerometers, and walking spaces.

Table 1 Test configurations with notations and simulated loads

No.	Configuration	Notation	Linear Load on Exterior Edge	Area Load
1	Baseline	BL	0	0
2	Baseline with Façade Load	FL	225 plf	0
3	Baseline with Service Load	SL	0	12 psf

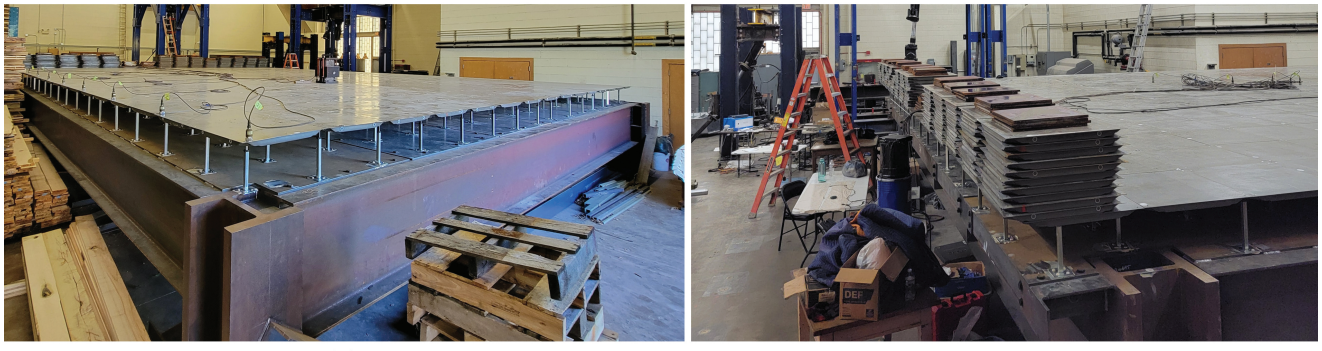

(a) (b)

Fig. 3 Configuration with façade load (FL) applied as a line mass of panels and plates simulating a 225 plf load on the exterior edge of the cantilever



Fig. 4 Configuration with service load (SL) applied as distributed mass simulating a 12 psf area load

Experimental Testing Results

Frequency Response Functions (FRFs)

Experimental modal analysis was performed using an electrodynamic shaker to obtain frequency response functions (FRFs) for all three test configurations. The shaker was positioned at the quarter-point along the centerline of module 3, and responses were measured at 300 points across the floor. The sensor grid was denser in the short direction to better capture plate bending modes with double curvature. Since both the input excitation and the output response were measured as acceleration, the resulting FRF magnitude is unitless. An overlay of all 300 FRFs for the baseline (BL) configuration is shown in Fig. 5.

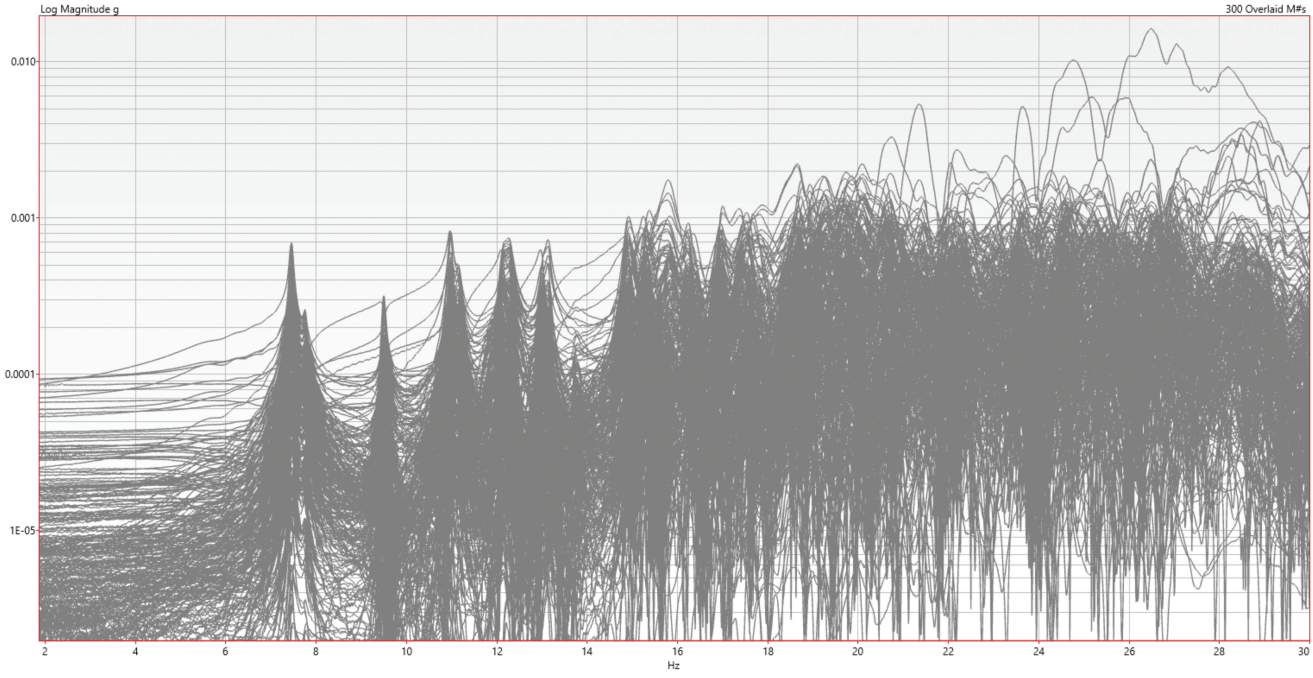

Fig. 5 Overlaid frequency response functions (FRFs) from 300 measurement points on the baseline (BL) configuration

To compare the effects of the added loads, the FRFs from a single point (the center of Module 3) are overlaid on a logarithmic scale in Fig. 6. This location captures responses from both beam and plate bending modes. The baseline (BL) FRF is characterized by the highest peak amplitudes at frequencies below 14 Hz. As expected, the added mass from the façade (FL) and service (SL) loads causes the FRF peaks to shift to lower frequencies. The frequency shift is more pronounced for the SL configuration due to its greater total mass.

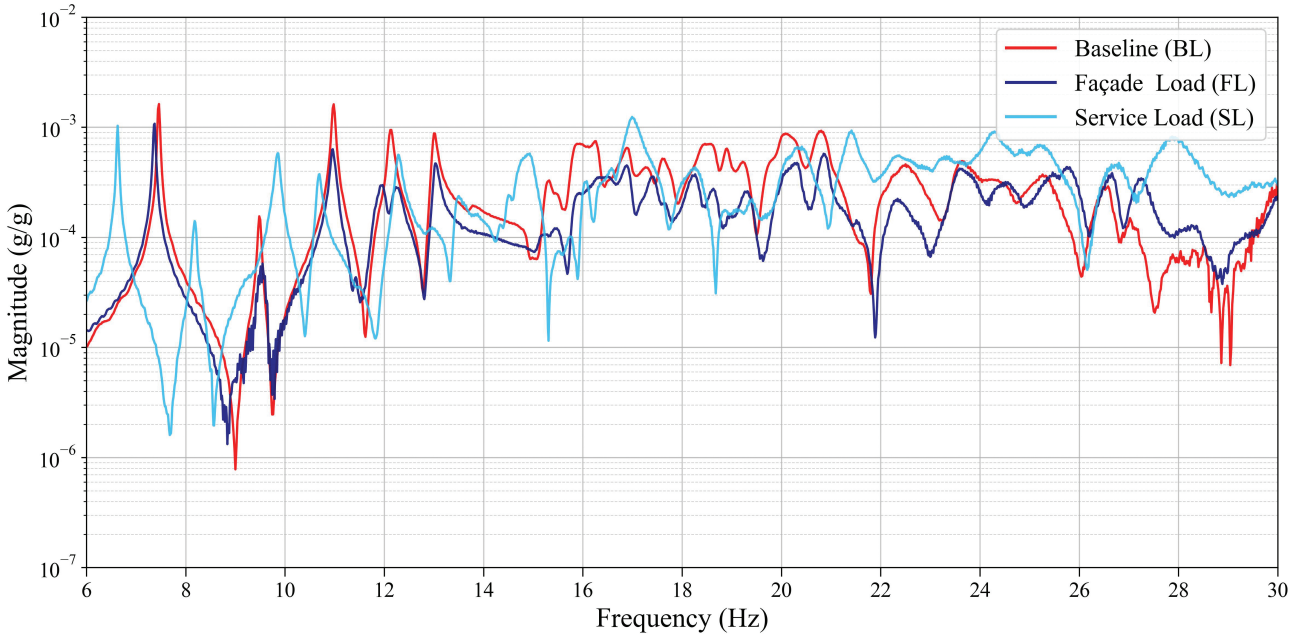

Fig. 6 Comparison of FRFs for all three configurations, measured at the center of module 3 (logarithmic scale)

Since the first (fundamental) mode has the highest mass participation and typically dominates the floor's vertical vibration response, it is examined more closely. The shape of this primary bending mode is shown in Fig. 7. A detailed view of the FRFs near the fundamental mode is presented on a linear scale in Fig. 8. Compared to the baseline, the peak magnitudes for both the FL and SL configurations are reduced. Both loaded configurations show a similar reduction in the first peak's magnitude, which is approximately 30% lower than that of the baseline.

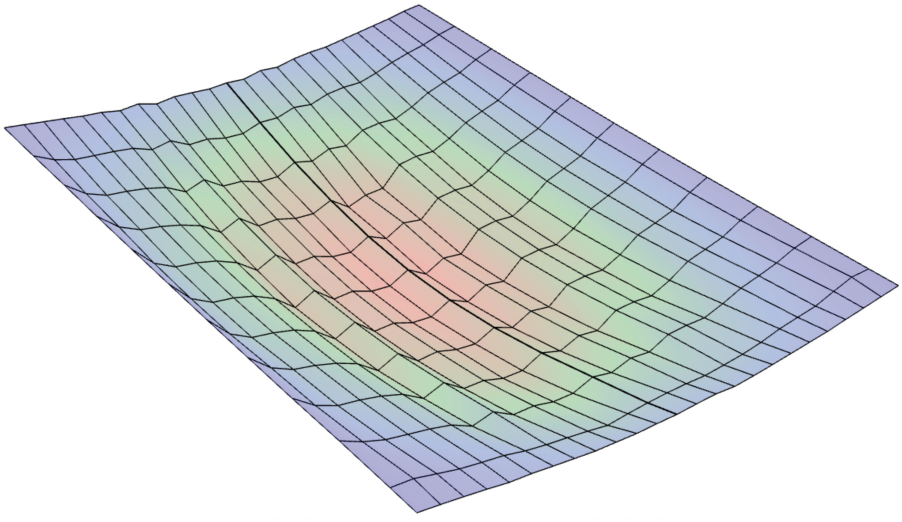

Fig. 7 The first (fundamental) mode shape, showing the major bending behavior of the floor

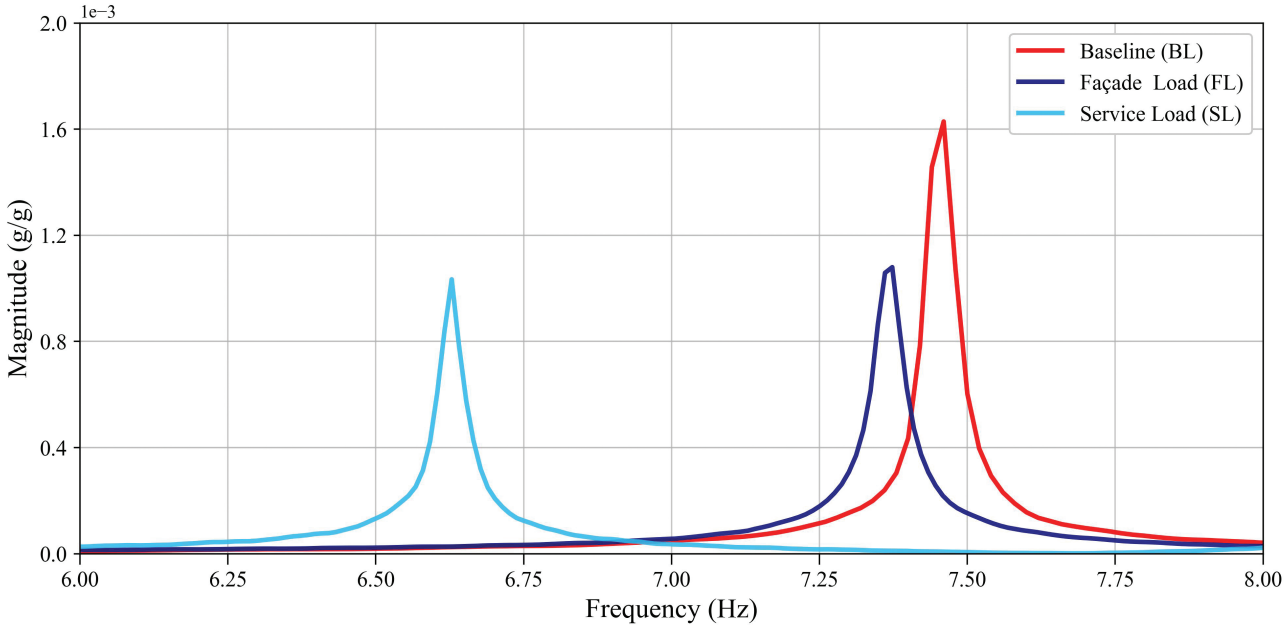

Fig. 8 Linear-scale FRFs showing the detailed response near the fundamental mode for all three configurations

Structural Damping

The effect of the added service load on the floor's overall structural damping ratio (β) was quantified using free-vibration decay tests. These tests were conducted for the baseline (BL) and service load (SL) configurations only. The procedure involved exciting the floor to a steady-state resonance at its fundamental frequency using low-amplitude shaker inputs. The excitation was then abruptly stopped, and the subsequent decay was recorded. The acceleration signals were pre-processed by detrending and applying a Butterworth filter, after which the damping ratio (β) was extracted by fitting an exponential function to the decaying peaks.

The results, illustrated by the decay curves in Fig. 9, show that the addition of the 12 psf service load increased the floor's structural damping. Under low-amplitude excitation, the damping ratio for the baseline configuration was found to be 0.25%. For the SL configuration, the damping increased to 0.35%, representing a 40% increase due to the presence of the service load.

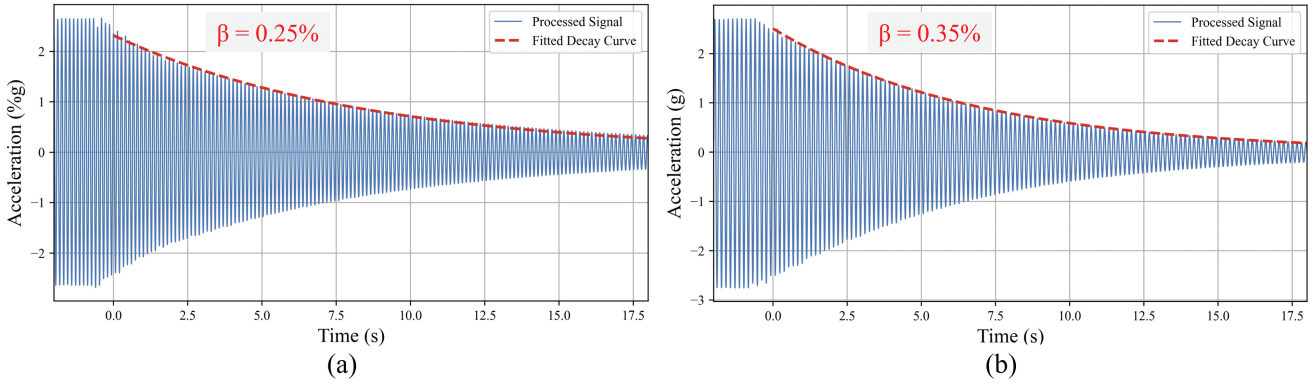

Fig. 9 Comparison of free-vibration decay curves for the (a) baseline (BL) and (b) service load (SL) configurations, showing the increase in damping under low-amplitude excitations

Response to Human Walking

To measure the response under footfalls, a series of walking tests was performed on each floor configuration. During these tests, four individuals walked along the centerline of module 4. A metronome was used to maintain a consistent step frequency equal to the fourth subharmonic of the floor's fundamental frequency (f_n /4). This pacing is known to be effective for exciting a resonant buildup in such structures. The resulting vibrations were recorded by an accelerometer at the center of module 3.

The recorded acceleration data was then processed using the Equivalent Sinusoidal Peak Acceleration (ESPA) method to evaluate the floor against established human comfort criteria. In accordance with procedures from AISC Design Guide 11 and SCI P354, the ESPA for each test was calculated by identifying the maximum one-second root-mean-square (RMS) value from the filtered acceleration signal and multiplying it by $\sqrt{2}$ [1, 10].

To account for the inherent variability in human footfalls over multiple trials, the 90th percentile ESPA was used as the final, representative metric for comparison. This statistical approach provides a robust value that is less influenced by outlier measurements, which is particularly important for low-damping systems where response data can be more scattered.

The results of the walking tests, summarized in Table 2, show that the two load types had different effects on the floor's vibration response. The simulated façade load (FL) did not improve the floor's performance. In fact, the mean, maximum, and 90th percentile ESPA values all increased slightly compared to the baseline. This outcome is likely attributed to the fact that the concentrated line load did not significantly increase the overall system damping. In contrast, the service load (SL) led to a reduction in the vibration response. The 90th percentile ESPA decreased from 1.79 %g to 1.59 %g, an 11% decrease. This reduction is a direct result of the added structural damping provided by the distributed mass. The findings suggest that while edge mass may not benefit serviceability, broadly distributed service loads can provide a modest but helpful improvement in vibration performance.

Table 2 Statistical summary of damping and ESPA values from the human walking tests

			Equivalent Sinusoidal Peak Accelerations (ESPAs) [%g]				
Configuration	**# of Walking Tests**	**Step Frequency (steps/min)**	**Mean (μ)**	**Min**	**Max**	**STD (σ)**	**90th Percentile (μ+1.28σ)**
BL	28	112	1.46	1.09	1.92	0.26	1.79
FL	28	111	1.49	1.07	2.13	0.26	1.82
SL	28	99	1.30	0.93	1.87	0.23	1.59

Conclusions

This paper presented an experimental investigation into the effects of simulated façade and service loads on the vibration response of a full-bay modular all-steel floor. The study compared an unloaded baseline configuration with two loaded cases: a concentrated line load representing a façade and a distributed area load representing a service load. The key findings are as follows:

1. The addition of mass from both the façade and service loads reduced the floor's natural frequencies, with the service load causing a more significant reduction due to its greater total mass.
2. The distributed service load (SL) provided a measurable benefit to the floor's performance. It increased the overall structural damping ratio by 40% (from 0.25% to 0.35%) and consequently reduced the 90th percentile walking-induced vibration response (ESPA) by 11%.
3. In contrast, the façade load (FL) did not improve the vibration serviceability. The 90th percentile ESPA increased slightly compared to the baseline, which is attributed to the line load not contributing significantly to the system's overall damping.

These findings demonstrate that while all superimposed dead loads reduce a floor's natural frequency, only broadly distributed loads that also contribute to system damping may provide a tangible benefit to its vibration serviceability. The location and type of non-structural mass are therefore critical considerations in the vibration analysis of modern floor systems.

Acknowledgments This work was sponsored by the Charles Pankow Foundation, American Institute of Steel Construction (AISC), MKA Foundation, Nucor, Schuff Steel, Herrick Steel, Cives Steel, Zekelman Industries (Atlas Tube/Shuriken), and Metals Fabrication. In-kind support was provided by Cerami, Sherwin-Williams, Cooper Steel, Clark Construction, and Hensel Phelps. Any opinions, findings, and conclusions or recommendations expressed in this material are those of the authors and do not necessarily reflect the views of the sponsors and supporters.

References

1. T. M. Murray, D. E. Allen, E. E. Ungar, and D. B. Davis, "Design Guide 11: Vibrations of Steel-Framed Structural Systems Due to Human Activity (Second Ed.) | American Institute of Steel Construction."
2. FastFloor – The Need for Speed – Session 1 [N24] 2024 | AISC. [Online Video]. Available: https://learning.aisc.org/local/catalog/view/product.php?productid=2508
3. B. Schafer, O. Avci, W. S. Easterling, M. R. Eatherton, and J. Hajjar, "FastFloor – Development of A Novel Modular Steel Floor System for Commercial Construction in The United States," Dec. 02, 2024, Engineering Archive. doi: 10.31224/4183.
4. O. Avci et al., "Vibration Testing of an All-Steel Modular Floor Assembly," in Dynamics of Civil Structures, Vol. 2, M. Whelan, P. S. Harvey, and F. Moreu, Eds., Cham: Springer Nature Switzerland, 2025, pp. 17–23. doi: 10.1007/978-3-031-68889-8_3.
5. S. Rifai et al., "Modal Testing and Finite Element Model Updating of a FastFloor Specimen: A Modular All-Steel Floor System," in Dynamics of Civil Structures, Vol. 2, River Publishers, 2025. doi: 10.13052/rp-9788743801597A004.
6. O. Avci and M. A. M. Celin, "Vibration Serviceability Evaluation of a Modular Steel Plate Floor Assembly," in Dynamics of Civil Structures, Volume 2, Springer.
7. M. A. Mercado Celin, "Vibration Serviceability Assessment of a Steel Modular Floor System," Virginia Tech, 2023.
8. S. Rifai, Abla, Feras, A. Rababah, R. C. M. Kumar, B. W. Schafer, and M. R. Eatherton, "Vibration Serviceability Evaluation of an All-Steel Floor System using the High-Frequency Floor Procedure," in Dynamics of Civil Structures, Vol. 2, River Publishers, 2025. doi: 10.13052/rp-9788743801597A010.
9. S. Rifai et al., "Effect of Bottom Flange Angle Blocking on the Dynamic Re- sponse of Two All-Steel Laboratory Floors," in Dynamics of Civil Structures, Vol. 2, River Publishers, 2025. doi: 10.13052/rp-9788743801597A003.
10. A. L. Smith, S. J. Hicks, and P. Devine, Design of Floors for Vibration: A New Approach (2009).

Chapter 10
Influence of Electrical Components and Supports on the Modal Characteristics of Timber Distribution Poles

Timothy Kernicky and Matthew Whelan

Abstract Inspection and asset management of timber distribution poles is critical for ensuring the reliability of the electrical distribution network and safety of powerline technicians requiring physical access to supported electrical infrastructure. Techniques for structural health monitoring and nondestructive evaluation of timber poles, including vibration-based methods, have been developed to detect belowground deterioration caused by fungal decay and wood-damaging insects that is not readily detected without costly and time-consuming excavation of soil around the pole. However, published literature on the modal characteristics of timber distribution poles has largely been limited to isolated and free-standing poles. The influence of supported components, such as conductors, crossarms, transformers, and lights, on the modal parameters of distribution poles has not been well established, which complicates the development of physics-based models to support structural health monitoring of the pole. To address this limitation, experimental modal analyses were conducted on a distribution pole under different configurations by sequentially adding and removing supported components. By conducting the test program on a de-energized circuit, an array of accelerometers could be installed along the entire exposed height of the pole in orthogonal directions to enable the experimental estimate of mode shapes from the free decay vibration response. The influences of individual components on the frequency response functions, natural frequencies, damping ratios, and mode shapes of the pole are presented.

Keywords Distribution poles · Energy infrastructure · Experimental modal analysis · Timber poles · Vibration-based structural health monitoring

Introduction

Although vibration-based techniques have been proposed for condition assessment of timber distribution poles by numerous studies [1], referenced within patents [2], and included in comprehensive reviews of nondestructive evaluation techniques [3], the experimental modal analysis of in-situ timber distribution poles has not been published to-date. Although the monopole nature of the primary structure suggests a relatively simple and readily predictable dynamic response, there are several complicating factors that may limit the accuracy of analytical formulas when applied to estimate the modal parameters of timber distribution poles. Timber poles are naturally grown and therefore exhibit a tapered geometry, orthotropic material properties, and local variations due to knots and other growth features. Furthermore, distribution poles are partially embedded in soil and the soil-structure interaction over the depth of embedment affects the dynamic response of the pole. The purpose of distribution poles is to support electrical infrastructure, including distribution lines, transformers, and street lights, which introduce additional mass, stiffness, and damping contributions. The dynamics of some of this infrastructure, such as the conductors, and additional components required to support the infrastructure, like crossarms, may be coupled to the dynamics of the pole. Lastly, additional structural support provided to the pole to resist applied loads, such as guy wires and groundline

Timothy Kernicky · Matthew Whelan
Energy Production and Infrastructure Center
e-mail: mwhelan3@charlotte.edu; mwhelan3@charlotte.edu

Timothy Kernicky · Matthew Whelan
Department of Civil and Environmental Engineering, EPIC Building, 9201 University City Blvd
University of North Carolina at Charlotte, Charlotte, NC 28223-0001
e-mail: mwhelan3@charlotte.edu; mwhelan3@charlotte.edu

© The Author(s), under exclusive license to River Publishers 2026

Kristin B. Zimmerman, PhD (eds.), *Dynamics of Civil Structures, 2026, Vol. 2*, Conference Proceedings
of the Society for Experimental Mechanics Series, https://doi.org/10.13052/rp-9788743814139

reinforcements, may likely affect the modal parameters of the pole. Analytical models proposed for estimating the natural frequencies and mode shapes of utility poles do not account for many of these complicating factors, aside from the soil-structure interaction [4]. However, the limited experimental data on the effects of electrical components and supports on the dynamic properties of distribution poles provides little basis for justifying the development of more complex models and validating the predictive fidelity of such models.

Research related to the application of vibration-based methods for nondestructive evaluation of in-service timber distribution poles has been largely performed using laboratory scale models or tests on poles in idealized and simplified configurations. Following a laboratory test program conducted on short pole segments, Prestage [5] acquired frequency response functions from a full-length timber distribution pole both prior to and after simulating several stages of decay by drilling holes in the pole near the groundline. The experimental results provided evidence of the sensitivity of the natural frequencies of the pole to the severity of groundline decay. However, the test program was limited to a single freestanding pole without any supported electrical components. Through laboratory testing, Downer [6] provided empirical evidence of a correlation between pole static strength and modal damping ratios as well as the ratio of measured fundamental natural frequency to that predicted by a finite element model. This study involved experimental modal analysis of fourteen full-scale timber utility poles, however the testing was performed with the poles clamped in a rigid fixture to simulate groundline support rather than in-situ. Furthermore, the poles were oriented horizontally and did not support any electrical infrastructure. Using a similar laboratory setup with idealized boundary conditions, González de Paz et al. [7] measured natural frequencies of six full-scale timber distribution poles using impulse hammer testing. Natural frequencies calculated by an analytical model for tapered bars were found to exhibit greater prediction errors for poles with unspecified deterioration than for structurally sound poles. Lastly, Jalali [8] empirically demonstrated the effect of conductors on the dynamic response of timber distribution poles by comparing Frequency Response Functions (FRFs) acquired from two poles with and without the conductors being supported by the pole. The measurements reflected that the presence of the conductors led to decreases in natural frequencies, increases in modal damping, and generally less apparent resonance frequencies in the FRFs.

Full-scale experimental modal analysis has been performed for monopole distribution and transmission structures constructed of materials other than wood. Dai et al. [9] experimentally obtained natural frequency and mode shape estimates for a tapered concrete monopole transmission structure partially embedded in soil as well as suspended in the air. This testing was performed while no electrical infrastructure was supported by the pole, so effects of these components on the dynamic response were not reflected. However, finite element analyses of the pole in two configurations confirmed that strong model correlation for the modal parameters could be obtained when the soil-structure interaction was be modeled with only linear elastic springs. Chen and Dai [10] conducted experimental modal analysis on two in-service monopole transmission poles, one constructed of steel and one constructed of prestressed concrete. Both poles were partially embedded in soil and featured arms, insulators, and multiple supported transmission lines. Several guy wires provided additional structural support to the steel transmission pole. The authors noted significant differences in the FRFs obtained using a roving impulse hammer technique applied to both poles, with clear indications of resonance frequencies in the measurements acquired for the prestressed concrete pole and only one mode identified from the measurements acquired from the steel pole. The authors attributed the challenge in experimental modal analysis of the steel pole to coupling of the dynamic response of the pole with the conductors and guy wires. For the prestressed concrete pole, the authors demonstrated the application of a numerical model to account for coupling of the pole with the transmission line dynamic response.

In this paper, an experimental test program aimed at developing an understanding of the influence of electrical components and supports on the modal parameters and dynamic response of timber distribution poles is introduced. Experimental modal parameter estimates are presented for a subset of the configurations included in the experimental test program. Finite element analyses are also presented to provide insight into how specific supported components affect the modal parameters of the pole.

Description of experimental study

The experimental program was conducted on a full-scale, de-energized, timber distribution pole located within a lineman training facility. In contrast to prior laboratory test programs, the pole was installed in service conditions with direct embedment in soil consistent with field practice. This setting provided a unique opportunity to investigate the modal properties of a timber distribution pole with realistic boundary conditions, attachments, and supports. Figure 1 presents photographs of the pole specimen that serves as the focus of this paper. The pole was Southern Yellow Pine. It had a total length of 12.19 m and, since the portion extending above the groundline was measured at 10.10 m in length, the depth of embedment was 2.09 m. The circumference of the pole at an elevation of 0.30 m from the ground line was measured with a flexible tape measure to be 88.9 cm, while the circumference at an elevation of 1.83 m from the ground line was measured to be 87.6 cm. The test

specimen included the full complement of electrical infrastructure typically found on an energized distribution line. These attachments consisted of a mounted transformer, a street light, a crossarm assembly with tie top line post insulators, three phase conductors, a neutral line, and a secondary line. In addition, a service tap line was present to replicate in-field loading conditions. In addition to the supported electrical infrastructure, two guy wires were also installed on the pole to provide restraint in two directions. The presence of these attachments produced complex mass, stiffness, and damping contributions, thereby offering an opportunity to assess the influence of electrical infrastructure, ancillary hardware, and structural supports on the global dynamic response of the pole.

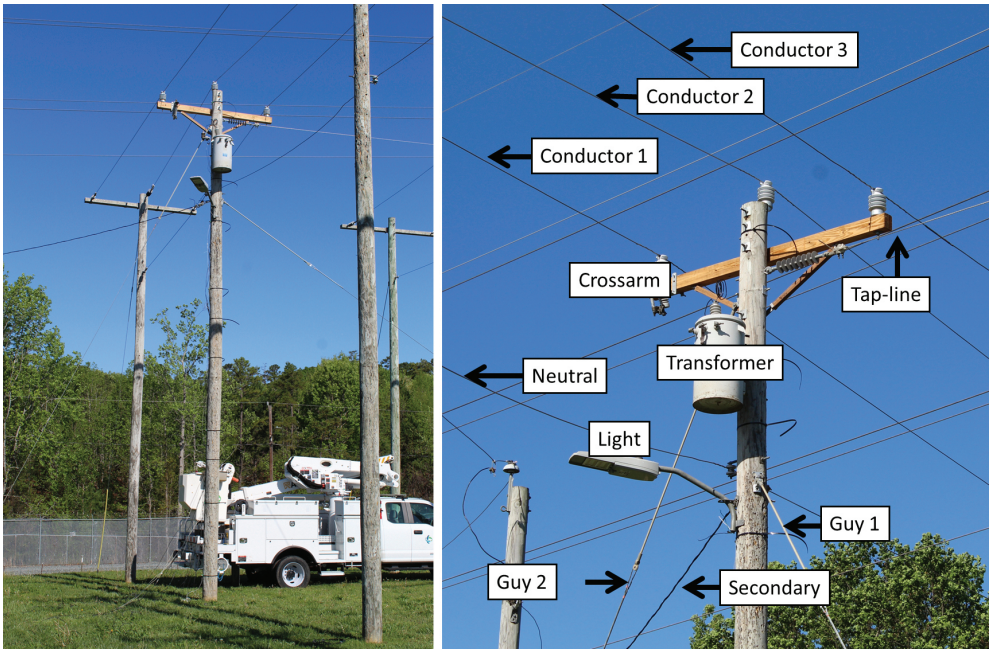

Fig. 1 Photographs of instrumented distribution pole and all of the electrical components and supports included in the test program

Identifying the effect of individual components on the dynamic response of the pole would be plagued by uniqueness challenges if limited to using only measurements acquired from the fully configured state. Consequently, experimental modal analyses were conducted for 15 distinct configurations of the pole that were created by removing and selectively reinstalling different electrical components and structural supports. Table 1 provides a summary of the components present for each of the 15 configurations under which the experimental modal analysis was performed. In this table, a cell filled with gray indicates that the component was present for the corresponding configuration. The first configuration represented the in-service condition with all attachments present, including the crossarm, conductors, neutral line, secondary line, tap line, light, transformer, and guy wires. The final configuration resulted in a free-standing pole embedded in the soil with all attachments removed. Since components were removed or added one at a time, the progression of configurations provided a structured basis for isolating the effects of individual attachments on the global dynamic response. In the exploration of the experimental test data, the final configuration is first investigated, since it corresponds to the simplest case and one that most closely replicates conditions assumed by existing analytical models for predicting the natural frequencies and mode shapes of utility poles.

The experimental modal analyses of the pole were performed using a stationary array of accelerometers and impulse excitation applied at elevations within reach from the ground. This test setup was selected for two reasons. First, a roving hammer approach would be time consuming to perform since it would require repeatedly positioning an individual at different elevated positions to apply the impulse excitations. Second, vibration-based nondestructive evaluation techniques for condition assessment of timber distribution poles typically rely on excitation applied by personnel on the ground, since that is convenient, time efficient, and safer with respect to electrical hazards. A total of 16 PCB Piezotronics J320C33 uniaxial accelerometers were installed along the exposed height of the pole in orthogonally oriented pairs at 1.37 m intervals. The lowest pair was positioned 0.46 m above the ground line, with the remaining sensors continuing upward to the top of the pole. Figure 2 depicts the location of the accelerometers on the pole, as well as the location and orientation of the supported electrical components. The accelerometer layout permitted the acquisition of the lateral dynamic response in both principal

bending directions, while providing sufficient spatial resolution to resolve higher-order mode shapes. These accelerometers provide a nominal sensitivity of 100 mV/g, a measurement range of ±50 g, and a frequency response extending from 0.5 Hz to 10 kHz. Sensors were securely mounted using a 3D printed bracket and large cable ties, with cable runs secured to minimize extraneous vibration.

Table 1 Summary of different configurations of the pole under which experimental modal analysis was performed

Component	Configuration														
	1	2	3	4	5	6	7	8	9	10	11	12	13	14	15
Crossarm	✓	✓	✓	✓	✓	✓	✓	✓	✓	✓	✓	✓	✓	✓	
Conductor 1	✓	✓	✓	✓	✓							✓	✓	✓	
Conductor 2	✓	✓	✓	✓							✓	✓			
Conductor 3	✓	✓	✓	✓	✓							✓	✓		
Neutral	✓	✓	✓	✓	✓	✓	✓								
Secondary	✓	✓	✓	✓	✓	✓	✓	✓							
Tap-line	✓	✓													
Light	✓	✓	✓		✓	✓	✓	✓	✓						
Transformer	✓	✓	✓	✓	✓	✓									
Guy 1	✓	✓	✓												
Guy 2	✓														

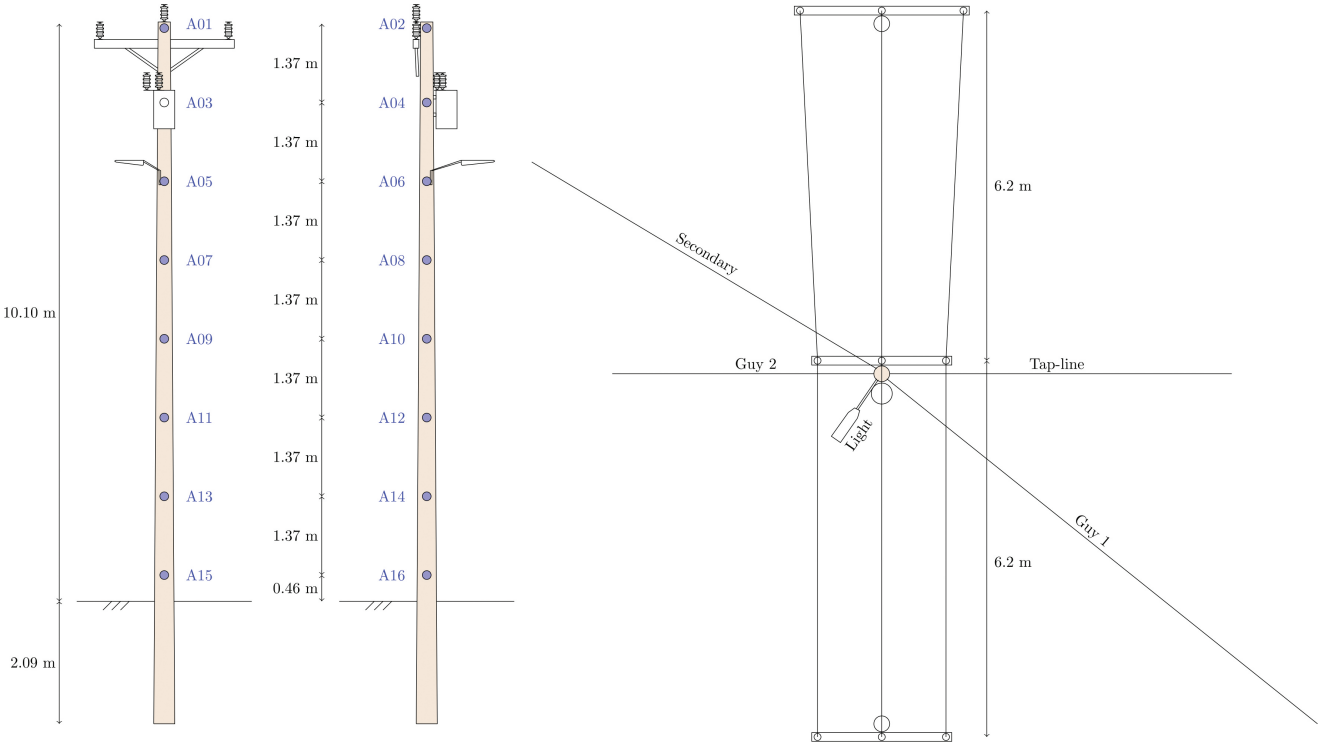

Fig. 2 Elevation and plan views of the pole configuration with locations of accelerometers denoted

The pole was excited using an PCB Piezotronics model 086D20 impulse hammer with a dynamic force transducer integrated in the hammer head. The hammer mass was 1.1 kg and the super soft (gray) tip was used during the testing to concentrate the energy from the excitation into the frequency bandwidth below 100 Hz. Impulse excitations were applied at elevations of 1.22 m (4 ft) and 1.83 m (6 ft) above the groundline in the two orthogonal directions corresponding to the positioning of the accelerometers. At each location and orientation, five impulses were applied to provide a basis for averaging in the development of FRFs. The hammer force and accelerometer response data were acquired using National Instruments PXIe-4497 sound and vibration modules. These modules provide the Integrated Electronic Piezo-Electric (IEPE) signal conditioning for the accelerometers and the load cell integrated into the impulse hammer, as well as anti-alias low-pass

filtering and 24-bit simultaneous sampling. An analog reference trigger was established using the signal from the impulse hammer such that the rising edge of the excitation signal was aligned for all recorded data with the same number of pretrigger samples. A sampling rate of 3200 Hz and duration of 4 seconds was used to acquire time histories for each impulse.

Following preprocessing of the measurement data to apply sensitivities provided by manufacturer calibration of the sensors, remove offsets, and window the force measurement to suppress any noise in the signal following the impulse, FRFs were computed using the classical H1 estimator. Impulse responses were then computed by the inverse fast Fourier transform of the FRFs. System identification was performed for each of the configurations using the Eigenvalue Realization Algorithm [11]. Modal parameter estimates obtained for each of the four impulse locations were extracted for multiple model orders after applying stabilization criteria on the undamped natural frequency, damping ratios, and complex mode shape estimates. Final modal parameter estimates for each configuration were then obtained by averaging estimates obtained for each impulse location after matching modes with Modal Assurance Criteria values greater than 0.95 and scaling the consistent modes with the Modal Scale Factor.

Results

The final configuration included in the experimental test program produced data to characterize the simplest case of a free-standing pole with typical soil embedment but no supported electrical components or guy wires. Figure 3 presents the experimental modal parameter estimates obtained for this configuration. The mode shape estimates shown in this figure depict only the exposed region of the pole, since no sensors were placed below the ground line. The modal parameter estimates reflect a lightly damped response characterized by nearly identical flexural modes in each direction. The undamped natural frequencies of the pole were found to be slightly different for the two axes of flexure. This could be the result of differences in material and geometric properties of the cross section, since the cross section of a pole is not perfectly round, wood is not homogeneous material, and holes were drilled in the pole for different attachments. Differences in soil stiffness in each direction of flexure may also contribute to the variation in undamped natural frequencies between the principal axes.

The second simplest configuration included in the test program introduced the crossarm to the pole. This crossarm was dimensional lumber of 2.44 m in length and a 15 cm x 10 cm cross section. Two tie top line post insulators were

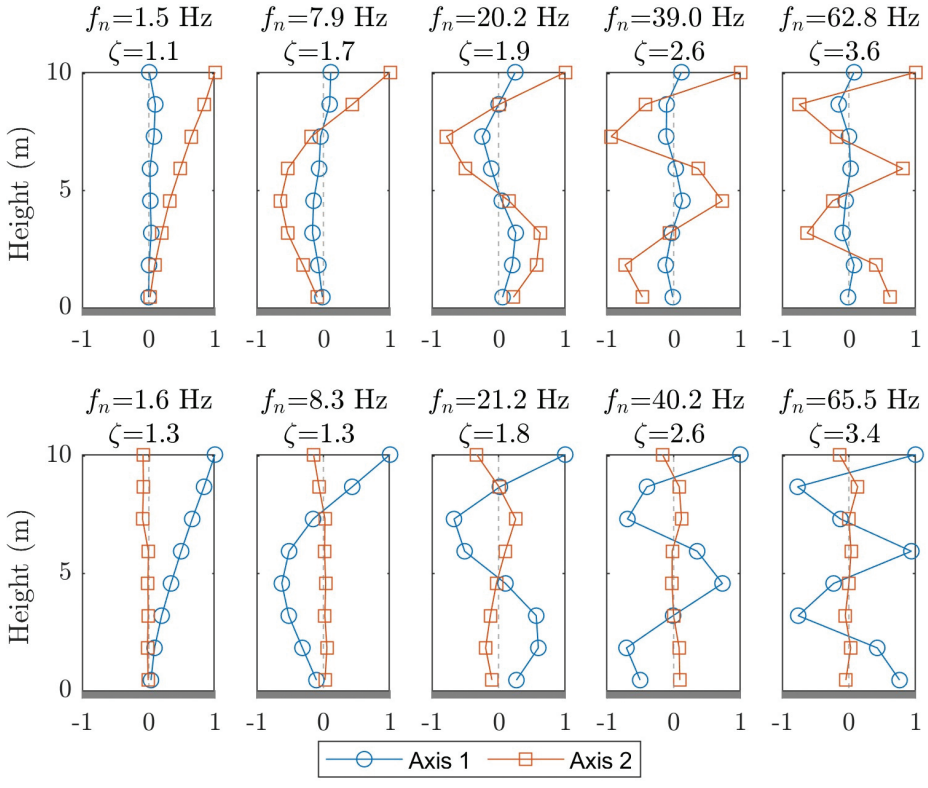

Fig. 3 Experimental modal parameter estimates for free-standing pole with no attachments (Configuration 15)

also installed on the crossarm during the testing, but the conductors were not attached to the crossarm for this particular configuration. Figure 4 presents the average of the mobility FRFs obtained for impulses applied at the 1.83 m elevation for this configuration alongside those obtained for the testing performed on the free-standing pole. While resonance frequencies are observed to decrease as a result of the additional mass introduced by the crossarm, the changes in the FRFs due to the presence of the crossarm reflect greater influence than just the mass. Additional resonance frequencies appear in the FRFs for both directions, indicating a coupling of structural modes of the crossarm with the modes of the pole within the frequency bandwidth of interest. Figure 5 presents the experimentally estimated modal parameter estimates for the pole with the crossarm. The results confirm the presence of additional modes within the bandwidth of interest and show visible differences in the mode shapes that were estimated for the freestanding pole configuration, even for the lower-order flexural modes. Changes in natural frequencies were generally greater for the modes exhibiting flexure about axis 1 than those exhibiting flexure about axis 2. However, modal damping does not appear to be significantly affected by the presence of the crossarm. One exception is the damping ratio estimate for the fundamental mode associated with flexure about axis 1. However, system identification of this mode shape was particularly challenging and, as a result, far fewer stable poles were included in the averaging that led to the final estimate.

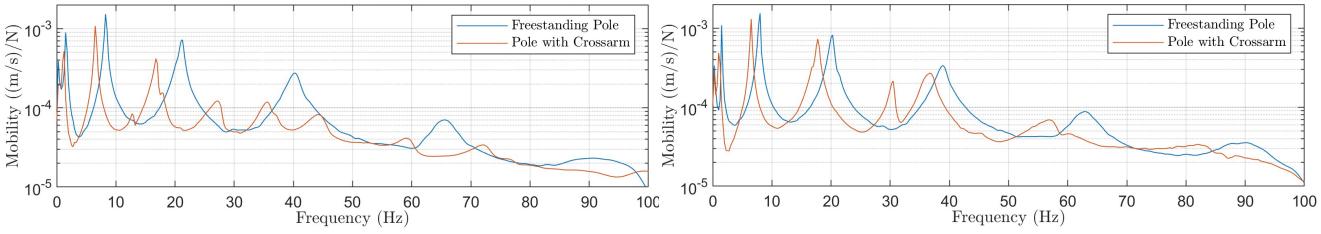

Fig. 4 Comparison of the average mobility FRF for Configurations 10 and 15: a) axis 1 and b) axis 2

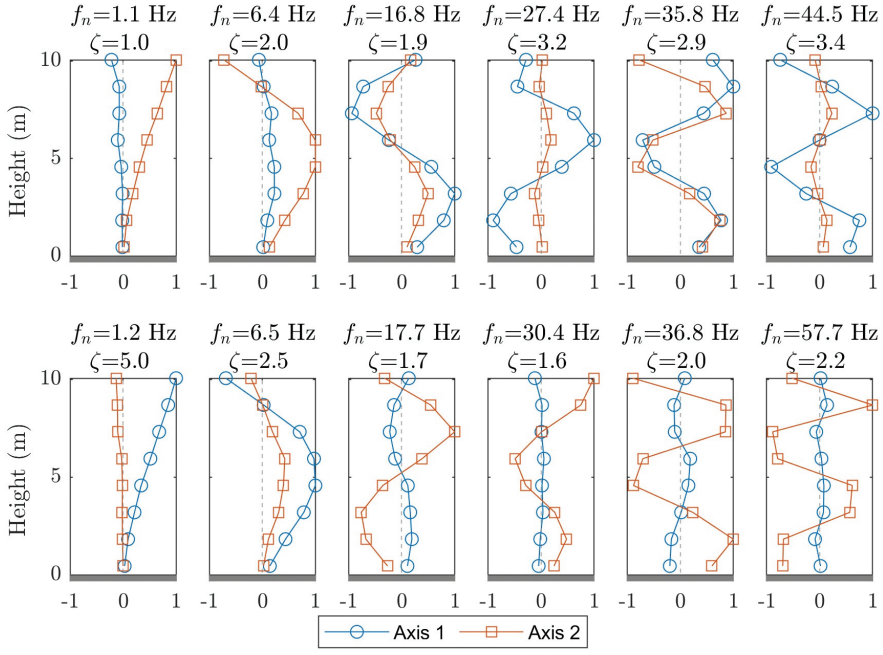

Fig. 5 Experimental modal parameter estimates for pole with crossarm (Configuration 10)

The experimental modal parameter estimates provide clear evidence that the presence of the crossarm has a significant effect on the modal parameters of the pole. To provide greater insight into the nature of the effect, a complementary numerical study was conducted to examine how the introduction of a crossarm affects the natural frequencies and mode shapes of a typical timber distribution pole. First, a finite element model of the free-standing pole configuration was developed. The finite element model used Timoshenko frame elements to model the pole, with axial, shear, flexural, and torsional stiffnesses

calculated using assumed orthotropic properties for the timber. The tapered geometry of the pole was approximated by decreasing the diameter used to calculate the section properties in a piecewise constant manner along the length of the pole. Soil-structure interaction was modeled using linear elastic springs along the embedded portion of the length, with the stiffness of the springs increasing linearly with depth. Since the purpose of the model was simply to provide additional insight into the experimentally observed changes in modal parameters, the model was constructed with assumed material properties and no effort was made to calibrate uncertain parameters in the model. A second finite element model was created by extending this model to include a crossarm located at the same height as the crossarm in the experimental test. This crossarm was modeled with Timoshenko frame elements and connected to the elements representing the pole with a shared node. However, to approximate the single through bolt connecting the crossarm to the pole, the rotational degree of freedom associated with rotation of the crossarm about an axis running normal to the surface of the pole was not shared. The braces supporting the crossarm were modeled with truss elements. Furthermore, the post insulators on the crossarm were represented as point masses in the model.

Linear eigenanalysis was conducted for each model to arrive at predictions for the undamped natural frequencies and mode shapes for each configuration. Figure 6 presents the results for the model of the free-standing pole partially embedded in soil with no supported electrical components or supports. The predictions correlate strongly with the experimental estimates obtained for this configuration, which supports the plausibility of the finite element model. Figure 7 presents the natural frequencies and mode shapes predicted using the second finite element model that included the crossarm and crossarm bracing in the model. Consistent with the experimental observations, the results confirm that the crossarm not only reduces the natural frequencies and introduces changes in the mode shapes, but also produces new mode shapes that interrupt the classical progression of modes compared to the free-standing case. The finite element analysis reveals that the dynamics of the crossarm are coupled to the dynamics of the pole. This is particularly apparent in the mode shapes predicted by the finite element analysis at 36.0 Hz and 42.9 Hz. These results indicate that physics-based models for predicting the natural frequencies and mode shapes of timber distribution poles should neither neglect the crossarm nor rely on simplified representation of it, such as treating it as a point mass.

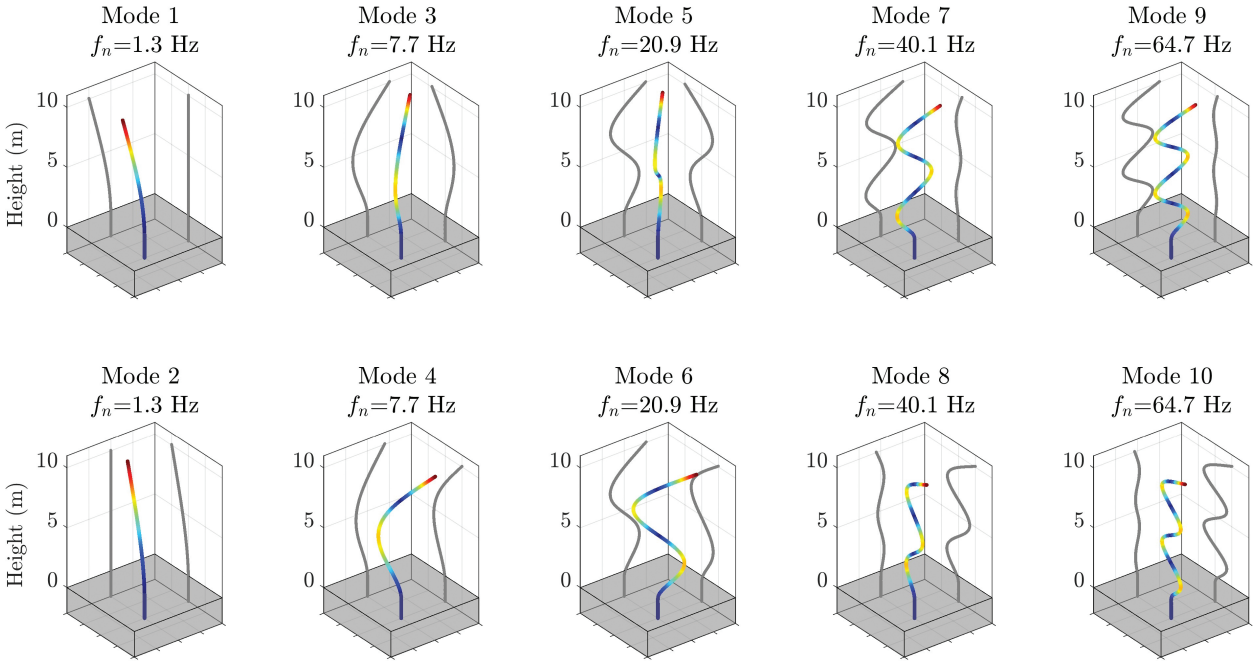

Fig. 6 Modal parameters predicted by finite element model of free-standing pole with no attachments (Configuration 15)

Figure 8 provides some early insight into the effect and relative significance of several additional components on the dynamic response. This figure presents the average mobility FRFs measured for impulse excitation at the 1.83 m elevation in each direction for different configurations involving the crossarm, light, secondary and tap lines, and the transformer. Since these components were added sequentially, their relative influence can be directly inferred through the changes reflected in the average mobility FRF for each configuration. The addition of the light has only a minor influence on the response that is reflected by a small decrease in the resonance frequencies. However, no evidence of coupled modal response of the light with the dynamics of the pole is observed in the measurement. The addition of the service and tap lines has no notable effect on

the average mobility FRF for either direction. However, the introduction of the transformer to the pole resulted in significant changes in FRFs. Similar to the addition of the crossarm, it appears that the presence of the transformer results in coupled dynamics that introduce additional modes within the frequency bandwidth of interest. The effect of the transformer appears to be significantly more pronounced in one direction of response than the other. Future papers will provide greater insight into the influence of these and other electrical components and supports on the modal parameters of timber distribution poles.

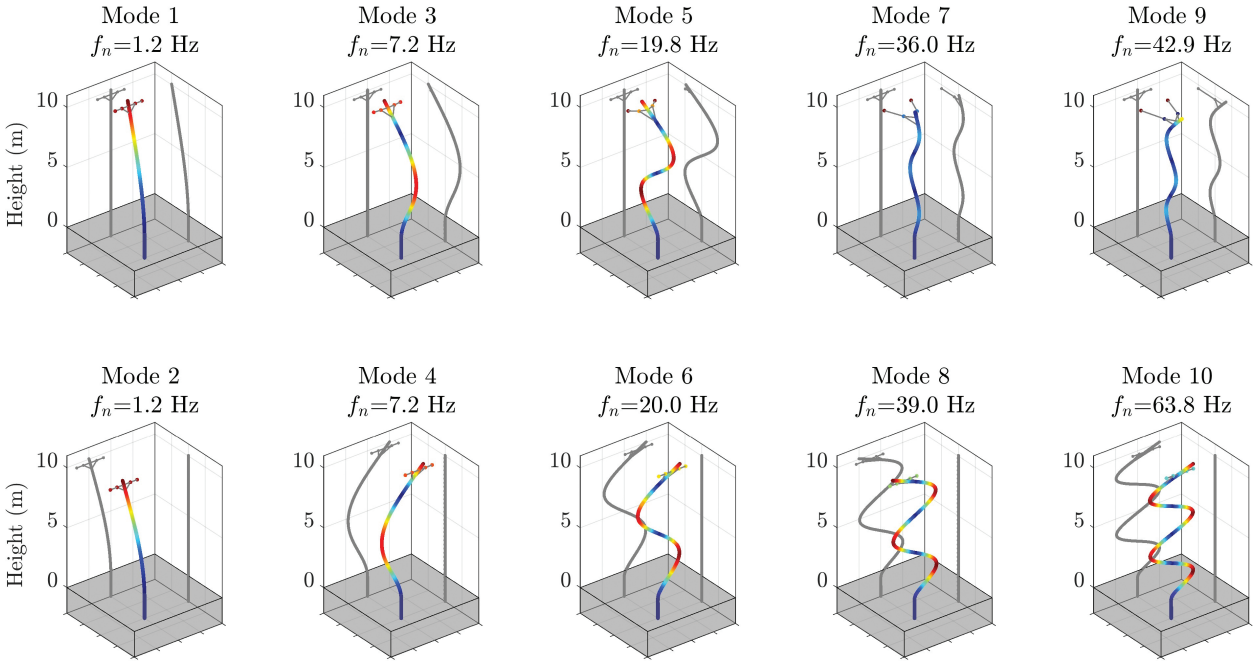

Fig. 7 Modal parameters predicted by finite element model of pole with crossarm (Configuration 10)

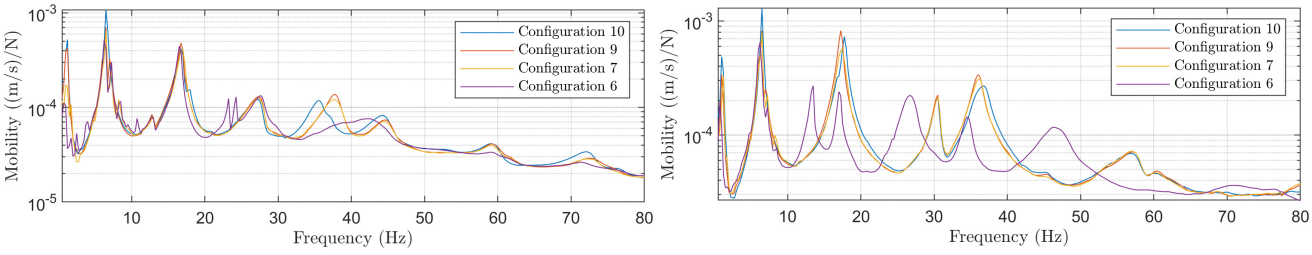

Fig. 8 Comparison of the average mobility FRF for additional configurations: a) axis 1 and b) axis 2

Conclusion

An experimental test program involving a structured basis for investigating how supported electrical components and structural supports influence the dynamic response of timber distribution poles was presented. By progressing from the fully configured in-service condition to a free-standing pole with no attachments, it was possible to isolate the effects of individual components and to observe how their removal or reintroduction altered the modal characteristics of the structure. The results demonstrated that even the introduction of a single attachment, specifically a crossarm, can have a pronounced effect on the modal response. Coupled dynamic response of the crossarm with the pole led to reductions in natural frequencies, distortions in the measured mode shapes, and additional modes within the frequency bandwidth of interest. Complementary finite element analyses confirmed the experimental observations and provided greater insight into the influence of the

crossarm on the modal parameters. The findings reinforce the importance of explicitly modeling the crossarm when developing predictive models for vibration-based condition assessment of in-service distribution poles. As additional electrical components and supports are introduced, the effects become more significant with further shifting of natural frequencies, increased damping, and additional coupling of component dynamic responses with the pole leading to additional resonance frequencies. These findings highlight the complex dynamic behavior of timber distribution poles, despite their seemingly simple structural form, and underscore the limitations of existing analytical models formulated with assumptions that neglect or simplify the presence of supported electrical components and supports. Future work will explore in greater depth the additional configurations included in the experimental program and extend the study to other in-service poles with various attachments and boundary conditions to further inform the development of physics-based models for condition assessment.

Acknowledgments This study was performed with financial and logistical support provided by Duke Energy Corporation. In particular, the authors would like to acknowledge on-site technical and logistical contributions provided by Jerry Ivey, Guneet Bedi, Jeremiah Gilbert, Keith Byrne, and Dustin Gregory. The contents of this paper reflect the views of the authors and not necessarily the views of Duke Energy Corporation.

References

1. Budipriyanto, A., Swamidas, S., Adluri, S., and Haldar, A. (2008) "Nondestructive assessment of wood beams using vibration response," *Nondestructive Testing and Evaluation*, 233, 175-193, DOI: 10.1080/10589750701850099.
2. Franklin, D., Murphy, M., and Palylyk, R. (1989) "Apparatus and method for testing wooden poles," (U.S. Patent Number 4,926,691) U.S. Patent and Trademark Office
3. Bandara, S., Rajeev, P., and Gad, E. (2023) "Structural health assessment techniques for in-service timber poles," *Structure and Infrastructure Engineering*, 194, 439-459, DOI: 10.1080/15732479.2021.1951775.
4. Makris, N. and Kalfas, K. (2021) "The eigenvalues of a partially embedded flexural, prismatic column," *Earthquake Engineering and Structural Dynamics*, 503, 1-18, DOI: 10.1002/eqe.3515.
5. Prestage, B. (1997) The In-Service Non-Destructive Evaluation of Wooden Transmission Line Poles, M.S. Thesis, Department of Mechanical Engineering, University of Cape Town, South Africa.
6. Downer, Lee (2010) Detecting damage in beams and structures through modal analysis, M.S. Thesis, Engineering and Applied Sciences, Memorial University of Newfoundland, St. John's, Canada.
7. González de Paz, L, Ortega, N. and Rosales, M. (2018) "Assessment of wood utility poles' deterioration through natural frequency measurements," *Journal of Civil Structural Health Monitoring*, 91, 53-61. DOI: 10.1007/s13349-018-0314-3.
8. Jalali, M. (2021) Development of a vibration-based non-destructive testing method for in-service utility poles, Ph.D. Dissertation, Engineering and Applied Sciences, Memorial University of Newfoundland, St. John's, Canada.
9. Dai, K., Chen, S., Qi, W., Connor, E., Erdle, J., and Galloway, C. (2011) "Field testing of directly embedded poles," *Experimental Techniques*, March/April, 14-23, DOI: 10.1111/j.1747-1567.2009.00595.x.
10. Chen, S. and Dai, K. (2010) "Modal characteristics of two operating power transmission poles," *Shock and Vibration*, 17(4-5), 551-561, DOI: 10.3233/SAV-2010-0547.
11. Juang, J.-N. and Pappa, R. (1985) "An eigensystem realization algorithm for modal parameter identification and model reduction," *Journal of Guidance, Control, and Dynamics*, 85, 620-627, DOI: 10.2514/3.20031

Chapter 11
Preliminary Design of Liquid-Based Damping Systems for Building Motion Control in Wind

Lee, Chien-Shen, McNamara, Kevin, Mills, Matthew J., and Robinson, Jamieson K.

Abstract Supplementary Damping Systems (SDS), such as tuned mass dampers (TMDs), tuned sloshing dampers (TSDs) and tuned liquid column dampers (TLCDs) have been successfully employed to reduce building motions during wind events by dissipating the vibrational energy of the building. A liquid-based damping system known as "Hummingbird damping system" has been developed, which consists of water cylinders and air springs. The water is contained within the cylinder between two flexible membranes that are connected to an air spring. All systems are designed to operate at a natural frequency that is close to the natural frequency of the structural vibration mode to be controlled, and each system is designed to exhibit a specified amount of damping (energy dissipation). As the building moves under dynamic wind loads, the mass of the damping system will begin to move out-of-phase with the motion of the tower and energy is extracted by the integrated energy dissipation devices. A concept design of implementing liquid-based damping systems, including a Hummingbird damping system and TSDs, was developed for a building in Taiwan to reduce wind-induced motion. Unlike traditional damping systems, this TSD system is modular, simplifying both design and installation. The proposed system is found to be an effective and affordable means to reduce the wind-induced resonant response of buildings.

Keywords Tuned mass damper · Tuned sloshing damper · Vibration control · Structural dynamics · Wind engineering

Problem description

Building motions due to wind may affect structural integrity. Furthermore, it could cause discomfort to the building occupants. It becomes a challenge for structural engineers and architects to keep the wind-induced building motion within acceptable limits. Depending on the building surroundings, the building motions can be induced by across-wind excitation by vortex shedding, or through general wind buffeting due to the roughness of the surroundings (Irwin, P. A. 2008).

A 25-story steel structural building is selected as an example for this study. The building is located in a dense urban area adjacent to other towers and is affected by both vortex shedding and buffeting resulting in wind-induced building motions. The signature dynamic effects of the building response due to vortex shedding can be identified through the wind tunnel test results. Figure 1(a) shows an example of the predicted base bending moment of the building for all wind directions based on the wind tunnel test results. At around 110 degrees heading of wind direction, the mean response is near zero, but the peak responses of the positive and negatives reach the maximum, which implies that dynamic effects dominate the response from this wind direction. Figure 1(b) shows the predicted accelerations of the building as a function of the wind direction, and the maximum acceleration also occurs at 110 degrees, as expected, due to the dynamic responses induced by wake buffeting. The predicted peak accelerations exceed the comfort criteria.

Established engineering strategies were employed to mitigate building accelerations, including enhancements to both mass and structural stiffness. Figure 2(a) shows the sensitivity analysis of the building accelerations to its mass and stiffness. It can be observed that increasing mass and/or increasing stiffness (i.e. reducing the building period) can generally reduce the building accelerations for this building.

Lee, Chien-Shen · McNamara, Kevin · Mills, Matthew J. · Robinson Jamieson K.
Motioneering Inc., 600 Southgate Dr, Guelph, ON N1G 4P6 Canada
e-mail: Tom.Lee@motioneering.ca; Kevin.McNamara@motioneering.ca; Matthew.Mills@motioneering.ca; Jamieson.Robinson@motioneering.ca

© The Author(s), under exclusive license to River Publishers 2026

Kristin B. Zimmerman, PhD (eds.), *Dynamics of Civil Structures, 2026, Vol. 2*, Conference Proceedings of the Society for Experimental Mechanics Series, https://doi.org/10.13052/rp-9788743814139

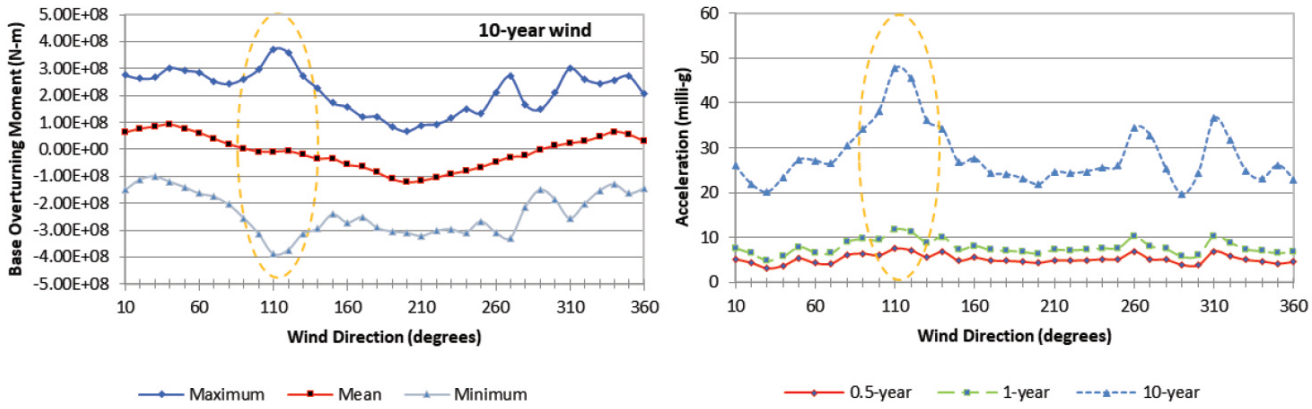

Fig. 1 Example of Wind Responses of the Building (a) base overturning moment (b) acceleration

However, achieving the required 35% reduction in acceleration cannot be effectively accomplished through increases in mass and stiffness alone. Even a 20% increase in mass combined with a 24% reduction in structural period falls short of meeting the performance criteria. Additionally, the structural costs associated with pursuing this approach would be substantial.

While increasing mass and stiffness can help reduce wind-induced accelerations, it also leads to significantly higher seismic design loads. This introduces further complexity and challenges for the structural design, potentially offsetting the benefits gained.

Similarly, Figure 2(b) shows the sensitivity analysis results of the building accelerations to its damping. Increasing the damping from 1% to 2% can reduce the acceleration by approximately 30%.

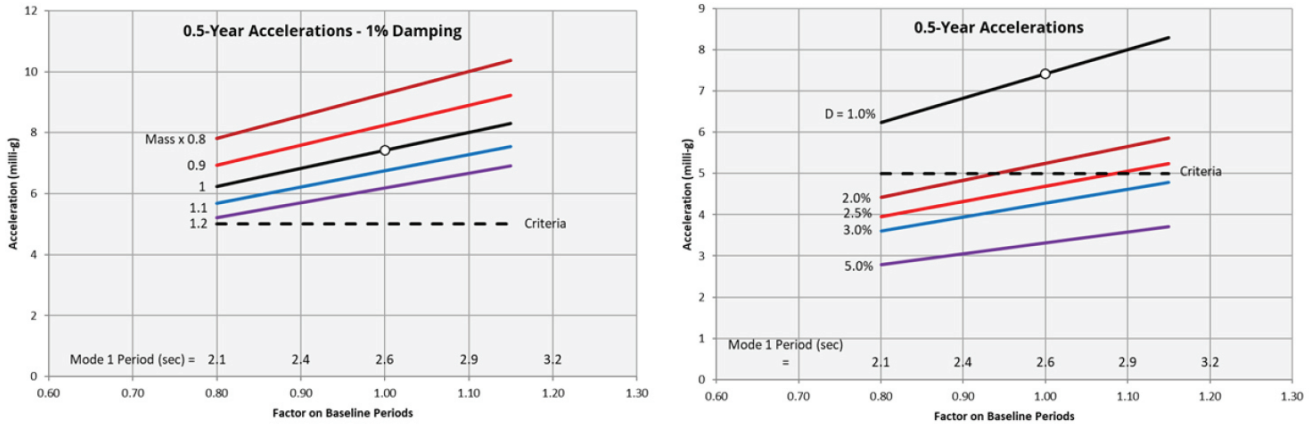

Fig. 2 Example Sensitivity Analysis of Wind Responses of the Building (a) accelerations to mass and period (b) accelerations to damping and period

If the damping can be increased to 2.5%, the resulting reduction in acceleration brings the building's performance within acceptable limits. Enhancing damping through a supplemental damping system offers a practical advantage—it does not require major modifications to the structural system, thereby avoiding the significant costs associated with structural measures aimed at reducing building accelerations.

Given these benefits, the design team has opted to implement a supplemental damping system to effectively control wind-induced building motions.

Solution: Damping system

Supplemental Damping Systems

Tuned types of dampers, such as a tuned mass damper (TMD) and a tuned sloshing damper (TSD), have been implemented in high-rise buildings to reduce wind-induced building motions by providing additional effective damping to the structure (Morava et al. 2012). The damper reduces the building response by moving out of phase with the building motions. As a TMD moves, energy is extracted from the TMD system through its damping mechanism. Similarly, a TSD consists of a tank partially filled with liquid (typically water) and energy dissipation mechanisms. As the structure experiences a resonant response, the liquid in the TSD tank will begin to slosh. Vibrational energy is thereby transferred from the structure to the TSD, where it can be dissipated by the damping mechanisms within the tank.

Hummingbird damper was developed by Thornton Tomasetti in collaboration with the National Aeronautics and Space Agency (NASA) (Ghisbain et al. 2017). The system consists of water cylinders and air springs. It is intended to reduce building movement using the same physics that TMDs and TSDs employ. All systems are designed to operate at a natural frequency close to the natural frequency of the structural vibration mode to be controlled. Each system is designed to exhibit a specified amount of damping (energy dissipation).

Damping System Preliminary Design

The considered design example of a 25-story building has a generalized mass of 4,000 tonnes, an inherent damping ratio of 1% of critical for the acceleration analysis, and a natural vibration period of 2.63 sec (frequency of 0.38 Hz) for the mode of vibration to be controlled. The uncontrolled building acceleration is near 7.5 milli-g (mean peak hourly) at 6-month return period winds. Some space on the roof was allocated for implementing this damping system. The target performance for the damping system is to reduce the acceleration by approximately 35% for 6-month and higher return period winds. The equivalent total damping ratio is expected to be increased from 1.0% to 2.3% of critical damping for the considered return period winds after installing the damping systems.

A damping system combined with TSD and Hummingbird was selected by the design team as the preferred option by considering the building vibration frequency, the available space for the damping system, the ability for installation sometime after the building construction is complete, and the required additional damping. The damping system is comprised of five (5) Tuned Sloshing Dampers (TSDs) and a Hummingbird Damper, as shown in Figure 3. Two (2) bi-directional TSDs are oriented longwise in the X-Direction. Three (3) uni-directional TSDs and the Hummingbird Damper are oriented in the Y-Direction.

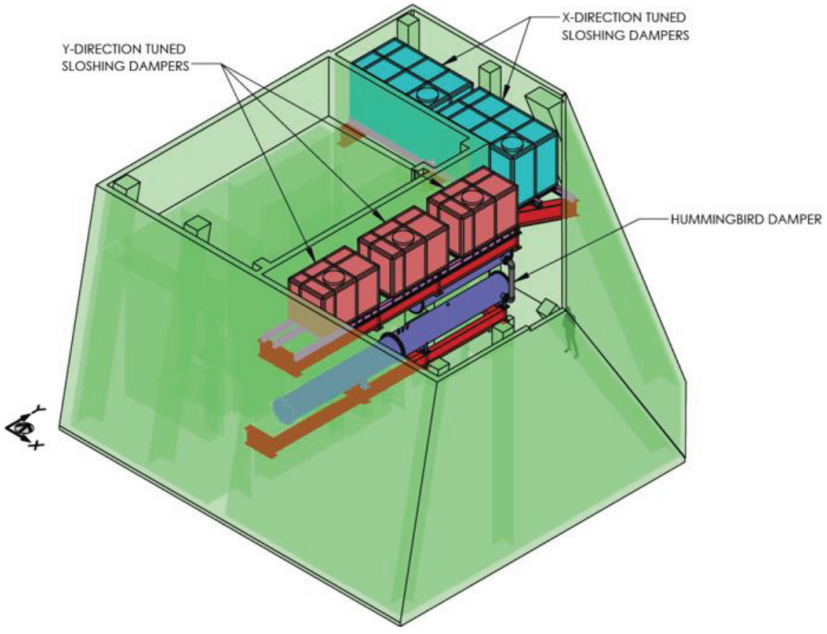

Fig. 3 Overview of Proposed Damping System for the Building

Analytical Modelling of the Damping System with the Building

A single-degree-of-freedom (SDOF) system is used to represent the dynamic response of a structure vibration mode, as defined mathematically by Equation (1). M_s and K_s represent the generalized mass and stiffness of the structural vibration mode, respectively. C_s is the modal damping, and *F(t)* is the generalized force acting on the structure. Stationary wind loads are considered in this study.

$$M_s\ddot{X}_s + C_s\dot{X}_s + K_sX_s = F(t) \tag{1}$$

A damping system can be modelled as an additional mass-spring-damper system attached to the primary structure. The dynamic responses of a structure vibration mode equipped with damping system along Y-direction can be analysed using a 3DOF system as shown in Figure 4, where the coupled equations of motion are:

$$\begin{bmatrix} 1+\mu_{TSD}+\mu_{HB} & \mu_{TSD} & \mu_{HB} \\ \mu_{TSD} & \mu_{TSD} & 0 \\ \mu_{HB} & 0 & \mu_{HB} \end{bmatrix} \begin{pmatrix} \ddot{X}_s \\ \ddot{y}_{TSD} \\ \ddot{y}_{HB} \end{pmatrix} + \begin{bmatrix} 2\zeta_s\omega_s & 0 & 0 \\ 0 & 2\mu_{TSD}\zeta_{TSD}\omega_{TSD} & 0 \\ 0 & 0 & 2\mu_{HB}\zeta_{HB}\omega_{HB} \end{bmatrix} \begin{pmatrix} \dot{X}_s \\ \dot{y}_{TSD} \\ \dot{y}_{HB} \end{pmatrix} + \begin{bmatrix} \omega_s^2 & 0 & 0 \\ 0 & \mu_{TSD}\omega_{TSD}^2 & 0 \\ 0 & 0 & \mu_{HB}\omega_{HB}^2 \end{bmatrix} \begin{pmatrix} X_s \\ y_{TSD} \\ y_{HB} \end{pmatrix} = \begin{pmatrix} \frac{F(t)}{M_s} \\ 0 \\ 0 \end{pmatrix} \tag{2}$$

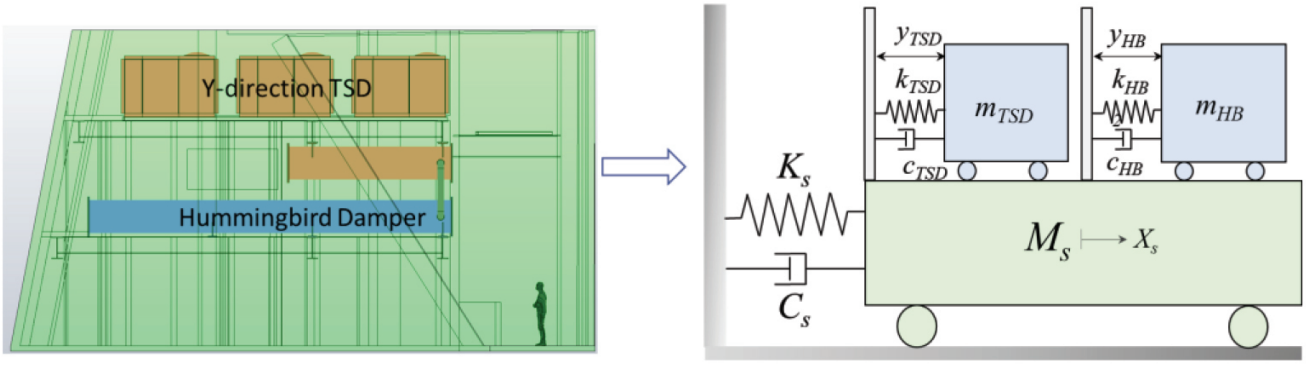

Fig. 4 An illustration of the 3DOF of structure - damping system (Y-direction)

Where X_s is the displacement of the structure and y_{TSD} and y_{HB} are the relative displacement between the centre of mass of the TSD and the Hummingbird damper system and the structure, respectively. In this manner, each damper has a distinct mass, damping constant, stiffness, and relative displacement with respect to the structure. For each damper, the natural angular frequency and damping ratio are defined as:

$$\omega_s = \sqrt{\frac{K_s}{M_s}};\ \omega_{TSD} = \sqrt{\frac{k_{TSD}}{m_{TSD}}};\ \omega_{HB} = \sqrt{\frac{k_{HB}}{m_{HB}}}$$

$$\zeta_s = \frac{C_s}{2\omega_s M_s};\ \zeta_{TSD} = \frac{c_{TSD}}{2\omega_{TSD}m_{TSD}};\ \zeta_{HB} = \frac{c_{HB}}{2\omega_{HB2}m_{HB}}$$

Two mass ratios have been defined for the damping systems:

$$\mu_{TSD} = \frac{m_{TSD}}{M_s};\ \mu_{HB} = \frac{m_{HB}}{M_s}$$

The total mass ratio of the damping system is approximately 0.35%. Multiple-TMD or multiple-TSD theory has been introduced to improve the efficiency of the damping system using spread-tuning, whereby each supplemental damper is tuned to a slightly different frequency close to the target structural frequency (Love and Haskett 2014). Multiple-TSDs have been employed for tall buildings to reduce the building motions induced by winds, and the performance of the damping system

has been verified and reported (Love et al. 2020 and Lee et al. 2021). The damping system can also utilize spread-tuning, where the different damper units are tuned to different frequencies, since it contains two units along each vibration direction.

The optimal parameters are obtained by minimizing the variance of the structural response. The effectiveness of the damping systems can be evaluated using this 3DOF system during the concept design phase. With the wind tunnel data and the structural model for the tower, frequency domain-based analysis and time domain-based simulations are applied to evaluate the performance for the preliminary design. Several iterations were performed to study the nonlinear damping to control high return period amplitudes while maintaining the desired motion reduction performance during common wind events.

Predicted Performance of the Damping System

The damping system performance is assessed by determining the effective damping of the system, ζ_{eff}, which is calculated based on:

$$\zeta_{eff} = \zeta_s \frac{\sigma_{s-0}^2}{\sigma_s^2}$$

where σ_s and σ_{s-0} are the response variances of the structure with and without the damping system, respectively.

The predicted results indicate that the damping system can achieve a total equivalent damping of 2.3% of critical corresponding to 35% of acceleration reduction to meet the 6-month wind comfort criteria. The frequency-domain responses of the building with and without the damping system are shown in Figure 5.

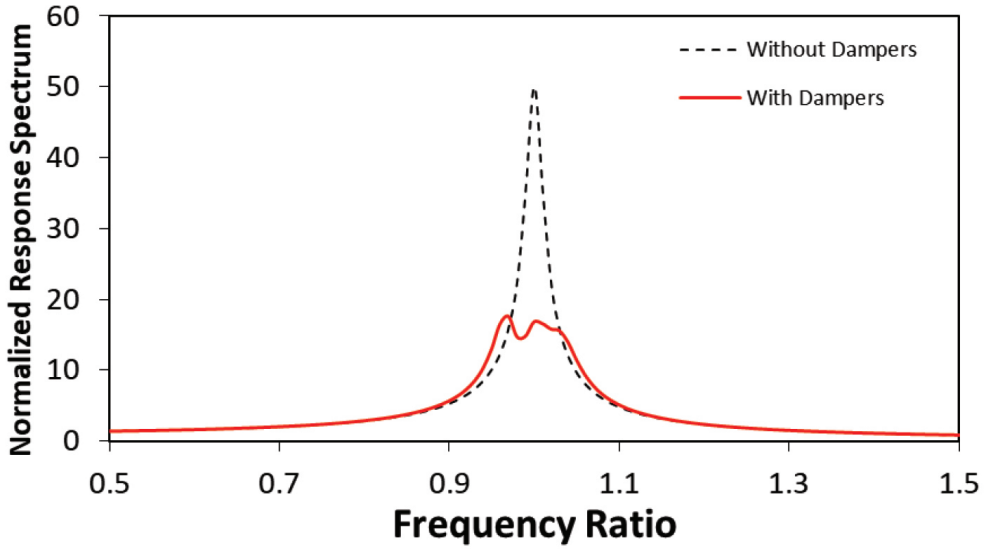

Fig. 5 Frequency domain responses – with and without the damping systems

Conclusion

This study demonstrates the effectiveness of a liquid-based damping system in controlling wind-induced building motion. After a comprehensive evaluation of the building's dynamic characteristics, spatial constraints, and post-construction feasibility, the design team selected a combination of tuned sloshing dampers and a Hummingbird damping system as the optimal solution. A 3DOF numerical model was developed to simulate the interaction between the structure and the damping system, using optimized parameters to assess performance. The results indicate that the proposed system can increase effective structural damping from 1% to 2.3%, successfully reducing building accelerations to meet the 6-month wind comfort criteria. Given its performance, cost-effectiveness, and minimal impact on the structural design, the liquid-based damping system presents a practical and innovative solution for mitigating wind-induced motion in tall buildings.

References

1. Irwin, P. A., 2008. Bluff body aerodynamics in wind engineering. Journal of Wind Engineering and Industrial Aerodynamics 96: 701–712.
2. Morava, B., Haskett T., and Smith, A., 2012. Enhancing the serviceability performance of tall buildings using supplemental damping systems. Ingegneria Sismica, XXIX(1): 60-69.
3. Ghisbain P, Mendes S, Pinto M, Malsch E and Scarangello T., 2017. Design and Commissioning of a New Liquid Damper System for Wind - Induced Vibrations of Buildings. 39th IABSE Symposium – Engineering the Future, Vancouver, Canada.
4. Zuo, L. 2009. Effective and robust vibration control using series multiple tuned-mass dampers. Journal of Vibration and Acoustics, 131.
5. Love, J. S., and Haskett, T. C., 2014. Using Multiple Tuned Sloshing Dampers (MTSDs) with Distributed Tuning for Improved Motion Control of Buildings. 6th World Conference on Structural Control and Monitoring.
6. Lee, C. S., Love, J. S., Haskett, T. C., and Robinson, J. K., 2021. Concept Design of a Parallel-type Tuned Mass Damper- Tuned Sloshing Damper System for Building Motion Control in Wind. International Journal of High-Rise Buildings, Vol 10, No 2, 93-97. https://doi.org/10.21022/IJHRB.2021.10.2.93.

Chapter 12
Modal Identification and MCMC-Based Bayesian Model Updating for Optimization of Material Parameters in Bridges

Sangwon Park and Minwoo Chang

Abstract As the number of aging bridges increases in Korea, the limitations of conventional visual inspection methods—particularly for third-class bridges—are becoming increasingly evident. Many of these structures lack original design drawings, highlighting the need for advanced structural health monitoring (SHM) techniques capable of quantitatively assessing structural integrity. Although image-based monitoring using drones or smartphones has recently gained attention, such methods have fundamental limitations in capturing time-dependent structural responses and internal damage influenced by environmental factors such as temperature. To address these challenges, this study proposes a framework based on Bayesian finite element model updating to identify and update key structural parameters. Ambient vibration and temperature data were collected over an eight-day period from a steel box girder bridge using accelerometers and thermometers. The subspace state-space system identification algorithm (N4SID) was applied to extract major dynamic parameters, including natural frequencies and mode shapes. Subsequently, Bayesian inference based on the Markov Chain Monte Carlo (MCMC) algorithm was employed to update the model while accounting for uncertainties in structural properties. Both natural frequencies and mode shapes were incorporated into the fitness function, with optimized weighting factors and sampling iterations. Furthermore, the choice of prior distribution functions was examined to improve the accuracy of model updating. Through this analysis, we aim to present a practical framework for effectively managing structural uncertainties in bridge condition assessment.

Keywords Structural health monitoring · Markov chain monte carlo · Bayesian model updating · System identification · Long-term monitoring

Introduction

Many bridges constructed during Korea's rapid urbanization have been exposed to decades of repeated traffic loads, harsh environmental conditions, and material deterioration, resulting in gradual degradation of structural performance. In particular, third-class bridges often lack original design drawings, which makes it difficult to quantitatively assess structural behavior over time or to detect internal damage caused by temperature variations using conventional visual inspection methods. As such, there is an increasing need for more systematic and quantitative structural health monitoring (SHM) technologies to ensure the long-term safety and reliability of aging infrastructure. Previous studies have attempted to assess structural condition using drone-based imaging, visual surveys, and time-series analysis. However, these approaches are mostly limited to static or short-term observations and are not well suited to capture long-term nonlinear variations in material properties or structural responses under changing environmental conditions. Furthermore, many of these methods do not account for the uncertainty of structural parameters in a quantitative manner, limiting their applicability in practice.

Sangwon Park
Engineer, Technology Development Center, Saman Corporation,
315, Macheon-ro, Songpa-gu, Seoul, Republic of Korea
e-mail: swpark3@samaneng.com

Minwoo Chang
Associate Professor, Department of Civil and Environmental Engineering,
Myongji University, 116 Myongji-ro, Cheoin-gu, Yongin-si, Gyeonggi-do, 17058 Republic of Korea
e-mail: cmw321@mju.ac.kr

© The Author(s), under exclusive license to River Publishers 2026

Kristin B. Zimmerman, PhD (eds.), *Dynamics of Civil Structures, 2026, Vol. 2*, Conference Proceedings
of the Society for Experimental Mechanics Series, https://doi.org/10.13052/rp-9788743814139

To address these limitations, this study proposes an integrated framework for quantitatively estimating the time-varying dynamic characteristics of bridge bearings under real environmental conditions. For this purpose, eight days of high-frequency ambient vibration and temperature data were collected from a steel box girder bridge located in Gyeonggi Province, South Korea. Modal parameters, including natural frequencies and mode shapes, were extracted using an output-only subspace system identification method based on the Numerical Algorithms for Subspace State-Space System Identification(N4SID) algorithm. A Finite Element (FE) model was constructed to replicate the structural configuration, and its modal properties were compared with the identified data. Based on this comparison, Bayesian model updating was performed using the Markov Chain Monte Carlo (MCMC) algorithm. By simultaneously employing various prior distribution functions (such as normal, Weibull, and lognormal), adjusting the weighting coefficients between the errors in natural frequencies and mode shapes, and ensuring sufficient sampling, the uncertainty inherent in the model updating process could be quantitatively assessed. The proposed framework can be applied to structures with limited design information and serves as a practical alternative to conventional visual inspection methods, providing a solid foundation for systematic maintenance and long-term safety management of aging infrastructure.

Background

Accurate tracking of time-varying structural parameters is essential for assessing the long-term performance of aging bridges, particularly for components like bridge bearings that are highly sensitive to environmental influences. Bearings play a critical role in transferring loads between the superstructure and substructure and are prone to changes in stiffness and Young's modulus due to thermal fluctuations, aging, and material degradation. These variations can alter the global dynamic characteristics of the bridge, such as modal frequencies and mode shapes. Without proper consideration of such time-dependent behavior, modal interpretations may be inaccurate or misleading. Although output-only subspace identification techniques such as N4SID have proven effective in extracting modal parameters from ambient vibration data, the results can be significantly affected by uncontrolled variables especially temperature. In many small- and medium-span bridges, which often lack original design documentation, the effects of environmental conditions on structural dynamics are typically underestimated or neglected in practice. This limitation highlights the need for a continuous monitoring system capable of capturing changes in modal parameters and material characteristics arising from environmental conditions and parameter uncertainty.

To address this challenge, Bayesian model updating has been introduced as an effective method for calibrating FE models by incorporating measured modal data and quantifying the uncertainty of physical parameters. This probabilistic framework allows for the continuous refinement of structural parameters such as bearing stiffness and elastic modulus based on field measurements, even under time-varying operational conditions. Recent efforts have emphasized the importance of selecting appropriate prior distributions and optimizing fitness functions to improve model accuracy and reliability. This study proposes a framework that combines output-only system identification with Bayesian finite element model updating, aiming to enable reliable tracking and updating of structural parameters in bridges. By effectively capturing changes in key dynamic properties such as bearing stiffness and elastic modulus, the proposed approach is expected to provide a more reliable and data-driven basis for structural performance evaluation and maintenance decision-making in bridges.

System Identification and Verification of Bridge Dynamics via FE Modeling

In this study, accelerometers and temperature sensors were installed at key locations of the bridge, as shown in Fig. 1(a), and dynamic responses were measured over a period of eight days at ten-minute intervals. The collected output data were processed using the N4SID algorithm, implemented in the Structural Modal Identification Toolsuite (SMIT). The measured output signals were organized into a block Hankel matrix according to time history, and an oblique projection Q_{Y_f/Y_p} was applied using past and future output matrices to extract modal information. This projection was subsequently decomposed using Singular Value Decomposition (SVD) as follows:

$$Q_{Y_f/Y_p} = U\Sigma V^T \tag{1}$$

In Eq. (1), Σ is a diagonal matrix containing the singular values, each of which represents the energy contribution of a corresponding mode and is used to estimate the system order. The matrices U and V contain the left and right singular vectors, respectively, and are used to transform the data into modal coordinates. A stabilization diagram was then used to select consistent modal responses over time, allowing the extraction of a total of 1,152 modal parameters, including natural frequencies, damping ratios, and mode shapes. As illustrated in Fig. 1(b), the extracted modal parameters were

compared with the results obtained from a finite element model constructed using Midas civil based on the bridge's design specifications, confirming a high degree of similarity between the identified and simulated modal characteristics.

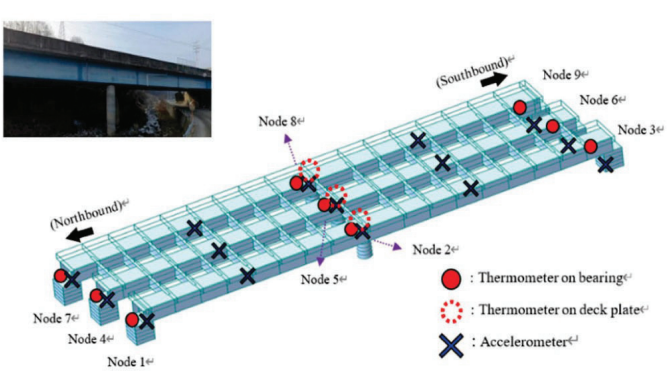

(a) Overview of Deokpyeong 1 bridge and sensor locations

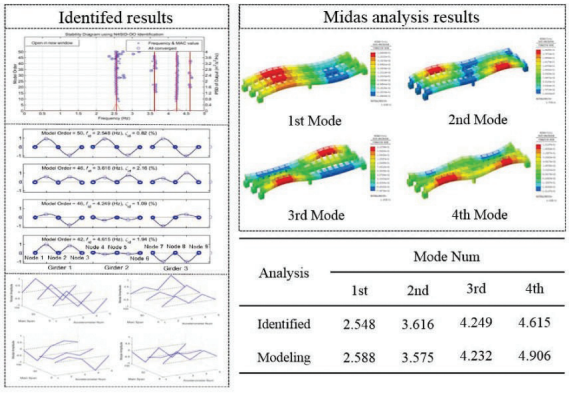

Analysis	Mode Num			
	1st	2nd	3rd	4th
Identified	2.548	3.616	4.249	4.615
Modeling	2.588	3.575	4.232	4.906

(b) Identified modal parameters

Fig. 1 Sensor configuration of Deokpyeong 1 Bridge and comparison between identified and finite element modal results

MCMC based bayesian FE model updating

Bayesian model updating aims to reduce the discrepancy between measured data and the analytical model by estimating uncertain structural parameters. In this study, the posterior distribution of the parameters is derived by combining the prior distribution with the likelihood function based on modal properties such as natural frequencies and mode shapes. The posterior probability is given by:

$$p(\theta \mid K) \propto p(K \mid \theta) \cdot p(\theta) \tag{2}$$

In Eq. (2), $p(\theta)$ is the prior distribution and $p(K \mid \theta)$ is the likelihood function representing the probability of observing the measured data given a parameter set θ. The likelihood is expressed as an exponential function of the fitness function $J(\theta)$, which quantifies the mismatch between measured and simulated modal responses.

$$p(K \mid \theta) = c_0 exp\left(-\frac{1}{2k^2} J(\theta)\right) \tag{3}$$

In Eq. (3), c_0 is a normalization constant that ensures the total value of the probability density function integrates to 1. The term k^2 represents the error variance, which controls the degree of sensitivity to modeling error. The function $J(\theta)$ is a fitness function used to quantitatively evaluate how well the predicted model matches the observed data. To efficiently sample from the posterior distribution defined in Eq. (2), the MCMC method is employed. Specifically, the Metropolis–Hastings algorithm is used to explore the parameter space by generating candidate values based on a proposal distribution and probabilistically accepting or rejecting them. The acceptance probability is calculated as follows:

$$p\left(\theta^* \mid \theta^t\right) = min\left(1, \frac{p(\theta^* \mid K)\, q(\theta^t \mid \theta^*)}{p(\theta^t \mid K)\, q(\theta^* \mid \theta^t)}\right) \tag{4}$$

In Eq. (4), $p(\theta^* \mid K)$ denotes the posterior probability of the proposed parameter value θ^*given the observed data K while $q(\theta^t \mid \theta^*)$ is the proposal distribution that represents the probability of transitioning back to the current value θ^t from the candidate θ^*. The denominator $p(\theta^t \mid K)\, q(\theta^* \mid \theta^t)$ reflects the probability of the current state and the likelihood of proposing θ^* from it. The acceptance probability is thus determined by the relative plausibility of the proposed and current parameter values, enabling efficient exploration of the parameter space even when the posterior distribution is complex or analytically intractable.

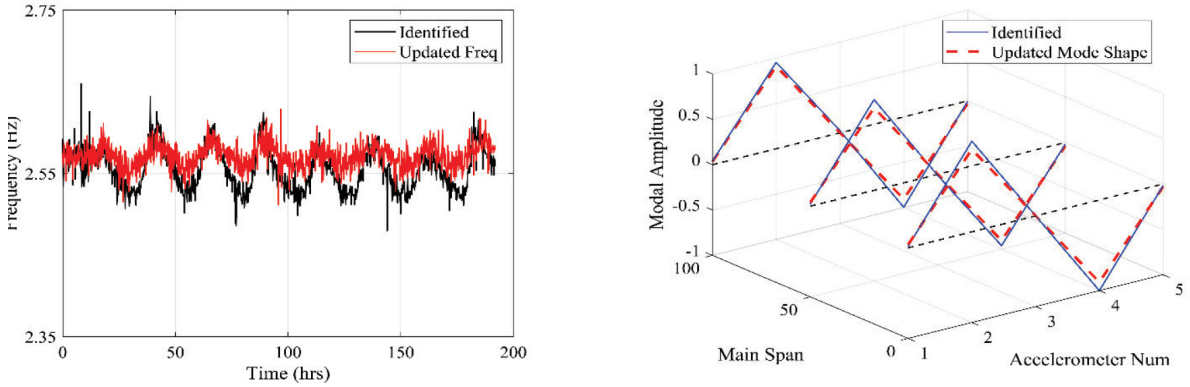

(a) 1st mode natural frequency and shape

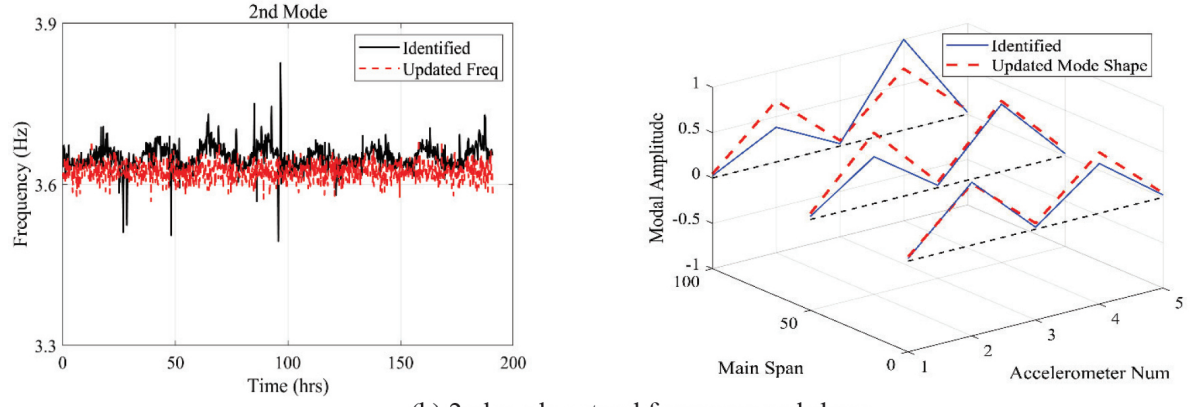

(b) 2nd mode natural frequency and shape

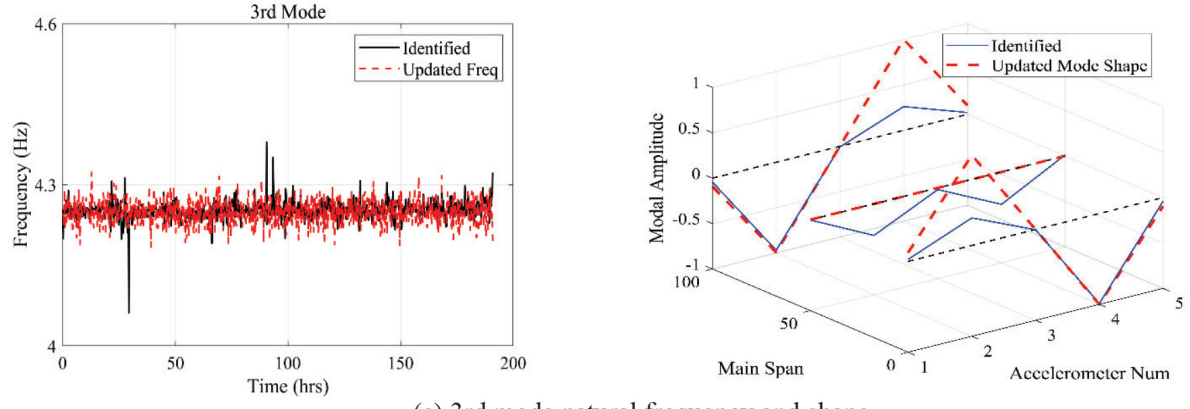

(c) 3rd mode natural frequency and shape

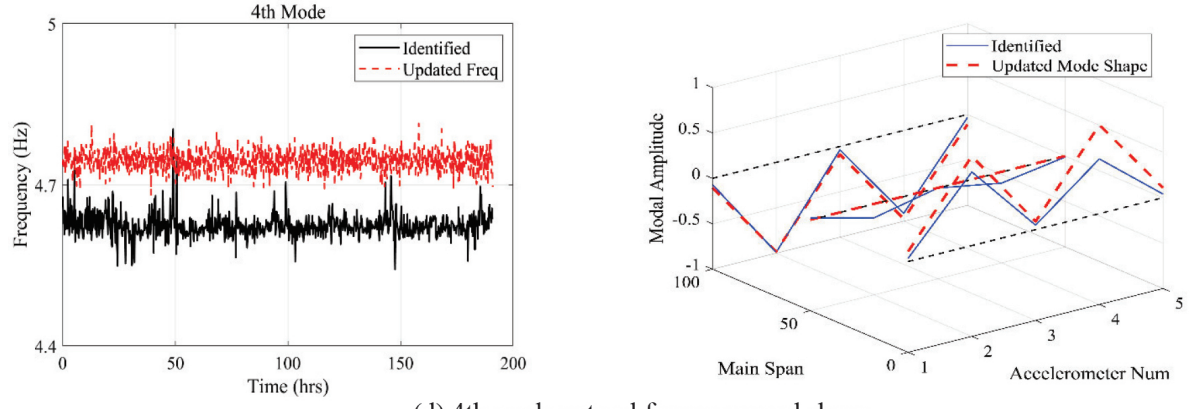

(d) 4th mode natural frequency and shape

Fig. 2 Comparison of FE Model updating results with measured natural frequencies and Mode Shapes

The proposed framework for updating bearing stiffness and Young's modulus

To quantitatively compare the differences between measured and simulated modal responses, this study defines a fitness function based on natural frequencies and mode shapes. The fitness function is expressed as:

$$J(\theta) = \alpha \sum_{i=1}^{m} \left(\frac{v_i^{obs} - v_i^{sim}(\theta)}{v_i^{obs}} \right)^2 + \beta \sum_{i=1}^{m} (1 - MAC_i(\theta)) \tag{5}$$

In Eq. (5), v_i^{obs} and $v_i^{sim}(\theta)$ denote the observed and simulated natural frequencies for the i-th mode, respectively, and $MAC_i(\theta)$ represents the modal assurance criterion (MAC) value for the i-th mode. The coefficients α and β are weighting factors for natural frequency and mode shape, respectively. These weighting factors were adjusted to various values to optimize the fitness function, and the effects of different weightings on the model updating results were analyzed. The number of considered modes is represented by m. This fitness function $J(\theta)$ is incorporated into the likelihood term of the Bayesian posterior distribution and is used to determine sample acceptance in the Metropolis-Hastings MCMC algorithm. Lower values of $J(\theta)$ indicate higher consistency between the simulated and identified modal parameters.

In the Bayesian model updating framework, the prior distribution mathematically expresses pre-existing uncertainty in structural parameters before measured data are incorporated. While the Gaussian distribution is widely used, this study also employed alternative distributions such as Weibull and lognormal distributions to evaluate their impact on probabilistic parameter representation and estimation. The probability density function of the Weibull distribution is defined as:

$$f(\xi; \lambda, \eta) = \frac{\eta}{\lambda} \left(\frac{\xi}{\lambda} \right)^{\eta - 1} e^{-\left(\frac{\xi}{\lambda}\right)^{\eta}}, \quad \xi \geq 0 \tag{6}$$

In Eq. (6), ξ a structural parameter such as bearing stiffness or Young's modulus. λ and η are the scale and shape parameters of the distribution, respectively. This distribution is suitable for modeling skewed uncertainty in positive-valued parameters. The probability density function of the lognormal distribution is given by:

$$f(\tau; \mu, \sigma) = \frac{1}{\tau \sigma \sqrt{2\pi}} e^{\left(-\frac{(ln\tau - \mu)^2}{2\sigma^2} \right)}, \quad \tau \geq 0 \tag{7}$$

In Eq. (7), μ and σ are the mean and standard deviation of the underlying normal distribution for $ln\tau$. The lognormal distribution is useful for modeling physical quantities that are strictly positive and exhibit multiplicative variability.

Table 1 Bayesian model updating results under different hyperparameter settings

Hyperparameter set	Configuration	RMSE				MAC			
		1st	2nd	3rd	4th	1st	2nd	3rd	4th
Distribution function ($\alpha = 0.5, \beta = 0.5$)	normal (suggested)	0.044	0.039	0.027	0.124	0.996	0.760	0.698	0.949
	Weibull	0.051	0.268	0.207	0.212	0.980	0.865	0.775	0.895
	lognormal	0.028	0.144	0.048	0.041	0.992	0.782	0.729	0.927
Fitness function weight coefficient (normal distribution)	$\alpha = 1, \beta = 0$	0.043	0.031	0.024	0.135	0.995	0.761	0.698	0.951
	$\alpha = 0.8, \beta = 0.2$	0.038	0.033	0.024	0.133	0.996	0.761	0.698	0.951
	$\alpha = 0.2, \beta = 0.8$	0.037	0.032	0.025	0.132	0.996	0.759	0.699	0.950
	$\alpha = 0, \beta = 1$	0.043	0.035	0.029	0.135	0.996	0.761	0.699	0.951

Conclusion

This study proposed an integrated framework that combines consecutive system identification and Bayesian finite element model updating to quantitatively assess key structural parameters of a steel box girder bridge under in-situ conditions. Using

8 days of measured vibration and temperature data, a total of 1,152 modal parameters including natural frequencies and mode shapes were extracted via the N4SID algorithm and used for FE model calibration as illustrated in Fig. 2. To account for the uncertainty of physical parameters, a Bayesian model updating strategy based on the Metropolis Hastings MCMC algorithm was adopted. The prior distributions for bearing stiffness and Young's modulus were configured using Normal, Weibull, and lognormal forms. In addition, the fitness function was designed to balance modal frequencies and mode shapes with equal weighting, and the sensitivity to modeling errors was controlled by a fixed tolerance factor.

The analysis showed that the baseline configuration (normal prior, $\alpha = 0.5$, $\beta = 0.5$) produced low RMSE and high MAC values for the first and fourth modes, indicating reliable agreement between the updated and measured modal properties (Table 1). However, for the second and third modes, MAC values were relatively low, while the application of the Weibull prior notably improved MAC in these modes but resulted in significantly higher RMSE, suggesting that improvements in mode shape agreement can come at the expense of frequency prediction accuracy depending on the chosen prior. The lognormal prior yielded results similar to or slightly better than the baseline in certain modes, but overall differences were not substantial. Adjusting the weighting coefficients in the fitness function did not significantly affect the RMSE or MAC values, indicating that both natural frequency and mode shape information are important in the model updating process.

While the proposed framework demonstrated high accuracy, its practical real-time application may be limited by the high sensor density and computational demand. Future research should focus on enhancing efficiency, generalizability, and robustness to incomplete data by incorporating techniques such as data augmentation, uncertainty filtering, and adaptive model calibration. These advancements are expected to broaden the applicability of the framework for structural health monitoring across diverse bridge types.

Acknowledgments This work was supported by the National Research Foundation of Korea (NRF) grant funded by the Korea government (MSIT) (No. 2025-00516404).

References

1. Andrieu, C., & Thoms, J. (2008). A tutorial on adaptive MCMC. *Statistics and Computing, 18*, 343-373. https://doi.org/10.1007/s11222-008-9110-y
2. Aria, M., & Akbari, R. (2013). Inspection, condition evaluation and replacement of elastomeric bearings in road bridges. *Structure and Infrastructure Engineering*, *9*(9), 918-934. https://doi.org/10.1080/15732479.2011.638171
3. Biondini, F., & Frangopol, D. M. (2016). Life-cycle performance of deteriorating structural systems under uncertainty. *Journal of Structural Engineering*, *142*(9), F4016001. https://doi.org/10.1061/(ASCE)ST.1943-541X.0001544
4. Chang, M., Leonard, R. L., & Pakzad, S. N. (2012). Structural modal identification toolsuite (SMIT) user's guide. *Lehigh University*, Bethlehem, PA
5. Chang, M., & Pakzad, S. N. (2014). Modal parameter uncertainty quantification using PCR implementation with SMIT. *In Model Validation and Uncertainty Quantification, Volume 3: Proceedings of the 32nd IMAC, A Conference and Exposition on Structural Dynamics*, 2014 (pp. 185-193). Springer International Publishing
6. Chang, M. (2018). Application studies on structural modal identification toolsuite for seismic response of shear frame structure. *Journal of the Earthquake Engineering Society of Korea*, 22(3), 201-210. https://doi.org/10.5000/EESK.2018.22.3.201
7. Chen, R., & Ni, Y. Q. (2023). A nonparametric bayesian approach for bridge reliability assessment using structural health monitoring data. *Structural Control and Health Monitoring*, *2023*(1), 9271433. https://doi.org/10.1155/2023/9271433
8. Cunha, Á., & Caetano, E. (2005). From input-output to output-only modal identification of civil engineering structures. In *1st International Operational Modal Analysis Conference (IOMAC)*. https://hdl.handle.net/10216/71418
9. Dutta, C., Kumar, J., Das, T. K., & Sagar, S. P. (2021). Recent advancements in the development of sensors for the structural health monitoring (SHM) at high-temperature environment: A review. *IEEE Sensors Journal, 21*(14), 15904-15916. https://doi.org/10.1109/JSEN.2021.3075535
10. Garcia-Palencia, A. J., & Santini-Bell, E. (2014). Structural model updating using dynamic data. *Journal of Civil Structural Health Monitoring, 4*, 177-194. https://doi.org/10.1007/s13349-014-0073-8
11. Keshmiry, A., Hassani, S., Mousavi, M., & Dackermann, U. (2023). Effects of environmental and operational conditions on structural health monitoring and non-destructive testing: A systematic review. *Buildings, 13*(4), 918. https://doi.org/10.3390/buildings13040918
12. Liu, X., Qiao, S. F., Chen, H., Tang, M. X., He-Song, H., & Zhu, Y. (2023). Prediction method of structural health monitoring data based on CNN-LSTM. In *Advances in Frontier Research on Engineering Structures Volume 2* (pp. 309-318). CRC Press. https://doi.org/10.1201/9781003363217-39
13. Ni, Y. Q., Ye, X. W., & Ko, J. M. (2012). Modeling of stress spectrum using long-term monitoring data and finite mixture distributions. *Journal of Engineering Mechanics*, *138*(2), 175-183. https://doi.org/10.1061/(ASCE)EM.1943-7889.00003
14. Midas (2018). Civil On-line Manual – Civil structure design system.
15. Park, S., Chang, M., & Yazdanpanah, O. (2025) "A condition monitoring of steel box girder bridges based on consecutive system identification and model updating using a long-term monitoring database", *Structures*, 80, 109779. https://doi.org/10.1016/j.istruc.2025.109779
16. Rocchetta, R., Broggi, M., Huchet, Q., & Patelli, E. (2018). On-line Bayesian model updating for structural health monitoring. *Mechanical Systems and Signal Processing, 103*, 174-195. https://doi.org/10.1016/j.ymssp.2017.10.015

17. Van Overschee, P., & De Moor, B. (1994). N4SID: Subspace algorithms for the identification of combined deterministic-stochastic systems. *Automatica*, 30(1), 75-93. https://doi.org/10.1016/0005-1098(94)90230-5
18. Xia, H. W., Ni, Y. Q., Wong, K. Y., & Ko, J. M. (2012). Reliability-based condition assessment of in-service bridges using mixture distribution models. *Computers & Structures*, *106*, 204-213. https://doi.org/10.1016/j.compstruc.2012.05.003
19. Zhang, H., Wang, L., & Liu, Y. (2025). A hybrid model-based and data-driven method for mechanical-thermal dynamic load identification considering multi-source uncertainties. Computer Methods in Applied Mechanics and Engineering, 435, 117662. https://doi.org/10.1016/j.cma.2024.117662

Chapter 13
Impact of Support Settlement on the Seismic Fragility of a Substandard RC Frame with Plan Irregularity: Static Response and Fragility Assessment

Feras Abla, Shahin Huseynli, Ufuk Yazgan, and Onur Avci

Abstract Substandard reinforced-concrete (RC) buildings in seismic regions are susceptible to damage and collapse, particularly when differential foundation settlements coexist with earthquake excitation. This paper examines how support settlements alter (i) the gravity-load static response, and (ii) the seismic fragility of a three-story, plan-irregular, substandard RC frame (the SPEAR frame). A non-linear 3D OpenSees model is developed using fiber sections, plastic-hinge beam-column elements, and material constitutive laws calibrated to experimental data. Settlement scenarios (1, 2, and 3 cm) are imposed along axes X1, Y1, and simultaneously X1Y1. Gravity-only static analyses reveal pronounced axial-force and curvature/shear demand shifts in columns and beams near the settled axes and in the perpendicular framing direction. For 3 cm settlement, axial force in the critical interior column rises by up to 84% (two-axis case), and beam ends perpendicular to settlement reach or exceed yield curvature under gravity alone. Incremental Dynamic Analyses (IDA) and strain-based damage checks indicate that 1 cm settlement is sufficient to trigger slight damage even without seismic action; at 3 cm, the median collapse capacity drops by up to 9% depending on the settlement pattern. Findings underscore that settlement must be explicitly considered in performance assessments of substandard RC structures.

Keywords Differential settlement · Fragility analysis

Introduction

Substandard (RC frames in seismically active regions remain highly vulnerable to ground shaking. Past earthquakes, such as the 1999 Kocaeli and Düzce events in Turkiye, highlighted the poor performance of such structures, where noncompliance with seismic design codes led to widespread collapse [1]. These deficiencies are often tied to poor-quality materials, weak-column/strong-beam mechanisms, soft stories, and inadequate detailing, all of which significantly reduce seismic resilience. Differential support settlement compounds this vulnerability. Settlements can result from excavation activities, soil

Feras Abla(✉)
Graduate Student, Department of Civil and Environmental Engineering, Engineering Sciences Building, 1306 Evansdale Drive, West Virginia University, Morgantown, WV 26506
e-mail: fa00060@mix.wvu.edu

Shahin Huseynli
Postgraduate Researcher, School of Civil, Aerospace and Design Engineering, University of Bristol, Bristol, United Kingdom
e-mail: shahin.huseynli@bristol.ac.uk

Ufuk Yazgan
Professor, Disaster Management Institute, Istanbul Technical University, Istanbul, Turkey 34000
e-mail: ufukyazgan@itu.edu.tr

Onur Avci
Assistant Professor, Department of Civil and Environmental Engineering, Engineering Sciences Building, 1306 Evansdale Drive, West Virginia University, Morgantown, WV 26506
e-mail: onur.avci@mail.wvu.edu

© The Author(s), under exclusive license to River Publishers 2026

Kristin B. Zimmerman, PhD (eds.), *Dynamics of Civil Structures, 2026, Vol. 2*, Conference Proceedings of the Society for Experimental Mechanics Series, https://doi.org/10.13052/rp-9788743814139

liquefaction, or poor soil conditions, and when combined with seismic actions, they introduce additional flexural and shear demands that conventional assessment methods often overlook.

Several studies have investigated the impact of differential settlement on structural response. Early works [2, 3, 4] examined tolerance levels of buildings to settlement induced by their own weight, using deflection ratio and angular distortion as indicators. Later research expanded to excavation-induced settlements, showing that geometry and soil–structure interaction strongly influence stress redistribution in RC frames [5, 6, 7]. In seismic contexts, studies found that liquefaction-induced settlements significantly affect the vulnerability of substandard RC buildings [8, 9], with settlement-induced stresses accelerating progression toward damage states. More recently, [10, 11] demonstrated that settlement reduces collapse capacity in both RC and steel frames, with reductions of up to 15% reported for heavy damage states.

Against this backdrop, the present study examines the combined effect of settlement and seismic loading on the fragility of a substandard RC frame with plan irregularity. By focusing on static redistribution and seismic fragility analyses, it highlights how even modest support settlements can significantly alter internal force distributions, reduce displacement capacities, and increase collapse probabilities.

Case Study Building and Numerical Model

The SPEAR Frame

The case study is the full-scale, three-story SPEAR frame shown in Figure 1, which was pseudo-dynamic tested in full-scale at the European Laboratory for Structural Assessment (ELSA) at Ispra, Italy within the project of Seismic Performance Assessment and Rehabilitation of Existing Buildings (SPEAR). The frame is a gravity-designed, plan-irregular, and substandard RC building representative of poor seismic detailing building. Typical deficiencies include plain bars, sparse/poor stirrup detailing without 135° hooks, lap splices at column ends, strong-beam/weak-column proportions, and irregular plan geometry. Story height is 3.0 m (2.5 m clear), columns are predominantly 250×250 mm except one 250×750 mm wall-like column; beams are 250 mm web with 500 mm total depth including slab.

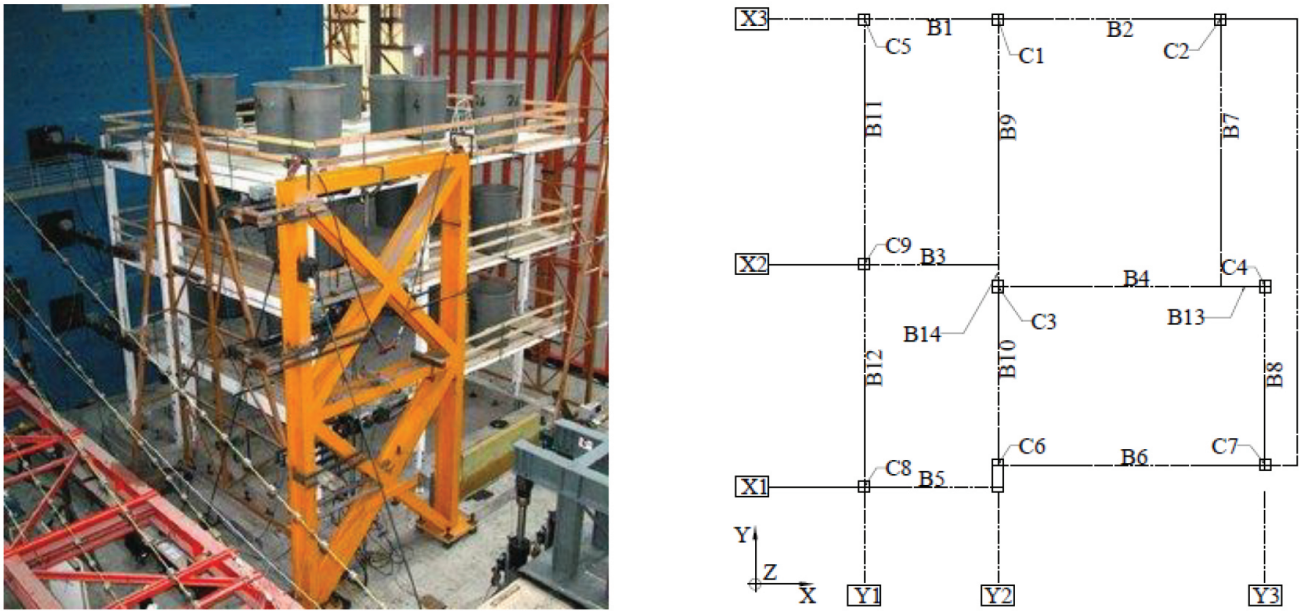

Fig. 1 SPEAR frame pseudo-dynamic test set up (a) (Courtesy [12]) and SPEAR frame layout (b).

Finite-Element Model

A three-dimensional OpenSees model (OpenSeesPy) [13] was developed to represent the substandard RC frame. Fiber sections were used to capture uniaxial material behavior, with beams modeled as T-sections according to an effective flange rule per span to account for slab participation. Torsional rigidity of the beams was increased to better reflect actual stiffness. Beam–column elements were modeled using beamWithHinges with Priestley-type plastic hinge lengths and Radau integration, except for element B14 where Gauss–Lobatto integration was adopted. P-Δ effects were incorporated, and rigid diaphragms were assigned at each floor level with the center of mass as the master node. Material behavior was simulated using Concrete04 for the confined core, Concrete02 for the unconfined cover, and the Giuffré–Menegotto–Pinto steel model with isotropic hardening for reinforcement [14]. To approximate bar slip and strain penetration effects observed in experiments, the steel initial tangent was reduced and hinge lengths were extended, reflecting premature cracking at joints. The applied loads included self-weight and tributary distributed loads, while lumped masses and mass moments of inertia were assigned to story centers of mass according to experimental data. Model validation demonstrated that the simulations successfully reproduced key experimental observations under bi-directional pseudo-dynamic testing, including peak third-story displacements (Figure 2) and story-drift envelopes, with acceptable bias in both principal directions.

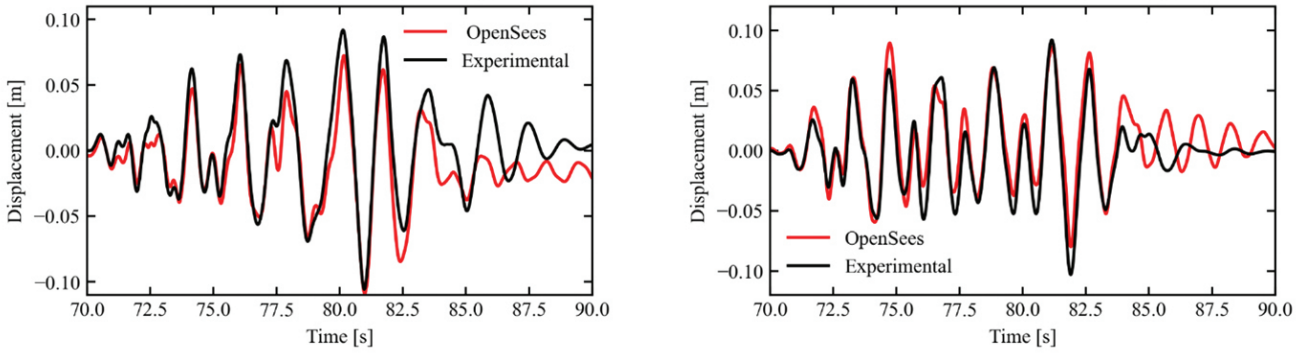

Fig. 2 The displacement time histories at the CM of the third story in both X (a) and Y (b) directions for PGA= 0.2g test.

Settlement Scenarios

Rigid-support vertical constraints are modified to impose settlements of 1, 2, and 3 cm along: (i) X1, (ii) Y1, and (iii) X1Y1 (two axes simultaneously). Gravity is applied in small increments to promote convergence with settlement-induced incompatibilities.

Analysis Method

Static Analysis under Gravity Loads

Gravity loads are applied with linear time series and small load steps using Newton iterations on a band-general solver with RCM numbering. Settlements are introduced via single-point constraints on base nodes of the targeted axes. Recorders capture axial forces in columns and curvature/shear demands at beam ends. Results are compared against the baseline (no settlement).

Fragility Assessment via IDA

IDA is conducted after gravity loads are established (held constant). Suites of ground motions are applied bi-directionally through uniform excitation with Newmark integration and Rayleigh damping. Damage states are defined using strain-based criteria consistent with low-ductility detailing (e.g., steel yield, concrete spalling at ε_c = 0.002, and ultimate concrete ε_c = 0.004 or shear failure for columns). For each settlement scenario, the fraction of records exceeding a limit state at intensity

measure (IM) levels is fit with a lognormal fragility (parameters by maximum likelihood), yielding median θ and dispersion β for slight (steel yielding), moderate (concrete spalling), and collapse (concrete crushing) damage thresholds.

Results: Static Redistribution under Settlement

Baseline (No Settlement)

Gravity-only demands concentrate axial force in the interior column (C3); soft-edge columns (X3/Y3) carry appreciable load. Beams show notable shear-capacity utilization in select spans even without settlement, but curvature demands remain well below ultimate capacities.

X1 Settlement

Figures 3a–3b illustrate the redistribution of internal forces in the beams under X1 settlements of 1–3 cm. The results highlight that settlement along this axis produces progressive increases in demand-to-capacity ratios for both yield curvature and shear forces, particularly in beams connected to or adjacent to the settled frame. The heatmap in Figure 3a shows that beams B8, B10, and B12 experience the sharpest rise in curvature demands. At 3 cm, the exceedance becomes critical, with B8 surpassing its yield curvature by over threefold, and B12 approaching similar levels. Shear demands (Figure 3b) also

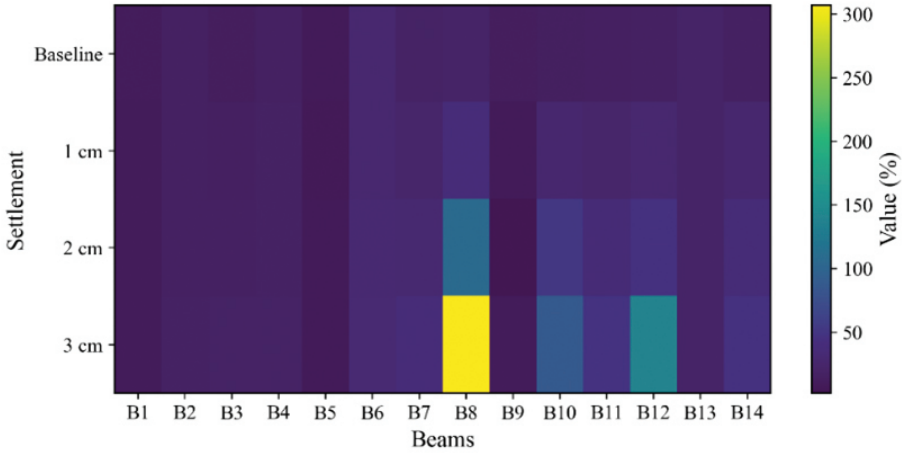

(a)

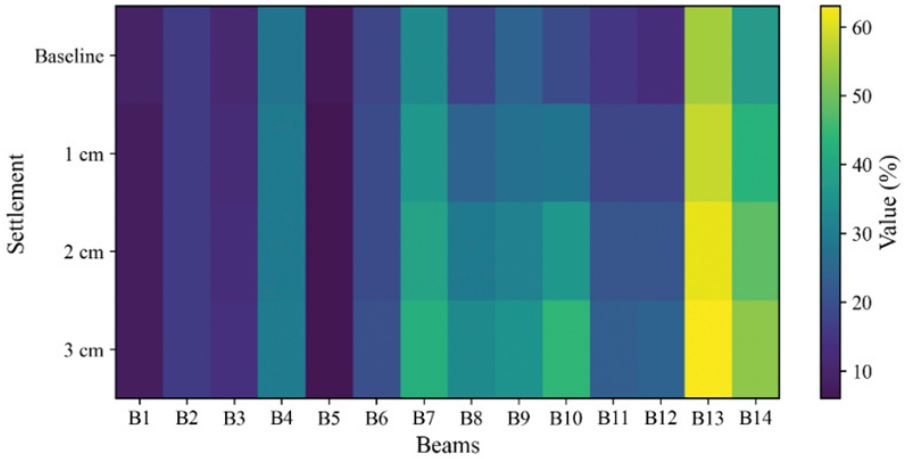

(b)

Fig. 3 Demand to capacity ratios for yield curvature (a), and shear force (b) for the X= 1–3 cm

escalate significantly; B13 and B14, already highly stressed in the baseline case, reach more than half of their shear capacity at 2 cm and continue to rise with increased settlement. Figure 4 further illustrates how the axial force ratios in columns redistribute, with C3 absorbing a much larger share of load, while columns in the settled frame (C6–C8) lose axial load, some dropping close to tension. This shift reduces ductility in C3 and C4 but enhances curvature capacity in the unloaded columns. Overall, the X1 settlement scenario demonstrates a clear concentration of demands on beams spanning between settled and adjacent frames, with a corresponding imbalance in axial load distribution across columns.

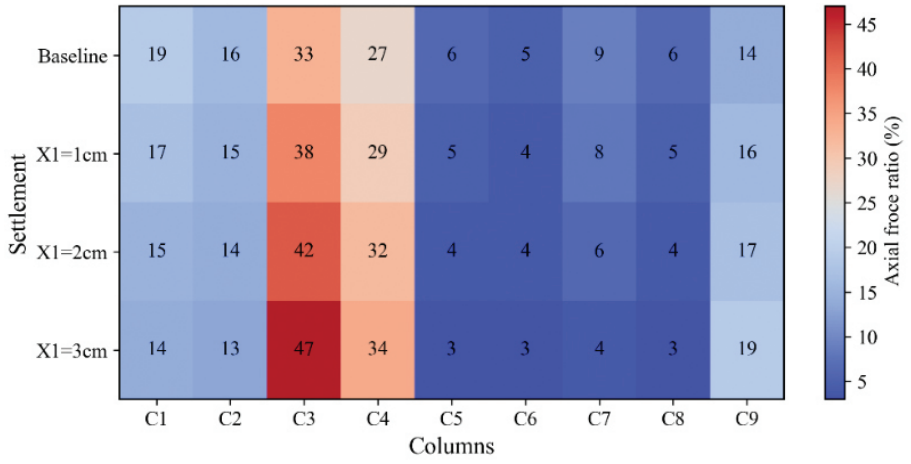

Fig. 4 Axial force ratio for X= 1–3 cm

Y1 Settlement

The redistribution pattern for the Y1 settlement scenario is presented in Figures 5a– 5b. Compared to the X1 case, settlements along Y1 exert more severe effects on beams aligned in the X-direction. As shown in Figure 5a, curvature demands on beams B1, B3, and B5 rise sharply, surpassing their yield capacities at 2 cm and 3 cm settlements. By 3 cm, B1 and B5 reach nearly four times their capacity. In terms of shear (Figure 5b), beams such as B4 and B14 approach critical demand levels, showing steep growth relative to the baseline. Column behavior is summarized in Figure 6, where the redistribution is evident: C1 and C3 accumulate higher axial loads, reducing their ultimate curvature capacities, while columns in the settled frame (C5 and C8) transition into tension. This redistribution reflects the asymmetry of the settlement influence, where beams orthogonal to the settlement axis suffer disproportionate increases in demand.

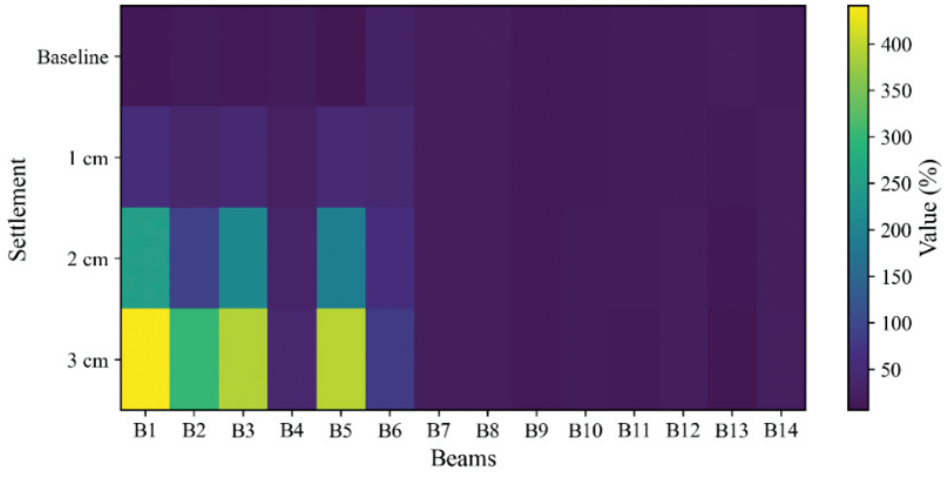

(a)

Fig. 5 *Continued*

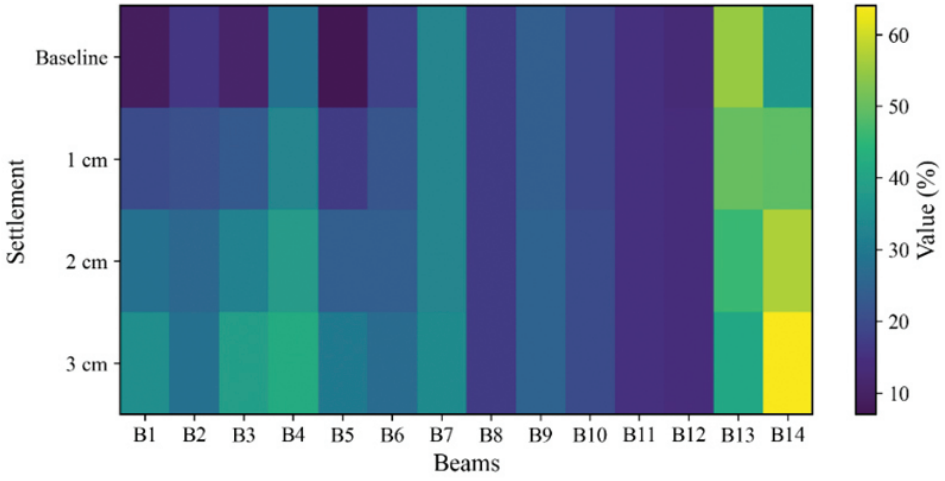

(b)

Fig. 5 Demand to capacity ratios for yield curvature (a), and shear force (b) for the Y= 1–3 cm

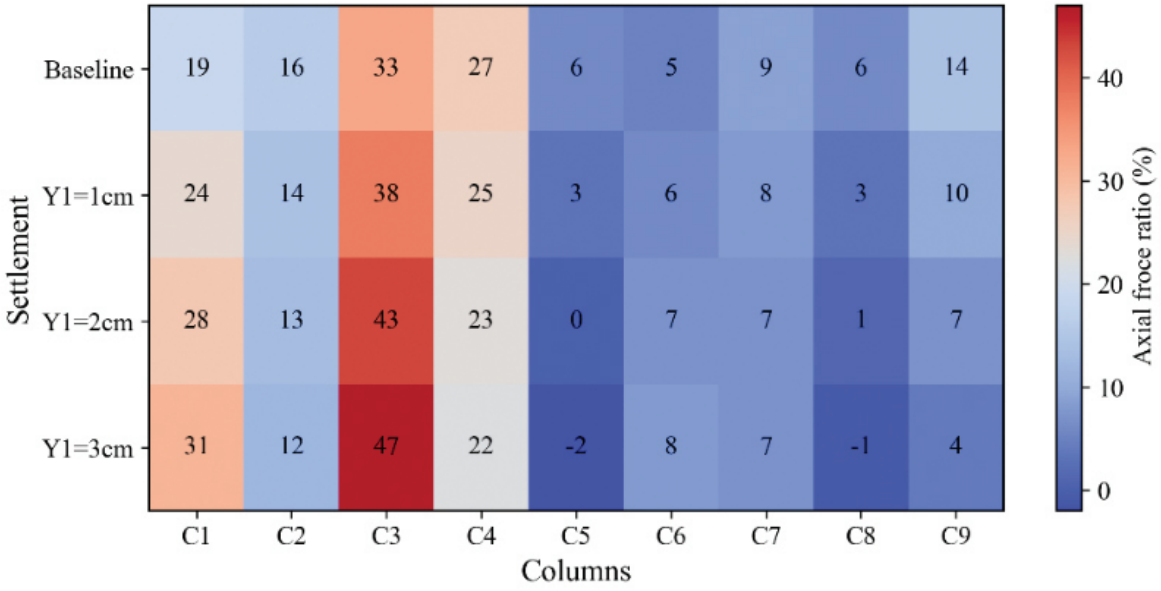

Fig. 6 Figure 4: Axial force ratio for Y= 1–3 cm.

X1Y1 Settlement (Two Axes)

Figures 7a– 7b display the combined settlement scenario where both X1 and Y1 frames undergo settlement simultaneously. This case produces the most severe redistributions, with both X- and Y-spanning beams heavily affected. Yield curvature demands (Figure 7a) are particularly critical in B1, B3, B8, and B10. At 3 cm settlement, B3 shows an eightfold exceedance of its yield capacity, while B8 and B10 also reach extreme levels. Shear demands (Figure 7b) rise steeply, especially in beams B1, B3, and B14, with B14 consuming up to 78% of its shear capacity. Figure 8 illustrates column axial redistribution: C3 becomes increasingly overloaded (approaching 60% axial force ratio at 3 cm), while several columns in the settled frames (C5, C6, C9) drop into near-zero or tensile loads. These shifts markedly reduce ductility in C3 while enhancing it in unloaded columns. The dual settlement case demonstrates how simultaneous differential settlements can push multiple members—both beams and columns—closer to critical states, magnifying the vulnerabilities observed in single-axis settlement scenarios

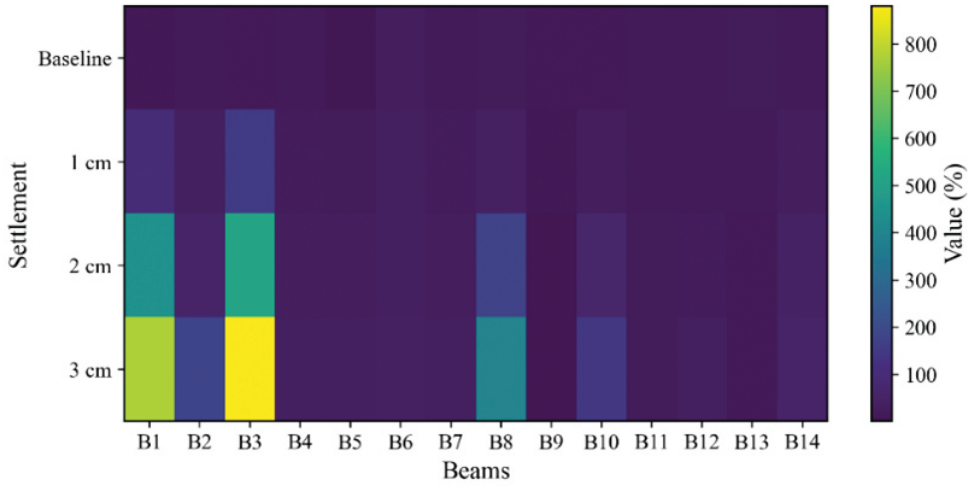

(a)

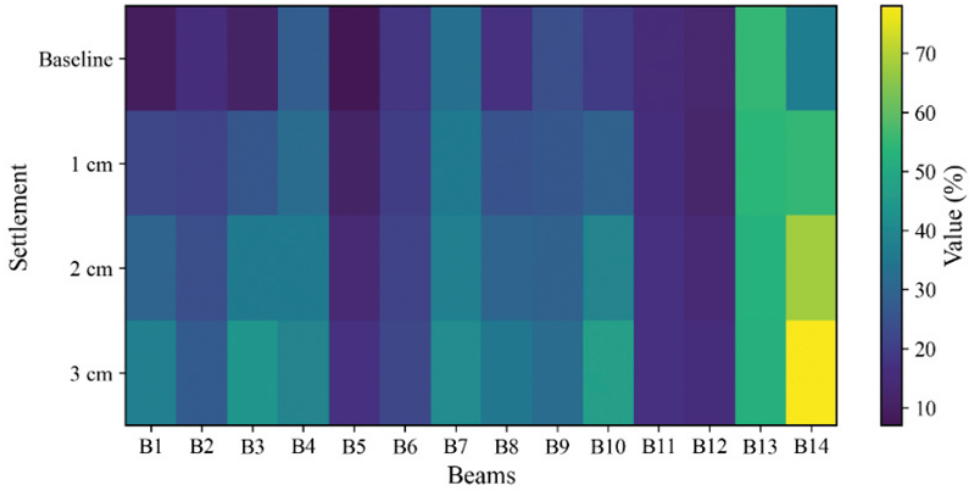

(b)

Fig. 7 Demand to capacity ratios for yield curvature (a), and shear force (b) for the XY= 1–3 cm

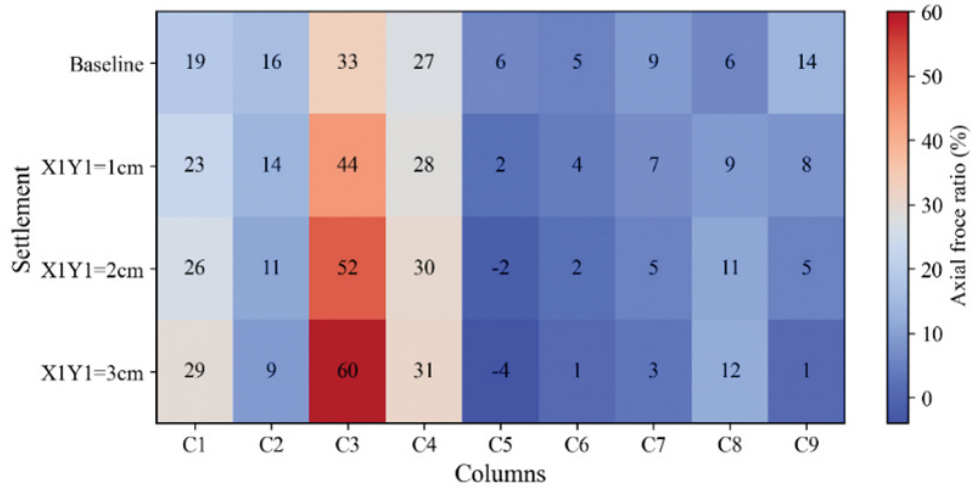

Fig. 8 Figure 6: Figure 4: Axial force ratio for XY= 1–3 cm.

Results: Seismic Fragility

Slight Damage State

Figure 9 illustrates the fragility curves for the slight damage state under all settlement scenarios. In the baseline case, the median capacity is already low (m = 3.8 cm/s), meaning the frame is vulnerable to even low levels of ground shaking. When differential settlement is introduced, the fragility curves in all cases confirm that as little as 1 cm of settlement is enough to induce slight damage without any seismic input. Increasing settlement magnitude (to 2 cm and 3 cm) does not affect the median significantly because the structural members have already reached their damage threshold at minimal excitation.

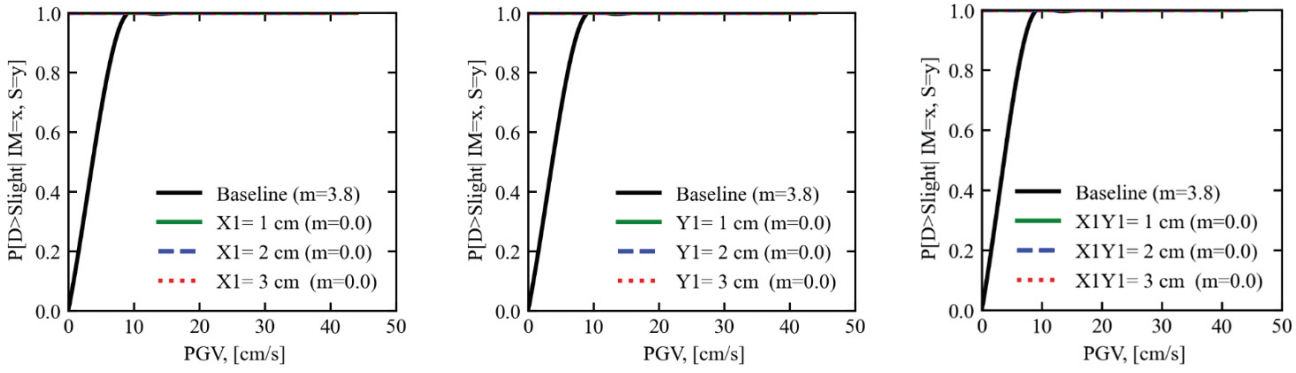

(a) (b) (c)

Fig. 9 Fragility curves for slight damage case

Moderate Damage State

For the moderate damage state (Figure 10), the baseline median PGV is about 9.9 cm/s. Settlement along X1 produces only minor reductions of 5–7% in the median capacity. In contrast, Y1 settlements of 1 cm and 2 cm slightly improve the median capacity by 10% and 7%, likely due to reductions in period and eccentricity favoring elastic response; however, at 3 cm, the capacity drops marginally by 1%. The X1Y1 case shows fluctuations between 10.9 cm/s and 9.8 cm/s, also reflecting the influence of reduced eccentricity ratios. Overall, the impact of settlement on the moderate damage state remains limited, with only small variations in capacity.

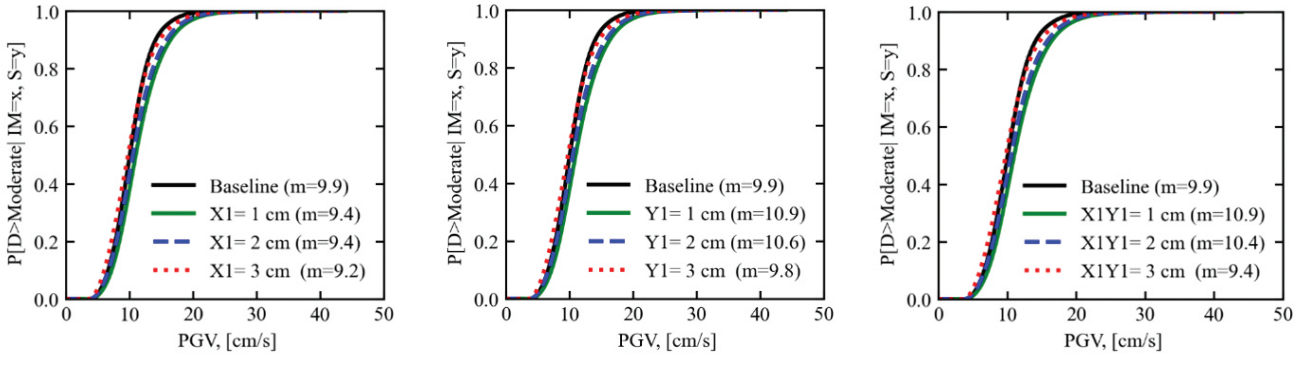

(a) (b) (c)

Fig. 10 Figure 9: Fragility curves for moderate damage case.

Ultimate Damage State

The most significant influence of settlement is seen at the ultimate damage state, as depicted in Figure 11. The baseline case shows a median capacity of approximately 22.1 cm/s PGV. Introducing settlement reduces this median progressively. For X1 (Figure 11a), the median decreases from 22.1 cm/s in the baseline to around 20.6 cm/s at 3 cm settlement. In the Y1 scenario (Figure 11b), the drop is even more marked, with the median reducing from 22.7 cm/s at 1 cm settlement to about 20.5 cm/s at 3 cm. The X1Y1 scenario (Figure 11c) demonstrates the steepest reduction, where the baseline median of 22.1 cm/s falls to about 20.3 cm/s under 3 cm settlement. This consistent trend confirms that settlement considerably reduces the collapse safety margin of the frame, lowering the ground motion intensity required to trigger ultimate damage. The combination of increased shear and curvature demands in beams and the redistribution of axial forces in columns explains the heightened fragility in this state. The results underscore that ignoring settlement in seismic assessments could significantly underestimate the likelihood of collapse for substandard RC frames

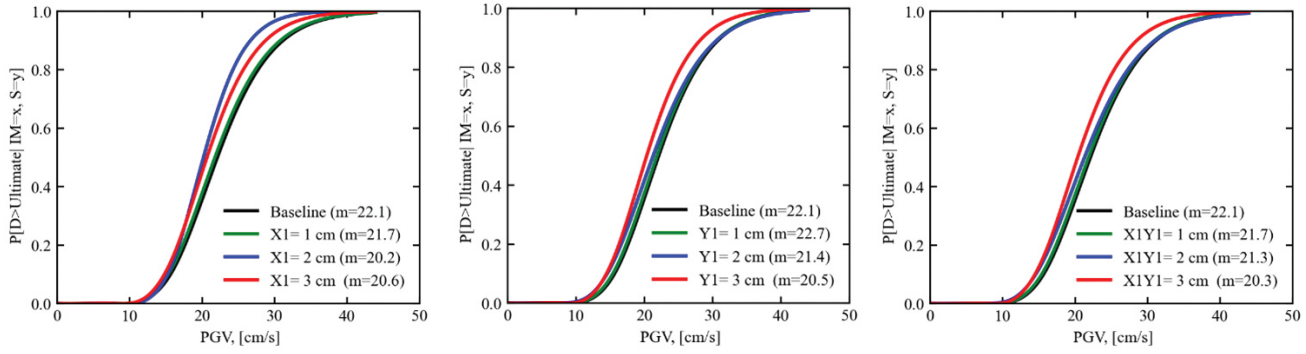

(a) (b) (c)

Fig. 11 Figure 10: Figure 9: Fragility curves for ultimate damage case.

Conclusions

The results demonstrate that support settlement significantly alters the behavior of substandard RC frames. Static analyses revealed that even small settlements cause major redistributions of internal forces. Beams spanning perpendicular to the settled axes experienced sharp increases in curvature and shear demands, in many cases exceeding yield capacities. Columns in the settled frames tended to unload, sometimes entering tension, while adjacent columns—especially C3—absorbed much higher axial forces, reducing their ductility. The combined X1Y1 settlement case produced the most severe effects, with widespread overstressing in both beams and columns and marked reductions in stiffness. Fragility analysis further confirmed that settlement amplifies seismic vulnerability. A differential settlement of only 1 cm was sufficient to place the frame in a slightly damaged state without seismic input. While moderate damage states showed limited sensitivity, ultimate damage states were highly affected. At 3 cm settlement, the median collapse capacity decreased by up to 9%, underscoring the reduction of the safety margin against failure.

These findings highlight the need to explicitly account for support settlement in the seismic assessment of existing substandard RC frames. Engineers should incorporate settlement effects into both static and dynamic analyses to avoid underestimating demands and collapse probabilities. Mitigation measures—such as soil improvement, foundation retrofitting, or redistribution of lateral resisting elements—should be prioritized in regions where poor soil conditions or excavation activities make differential settlement likely.

Acknowledgments The authors acknowledge the funding received from the Turkish Disaster and Emergency Management Presidency (AFAD) as a part of the project UDAP-Ç-21-34: “Monitoring of Surface Deformation in the Elazığ Sivrice Using Radar Remote Sensing.”.

References

1. Erdik, M. (2001). Report on 1999 Kocaeli and Düzce (Turkey) earthquakes. Structural control for civil and infrastructure engineering: World Scientific, 12, 149-186.
2. Skempton, A. W., & MacDonald, D. H. (1956). The allowable settlements of buildings. Proceedings of the Institution of Civil Engineers, 56, 727-768.
3. Meyerhof, G. G. (1953). Some recent foundation research and its application to design. The Structural Engineer, 316, 151-167.
4. Polshin, D. E., & Tokar, R. A. (1957, August). Maximum allowable non-uniform settlement of structures. In Proc., 4th Int. Conf. on Soil Mechanics and Foundation Engineering (Vol. 1, pp. 402-405). London: Butterworth's.
5. Boscardin, M. D., & Cording, E. J. (1989). Building response to excavation-induced settlement. Journal of Geotechnical Engineering, 1151, 1-21.
6. Laefer, D. F., Ceribasi, S., Long, J. H., & Cording, E. J. (2009). Predicting reinforced concrete frame response to excavation induced settlement. Journal of geotechnical and geoenvironmental engineering, 13511, 1605-1619.
7. Son, M., & Cording, E. J. (2011). Responses of buildings with different structural types to excavation-induced ground settlements. Journal of Geotechnical and Geoenvironmental Engineering, 1374, 323-333.
8. Fotopoulou, S., Karafagka, S., & Pitilakis, K. (2018). Vulnerability assessment of low-code reinforced concrete frame buildings subjected to liquefaction-induced differential displacements. Soil Dynamics and Earthquake Engineering, 110, 173-184.
9. Huseynli. S., Yazgan, U. (2021, October). Seismic Fragility Analysis of Seismically Deficient Buildings with Support Settlement. In Proceeding of 6th International Conference on Earthquake Engineering and Seismology.
10. Bao, C., Ma, X., Lim, K. S., Chen, G., Xu, F., Tan, F., & Abd Hamid, N. H. (2021). Seismic fragility analysis of steel moment-resisting frame structure with differential settlement. Soil Dynamics and Earthquake Engineering, 141, 106526.
11. Miano, A., Mele, A., & Prota, A. (2022). Fragility curves for different classes of existing RC buildings underground differential settlements. Engineering Structures, 257, 114077.
12. Jeong, S. H., & Elnashai, A. S. (2004). Analytical assessment of an irregular RD full scale 3D test structure.
13. McKenna, F., Scott, M. H., and Fenves, G. L. (2010) "Nonlinear finite-element analysis software architecture using object composition." Journal of Computing in Civil Engineering, 241:95-107.
14. Filippou, F. C., Popov, E. P., & Bertero, V. V. (1983). Effects of bond deterioration on hysteretic behavior of reinforced concrete joints.

Chapter 14
Dynamic Properties by OMA and Modal Updating of a Mayan Temple

T. Nunez and C. E. Ventura

Abstract This paper presents a study on the dynamic properties of the ancient Mayan Temple of the Masks (Temple II) in Tikal, Guatemala, using Operational Modal Analysis (OMA) and finite element (FE) model updating. Built around 700 A.D., the temple is a key funerary and ceremonial monument whose preservation requires continuous structural monitoring. Field OMA measurements were performed to identify modal frequencies, damping ratios, and mode shapes, establishing a baseline for FE model calibration. A simplified FE model was first tuned using geometric data, dynamic properties, and sclerometric test results that characterized the stone's mechanical strength. A refined model was then updated with field data to estimate the temple's seismic response and evaluate the effects of material degradation on long-term stability. This integrated methodology—combining ambient vibration testing and detailed numerical modelling—provides a robust framework for heritage conservation, highlighting how advanced monitoring and modelling techniques can safeguard culturally significant structures like Temple II.

Keywords SHM · Laser Scan · Heritage · Soil-Struct Interaction

Introduction

Significance of the Temple of the Masks in Tikal

The Temple of the Masks (Temple II) in Tikal, Guatemala, built around 700 A.D., reflects the architectural and ceremonial sophistication of the Classic Maya. Facing Temple I across the Great Plaza, it was likely dedicated to Lady Kalajuun Une' Mo', wife of King Jasaw Chan K'awiil I, and marks a period of cultural renewal. Preserving Temple II is crucial due to its historical significance and exposure to environmental and geotechnical hazards. As noted by Rossi and Bournas [3], safeguarding structural health is key for heritage conservation. Modern SHM techniques—vibration analysis, laser scanning, and material testing—provide essential data on performance and deterioration. The temple's location on unstable soil highlights the importance of soil–structure interaction, which is often overlooked in conservation. Interdisciplinary studies combining structural and geotechnical insights [1],[2] are key to minimizing potential hazards. Furthermore, its astronomical alignments [5] enhance its cultural importance. Integrating vibration monitoring, laser scanning, and computational modelling supports a holistic, sustainable strategy to preserve this emblematic Maya monument.

Importance of monitoring structural integrity for archaeological preservation

Preserving archaeological monuments like Temple II in Tikal is challenging due to limited architectural documentation, scarce data on material degradation, and few records of environmental or seismic impacts. These gaps make conservation efforts more difficult and increase the risk of unnoticed deterioration. SHM offers a quantitative framework to address these issues through tools such as ambient vibration monitoring, 3D laser scanning, drone photogrammetry, and ground-penetrating radar (GPR). Vibration monitoring identifies modal frequencies, damping ratios, and mode shapes—key indicators of structural change [6],[7]—while laser scanning and drones provide high-resolution geometric data for detecting deformations

T. Nunez · C.E. Ventura
The University of British Columbia, Department of Civil Engineering
e-mail: nuneztom@mail.ubc.ca; ventura@civil.ubc.ca

© The Author(s), under exclusive license to River Publishers 2026

Kristin B. Zimmerman, PhD (eds.), *Dynamics of Civil Structures, 2026, Vol. 2*, Conference Proceedings
of the Society for Experimental Mechanics Series, https://doi.org/10.13052/rp-9788743814139

in inaccessible areas [8],[9],[16]. GPR complements these techniques by mapping subsurface conditions, revealing soil instability or voids that affect foundation behavior [10]. Recent advances include digital twins; virtual models integrating real-time data to simulate and predict structural responses to hazards or interventions [11]. Combined with IoT technologies, these models enable adaptive and predictive conservation strategies. In summary, SHM has become essential for sustainable heritage management, bridging knowledge gaps and guiding preservation decisions. For monuments like Temple II, it ensures both structural stability and the enduring transmission of cultural and historical value.



Fig. 1 Left: Geographical location of Tikal National Park, WorldAtlas.com (red squared). Upper-right: The Temple of the Masks (Temple II), evaluated in this research. Downright: Temple of the Great Jaguar (Temple I)

On-Site Assessment Methodology

Ambient vibration tests

A series of ambient vibration tests were conducted at the temple to determine their dynamic modal properties. Nine portable-wireless sensors [14] were used for these tests. The testing program consisted of three measurement setups. The layouts of the sensors are illustrated in Figure 2. For all configurations, five out of nine sensors were considered as reference: four at level 3 and one at the ground level. The remaining four sensors were placed at level 2 for setup 1, at level 1 for setup 2 and level 4 for setup 3 as rovers. The duration for all setups was 20 minutes at a 128 Hz sample rate.

Sclerometric tests

Schmidt hammer tests were performed at 64 points on the pyramid to establish a characteristic value for the material's compressive strength. The method provides a non-destructive estimation of compressive strength by measuring the rebound number, which correlates with material hardness and strength. The relationship between the rebound number and compressive strength is established empirically and can be expressed as $f_c = a \cdot R^b$, where f_c is the compressive strength, R is the rebound number, and a and b are material-specific constants.

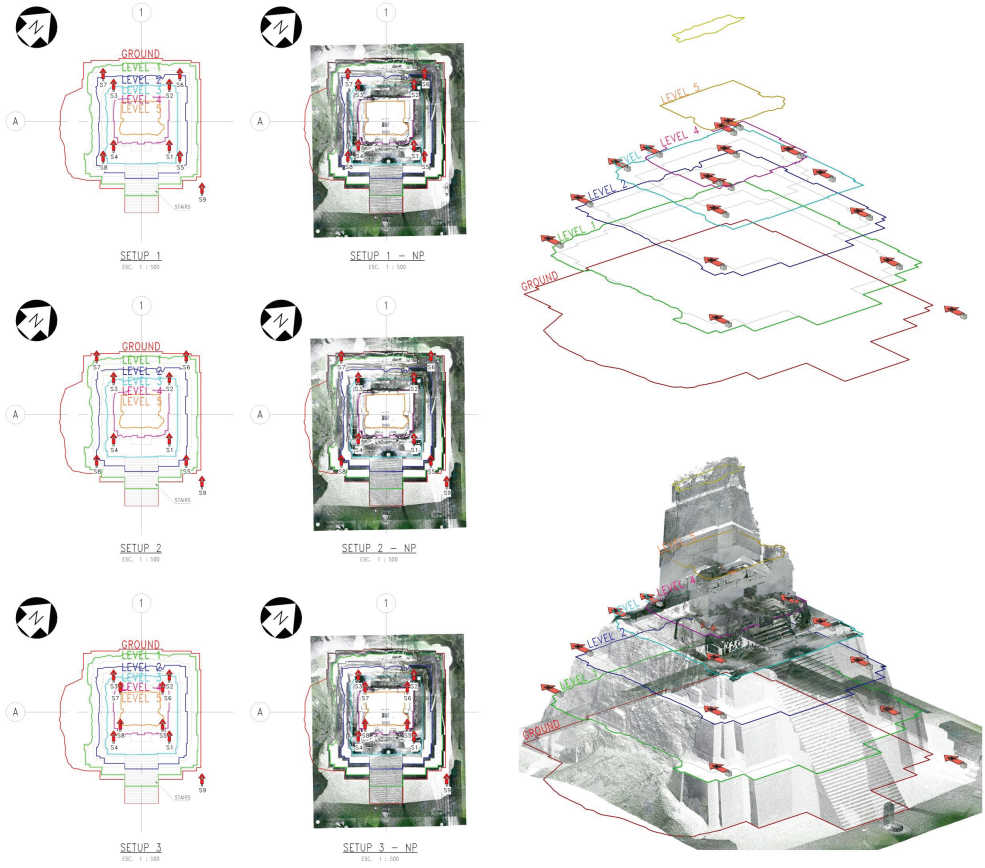

Fig. 2 Setup 1 to 3. Ambient vibration test setup (velocity)

3D Geometric Survey

A laser scanning survey was conducted around the pyramid to produce a high-resolution 3D point-cloud model. Thirty-one scan positions captured up to 360,000 points per second, accurately recording the structure's geometry and external features (Figure 3). The processed data provided a precise 3D reference for structural and geometric analysis, including assessments

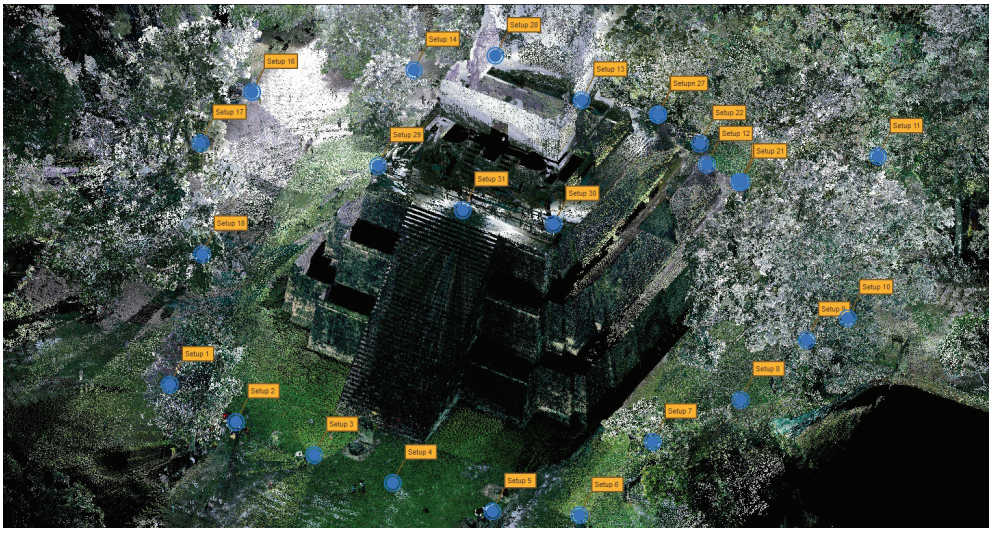

Fig. 3 Laser Scanner Positions during survey

of verticality and differential settlements. These measurements revealed potential tilting and foundation movements, offering key insights into the pyramid's current condition and long-term stability.

Results and Discussion

Dynamic properties

Well-established techniques were employed in both the frequency and time domains to obtain the dynamic parameters of the temple. The Enhanced Frequency Domain Decomposition (EFDD) was used for the frequency domain. For the time domain analysis, the Stochastic Subspace Identification (SSI) approaches—Unweighted Principal Components (UPC) and Canonical Variate Analysis (CVA)—were applied. All the analyses were developed using the ARTeMIS Modal software [15]. The results obtained from these analyses are presented below.

Table 1 Frequencies (f) and damping ratios (β). Ambient vibration tests (setup 1-2-3).

N°	Freq. [Hz] EFDD	Freq. [Hz] SSI-UPC	Freq. [Hz] SSI-CVA	**Freq. [Hz] Avg.**	β [%] EFDD	β [%] SSI-UPC	β [%] SSI-CVA	**β [%] Avg.**	**Predominant Direction Modal Shape**
1	4.07	4.08	4.07	**4.07**	0.5	1.6	1.0	**1.0**	Bending (X)
2	4.24	4.26	4.24	**4.25**	1.2	2.2	1.8	**1.7**	Bending (Z)
3	8.01	8.05	8.08	**8.05**	2.4	2.2	2.8	**2.5**	Vertical (Y)

Sclerometric tests

García de Miguel et al. [12] describe the nearby Great Jaguar Pyramid as composed of ashlar masonry walls filled with *embono*—a lime mortar with limestone fragments—forming a dense, low-void structure. The fine, porous limestone is prone

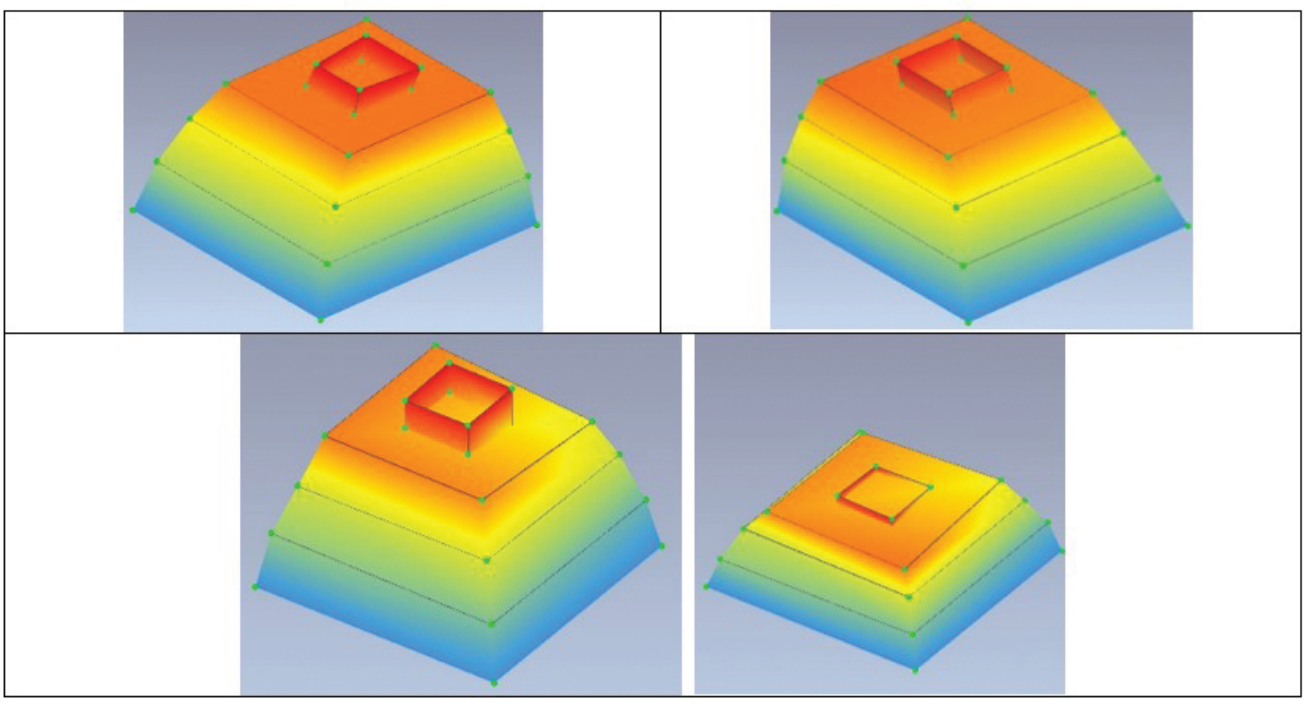

Fig. 4 Modal Shapes. Upper-left: f=4.07[Hz], upper-right: f=4.25[Hz], down f=8.05[Hz]. ARTeMIS Modal Software [15]

to erosion and biological growth. As Temple II shares similar materials and techniques, these findings likely apply to it as well, suggesting comparable deterioration mechanisms such as loss of *embono* cohesion and limestone decay, which offer key insights for its preservation.

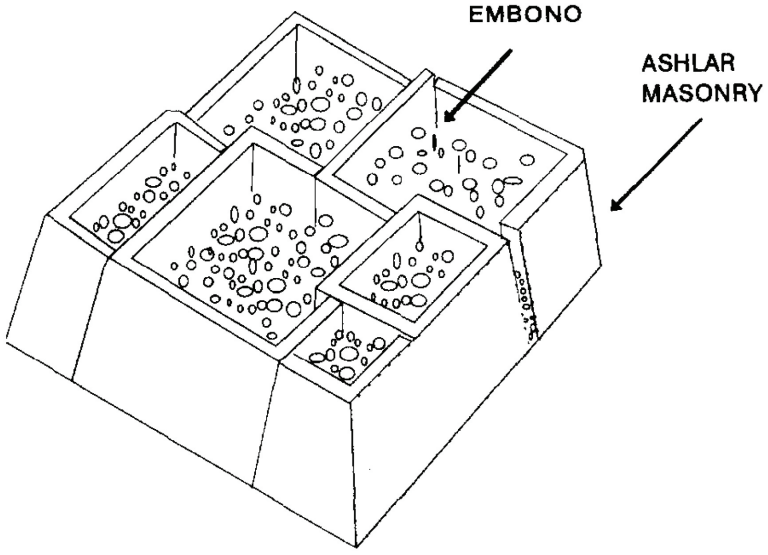

Fig. 5 The schematic material structure of the Temple [12]

According to M. Kržan et al. [13], the compressive strength of ashlar masonry depends on morphology and construction quality, averaging 6.05 MPa and typically ranging from 4 to 8 MPa. The Schmidt hammer tests on Temple II yielded a characteristic value of 5.97 MPa, showing an acceptable correlation with the previously cited study. As shown in Figure 6, values range from 3.7 to 8.3 MPa, reflecting the high heterogeneity also reported in their work and confirming the correlation between rebound number and compressive strength. The characteristic compressive strength was obtained using a Kernel Density Estimation (KDE) method, which identifies the most probable value within the empirical distribution of test results. Following the configuration described by García de Miguel et al. [12], a significant portion of the structure consists of embono, a lime mortar with limestone fragments forming a dense, low-void matrix. Under the BS EN 459-1 [17] classification,

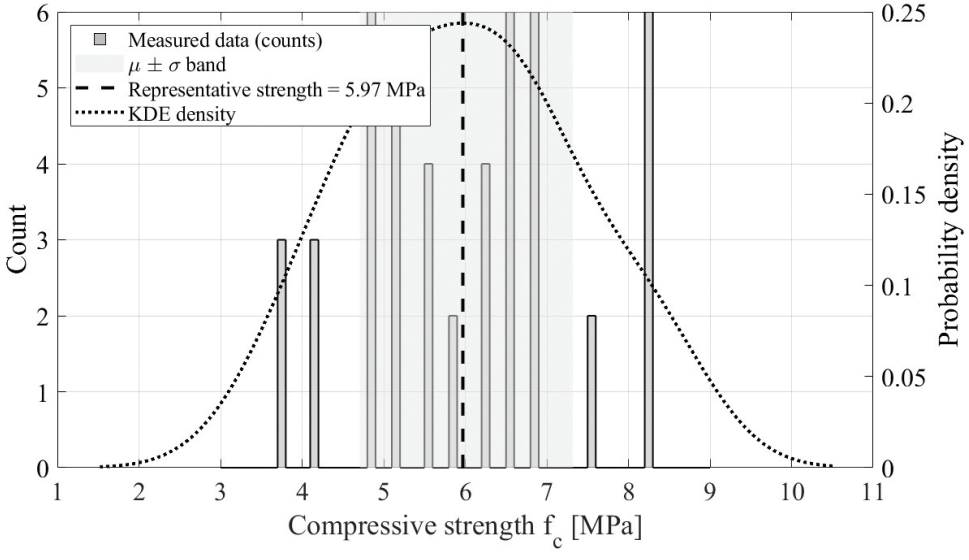

Fig. 6 Estimation of compressive strength for ashlar masonry using KDE method

this material can be conservatively considered as an NHL 2 lime mortar (f'_n = 2 MPa). Since most of the pyramid is composed of embono while the mechanical characterization was performed only on the ashlar masonry, an equivalent structural compressive strength was estimated assuming a contribution of 30 % from the ashlar masonry and 70 % from the embono. Based on the characteristic values reported, the pyramid's overall characteristic compressive strength was therefore taken as 3.2 MPa, for use in material characterization and subsequent numerical modeling.

Geometry survey

The laser scanning survey produced a detailed 3D dataset that enabled a comprehensive analysis of the pyramid's geometry and structural behaviour. The resulting point cloud accurately captured its dimensions and allowed assessment of external contours, vertical alignment, and overall stability. The analysis revealed differential settlements (rocking) across structural blocks, decreasing from base to top: 278 mm at the first block, 169 mm between levels 1–2, and 68 mm between levels 2–3. These settlements are critical for structural evaluation, while no differential movement was observed in the opposite direction.

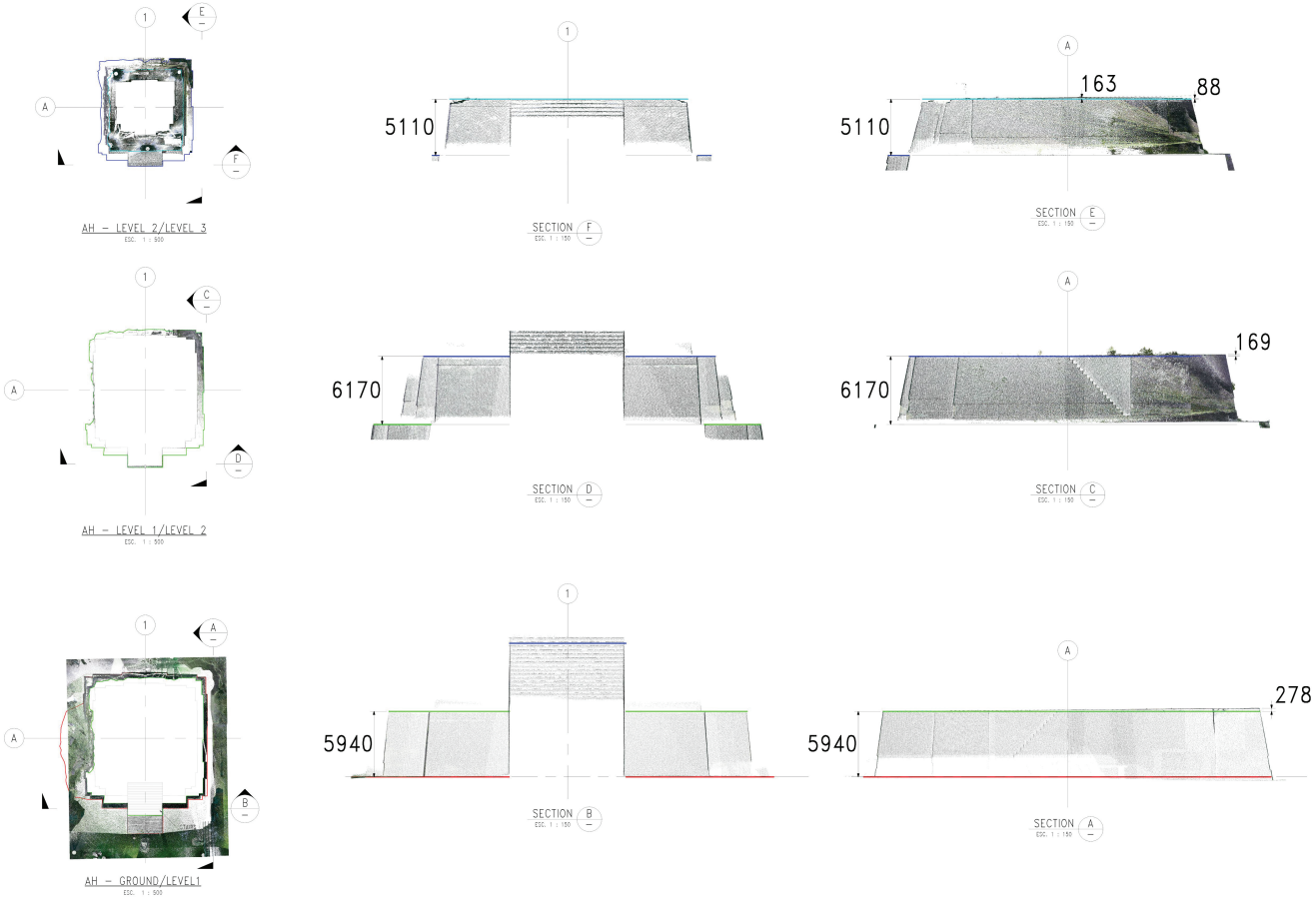

Fig. 7 Estimated rocking between pyramid blocks using 3D laser scanning. Up: upper block, between level 3 and 2. Middle: middle block, between level 2 and 1. Down: ground block, between level 1 and ground

Calibrated model

A key step after structural assessment and SHM analysis is calibrating a mathematical model to evaluate the structure's condition and simulate its response to earthquakes, soil effects, extreme weather, or long-term degradation. To develop such a model, it was essential to obtain on-site data: the geometry provided a volumetric measure of the structure, the sclerometric tests allowed the derivation of mechanical properties, and the vibration measurements enabled model calibration for subsequent scenario simulations. Regarding the characteristic values of mechanical strength, Table 2 summarizes those considered for the model.

Table 2 Calibrated mechanical properties for simplified model

N°	Variable	Symbol	Value	Unit	Comments
1	Density	γ	2200	kg/m^3	Calibrated based on clay soils improved with lime or cement: 1700-2200 kg/m^3
2	Compressive Strength	$f_c^{'}$	3.2	MPa	Average value from the sclerometric test
3	Young's Modulus	E	480	MPa	$E = 150 f_c^{'}$
4	Poisson Ratio	ν	0.15	MPa	Calibrated based on clay soils improved with lime or cement: 0.15 – 0.35
5	Shear Modulus	G_c	209	MPa	$G_c = E/2(1+\nu)$

The density in Table 2 follows M. Kržan & V. Bosiljkov (2023) [13], while compressive strength was obtained considering a weighting of 30 % for the characteristic compressive strength of the ashlar masonry (5.97 MPa) and 70 % for the *embono* material (2 MPa), a uniform characteristic compressive strength of 3.2 MPa was assumed for the pyramid. The remaining parameters were estimated from empirical and reference data to define the model's stiffness. Based on these parameters, a finite element model was developed in Ansys software. The model was built from the point cloud obtained through laser scanning, which was cleaned and processed to generate a geometry suitable for meshing. A solid mesh was created with approximately 94,000 quadratic elements, using finer discretization in areas with sharp angles or geometric details requiring higher resolution, shown in Figure 8:

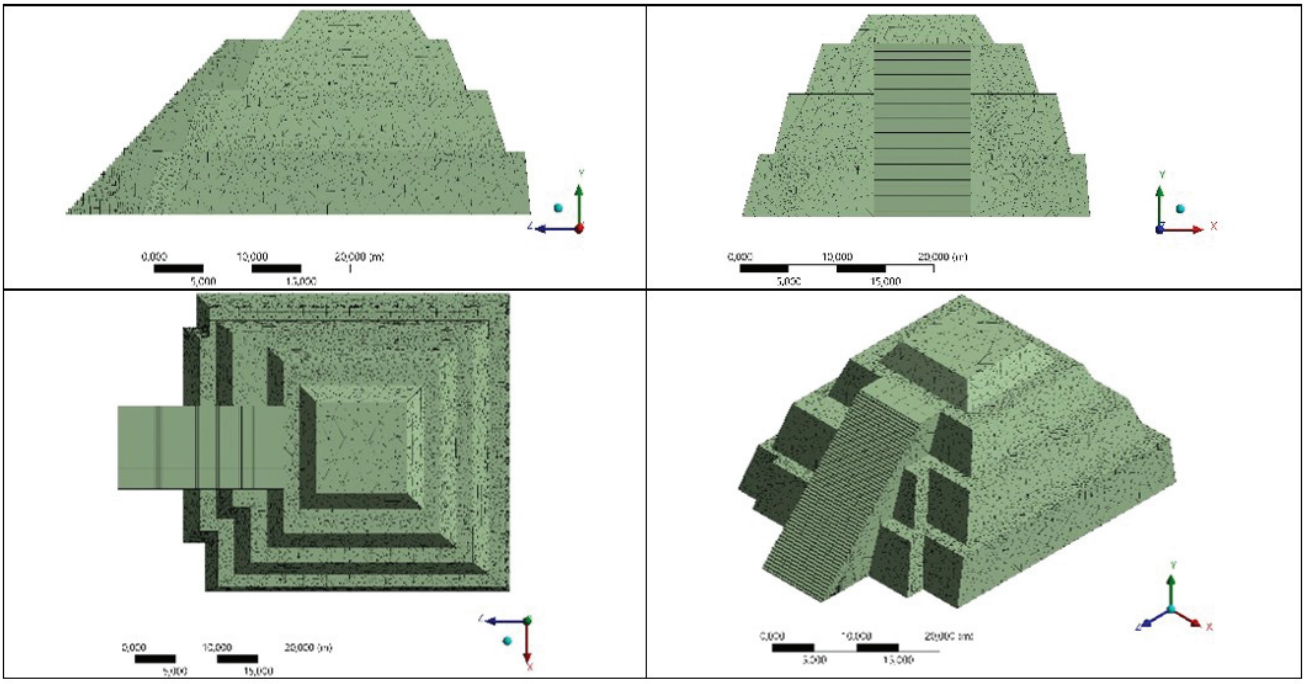

Fig. 8 Different views for the FE model developed in Ansys

The model included only self-weight loading to estimate the natural frequencies and mode shapes. Thirty modes were initially computed to assess the cumulative effective modal mass. The main modal shapes and their corresponding frequencies are presented below.

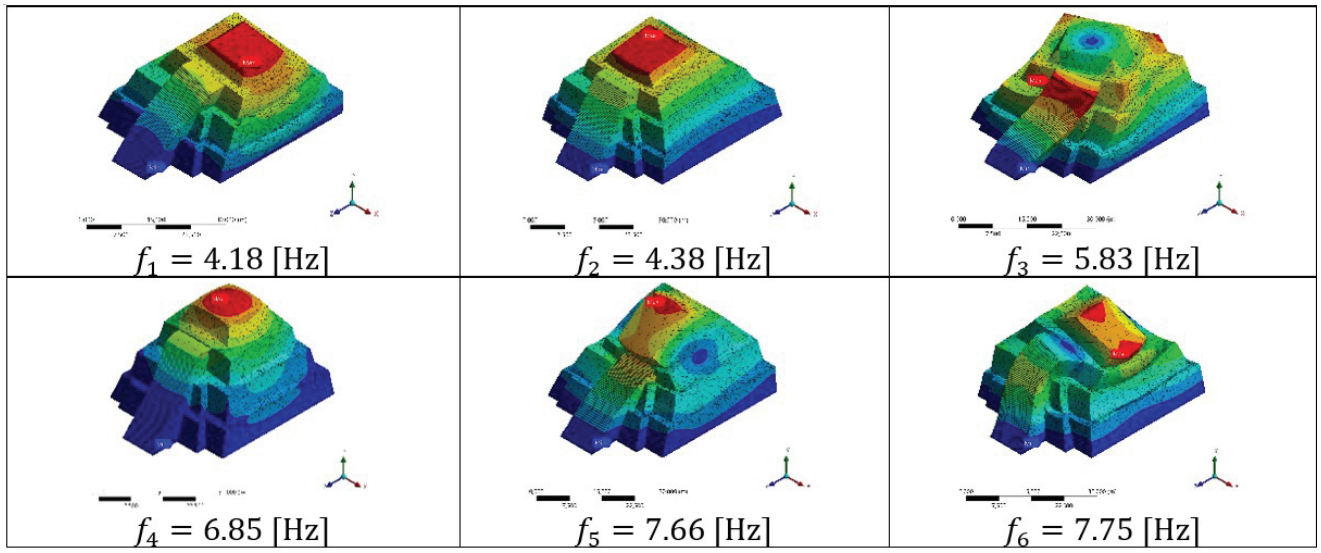

Fig. 9 Modal frequencies and shapes for the FE model

Table 3 Modal frequencies and modal mass percentage for each mode. FE model

Mode	Modal Freq. [Hz] Model	Predominant direction	% Modal Mass X	% Modal Mass Z	% Modal Mass Y (vert.)
1	4.18	Bending	55.60	0.07	-
2	4.38	Bending	0.08	57.20	0.02
3	5.83	Torsional	0.15	-	-
4	6.85	Vertical	-	-	52.26
5	7.66	Bending	0.01	13.82	0.06
6	7.75	Bending	17.23	-	-

Finally, Table 4 presents a comparison between the natural frequencies obtained from ambient vibration testing and those derived from the finite element model, which was developed based on the field survey data. From the table, it can be observed that the frequencies predicted by the model are in reasonable agreement with those identified from ambient vibration measurements, confirming that the calibrated numerical model provides an acceptable representation of the structure's dynamic behavior.

Table 4 Frequency comparison. Ambient vibration results and FE model

Mode	Modal Freq. [Hz] Ambient Vibration	Modal Freq. [Hz] FE Model	Difference [%]	Predominant direction
1	4.07	4.18	2.7	Bending
2	4.25	4.38	3.1	Bending
3	8.05	6.85	14.9	Torsional

Conclusions

This study presents a structural assessment of Temple II, focusing on its dynamic behaviour, geometry, and material properties. Ambient vibration testing identified modal frequencies, damping ratios, and mode shapes, while 3D laser scanning

detected differential settlements and deviations from verticality. The analysis revealed up to 278 mm of settlement (tilt ≈ 0.43°) along one principal direction. Schmidt Hammer tests showed variable compressive strength (5.97 MPa characteristic value), consistent with Kržan [13] and confirming the reliability of this non-destructive method. A FE model, calibrated with field data, provided a reasonable representation of the temple's dynamic response. The findings indicate potential risks related to settlement and emphasize the need for long-term monitoring and improved material characterization. Further soil–structure interaction evaluation is recommended for a better understanding of its role in the observed deformation and stability. This work demonstrates the value of an integrated SHM approach—combining vibration testing, geometric surveys, and non-destructive material evaluation—to assess structural integrity while minimizing intervention. Continuous monitoring enables early detection of deterioration and supports preventive conservation. Future efforts should include permanent sensor systems, refined soil–structure studies, and advanced digital modelling (e.g., digital twins and parametric simulations). Extending this methodology to nearby temples and simulating extreme events such as earthquakes or severe weather will improve predictive analysis and support long-term preservation of Tikal's heritage.

References

1. M. Sangirardi, A. Amorosi, G. de Felice (2020). A coupled structural and geotechnical assessment of the effects of a landslide on an ancient monastery in Central Italy, Engineering Structures, Volume 225, 111249, ISSN 0141-0296, https://doi.org/10.1016/j.engstruct.2020.111249.
2. R. Aguilar, M. Pando, C. Briceño, G. Zavala, B. Castañeda, R. Perucchio, S. Uceda (2018). Structural and geotechnical engineering assessment of Huaca de la Luna – A massive earthen Moche culture pyramid in Northern Peru, Journal of Cultural Heritage, Volume 34, Pages 83-94, ISSN 1296-2074, https://doi.org/10.1016/j.culher.2018.04.006.
3. M. Rossi and D. Bournas (2021). Structural Health Monitoring and Management of Cultural Heritage Structures: A State-of-the-Art Review. Journal of Civil Engineering and Management, 27(3), 134–148. https://doi.org/10.3846/jcem.2021.14202
4. Coe, W. R. (1986), Tikal: A Handbook of the Ancient Maya Ruins. University of Pennsylvania Museum.
5. I. Šprajc (2016). Astronomical Alignments in Ancient Maya Architecture. Latin American Antiquity, 27(2), 143-160.
6. S. Mazzetto (2024). Integrating Emerging Technologies with Digital Twins for Heritage Building Conservation: An Interdisciplinary Approach with Expert Insights and Bibliometric Analysis. Heritage, 7(11), 6432-6479. https://doi.org/10.3390/heritage71103002
7. P. Clemente (2018). Extending the Life-Span of Cultural Heritage Structures". Journal of Civil Structural Health Monitoring. 8:171–179. https://doi.org/10.1007/s13349-018-0278-3(0123456789().,-volV)(0123456789().,-volV)
8. N. Xu, D. Huang, S. Song, X. Ling, C. Strasbaugh, A. Yilmaz, R. Qin, R. (2021). A volumetric change detection framework using UAV oblique photogrammetry – a case study of ultra-high-resolution monitoring of progressive building collapse. International Journal of Digital Earth, 14(11), 1705–1720. https://doi.org/10.1080/17538947.2021.1966527
9. Y. H. Jo & S. Hong (2019). Three-Dimensional Digital Documentation of Cultural Heritage Site Based on the Convergence of Terrestrial Laser Scanning and Unmanned Aerial Vehicle Photogrammetry. ISPRS International Journal of Geo-Information, 8(2), 53. https://doi.org/10.3390/ijgi8020053
10. A. Kanli, G. Taller, P. Nagy, P. Tildy, Z. Pronay, E. Toros (2015). GPR survey for reinforcement of historical heritage construction at fire tower of Sopron, Journal of Applied Geophysics, Volume 112, Pages 79-90, ISSN 0926-9851, https://doi.org/10.1016/j.jappgeo.2014.11.005.
11. A. Darwish & A.E. Hassanien (2022). IoHCT: Internet of Cultural Heritage Things Digital Twins for Conservation and Health Monitoring of Cultural in the Age of Digital Transformation. In Digital Twins for Digital Transformation: Innovation in Industry (pp. 1–21). Springer. https://doi.org/10.1007/978-3-030-96802-1_1
12. J.M. Garcia De Miguel, L. Sanchez-Castillo, J.J. Ortega-Calvo, J.A. Gil, C. Saiz-Jimenez (1995), Deterioration of building materials from the Great Jaguar Pyramid at Tikal, Guatemala, Building and Environment, Volume 30, Issue 4, Pages 591-598, ISSN 0360-1323, https://doi.org/10.1016/0360-1323(94)00055-W.
13. M. Kržan & V. Bosiljkov. (2023) Compression and In-plane Seismic Behaviour of Ashlar Three-leaf Stone Masonry Walls. International Journal of Architectural Heritage 17:6, pages 829-845.
14. Micromed (2012) Tromino: Portable ultra-light acquisition system for seismic noise and vibration- User's manual. Macromed, Italy.
15. Structural Vibration Solutions (2016) ARTeMIS modal software. Version 6. SVS, Denmark.
16. Canuto, M. A., Estrada-Belli, F., Garrison, T. G., Houston, S. D., Acuña, M. J., Kováč, M., Marken, D., Nondédéo, P., Auld-Thomas, L., Castanet, C., Chatelain, D., Chiriboga, C. R., Drápela, T., Lieskovský, T., Tokovinine, A., Velasquez, A., Fernández-Díaz, J. C., & Shrestha, R. (2018). Ancient lowland Maya complexity as revealed by airborne laser scanning of northern Guatemala. Science, 361(6409), eaau0137. https://doi.org/10.1126/science.aau0137csu-sdsu.primo.exlibrisgroup.com+8datadryad.org+8hal.science+8
17. BSI Standards Publication. (2015). BS EN 459-1:2015, Building lime—Part 1: Definitions, specifications and conformity criteria. BSI.

Chapter 15
The Great Train Disaster of 2025: Isolating Sensitive Equipment from Rail-Induced Vibration

Michael J. Wesolowsky, Ph.D., P.Eng., Muhammad Rahman, M.A.Sc., P.Eng., Rabih Alkhatib, Ph.D., P.Eng., Brad Pridham, Ph.D., P.Eng.

Abstract Ground-borne vibrations from railroads are often assessed for their impacts on human comfort and vibration-sensitive equipment in nearby structures, but in rare cases, there is vibration-sensitive equipment located directly on the tracks and supporting structure itself. One such example is known as an Impedance Bond (Bond), which is a crucial component in railway signaling systems, particularly on electrified railways. It allows traction current to flow through the rails while simultaneously blocking the flow of alternating current (AC) used for signaling, ensuring both traction and signaling systems can operate independently and safely on the same track. Bonds typically have vibration criteria, which, due to the circuit boards in them that contain several delicate components, can be very strict at frequencies much higher than are usually considered for human comfort or typical vibration-sensitive equipment.

This paper describes a project on a major commuter rail line in the United States where several Bonds were failing repeatedly at a discrete number of locations on the system. Extensive measurements and investigation determined that that a combination of locally poor track conditions and inadequately designed isolation systems were responsible. Several new isolation systems were considered, as well as track quality improvements in order to eliminate the repeated failures that were causing significant issues with the operations of the rail network.

Keywords Vibration Serviceability · Ground-borne Vibration · Vibration Isolation · Vibration Measurements · Model Validation · Dynamic Loading

Introduction

Impedance Bonds (Bonds) (example shown in Figure 1) are crucial components in railway signaling systems, particularly on electrified railways. It allows traction current to flow through the rails while simultaneously blocking the flow of alternating current (AC) used for signaling, ensuring both traction and signaling systems can operate independently and safely on the same track. These components are typically installed within the track gauge and are subjected to vibrations from passing trains, the intensity of which is influenced by local track conditions and mounting configurations, which usually include local vibration isolation systems. These isolation systems, which are provided by the Bond supplier as part of the overall system, are typically 3/8" neoprene pads that sit between the Bond the mounting frame below. Critically, the Bonds have bolts that penetrate the isolation pad that end with washers and nuts on the lower side of the mounting frame, which provides a destructive short-circuiting of the isolation system. The effects of this deficient mounting configuration will become evident throughout the course of this paper.

This paper describes a project on a major commuter rail line in the United States where several Bonds were failing repeatedly at a discrete number of locations on the system. An extensive testing regiment was conducted to understand the failure mechanisms of the Bonds, which also included microscopic investigation of the internal components to determine how each failed.

Michael J. Wesolowsky · Muhammad Rahman · Rabih Alkhatib · Brad Pridham
Thornton Tomasetti, 23-366 Revus Ave., Mississauga, ON, Canada, L5G 4S5
e-mail: mwesolowsky@thorntontomasetti.com; srahman@thorntontomasetti.com; ralkhatib@thorntontomasetti.com; bpridham@thorntontomasetti.com

© The Author(s), under exclusive license to River Publishers 2026

Kristin B. Zimmerman, PhD (eds.), *Dynamics of Civil Structures, 2026, Vol. 2*, Conference Proceedings of the Society for Experimental Mechanics Series, https://doi.org/10.13052/rp-9788743814139



Fig. 1 Typical Impedance Bond

Vibration Criteria

Impedance Bonds are intended to be designed in accordance with the vibration protocol specified in the American Railway Engineering and Maintenance-of-Way Association (AREMA) Communications & Signals (C&S) Manual [1], which serves as the basis for their conformance and acceptance testing. This protocol involves a sinusoidal vibration sweep characterized by a constant amplitude of 0.2 inches for frequencies between 5 Hz and 20 Hz, and a constant acceleration of 4.2 g for frequencies above 20 Hz up to 200 Hz (see Figure 2), along with a 10 g shock limit lasting 0.11 milliseconds. The assessment criteria are denoted as Class A Roadbed which is applicable to the equipment located on a track.

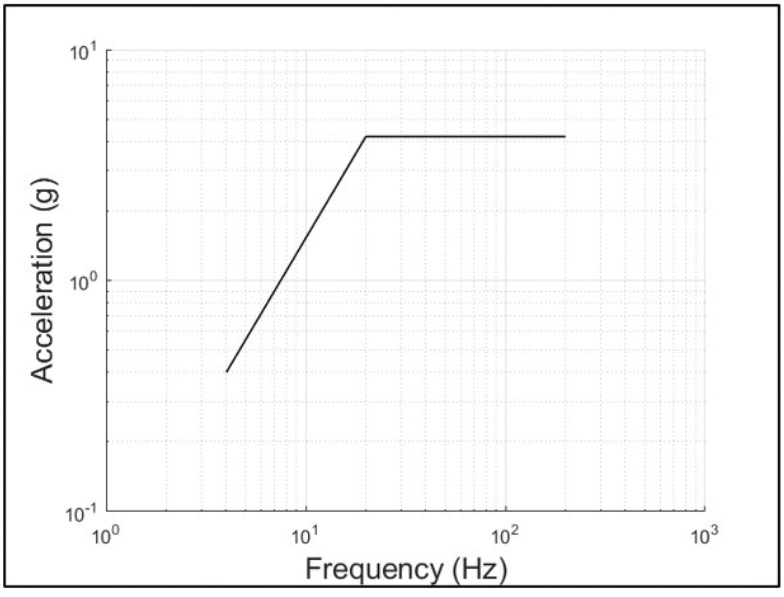

Fig. 2 AREMA Class A Vibration Assessment Criteria

Initial Testing

Initial testing was conducted at the location of one of the Bonds that had been failing repeatedly. The purpose of the testing was to measure the vibrations experienced on frame below the Bond, as well as the Bond itself (which was intended to be isolated by 3/8" thick neoprene pad). These measurements were then compared to the AREMA criteria to determine if those acceptance levels were being exceeded. The efficacy of the isolation system was also calculated. The following conclusions were drawn from the initial testing:

- Consistently high-magnitude energy content at high frequencies between 700 Hz and 1000 Hz were measured. See Figure 3 for one-third frequency content in the vertical direction atop the Bond. These high magnitude forces at these high frequencies are generated by the wheel-rail interaction, particularly when the trains are running at high speed. It is noted that significant rail corrugation was observed at the failure location. The existence of rail corrugation and high speed of the train pass-bys could be attributed to these high vibration levels at these frequencies.
- It should be noted that measurements were taken at frequencies considerably higher than the 200 Hz upper limit of the AREMA criteria. As can be seen in Figure 3, the levels of the accelerations above 200 Hz are an order of magnitude higher than those below 200 Hz, which points to a potential deficiency in the criteria limits used by AREMA.

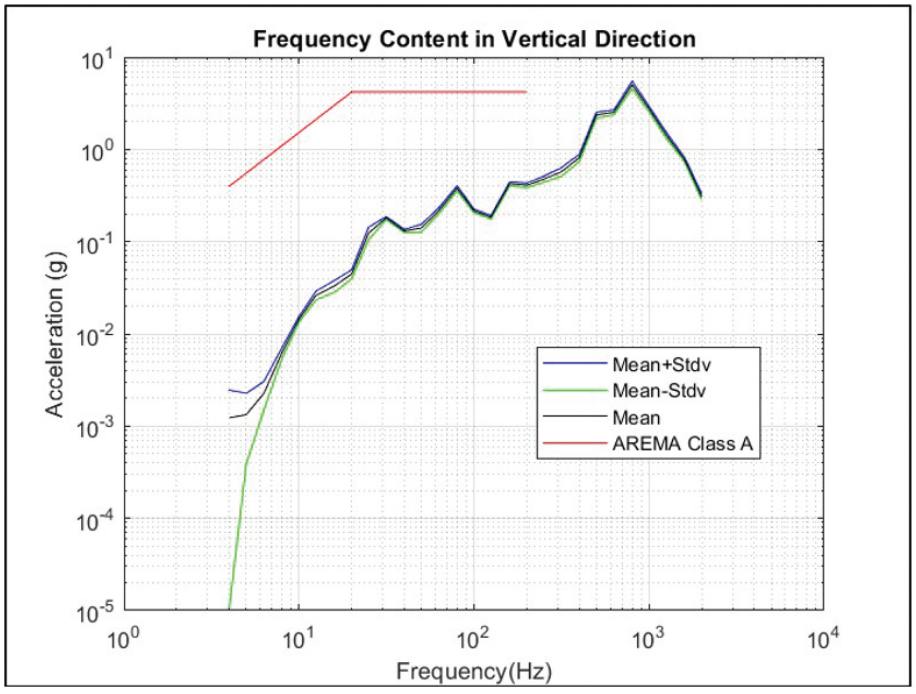

Fig. 3 Frequency Content of the Measured Vertical Vibration Data on the Bond

- Measurements showed that the vibrations on the Bond were in order of approximately 40% of the levels on the frame below, indicating that the 3/8" thick neoprene isolators are not effective in mitigating vibration (as properly installed isolation systems should provide 90%+ isolation efficiency). As such, the Bond is exposed to repeated high-level stress reversals which increases the possibility of fatigue failure. It is our opinion that the failure of the Bond is related to fatigue failure due to these high magnitude forces at these frequencies.
- In order to assess the impact of train speed on the high frequency vibration levels, it was then recommended to perform additional controlled tests at a variety of speeds during the data acquisition period.

Speed Effects Testing

Further testing was then conducted at the same location as described in Section 3, but with the train passing at predetermined speeds in order to explore these velocity-related effects. The following conclusions were drawn from this subsequent testing:

- The overall vertical vibration levels at different speed limits are presented in Figure 4. The corresponding one-third octave frequencies are also presented in Figure 4.
- As expected, the vibration levels increased with the speed of the train pass-by. The highest vibration levels were observed due to train pass-by at 55 mph.
- Up to 200 Hz, the energy contents are similar, irrespective of train speed, indicating that the vibration response of the Bonds is governed by the substructure stiffness at these frequencies. Above 200 Hz, the energy contents increased with the speed of the train. As noted in the initial testing, the energy contents at the high frequencies are related to wheel-rail interaction at speeds 35 mph and above. The high amplitudes of vibration at these frequencies are directly related to existing rail corrugation at the subject site.
- To corroborate this, another measurement location was selected along the track where the train can speed up to 35 mph. The measured vibration levels are plotted in Figure 5. As noted, at this location the vibration levels between 700

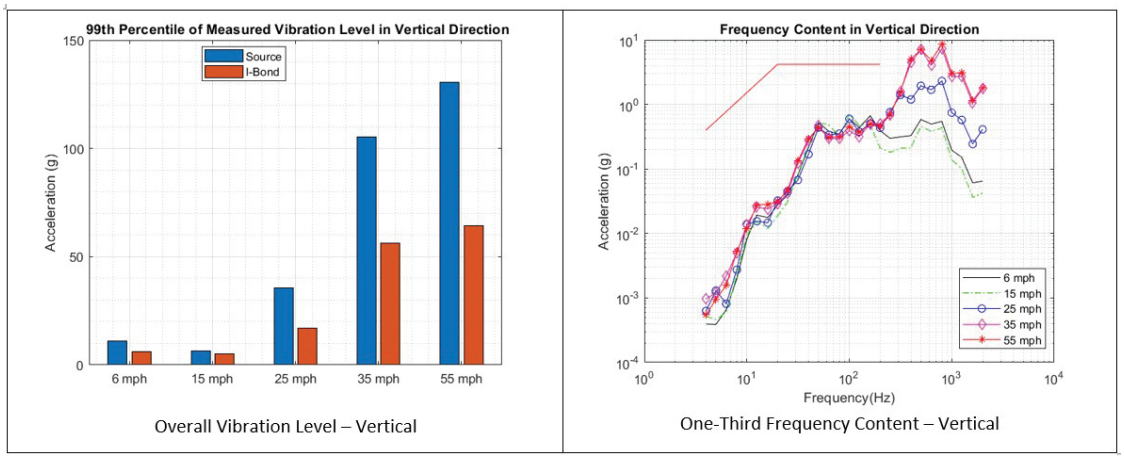

Fig. 4 Vibration as a Function of Train Speed

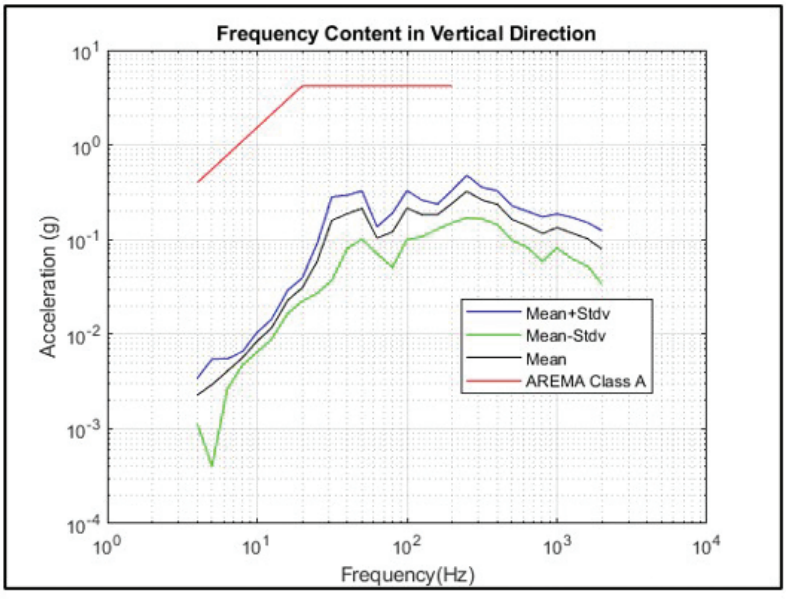

Fig. 5 Measured Vibration Levels at Location – without Rail Corrugation

and 1000 Hz are measured to be 0.4 g compared to a maximum vibration level of 10g where there is significant rail corrugation (Figure 4).

- The existing isolation details with 3/8" thick neoprene pad were also reviewed. Based on the assessment, an axial force of approximately 5000 lbs was predicted at the location of the bolts. This is expected to exceed the elastic load range of the 3/8" thick isolators. Therefore, in the vicinity of the bolts, the neoprene isolator is acting as a rigid connection, allowing transfer of vibration from the rail track to the Bonds. Also, it is noted that the bolts are not entirely resiliently decoupled. Thus, the currently installed isolators are not effective in mitigating vibration transfer to the Bond.
- Based on the conclusion that the existing isolation system was deficiently designed and installed, additional testing was then conducted to determine the efficacy of an alternative system, which was based on wire-rope isolators (example shown in Figure 6).



Fig. 6 Wire Rope Isolator Example

Wire Rope Isolator Testing

Testing was then conducted at a number of locations to determine the relative effects between using the existing neoprene pad isolation system and proposed wire rope isolators. The following conclusions were drawn from this subsequent testing:

- A typical isolation curve for wire rope isolator and 3/8" thick neoprene isolators are presented in Figure 7. Note that positive values in Figure 7 show effective isolation while negative values indicate amplification of vibration. Based on

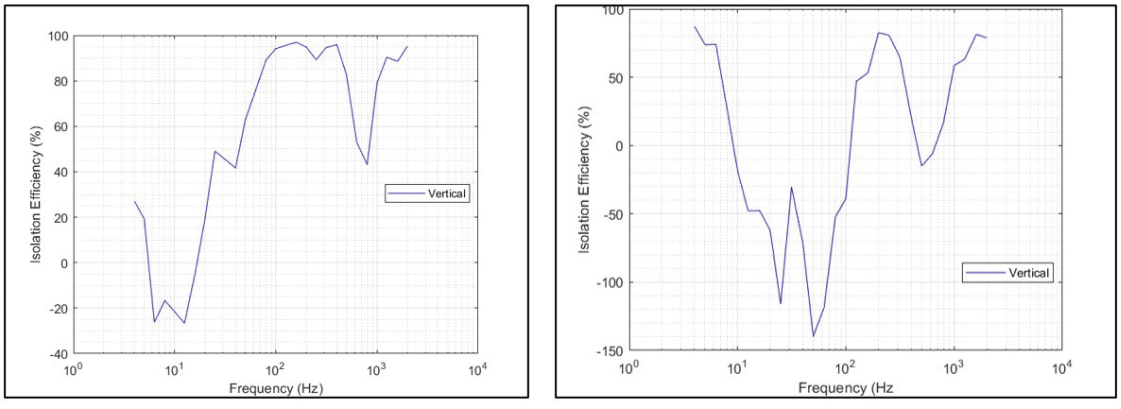

Vibration Isolation with Wire Rope Isolator

Vibration Isolation with 3/8" thick Neoprene Pad

Fig. 7 Comparison of Vibration Isolation Between Wire Rope Isolator and 3/8" Thick Neoprene Isolator

the assessment, isolation efficiency in the vertical direction is the governing factor for overall isolation performance, and as such, the details for lateral and longitudinal directions are not included in this paper.

- There is no isolation up to approximately 100 Hz with 3/8" thick neoprene pads. The isolation efficiency is also negative between 300 Hz and 500 Hz indicating that the neoprene configuration is not effective in isolating vibration at these frequencies.
- In the case of wire rope isolators, there is no significant isolation up to approximately 50 Hz. Above 50 Hz, the performance of wire rope isolator is significantly better than 3/8" thick neoprene pads. Overall, the isolation performance of wire rope isolators was significantly better than that of neoprene pads. The vertical isolation efficiency, averaged over different measurement locations is presented in Figure 8.

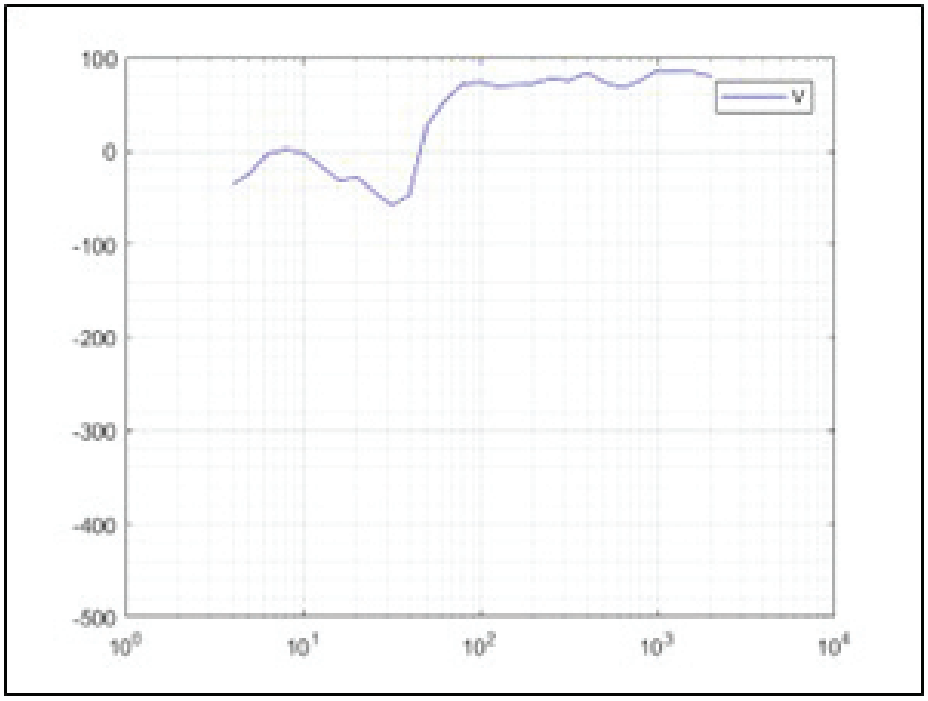

Fig. 8 Average Vertical Isolation Efficiency of Wire Rope Isolators

- It should be noted that an additional potential isolation short-circuiting path may be present in the system through the electrical cables that connect the Bonds to the tracks (which can be seen in Figure 1). It was decided to conduct additional measurements at one location to quantify vibration transfer through the electrical cable connection. At this locationn, the measurements were first conducted with the cable connections to the Bonds (typical installation). In the second setup, vibration levels were measured at the Bonds without these cable connections in place.
- Figure 9 provides a comparison of the isolation efficiency of these setups, which confirmed that vibration transfer through the cable connection was minimal. As noted previously, efficiency in the vertical direction governs the isolation design under the operating conditions.
- Based on the product data sheet for the wire rope isolator, the dominant frequency of the wire rope isolator is calculated to be 10 Hz. However, during the field testing, the dominant frequency was measured to be 20 Hz with two additional peaks at 30 and 32 Hz.
- In an effort to understand the discrepancy between theoretical and measured frequencies, the load-deflection curve and measured vibration levels were further examined.

    - At the frame below the Bonds, the root mean square (RMS) vertical vibration level was measured to be approximately 3g. This would roughly translate to 9 lbs force with a maximum RMS displacement of 0.04 mm.

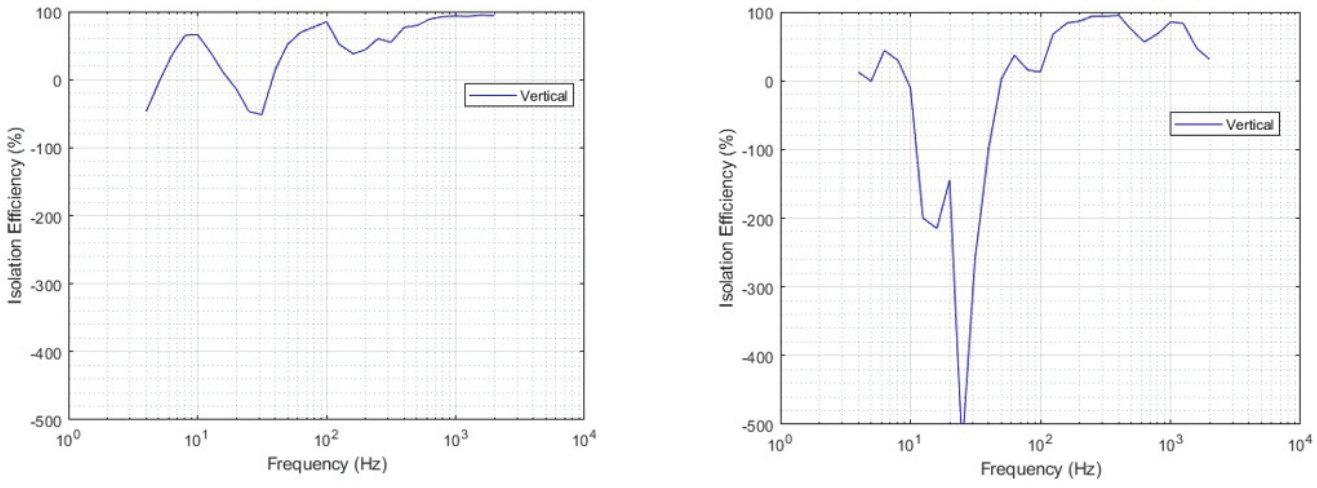

Fig. 9 Typical Isolation Performance with Wire Rope Isolator With and Without Cable

- As per the force-displacement curve, this falls within the initial region of the curve where stiffness is higher than the presented value in the product data sheet. With the higher stiffness values, the frequency of the as-built system is expected to be higher than 10 Hz.

- It was requested that the vendor of the wire rope isolator, provide more information on the load-deflection curve in the region of low amplitude displacement. The data provided was then extrapolated to estimate the stiffness of the wire rope isolator under the operating load regime. See Figure 10.

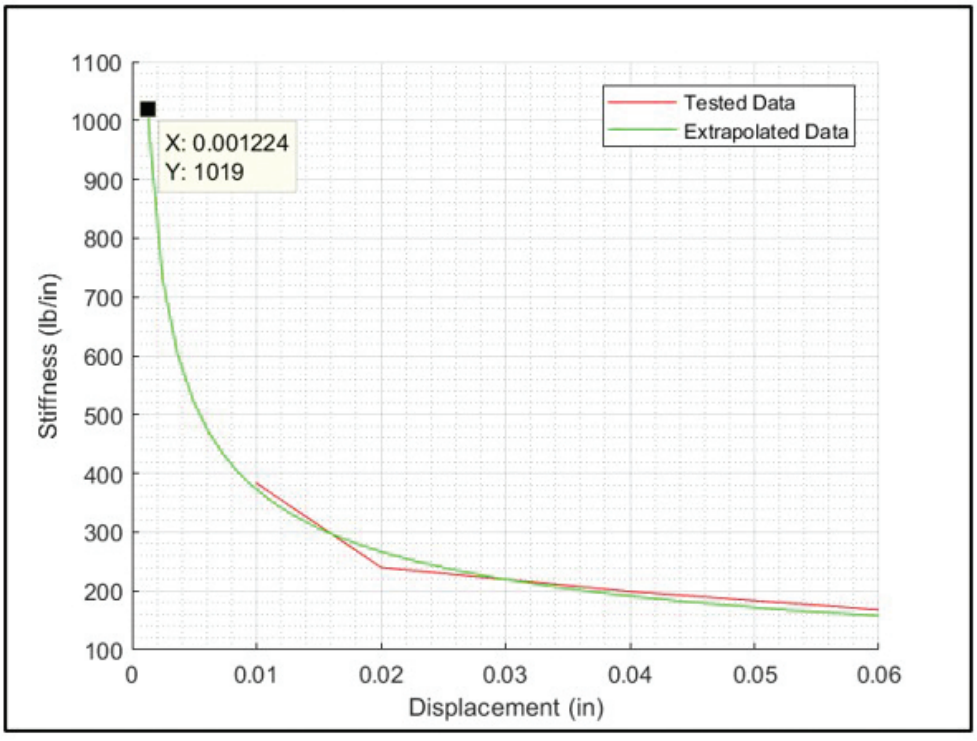

Fig. 10 Stiffness of Wire Rope Isolators Under Operating Conditions

- Based on the updated stiffness parameter under the operating load regime, the dominant frequency was predicted to be 19.80 Hz. Further, the load distribution of the wire rope isolator was noted to be non-uniform.
- Using the dimension and unsymmetric weight distribution of the Bonds atop the wire rope isolators, the rocking modes of the as-built system are predicted to be 31.6 and 33.3 Hz. These predicted frequencies correlate well with the measured frequencies of 20 Hz, 30 Hz and 32 Hz for wire rope isolators.
- Based on the measured vibration response and load distribution on the isolators, it was determined that achieving an isolation frequency of less than 20 Hz would require significantly reducing the stiffness of the wire rope isolators. This would correspond to a lower diameter strand of wire rope which itself is prone to fatigue failure under operating conditions.
- Based on this assessment, the recommendations for the wire rope isolators were modified so that the isolation performance was improved under operating conditions. The specifications for the final design of the wire rope isolators are summarized as follows:
    - Natural frequency of the isolator under operating condition <=20 Hz
    - Wire rope isolators at the front side (with more load from the Bonds) will have 4 loops
    - Wire rope isolators at the back side (with less load from the Bonds) will have two loops
    - Additional mass as shown in Figure 11 should be added to limit the contribution of rocking modes.
    - The maximum acceleration should be 150g with a duration of 2 ms.
    - The maximum dynamic deflection under operating condition should be 2 mm.

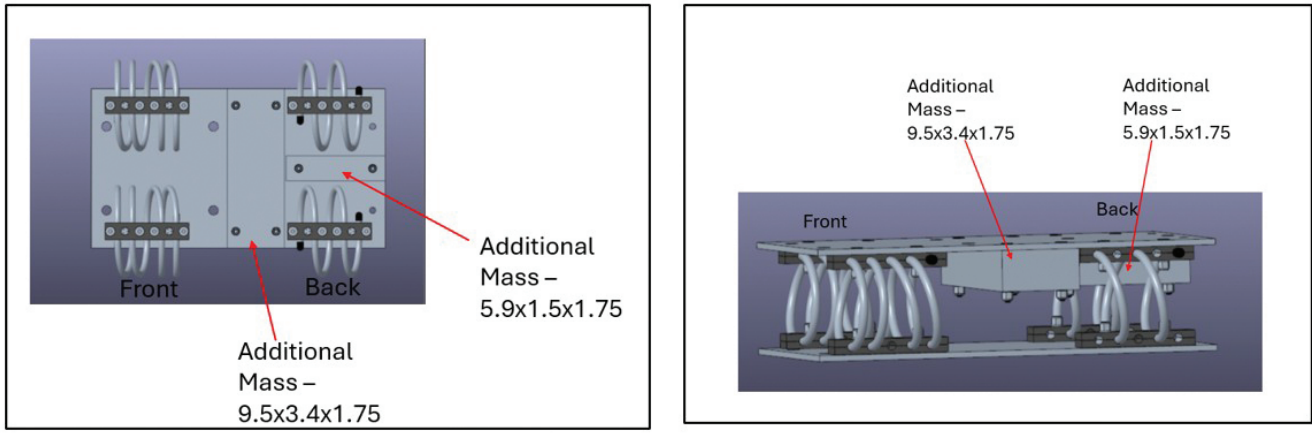

Fig. 11 Proposed Modifications to the Wire Rope Isolators

Mitigated Vibration Levels

In order to assess high magnitude energy content at frequencies between 700 Hz and 1000 Hz, the original AREMA limit at 200 Hz was proposed to be extended to 2000 Hz. Vibration levels below this modified limit were considered compliant for the assessment.

Using the isolation efficiency of the wire rope isolator setup, predicted mitigated levels from the measured highest vibration levels were obtained. The predicted mitigated results in the vertical direction are shown in Figure 12.

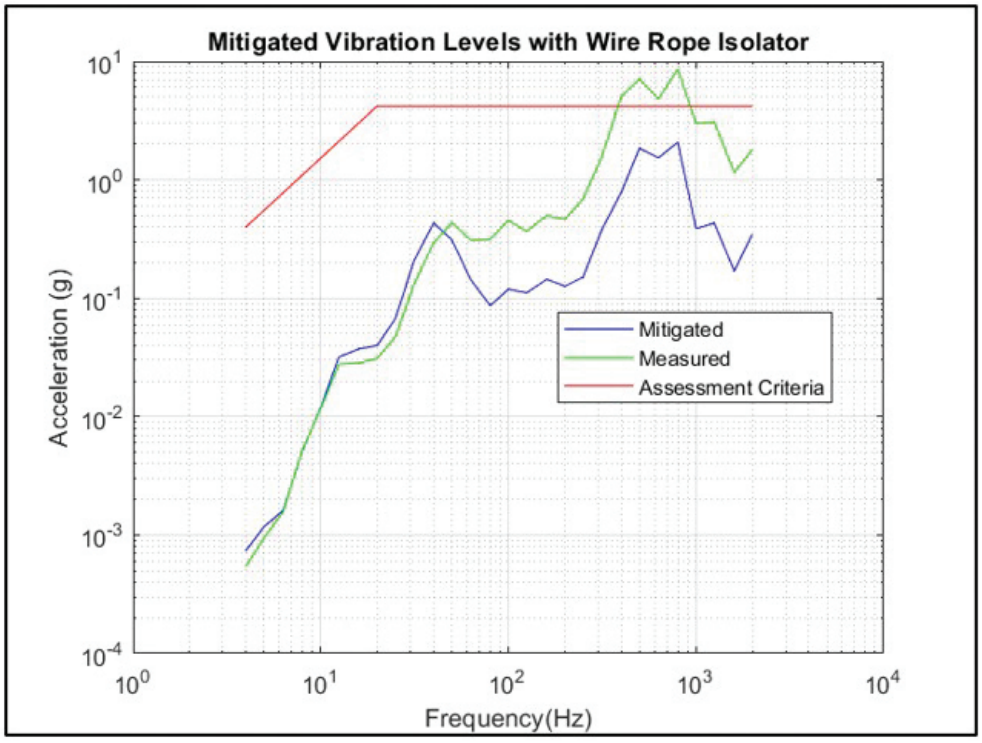

Fig. 12 Predicted Mitigated Vertical Vibration Level using Wire Rope Isolator

Conclusions

In order to determine repeated failures of the Bonds on a major commuter track, extensive vibration measurements were conducted. Consistently high magnitude energy content was measured at frequencies between 700 and 1000 Hz, which are related to wheel rail interaction, particularly due to trains operating at high speed. It was further noted that significant rail corrugation existed at the subject site. The combined effect of trains running at high speed and existing track conditions were concluded to be responsible for generating high vibration levels, which in turn were causing repeated failure of these Bonds.

Based on the existing vibration levels, wire rope isolators were proposed as an effective mitigation measure to isolate these Bonds from track vibrations. Considering the operating conditions, several modifications were proposed to improve the isolation performance of the wire rope isolators. The isolation efficiency of the wire rope was measured to be at least 80% in the frequency range of 700 to 1000 Hz. Overall, the isolation efficiency of the wire rope isolators were significantly better than the current isolation scheme involving 3/8" thick neoprene pad.

The following conclusions have been made:

- Adhering to AREMA Standard for assessing vibration levels on the Bonds may not be sufficient, as significant vibration levels were measured above the currently-specified 200 Hz upper limit of the AREMA criteria. As the PCB board located inside the Bonds could have resonance between 10 Hz and 2000 Hz, it is recommended to extend the measurement range up to 2000 Hz.
- In the design of vibration isolation, care should be taken to address any potential short circuits to reduce vibration transfer to the isolated structure. In addition, the elastic load range of the isolation material should be considerably higher than the applied static and dynamic loads. In this case, the axial force on the bolts exceeded the capacity of the neoprene pad and thus acted as a short circuit pathway for vibration transfer to the Bonds.
- In the case of vibration isolation with wire rope isolators, care should be taken to appropriately characterize the load range under operating condition. The wire rope isolators are non-linear in stiffness, and the properties change with input load level. Stiffness values reported in the vendor product data sheet may not be accurate for the intended load levels. It is recommended that testing be conducted to determine stiffness properties consistent with the load range under expected operating condition.

- In addition to dominant modes of the isolator setup, rocking modes of the as-built set-up should be included in the calculation of isolation efficiency. Depending on the stiffness and load distribution, these additional modes might play a significant role in establishing the efficiency of an isolator configuration.

Reference

1. American Railway Engineering and Maintenance-of-Way Association. Communications & signals manual. AREMA, 2025.

Chapter 16
Design and Construction of a Low-Cost Portable Seismic Shaking Table

Eliú Pineda and A. Ortiz

Abstract Studying structural behavior under seismic events is fundamental to civil engineering and risk management. However, access to seismic simulation equipment is limited in many institutions due to its high cost. This work presents a breakthrough in developing a low-cost, portable seismic table for earthquake simulation, making it accessible to research and teaching laboratories. The platform is based on a microcontroller and a stepper motor, enabling the reproduction of real seismic signals. A motion control system, optimized using a sinusoidal function, ensures simulation accuracy through digital signal processing. The seismic table features a preloaded earthquake library, enabling the playback of historical records without requiring an external connection. This significantly facilitates its use in educational and experimental settings, as users can immediately select and execute various seismic scenarios. Furthermore, the system incorporates the Internet of Things (IoT) through wireless connectivity, allowing for remote management of the seismic table via a web browser. The developed seismic table represents a significant advancement in the democratization of research in earthquake engineering, offering a cost-effective solution with digital connectivity, the ability to reproduce preloaded earthquakes, and unprecedented portability.

Keywords Low-Cost · Shaking Table · Engineering Education

Introduction

Seismic event simulation is a key tool in the teaching and research of civil engineering, particularly when integrated with the experimental response of structures. However, the high cost of simulation equipment limits its implementation in educational institutions, particularly in regions with restricted resources. This has motivated the development of accessible solutions that democratize access to technological tools. This work presents the development of a low-cost portable seismic table with IoT connectivity (called P-Shaker). Its design focuses on portability, ease of use, and the ability to simulate real seismic records, making it an ideal tool for teaching structural dynamics and applied research in educational contexts.

System Design

The P-Shaker seismic table consists of a fixed base and a mobile platform displaced by a leadscrew-nut system coupled to a stepper motor. The platform's linear movement is generated by the rotation of the leadscrew, which is directly coupled to the stepper motor, allowing precise displacement control through the sequential activation of coils and microstepping (Hughes and Drury, 2019).

Eliú Pineda
P-Sensors Labs. Armenia, Colombia
e-mail: epargel@gmail.com

A. Ortiz
School of Civil Engineering and Geomatics, Universidad del Valle, Cali, Colombia
e-mail: alrortiz@gmail.com

© The Author(s), under exclusive license to River Publishers 2026

Kristin B. Zimmerman, PhD (eds.), *Dynamics of Civil Structures, 2026, Vol. 2*, Conference Proceedings of the Society for Experimental Mechanics Series, https://doi.org/10.13052/rp-9788743814139



Fig. 1 Design and execution of the P-Shaker in PLA

The control system is composed of a microcontroller (Espressif Systems, 2016) that coordinates the execution of simulations, processes signals, and hosts a web interface for remote control and monitoring. From this interface, accessible from any device connected to the local Wi-Fi network, users can select different types of simulations, configure parameters, and run experiments wirelessly.

The P-Shaker is designed to reproduce three main types of signals:

- Frequency sweep: allows for exploring the structural response to variations in excitation frequency, which helps identify natural vibration frequencies through resonance. (Figure 2)
- Sinusoidal control: the user can manually adjust frequency, amplitude, and acceleration to generate personalized oscillatory movements.
- Preloaded earthquake reproduction: The system has a library of real historical earthquakes obtained from the IRIS database. These signals are pre-processed in Python using numerical integration and smoothing techniques to avoid unwanted mechanical vibrations. The result is stored as .json files, containing the motor's target positions, which ensures trajectory fidelity and movement precision. (Figure 2)

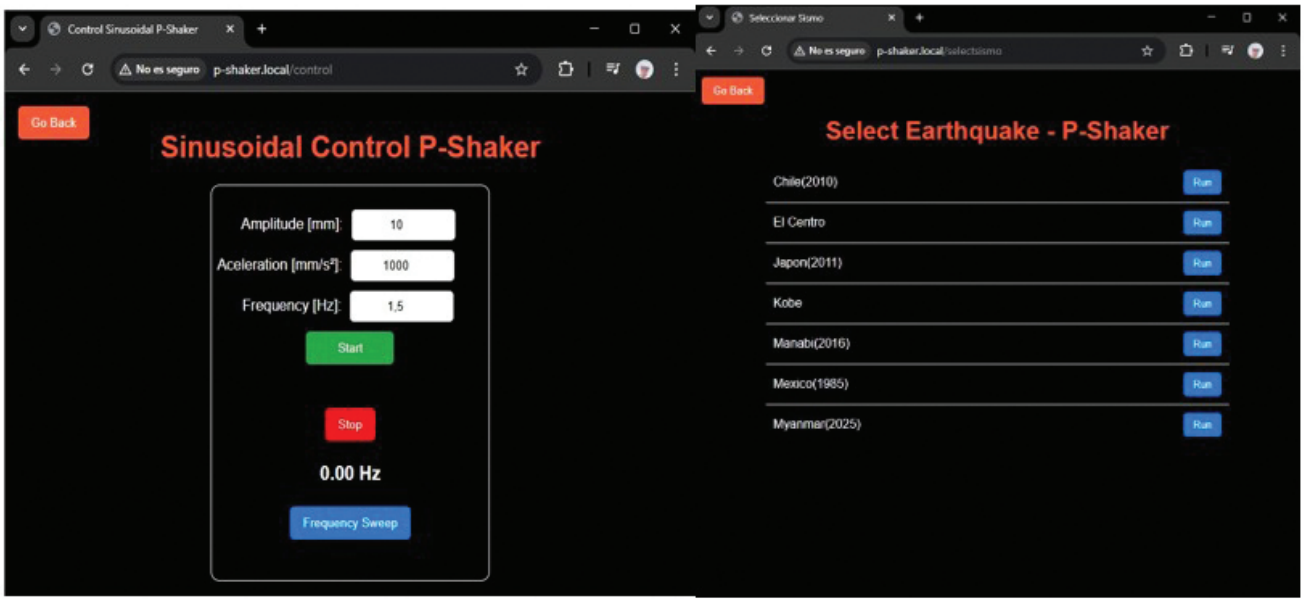

Fig. 2 Web access to the frequency sweep and sinusoidal control (left) and the preloaded earthquake reproduction dashboard of the P-Shaker (right)

Results and Discussion

Experimental simulation

To validate the table's dynamic behavior, simulations were conducted using both synthetic and real seismic signals. The system was capable of executing a sinusoidal function with frequencies ranging from 0.5 Hz to 10 Hz, demonstrating stability throughout its operational range. The input frequency was compared with the one obtained using FFT on the Android accelerometer app (Plaincode, s.f.). The maximum amplitude reached was 60 mm, with good linearity in displacement as shown in Figure 3.

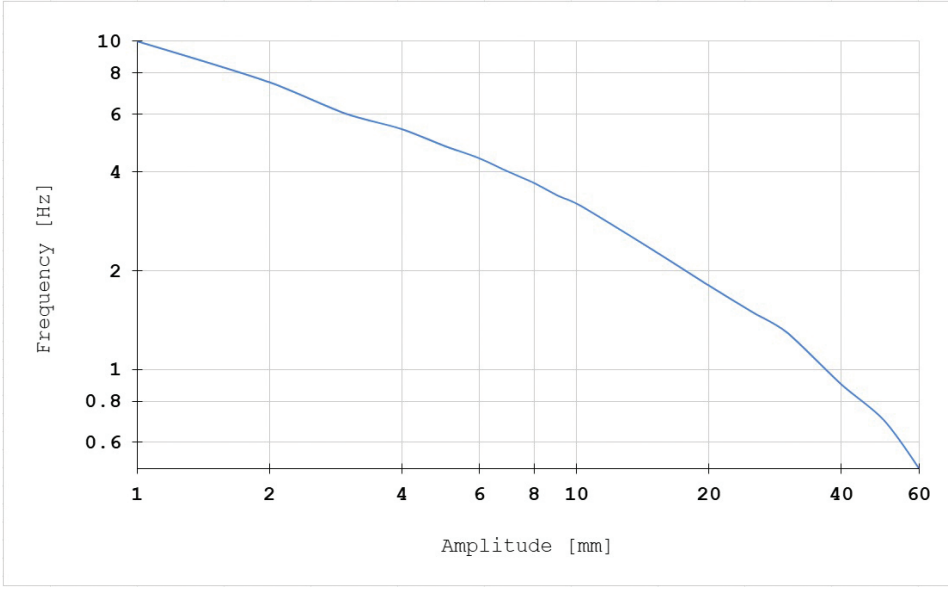

Fig. 3 Frequency response as a function of the maximum reached amplitude of the sinusoidal function

Records obtained from IRIS (NSF, 2013), such as the Myanmar earthquake (2025), were tested. The trajectories were reproduced satisfactorily, especially at the dominant frequencies.

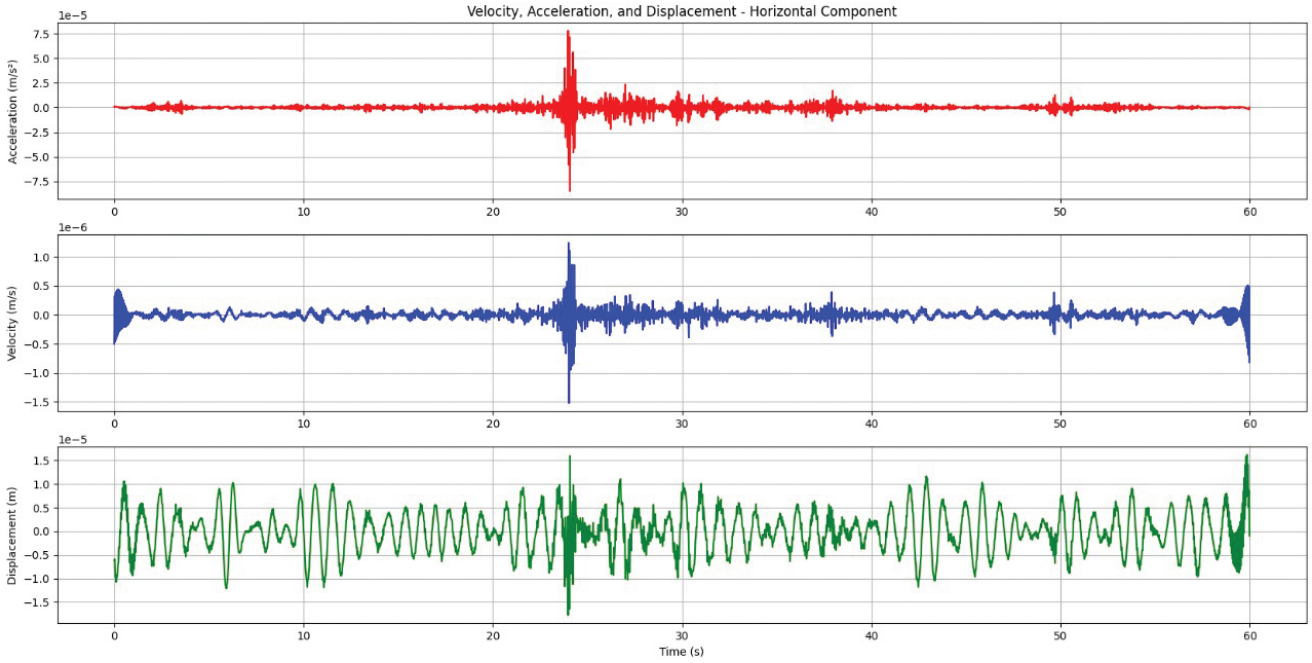

Fig. 4 Connection to IRIS, download of Myanmar information, and conversion to a format read by P-Shaker

Educational and research applications

The P-Shaker is currently on the market and has been used in university laboratory sessions to visualize structural responses in scale models. Engineering students were able to interact directly with the system, configuring parameters and observing

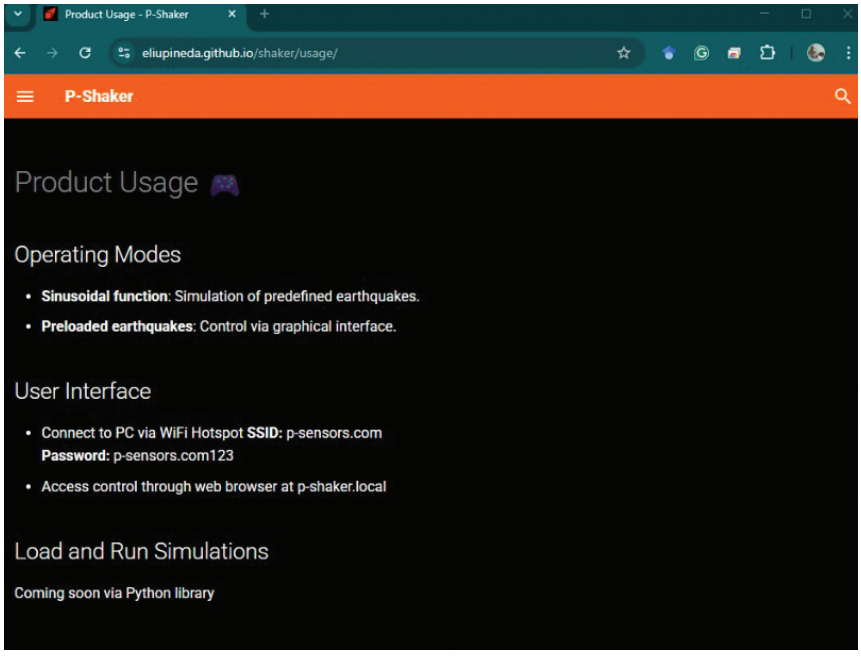

Fig. 5 P-Shaker documentation (P-Shaker, 2025) for education

phenomena such as resonance. Its use is also projected for research on structural reinforcement and active control tests in reduced structures, venturing into simulation areas studied in (Chopra, et al., 2017). The seismic table's website can be consulted here: https://eliupineda.github.io/shaker/.

Conclusions and Future Work

The development of the P-Shaker seismic table represents a significant step forward towards democratizing access to structural simulation tools in educational and research settings. Its low-cost design, portability, and remote connectivity make its implementation possible in university laboratories, technical schools, and training centers with limited resources. The experimental results have shown that the P-Shaker is capable of accurately reproducing different types of signals, ranging from sinusoidal functions to real earthquakes, which enables the study of phenomena such as resonance, damping, and the dynamic response of scaled structures. Further improvement of its fidelity is expected. Furthermore, the use of a web interface facilitates interactive learning and enables multiple users to operate the system without requiring programming or electronic expertise.

Future lines of work include extension to two degrees of freedom (X-Y), which will allow for simulating two-dimensional trajectories and torsional phenomena in structures; Implementation of closed-loop control with sensor feedback, which will improve the system's precision against external disturbances; Integration of real-time data visualization for immediate analysis of the performed tests; and the publication of the project as open source, promoting academic collaboration, continuous improvement, and the possibility of being replicated by other institutions.

Furthermore, the development of educational guides and laboratory manuals is planned to enable teachers and students to implement experimental practices using the seismic table in courses on structural dynamics, earthquake engineering, or seismic-resistant design. This educational vision, combined with accessible technology and connectivity, makes the P-Shaker a versatile and high-impact tool in training engineers who are better prepared for the challenges of seismic risk.

References

1. Hughes, Austin, and Bill Drury. Electric motors and drives: fundamentals, types and applications. Newnes, 2019.
2. Espressif Systems. (2016). Final report: ESP32 Datasheet. Online: December 3, 2022, at https://www.espressif.com/
3. Sumy, Danielle F., Russ Welti, and Michael Hubenthal. "Applications and evaluation of the IRIS earthquake browser: A web-based tool that enables multidimensional earthquake visualization." Seismological Society of America 91.5 (2020): 2922-2935.

Chapter 17
Performance Evaluation of a Damped Vibration Absorber for Traffic Signal and Sign Structures

Richard Christenson and Carl Macchietto

Abstract Transportation ancillary structures (traffic structures), including traffic signal support structures and sign structures, are typically characterized by their high flexibility and low inherent damping. These dynamic characteristics make these structures particularly susceptible to wind-induced vibration. Wind loading, including galloping, vortex shedding, natural wind gusts, and truck-induced gusts, can result in vibration of these traffic structures. The low natural frequencies of these structures overlap with the excitation frequency of winds and can result in large amplitude and cyclical response and repeated live load stress variations which can induce fatigue and significantly reduce the safe life of these structures. Reducing the effective stress range, the difference between the maximum and minimum stress in a cycle, by minimizing the wind-induced vibration can significantly increase the operational life of the structure.

At the design stage, traffic structure vibration is commonly addressed by increasing the stiffness and strength of the structure. This results in larger poles and mast arms as well as overbuilt connection details. A more effective alternative is the application of vibration absorbers to increase the damping of the structure and reduce the response. An innovative damped vibration absorber has been developed utilizing both eddy current and pneumatic damping to provide a robust and durable vibration absorber for traffic structures. This presentation will document the effective damping of the proposed device over a range of structures. A series of laboratory and field tests on in-service structures will be presented to illustrate the efficacy of the damped vibration absorber over a wide-range of structures.

Keywords passive structural control · vibration mitigation

Introduction

Traffic signal structures are often supported by cantilevered flexible structural elements with low damping which makes them susceptible to wind-induced vibration and corresponding fatigue and failure. These structures are often located adjacent to or directly over roadways where maintenance, repair or replacement is costly in terms of time and money. Failure of the structure can compromise the safety of the traveling public. The current AASHTO LRFD Specifications for Structural Supports for Signs, Luminaries, and Traffic Signals (AASHTO LRFD SLTS Specifications) [1] addresses potential failure due to wind vibrations by requiring members and connections to have nominal strengths more than the expected loadings by a sufficient margin to reduce risk of failure to an acceptable amount [2]. This requirement can result in inefficient structural designs that use large members and overbuilt connections, which is a poor use of material and financial resources. The AASHTO LRFD SLTS Specifications indicate that in lieu of designing to resist periodic galloping forces, effective vibration-mitigation devices can be used for cantilever sign and traffic signal structures, based on historical or research verification of its vibration damping characteristics and as approved by the Owner. Recently approved revisions to the specifications, that will be published in the next AASHTO LRFD and LTS Specification Editions, will provide for a quantitative procedure to evaluate and implement effective mechanical vibration devices into the retrofit and design of traffic signal structures. In

Richard Christenson
University of Connecticut, Storrs, CT 06269
e-mail: rchriste@engr.uconn.edu

Carl Macchietto
Vice President of Product & Management, Valmont Structures, Valley, NE 68064
e-mail: cmacchietto@valmont.com

© The Author(s), under exclusive license to River Publishers 2026

Kristin B. Zimmerman, PhD (eds.), *Dynamics of Civil Structures, 2026, Vol. 2*, Conference Proceedings
of the Society for Experimental Mechanics Series, https://doi.org/10.13052/rp-9788743814139

these revisions, an effective vibration-mitigation device can be accounted for in the design process by reducing the fatigue demand through use of a response modification factor (R, or R-factor). The use of an R-factor requires suitable testing and modeling of the vibration mitigation device is performed and documented.

Various devices have been considered to reduce excessive wind-induced vibrations in traffic signal structures. Vibration absorbers, such as tuned mass dampers, tuned liquid dampers, friction dampers, impact dampers, struts and elastomeric pads, work by dissipating the energy of the wind loading applied to the structure through mechanical means [3–11]. These devices have been observed to have various levels of success. Often, these mechanical damping devices must be tuned specifically for a given traffic signal structure or become ineffective. One particularly effective and robust mechanical damping device that does not require tuning is the Valmont TR1 damper. This presentation will present the laboratory and field testing of the TR1 vibration mitigation device for the use of dampers in the design and protection of traffic signal structures.

The device considered is the Valmont Industries TR1 damper (US Patent 9,470,288, 10,036,446, 11,181,165, 11,821,487, and various International Patents), which is intended to effectively reduce vertical mast arm and sign structure vibrations caused by wind vortex shedding, galloping, and truck gusts. The TR1 damper is a damped vibration absorber. The device consists of a 4.5” diameter by 43” long tube that is attached near the end of the mast arm, often hidden from view by signals or signs mounted on the mast arm, with a total weight of 35.75 lbs. The TR1 damper energy dissipation is through both eddy current damping and pneumatic damping. The eddy currents are circular electric currents induced within conductors by the movement of a magnet next to the conductive material. These circular currents are opposite the direction of movement creating a resistance and thus damping. The pneumatic damping occurs as the damper mass translates up and down within a sealed chamber. The exchange of air from the upper air chamber to the lower air chamber creates velocity dependent resistance.

Laboratory Testing

The TR1 damper is tested to determine its effect on the desired range of properties of target structures. Two traffic signal structures, both 50 foot (50’) long mast arms, with different cross sections and different added weights, are used to provide various combinations of frequency and dynamic weight for the laboratory testing in the Structures Research Laboratory at the University of Connecticut. The dynamic behavior characterized for the structure with the applied mechanical vibration mitigation device is the effective damping ratio, ζ, of the system. A strain sensor is installed on the mast arm near the connection to the pole. The damping ratio is determined through free vibration tests where the structure is manually excited vertically with a harmonic (sinusoidal) motion at the first natural frequency to an amplitude above 12” and the structure then released. The free vibration response is measured with the strain sensor and used to calculate the natural frequency and damping ratio.

The four traffic signal support structure configurations were realized by testing two different mast arms with and without added mass. Both mast arms were attached to the same shortened pole that was bolted to the strong floor. The steel pole had a height of 4.5 ft. with a 13.2” outside diameter (OD) at the base, a 12.5” OD at the tip, and a wall thickness of 0.2391”. Mast Arm 1 (Large 50’ Mast arm) was 50 ft. long with a 12.5” outside diameter (OD) at the base, a 5.5” OD at the tip, and a wall thickness of 0.2391”. Mast Arm 2 (Slender 50’ Mast arm) was 50 ft. long with a 10” outside diameter (OD) at the base, a 3” OD at the tip, and a wall thickness of 0.1793”. Damping in the first mode is determined from the free vibration tests to increase from 0.1% to between 2.3%-9.3%.

Field Testing

The damping performance verified with comprehensive field testing to ensure robust performance. Information on 17 field tests conducted in 11 different states and 1 foreign country will be provided in the presentation. The TR1 dampers have been applied to mast arms ranging from 45 ft to 75 ft and natural frequencies from 0.61 Hz to 1.2 Hz. The dampers have been observed to increase the first mode damping in the traffic signal structures from 30-60 times the inherent damping of the pole structure by itself. These field tests demonstrate definitively the performance achieved with the TR1 damper for various types of actual traffic signal structures.

References

1. AASHTO. LRFD Specifications for Structural Supports for Highway Signs, Luminaires, and Traffic Signals. First Edition, 2015. LRFDLTS-1.
2. AASHTO. Standard Specifications for Structural Supports for Highway Signs, Luminaires, and Traffic Signals. 6th Edition, 2013.
3. Lengel, J. S., and M. L. Sharp. Vibration and Damping of Aluminum Overhead Sign Structures. Highway Research Record, 1969. Issue 259:51–60.
4. Jo, I., T. Kaneko, S. Nagatsu, C. Takahashi, and M. Kimura. Development of Highway Light Pole with Resistance to Wind Vortex-Induced Oscillations. Technical Report 21, Kawasaki Steel Corporation, 1989.
5. Hamilton, H. R., G. S. Riggs, and J. A. Puckett. Increased Damping in Cantilevered Traffic Signal Structures. Journal of Structural Engineering, 2000. 126(4):530–537.
6. Cook, R. A., D. Bloomquist, D. S. Richard, and M. A. Kalajian. Damping of Cantilevered Traffic Signal Structures. Journal of Structural Engineering, 2001. 127(12):1476–1483.
7. Cook, R. A., D. Bloomquist, D. S. Richard, M. A. Kalajian, V. A. Cannon, D. P. Arnold, and M. H. Ansley. Design, Testing, and Specification of a Mechanical Damping Device for Mast Arm Traffic Signal Structures. Final Project Report, UF Project No. 4910 45 04 680 12, Structures and Materials Research Report No. BC-050, 2000.
8. McManus, P. S., H. R. Hamilton, and J. A. Puckett. Damping in Cantilevered Traffic Signal Structures under Forced Vibration. ASCE Journal of Structural Engineering, 2003. 129(3):373–382.
9. Hoque, S., and R. E. Christenson. Reducing Fatigue in Wind–Excited Traffic Signal Support Structures Using an Innovative Vibration Absorber. Transportation Research Record: Journal of the Transportation Research Board, 2011. No. 2251:16–23.
10. Christenson, R. Reducing Fatigue in Wind-Excited Traffic Signal Support Structures Using Smart Damping Technologies. NCHRP-IDEA Program Project Final Report, 2011.
11. Li, L., G. Song, M. Singla, and Y.-L. Mo. Vibration Control of a Traffic Signal Pole Using a Pounding Tuned Mass Damper with Viscoelastic Materials (II): Experimental Verification. Journal of Vibration and Control, 2015. 21(4):670–675.

Chapter 18
A Pilot Study on Pedestrian Comfort Under Vertical Vibrations

Rajesh Govindan, Bintian Lin, Genevieve K. R. Williams, and Stana Živanović

Abstract The pedestrian comfort to footbridge vibration is likely influenced by numerous parameters specific to the structure and the person crossing the bridge. In the current design practice, vibration magnitude is routinely considered when defining vibration serviceability limits. Some design standards, such as BS 5400 (outdated) and ISO 10137 (current), also define frequency-dependent vibration limits, while the exposure time and pedestrian's pacing frequency are routinely neglected.

This pilot study explores the perceptual effects of vertical vibration during walking, with relevance to vibrations experienced on footbridges, using a combination of controlled and randomized test parameters. Unlike previous studies that typically ignored the influence of one or more parameters of interest, this study examined combined effect of vibration magnitude, vibration frequency, pacing frequency, and exposure time.

The findings reveals that vibration magnitude, frequency, and exposure time are the principal determinants of subjective comfort, whereas derived parameters related to gait or its combination with vibration parameters such as pacing frequency, frequency ratio, and frequency deviation did not significantly influence perceived comfort.

Keywords Footbridges · Vibration serviceability · Pedestrian comfort · Vibration perception · Exposure time

Introduction

Pedestrian comfort on footbridges is influenced by both structural and human factors, with vibrations capable of evoking responses ranging from mild discomfort to instability. Current design practice primarily addresses vibration magnitude [1], while some standards BS 5400 (outdated) [2] and ISO 10137 [3], also include frequency-dependent limits. However, important factors such as exposure time and pacing frequency are not explicitly considered, despite their potential influence on perceived comfort.

Most previous research has concentrated on static postures (seated, standing, or supine) or on structural responses under pedestrian loading [4–6]. Studies directly addressing pedestrian comfort during walking are relatively limited. Pioneering investigations [7, 8] and later systematic studies [9–11] demonstrated that walking pedestrians perceive vibrations at much higher levels than standing individuals, and that factors such as pacing rate, age, and gender can influence tolerance. However, the combined effects of vibration magnitude, frequency, pacing frequency, and exposure time on comfort remain underexplored.

This pilot study addresses these gaps by systematically examining the perceptual effects of vertical vibration during walking, with relevance to footbridge vibrations, under controlled laboratory conditions. Unlike previous studies that typically ignored the influence of exposure time, this research explores the combined effect of vibration magnitude, vibration frequency, walking speed, and exposure time to identify key predictors of perceived discomfort. Following this introduction, Section 2 describes the methodology, including test participant, experimental setup, instrumentation, test protocols, and data processing. Section 3 presents the results on the simultaneous influence of these parameters on subjective comfort ratings.

Rajesh Govindan(✉) · Bintian Lin · Stana Živanović
School of Engineering, University of Warwick, Coventry, United Kingdom
e-mail: Rajesh.Govindan@warwick.ac.uk; Bintian.Lin@warwick.ac.uk; S.Zivanovic@warwick.ac.uk

Genevieve K. R. Williams
Department of Public Health and Sport Sciences, University of Exeter, Exeter-EX1 2LU
e-mail: g.k.r.williams@exeter.ac.uk

© The Author(s), under exclusive license to River Publishers 2026

Kristin B. Zimmerman, PhD (eds.), *Dynamics of Civil Structures, 2026, Vol. 2*, Conference Proceedings
of the Society for Experimental Mechanics Series, https://doi.org/10.13052/rp-9788743814139

Methodology

Test Participants

The pilot study was conducted with single voluntary participant (TP: Female, age 50, and body mass index 22.22 kg/m^2) from University of Warwick. Participant signed an informed consent before the beginning the experiment as required by the University's Biomedical and Scientific Research Ethics Committee. The participant was physically active with no history of motion sickness, vibration sensitivity and/or walking locomotion impairments and pregnancy.

Experimental Setup

The vertical vibration applied through octopod motion platform (VSimulators, University of Exeter) equipped with treadmill to allow prolonged walking during the experiments. The 3.7m $\times$ 3.7m motion platform reproduces motion with high fidelity within limits of $\pm$ 21 mm displacement and 2 m/s^2 maximum acceleration over a 0 to 40 Hz frequency range. An Optitrack motion capture system provided real-time full-body kinematic tracking using reflective markers with sampling rate of 100 Hz. Participant wore a wireless noise-cancelling headphones (Sony WH-1000xm4) to mask the sound produced by the motion platform (Fig. 1a).

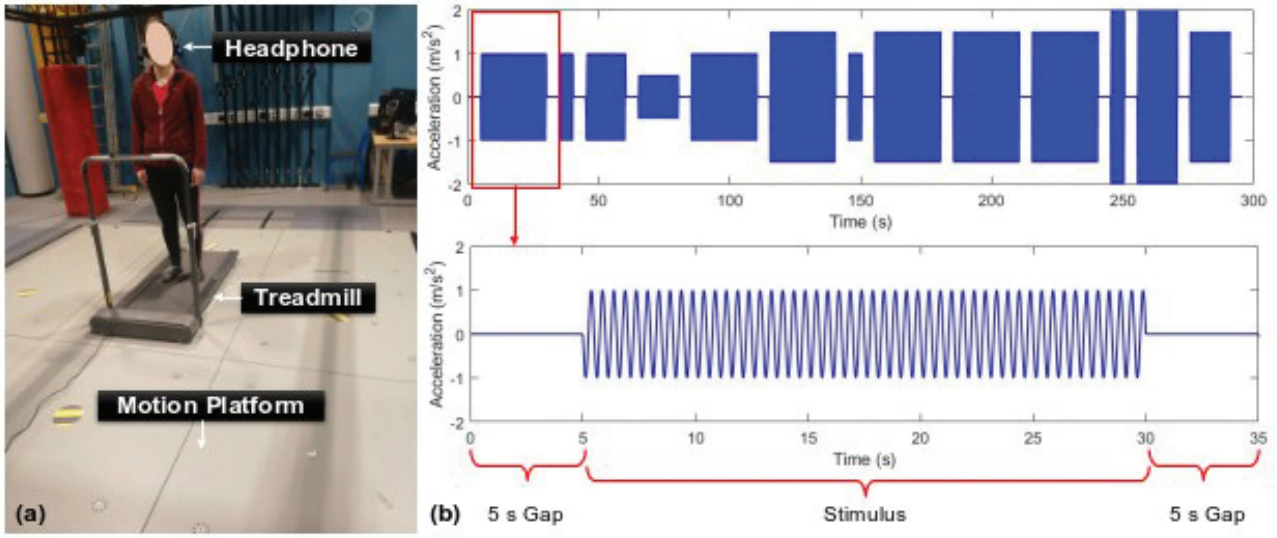

Fig. 1 (a) Test participant on the treadmill placed on the motion platform (b) Top: representative randomized vibration stimuli block; Bottom: representative 25 s exposure time stimulus with 5 s gaps

Test Protocol

The participant was exposed to four vibration magnitudes (0.5, 1.0, 1.5 and 2.0 m/s^2), eight frequencies between 1.587 and 8.0 Hz in 1/3 octave band, and three exposure times (5, 15 and 25 s), approximating the time required to cross the central span of 15 m, 45 m and 75 m bridges, respectively. Walking trials were conducted at three preferred speeds (Slow, Normal and Fast).

Experiments were completed over two sessions on separate days. At the start of first session, preferred walking speeds were established. Participants began walking on the treadmill at 2.5 km/h, with speed adjusted in 0.5 km/h increments to identify "normal" walking speed. Slow and fast speeds were determined by decreasing or increasing from the normal speed in 0.5 km/h increments until noticeably slower or brisk but still comfortable pace was reached. Trials at normal speed were conducted in the first session, while slow and fast speed trials were completed in the second session.

At each speed, participant exposed to 96 randomized vibration stimuli (four amplitudes $\times$ eight frequencies $\times$ three exposure time) including one no-vibration trial per exposure time. The combination of 2 m/s^2 and 1.587 Hz was excluded due to VSimulators performance limitation. To manage participant fatigue due to continuous walking, the 96 stimuli were divided into seven blocks of around five minutes each (including five-seconds gaps between stimuli). An example of the randomized

vibration stimuli block and a stimulus with five-seconds gaps is shown in Fig. 1b. Participant walked continuously during each block and rested for 150 s between blocks. Following each stimulus, during the five-second gap, participant rated their vibration comfort on a five-point scale: not perceived, comfortable, slightly uncomfortable, moderately uncomfortable or strongly uncomfortable.

Data Acquisition and Processing

Before the experimental session, two markers were placed on the heels of the participant shoes to detect the heel-strike event. The trajectories of the markers were filtered with 4th order low-pass Butterworth filter with a cut-off frequency of 16 Hz. The heel-strike event was identified as a time instance at which horizontal (fore-aft) velocity of leading leg heel marker changes from positive to negative [12]. The time between two successive heel-strikes of both feet gave the step time. The pacing frequency (f_p) was computed as the reciprocal of step time.

To determine the combined influence of pacing frequency and vibration frequency on subjective comfort, two additional measures were defined: frequency ratio and frequency deviation. The frequency ratio (FR) was computed as the ratio between the harmonic (n) of participant's mean pacing frequency (f_p) and the vibration frequency (f_v). Specifically, for each test i.e. response measured for the given stimulus, the frequency ratio was calculated as:

$$FR = \frac{nf_p}{f_v}, \text{ where } n = 1, 2, 3, 4 \tag{1}$$

The harmonic yielding the FR value closest to unity (i.e., the smallest absolute deviation from 1) was selected, and the corresponding FR was used for further analysis.

The frequency deviation ($|\Delta f|$) quantifies the absolute difference between the harmonics of participant's mean pacing frequency (f_p) and the vibration frequency (f_v). Specifically, for each test, absolute frequency deviation was calculated as:

$$|\Delta f| = |nf_p - f_v|, \text{ where } n = 1, 2, 3, 4 \tag{2}$$

The harmonic that minimized this difference was selected, and the corresponding $|\Delta f|$ value was used for subsequent analysis.

Data Analysis

The influence of test parameters (vibration magnitude (a_v), vibration frequency (f_v), exposure time (T_{exp}) and walking speed (w_s)) and derived parameters (pacing frequency (f_p), frequency ratio (FR), and frequency deviation (Δf)) on the subjective comfort of participant under vibration exposure were statistically analysed. Spearman's rank correlation (ρ) was used to assess monotonic relationship among test parameters, derived parameters and subjective comfort ratings. An ordinal regression analysis was applied to examine the simultaneous influence of test and derived parameters on subjective comfort ratings. Descriptive statistics of test and derived parameters is shown in Table 1.

Table 1 Descriptive statistics of test and derived parameters for walking condition on a vibrating surface

	N	Minimum	Maximum	Mean	Std. Deviation	Skewness		Kurtosis	
						Statistic	S.E.	Statistic	S.E.
Walking Speed (km/h)	279	3.860	5.470	4.720	0.663	-0.246	0.146	-1.505	0.291
Exposure Time (s)	279	5.000	25.000	15.000	8.180	0.000	0.146	-1.505	0.291
Vibration Magnitude (m/s^2)	279	0.500	2.000	1.226	0.552	0.051	0.146	-1.325	0.291
Vibration Frequency (Hz)	279	1.587	8.000	4.147	2.082	0.576	0.146	-0.889	0.291
Pacing Frequency (Hz)	279	1.549	1.999	1.776	0.143	-0.260	0.146	-1.459	0.291
Frequency Ratio (-)	279	0.710	1.320	0.995	0.151	0.099	0.146	-0.893	0.291
Frequency Deviation (Hz)	279	0.001	0.608	0.224	0.160	0.614	0.146	-0.335	0.291

N: Number of tests, S.E.: Standard Error

Results and Discussion

An ordinal logistic regression was conducted to assess the combined effects of vibration magnitude (a_v), vibration frequency (f_v), exposure time (T_{exp}), pacing frequency (f_p), frequency ratio (FR), and frequency difference ($|\Delta f|$) on subjective comfort rating (Table 2). All test and derived parameters were standardized using z-scores to place them on a common scale, facilitating comparability and ensuring that differences in measurement units did not bias the regression coefficients. Since strong correlations between test and derived parameters may introduce multicollinearity and affect reliability of regression model, Spearman's rank correlation (ρ) was used to assess the parameter association (Table 2).

Walking speed was found to be highly correlated with pacing frequency ($\rho = 0.941$, $p < 0.01$) and was therefore excluded from the regression analysis. Subjective comfort ratings showed a strong positive correlation with vibration magnitude ($\rho = 0.782$, $p < 0.001$), a weak positive correlation with exposure time ($\rho = 0.195$, $p = 0.001$) and a weak negative correlation with vibration frequency ($\rho = –0.187$, $p = 0.002$).

Table 3 presents ordinal logistic regression model for subjective comfort rating as a function of vibration magnitude (a_v), vibration frequency (f_v), exposure time (T_{exp}), pacing frequency (f_p), frequency ratio (FR), and frequency difference ($|\Delta f|$). The model was statistically significant ($\chi^2(6) = 345.73$, $p < 0.001$) and demonstrated excellent fit, explaining 75% of the variance in subjective comfort ratings (Nagelkerke R^2).

Table 2 Association among the test parameters, derived parameters and subjective comfort rating

Parameter	w_s	T_{exp}	a_v	f_v	f_p	FR	$\|\Delta f\|$	SR
				Spearman correlation coefficient (ρ)				
Walking Speed (w_s)	1	0	0	0	**0.941****	0.041	0.024	0.038
Exposure Time (T_{exp})	0	1	0	0	-0.013	0.021	-0.004	**0.195****
Vibration Magnitude (a_v)	0	0	1	0.068	0.012	-0.073	0.045	**0.782****
Vibration Frequency (f_v)	0	0	0.068	1	0.004	-0.114	**0.366****	**-0.187****
Pacing Frequency (f_p)	**0.941****	-0.013	0.012	0.004	1	0.027	0.002	0.04
Frequency Ratio (FR)	0.041	0.021	-0.073	-0.114	0.027	1	-0.042	0
Frequency Deviation ($\|\Delta f\|$)	0.024	-0.004	0.045	**0.366****	0.002	-0.042	1	-0.055
Subjective Rating (SR)	0.038	**0.195****	**0.782****	**-0.187****	0.04	0	-0.055	1

** Correlation is significant at the 0.01 level (2-tailed).

The estimated thresholds represent the cut-points on the latent comfort scale that separate adjacent subjective ratings. Among the predictors, vibration magnitude (a_v) was the strongest determinant of subjective comfort ($\beta = 3.006$, $p<0.01$), indicating that higher vibration magnitudes substantially increased the odds of reporting greater discomfort. Vibration frequency (f_v) showed a significant negative effect ($\beta = –1.174$, $p<0.01$), suggesting that increasing frequency was associated with lower odds of reporting higher discomfort. Exposure time (T_{exp}) also had a significant positive influence ($\beta = 0.843$, $p<0.01$), meaning longer exposure increased the likelihood of higher discomfort.

In contrast, the derived parameters (pacing frequency (f_p), frequency ratio (FR), and frequency difference ($|\Delta f|$)) were not statistically significant predictors, as their odds ratios were close to 1 and confidence intervals crossed unity, indicating little or no effect on subjective comfort within the tested conditions.

The present study demonstrates that vibration magnitude, frequency, and exposure time are the principal determinants of subjective comfort, whereas derived parameters related gait or its combination with vibration parameters such as pacing frequency, frequency ratio, and frequency deviation did not significantly influence perceived comfort once vibration characteristics were accounted for. The strong effect of vibration magnitude aligns with previous studies reporting that higher acceleration levels consistently intensify discomfort and reduce walking stability on vibrating structures [10, 11]. Similarly, the observed negative association with vibration frequency is consistent with evidence that, under constant acceleration, increasing frequency reduces vibration displacement amplitude, thereby making walking less uncomfortable [10]. The role of exposure time as a significant predictor is particularly noteworthy, as current vibration serviceability standards ISO 10137 and Sétra [1, 3] do not explicitly account for it. This finding is consistent with results from studies of statics postures, where prolonged exposure amplifies the cumulative effect of vibration on perceived discomfort up to certain threshold [13, 14]. Pacing frequency and frequency ratio, often highlighted in pedestrian-structure interaction studies [15] and have been as-

Table 3 Association between subjective comfort ratings and test and derived parameters

	Parameter	β	SE	95% CI for Odds Ratio		
				Lower	Odds Ratio	Upper
Threshold	Not Perceived	-6.438***	0.507	0.001	0.002	0.004
	Comfortable	-1.405***	0.21	0.162	0.245	0.371
	Slightly Uncomfortable	1.138***	0.204	2.09	3.12	4.657
	Moderately Uncomfortable	3.561***	0.301	19.514	35.204	63.508
Predictors	Vibration Magnitude (a_v)	3.006***	0.2309	12.855	20.214	31.785
	Vibration Frequency (f_v)	-1.174***	0.1607	0.226	0.309	0.423
	Exposure Time (T_{exp})	0.843***	0.1373	1.774	2.323	3.04
	Pacing Frequency (f_p)	0.109	0.1278	0.868	1.115	1.432
	Frequency Ratio (FR)	0.038	0.1295	0.806	1.038	1.338
	Frequency Deviation ($\|\Delta f\|$)	0.007	0.1407	0.764	1.007	1.327

β: Regression coefficient. SE: Standard error. CI: Confidence Interval. R^2 = 0.71 (Cox & Snell), 0.75 (Nagelkerke). Model $\chi^2(6) = 345.73$, $p < 0.001$. *** $p < 0.001$

sociated with reduced vibration sensitivity at higher walking speed [9]. The absence of such effects in the present study suggests that vibration sensitivity may be highly individual and influenced by participant-specific factors.

Conclusions

The study highlight the significance of vibration magnitude, frequency, and exposure time in shaping subjective comfort during walking under vertical vibration exposure. These results provide empirical support for existing vibration serviceability guidelines while also emphasizing the need to consider exposure time, which is not explicitly addressed in current standards. Future research involving larger and more diverse participant groups will be essential to validate and generalize these findings, offering a more comprehensive understanding of human comfort under vertical vibrations. Such evidence can contribute to the development of improved vibration design criteria for pedestrian bridges and similar structures.

Acknowledgments This work was supported by UKRI Horizon Europe Guarantee (MSCA Postdoctoral Fellowship) under Grant No. EP/Y027817/1 (SENSATION).

References

1. Sétra. Footbridges: Assessment of Vibrational Behaviour of Footbridges under Pedestrian Loading, Technical Guide.; Paris, 2006.
2. British Standards Institution (BSI) BS 5400. Steel, Concrete and Composite Bridges - Part 2. Specification for Loads. 2006, 32–34.
3. International Organization for Standardization ISO 10137.:2007. Bases for Design of Structures-Serviceability of Buildings and Walkways against Vibrations; Switzerland, 2007.
4. Qin, J. W.; Law, S. S.; Yang, Q. S.; Yang, N. Pedestrian-Bridge Dynamic Interaction, Including Human Participation. J. Sound Vib., 2013, 332 (4), 1107–1124. https://doi.org/10.1016/j.jsv.2012.09.021.
5. Ahmadi, E.; Caprani, C.; Živanović, S.; Heidarpour, A. Assessment of Human-Structure Interaction on a Lively Lightweight GFRP Footbridge. Eng. Struct., 2019, 199. https://doi.org/10.1016/j.engstruct.2019.109687.
6. Drygala, I. J.; Nisticò, N. Design and Validation of a Fiber-Reinforced Polymer Cable-Stayed Pedestrian Bridge: Human-Induced Actions vs. Comfort Levels. Materials (Basel)., 2024, 17 (12). https://doi.org/10.3390/ma17122842.
7. Leonard, D. R. Human Tolerance Levels for Bridge Vibration; Road Research Laboratory, 1966.
8. Smith, J. W. The Vibration of Highway Bridges and the Effects on Human Comfort. University of Bristol 1969.
9. Dang, H. V.; Živanović, S. Influence of Low-Frequency Vertical Vibration on Walking Locomotion. J. Struct. Eng., 2016, 142 (12). https://doi.org/10.1061/(asce)st.1943-541x.0001599.
10. Ma, R.; Ke, L.; Wang, D.; Chen, A.; Pan, Z. Experimental Study on Pedestrians' Perception of Human-Induced Vibrations of Footbridges. Int. J. Struct. Stab. Dyn., 2018, 18 (10), 1–19. https://doi.org/10.1142/S021945541850116X.

11. Feng, P.; Wang, Z.; Jin, F.; Zhu, S. Vibration Serviceability Assessment of Pedestrian Bridges Based on Comfort Level. J. Perform. Constr. Facil., 2019, 33 (5). https://doi.org/10.1061/(asce)cf.1943-5509.0001316.
12. Zeni, J. A.; Richards, J. G.; Higginson, J. S. Two Simple Methods for Determining Gait Events during Treadmill and Overground Walking Using Kinematic Data. Gait Posture, 2008, 27 (4), 710–714. https://doi.org/10.1016/j.gaitpost.2007.07.007.
13. Miwa, T. Evaluation Methods for Vibration Effect: Part 7. The Vibration Greatness of the Pulses. Ind. Heal., 1968, 6, 14.
14. Gallais, C. Effect of Vibration Exposure Duration on Discomfort, University of Southampton, 2008.
15. Živanović, S.; Pavić, A.; Ingólfsson, E. T. Modeling Spatially Unrestricted Pedestrian Traffic on Footbridges. J. Struct. Eng., 2010, 136 (10), 1296–1308. https://doi.org/10.1061/(ASCE)ST.1943-541X.0000226.

River Rapids

Dynamics of Civil Structures, Volume 2

P. Scott Harvey ■ Fernando Moreu

Dynamics of Civil Structures, Volume 2: Proceedings of the 44th IMAC, A Conference and Exposition on Structural Dynamics, 2026, the second volume of ten from the Conference brings together contributions to this important area of research and engineering. The collection presents early findings and case studies on fundamental and applied aspects of the Dynamics of Civil Structures, including papers on:

- Structural Vibration
- Dynamics of Bridges, Buildings, and Infrastructure Systems
- Innovative Sensors and Measurement Techniques for Structural Applications
- Structural Control and Vibration Mitigation
- Human Induced Vibrations and Human-Structure Interaction
- Modal Identification of Structural Systems
- Human Health Monitoring Using Structural Sensing
- Field Monitoring of Vibrations

ISBN 978-87-438-1441-2



River Publishers